Evaluation of the durability of elastomeric easy-release coatings

by

Anne-Claire Christiaen, B.S., M.S.

Dissertation submitted to the Faculty of the
Virginia Polytechnic Institute and State University
in partial fulfillment of the requirements for the degree of

Doctor of Philosophy

in

Mechanical Engineering

Norman S. Eiss, Jr., Chair
Michael J. Furey
Ron G. Kander
Irwin L. Singer
Brian Vick

July 1998

Blacksburg, Virginia

Evaluation of the durability of elastomeric easy-release coatings

Anne-Claire Christiaen, Ph.D.
Virginia Polytechnic Institute and State University, 1998
Advisor: Norman S. Eiss, Jr.

Abstract

Novel coatings have been designed to solve problems associated with biofouling of marine structures, particularly ship hulls. The best candidates to date are multilayered coatings incorporating silicone rubber technology. These materials are efficient because they exhibit excellent release properties. However, they are very soft and tend to be more susceptible to various forms of mechanical damage. Fundamental analysis of the durability of these coatings has been done using standard laboratory tests. Simulative studies are essential to screen candidates as well as to predict the true life of the systems. The goal of this project was to develop a testing protocol for the evaluation of the durability of elastomeric easy release coatings and to implement it on selected candidate coatings.

A brushing apparatus was designed and built to simulate the cleaning processes of ship hulls. Wear was measured with profilometry. The proposed methodology is valuable to study the processes of wear of the coatings, to screen various materials and to identify parameters, either functional or material, which would directly affect their durability.

Two groups of candidate coatings were tested: the EXS series and the NRL series. The EXS series samples showed better wear resistance than the NRL series samples and showed no dependence on the rotational speed of the brushes. The NRL series samples showed that increasing the sliding speed resulted in a decrease in wear. An increase in the applied load resulted in increased wear for both sample series. The effect of coating thickness was also investigated and discrimination between the proposed coatings could not be established because the tips of the bristles were sharp and irregular. Scratches matching

the path of the brush bristles were observed in the wear scars of both sample types under all load and speed conditions. The NRL samples also exhibited ridges perpendicular to the sliding direction similar to the abrasion pattern.

To Demi-Tasse

Acknowledgments

Dr. N. S. Eiss, Jr., thank you for advising me.
Dr. I. L. Singer, thank you for serving on my committee as well as for the valuable visit of the Naval Research Laboratories.
Dr. R. G. Kander, thank you for serving on my committee as well as for the use of your laboratory facilities.
Dr. Michael F. Furey and Dr. Brian Vick, thank you for serving on my committee.

The Office of Naval Research, thank you for partial funding of this project.

LaShaun J. Berrien, Aurélie Boyer, Carlos from EE, Sophie Casenave, Marc et Sylvie Christiaen, Jen Howard, Mitch Jackson, Dr. Rita Kline, Jerry Lucas, Dr. J. R. Mahan, Jerry Lucas, Dr. Carl and Linda Pfeiffer, Steve York, thank you for contributing to this dissertation in your own way.

Papa et Maman, Jim, Mary, Merci Mille Fois.
Vous seuls connaissez les sacrifices que ce projet nous a coutés!

Anne-Claire Christiaen

Virginia Polytechnic Institute and State University
July 1998

Contents

List of Tables

List of Figures

Chapter 1

Introduction

Biofouling is the settlement and growth of any organisms on man-made structures placed in water. Fouling is complex and diverse in time and space. It can be categorized into biofilms and macrofoulers. Biofilms are composed of bacteria, diatoms and other microalgae. Macrofoulers include soft species such as algae, sea grass, slimes, tunicates, sponges or bryozoans as well as hard species such as encrusting worms, mussels or barnacles. The latter have calcereous shells and are the hardest to remove from a surface.

Marine biofouling has been a major problem for the Navy. It greatly affects operations by reducing the maneuverability, the operational range and the performance of ships. It increases drag, reduces cruise speed, increases fuel consumption and increases acoustic noises of ships and submarines. As a result, the mission readiness and sustainability of the fleet are compromised. Biofouling attacks Navy systems other than ships and submarine hulls by blocking sea water intakes to nuclear reactor cooling systems, obstructing optical windows or clogging storage systems. The Navy faces high expenditures directly associated with biofouling. For example, in 1992, the US Navy spent $100 million on biofouling for hull cleaning, painting, repainting, and waste disposal associated with cleaning (Alberte et al., 1992). It is also estimated that $500 million is spent annually by the US Navy on drag-related fuel penalties (Schumacher, 1996).

The need to improve ship performance by limiting the amount of fouling on hulls traces back many centuries. The U.S. Navy has always been searching for the ideal technique to keep the hulls from fouling. With the introduction of steel hulls in the 19^{th} century, sheathing technology used on wood hulls was replaced by painting technology. The early

paints contained copper in the form of cuprous oxide which poisoned organisms, thereby protecting the hull. A major breakthrough came in the 1970's with the implementation of tri-n-butyl tin (TBT) paints whose gradual implementation for ship and submarine hulls was ordered by the Navy in 1986 (Alberte et al., 1992). In 1987, 90 % of the world's new fleet was coated with a form of a TBT copolymer paint. However, detrimental environmental effects were recorded in areas of concentrated ship activity (Alzieu et al., 1980; Alberte et al., 1992). Legislative restriction for the use of these paints followed shortly after. As a consequence, a tin-free ablative paint containing cuprous oxide as the primary antifouling agent was developed and implemented on the majority of the U.S. Navy fleet (Alberte et al., 1992).

In the 1990's, a novel approach was introduced with the developement of fouling release (FR) coatings. Containing no biocide, FR coatings do not inhibit biological adhesion like traditional metallic-based paints do. Instead, organisms do settle on the surface. But the reduced surface energy that most of the candidate coatings display alters biological adhesion and allows a much easier cleaning process because the required force to remove any form of biological organisms is greatly reduced. Silicone based elastomeric coatings have been shown to be the best candidates. Unfortunately, most of the FR coatings developed are much softer than the traditional coatings, hence they are more likely to be damaged while the ship is in service.

Mechanical damage to the ship hull can be caused by impacts with piers, flotsam or submerged objects, erosion by sand in shallow waters, and cleaning processes of the hulls. Biological and chemical damage has been observed as well (Leidheiser Jr. and Kendig, 1978; Preiser and Halpern, 1983): oil imbibing or bacteria attacks can lead to blistering and delamination of the coating (Meyer et al., 1995).

In order to optimize the cleaning process of the FR coatings and limit damage, Wathen (1994) and Schumacher (1996) determined the brushing force required to remove pseudo-barnacles from panels coated with FR materials as a function of brush and bristle characteristics as well as operational parameters such as the rotational speed and the translation speed of the brushes. The purpose of their studies was to help with the design of new hull cleaning devices which are adapted to the new generation of coatings.

However, Wathen (1994) and Schumacher (1996) do not address the damage caused to the coatings tested by the various brushes. Cleaning processes may lead to serious damage

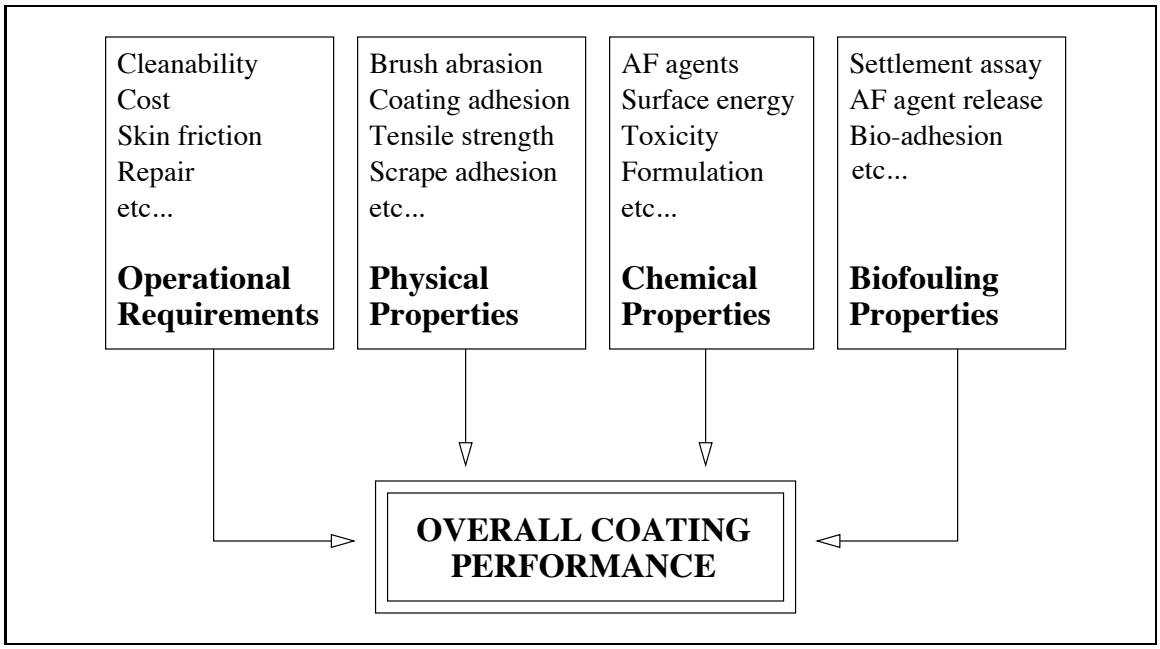

Fig. 1.1 Factors and properties which influence the performance of a marine coating system

to the coatings. Information on fouling release properties for a given coating formula is not sufficient to predict its overall performance as shown on figure 1.1. It is equally important to evaluate mechanical damage and eventual loss of fouling release properties caused by cleaning processes.

Conventional wear tests such as the falling sand test (ASTM D968, 1991) are not suitable because they do not discriminate amongst candidate coatings (Meyer et al., 1995). Alternate specialized durability tests are needed for the evaluation of FR coatings. A rotating brush apparatus was developed at the State University of New-York at Buffalo (SUNY-Buffalo) by Meyer et al. (1995). The wear tester is a toothbrush tester of dental materials which was adapted for the study of the abrasion of FR coatings. It provides excellent quantitative analysis of the wear resistance of FR coatings to cleaning brushes. Cooperation with tribologists is necessary to understand better the wear behavior of the candidate coatings. Dr. Singer at the Naval Research Laboratories developed a methodology including scratch and scrape tests, methodology which provides an accelerated evaluation of the failure of the novel FR coatings (Bolster and Singer, 1996). The methodology is very valuable as it provides a basic and systematic study of coatings. However, these tests do not simulate the field conditions.

Due to the limitations of the existing apparatus, the design of a new device is nec-

essary to study the wear behavior of the coatings under simulative conditions, i.e. under the action of cleaning brushes under water. This is the task undertaken in this study. The objectives are to:

- develop a test method to evaluate coating durability, including the design and construction of a new versatile brushing device,
- screen candidate coatings for use on hulls,
- study the processes of friction and wear of FR coatings in the case of multiple sliding contacts,
- identify parameters, either functional or material, which will directly affect wear and/or friction behaviors of the FR coatings,
- determine critical parameters in cleaning processes of the candidate coatings, and
- relate laboratory wear tests to field cleaning methods.

Predicting the durability of candidate FR coatings while in operation is the ultimate goal of the project.

Chapter 2

Background

2.1 What is biofouling?

As defined in the introduction, biofouling is the settlement and growth of any organisms on man-made structures placed in water. Understanding the generic features of biological adhesion has been the goal of many scientists. When the mechanism of attachment of biological organisms is known, then it will be easier to develop the ultimate paint system.

Typical mechanisms of attachment includes mechanical adhesion, adhesion by pressure difference, Stefan adhesion, and of course adhesion with glue. Most adult macrofoulers such as tubeworms or barnacles bond very efficiently to surfaces with glue.

Swain et al. (1992) developed a method to measure the shear strength of barnacles (ASTM D5618, 1994). A parallel study also showed that the adhesion of so-called pseudo-barnacles, beads of a two-part epoxy, can simulate the adhesion of real barnacles on silicone coatings without additives (Schultz and Swain, 1997; Swain et al., 1997): for these specific coatings, short-term laboratory tests can replace long-term tests for the evaluation of new fouling release candidate coatings.

2.2 Biofouling prevention

2.2.1 Cleaning techniques

Periodic underwater cleaning of the U.S. Navy fleet was initiated in 1978 to rejuvenate the copper-based paints which fouled heavily within 15 to 18 months of service.

Initially, survey of the existing underwater hull condition is conducted by visual

Table 2.1 Hull cleaning devices listed by Schumacher (1996)

Brushing device	MC311	Brushboat	SCAMP®	Sea Vac
Brush path width (ft)	3.3	20	5	6
Speed of travel (ft/min) [1]	197	20	90	100
Number of brushes	3	1	3	3
Max. cleaning rate (ft^2/min)	646	400	450	600
Brush type	disk	cylindrical	disk	disk

[1] maximum obtainable speed under ideal conditions

inspection with trained divers who identify and report conditions such as paint blistering and peeling, corrosion, fouling and superficial structural damage with reference to two scales (NAVSEA, 1989). The first scale, the fouling rating scale, describes the ten most frequently encountered fouling patterns. Condition 0 describes the ideal situation with a clean, foul free surface such as one that is observed on a ship out of dry dock. Condition 100 describes the worst situation where all forms of fouling are present. The second scale rates the paint deterioration from 0 to 100, with increasing severity. Conditions 10–30 represent surfaces with normal physical wear, whereas conditions 60-100 indicate advanced deterioration of the entire anticorrosion/antifouling paint system.

There are two common cleaning methods: the water jet technology and mechanical scrubbing (Delaney, 1982).

Water jets

Water jet technology consists of forcing water under pressure through a small nozzle. Conventional water jetting equipment operates at approximately 15,000 psi (Conn and Johnson Jr., 1974; Hilaris and Labus, 1979; Taylor and Chapman, 1991). It is primarily used for cleaning areas of the hulls which are not easily accessed (Seaward Marine Services Inc., 1993) and during dry dock maintenance.

Mechanical scrubbing

Mechanical scrubbing is the most common and most effective technique used to clean ship hulls. Several devices have been developed as presented in table 2.1.

The brushboat system uses a 20 foot cylindrical brush lowered against the side of the ship. It is limited to large, flat areas and is ineffective against hard macrofoulers.

Table 2.2 Types of disk brushes used on U.S. Navy ships according to NAVSEA (1989)

Navy I.D.	Diameter (in.)	Material	Bristle Diam. (in)	Bristle length (in.)
A	14	Polypropylene	0.5	1
C	13	Steel	Flatwire, 0.14×0.02	1.75
D	5/7/12	Silicon carbide in nylon	0.06	1
D3, D5[1]	7.5/9	Silicon carbide	N/A	N/A
E1	20	Galv. steel, 7×19 wire	0.1875	6, 2 rows, 60 bristles per brush
E2	20	Galv. steel, 7×19 wire with copper ferrules	0.1875	6, 2 rows, 60 bristles per brush, 15 ferrules max.

[1] 3- and 5-density abrasive marine cleaning disk brush

An Australian system was developed with three brushes mounted on a boom hung over the support vessel, with a diver controlling the speed and pressure of the brushes against the hull. In the United States, Seaward Marine Services, Inc. has been in charge of the underwater hull cleaning of the Navy fleet since 1979. For large hull areas, Seaward uses the SCAMP® machine, a multi-brush self-propelled cleaner (Butterworth Systems, 1981), which was first introduced in 1971. It is 6 feet in diameter and holds three large rotating brushes as seen on figure 2.1. Traveling underwater across the ship's hull on three traction wheels, the machine is either controlled by a professional diver, or operated remotely to advance, stop, reverse or hold a parallel line of motion as it makes approximately a five-foot cleaning swath at a traveling rate equal to $450\,\mathrm{ft}^2$/min. It is held against the hull by an impeller located in its center, resulting in a fixed clamping force of 1,000 pounds. The operating power is supplied by a nearby boat. The time required to perform a SCAMP® underwater cleaning ranges from 4 to 16 hours, depending upon the size of the vessel, the areas fouled or the extent of fouling. The brushes are selected according to the results of the hull survey conducted prior to cleaning. The brushes currently used by the U.S. Navy are listed in table 2.2. Since they are used on traditional metallic paints, they are very aggressive. A foul release coating such as a silicone-based elastomer would be destroyed with such brushes. In contrast, it was shown that the use of brushes composed of polypropylene bristles limits damage to copper coatings (Cologer et al., 1977) and are sufficiently effective to remove fouling from FR coatings (Wathen, 1994; Schumacher, 1996).

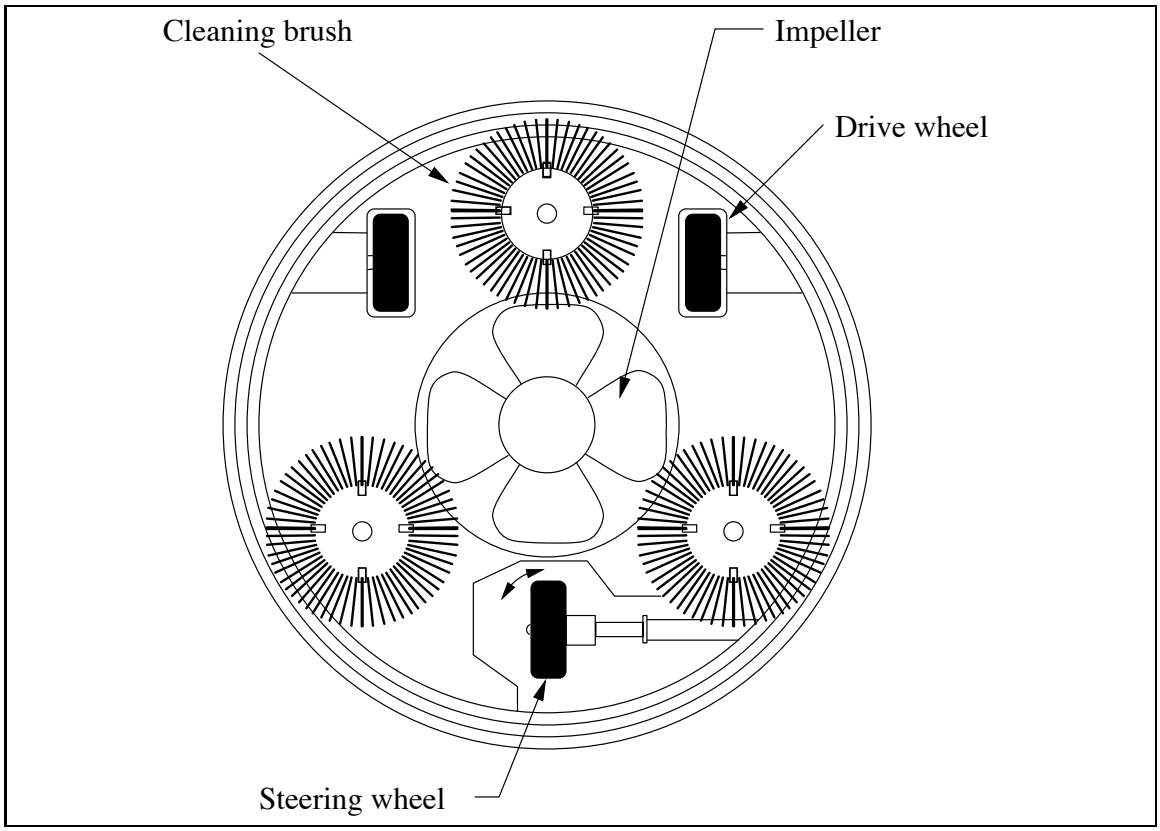

Fig. 2.1 The SCAMP® unit

In the case of metallic-based coatings, cleaning processes not only remove biofouling but they also rejuvenate the antifouling paint system. Seaward Marine Services, Inc. claims that no damage is caused to the hull of a ship coated with traditional antifouling paints. However, the current methods need to be adapted for the novel FR coatings.

2.2.2 Antifouling and fouling release coatings

Historical perspective

In Greece, tar and wax was the method of choice to control fouling on marine structures prior to the third century when lead sheathing was implemented. In the 18^{th} century, as the corrosive action of lead on iron was evidenced, copper sheathing replaced lead sheathing and became standard procedure. The antifouling action of copper was assigned to the dissolution of copper in sea water. In the 19^{th} century, iron ship hulls were introduced. Zinc replaced copper for a short period of time. As copper was proven to be the best antifoulant, efforts were made to insulate the ship hull from the corrosive copper sheathing. These costly procedures were quickly abandoned. Since then, the Navy has been searching for the ideal antifouling coating for steel hulls.

Traditional antifouling coatings

In the 1950's, the specification formula F121, a red cuprous oxide, vinyl rosin antifouling paint was developed by Mare Island Navy Shipyard to fill a 2-year expected life requirement and extend dry docking intervals to $5-7$ years (Alberte et al., 1992). The F121 paint becomes inert and a green surface layer composed of insoluble copper salts develops, blocking further release of copper. Serious fouling follows within 15 to 18 months of service. Periodic cleaning was then implemented in order to rejuvenate a F121-painted hull by removing the detrimental green layer and exposing fresh red paint. However, within 30–36 months, the surface of the hulls become impervious to repeated cleaning processes at increasing intervals and dry docking is necessary before the $5-7$ year requirement set by the Navy.

In the 1970's, antifouling coating technology was directed towards organotin copolymers. In order to increase the antifouling service life of the coatings as well as to minimize unnecessary pollution, efforts were directed towards controlling the release rate of toxicants. Following studies of many organotin copolymers including field tests and ship trials,

the concept of ablative antifouling coatings was introduced. These coatings were designed to slowly ablate from the surface in relation with the ship speed and time at sea. Not only did ablative antifouling coatings show the advantage of self-renewal, but they also provided a reduced drag by the alteration of surface roughness. However, in the late 1980's, regulatory pressures on organotin antifouling coatings started as excessive concentration of tin and subsequent detrimental effect of the ecolocical balance were observed in areas of extended ship activity (Alzieu et al., 1980; Alberte et al., 1992).

A tin-free ablative antifouling paint containing only cuprous oxide was developed and was juged satisfactory. In 1992, these coatings were in use for most naval applications and were still far superior to the F121 paint. However, the $5-7$ year in service requirement still remained to be met.

In the 1990's, the Office of Naval Research (ONR) and the Office of Naval Technology (ONT) developed a program to provide the Navy with an environmentally acceptable interim solution for the biofouling problem. The goals of the program included:

- develop advanced non-polluting antifouling or fouling release self-cleaning coatings with improved operational lifetime, and
- establish and refine testing protocols in order to provide rational and accelerated evaluation of novel coatings in laboratory, short-term field and quasi-operational conditions.

Guidelines of the program, which integrates programs from universities, Navy laboratories and industries, include the identification of naturally-occurring AF agents, the development of easy release coatings and the refinement of controlled-release systems for the AF agents. The program is divided into four sections, 6.1, 6.2, 6.3 and 6.4. Section 6.1 has been focusing on studies of biofouling, natural antifouling agents, molecular mechanisms of attachment as well as on silicone and fluoro polymer technologies. A combination of molecular biology, polymer and surface chemistry will help design the ideal surface and/or AF agents. Section 6.2 is entitled "biomolecular antifouling coatings". Researchers in the areas of easy-release polymers, control release technologies and non-toxic antifouling agents are working together to come up with the design of prototype coatings. These coatings will then be tested in the field as well as in laboratories for performance, cleaning and durability. Section 6.3 is directed by the Naval Sea System Command (NAVSEA) and targets the evaluation and commercialization of nontoxic coating systems. It addresses life cycle needs

as well as the coating durability. Section 6.4 is entitled "advanced nontoxic antifouling coatings". Its purpose is to demonstrate 6.2 technology on Coast Guard hulls and electrical power plant water intakes.

Novel coatings

The principles of antifouling and fouling release coatings are intrinsicly different. While antifouling coatings are effective in the prevention of the attachment of biological organisms, fouling release coatings are effective in the removal of any biofouling population. Indeed, antifouling paints limit biofouling by poisoning the organisms whereas fouling release coatings ease the detachment of any settled organism. The ultimate coating would be such that, while in operation, forces created along the submerged hull by the cruise speed of the ship would be sufficient to remove biofouling growths.

One major advantage of the fouling release coatings over antifouling coatings is that they are not toxic and are environmentally acceptable. The successful fouling release candidate coatings exhibit low surface tension in a range of $20 - 30$ mN/m (Meyer et al., 1994). The most successful coatings to date are based on silicone elastomers such as polydimethylsiloxane and were already known to control fouling in the early seventies. The use of silicone elastomers has been dictated by their unique properties.

Silicone elastomers Silicone rubber became commercially available in 1944 from Dow Corning Corporation and General Electric Company. It has been studied extensively (Mark, 1990; Bhowmick and Stephens, 1988; Lynch, 1978; Schwartz and Goodman, 1982). Silicone polymers have many applications: membranes, electrical insulators, water repellents, antifoaming agents, mold release agents, adhesives, protective coatings, release control agents for agricultural chemicals, encapsulation media and hydraulic, heat-transfer and dielectric fluids (Mark, 1990).

Composition Silicone rubbers consist of organic and inorganic sections. The backbone is made of alternating silicon and oxygen atoms. Each silicon atom has two organic groups attached to it, with the chain-end silicon atoms having a third group of organic, hydroxyl or alkoxy types. In the most common siloxane polymer, polydimethylsiloxane (PDMS), the side groups are methyl groups as represented on figure 2.2. There are three

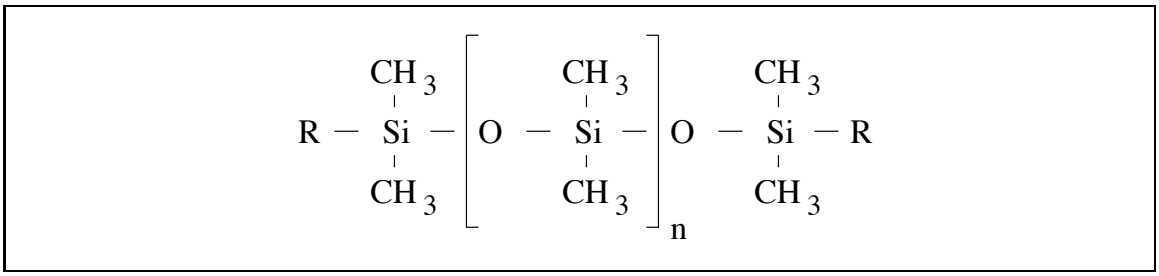

Fig. 2.2 The chemical structure of PolyDiMethylSiloxane where R is an organic, hydroxyl or alkoxy group.

main groups of silicone rubber: high-consistency compositions, room temperature vulcanizing (RTV) compositions and liquid silicone rubber (LSR) compositions. We will focus on the RTV composition.

Room temperature Vulcanizing is achieved through two mechanisms, with either one- or two-part systems. The two-part systems involve the mixing of two components to achieve cross-linking: a cross-linking element and a polymer containing silicone in one, a catalyst in other. The most reliable curing agents for the two-part RTV compounds are metallic soaps such as dibutyl tin dilaurate in concentration ranging from 0.1% to 0.5% by weight (Schwartz and Goodman, 1982). The one-part systems start to cross-link upon exposure to a reactant, normally from the atmosphere, such as water. Catalysts can be added to the one-part systems to accelerate the desirable reactions.

Properties The properties of silicone rubbers covers a very wide range. For example, they are capable of excellent weather and thermal stability, high water repellency, insolubility in water, good ozone and oxidation resistance, good solvent and oil resistance, extreme low-temperature flexibility, low environmental hazard, and high compressibility and damping action.

Mechanical properties

Elastomers behave differently than common engineering materials, such as metals. The modulus of elasticity is of prime interest for rubber materials and is different from the Young's modulus of rigid materials. Indeed, for rubber materials, it refers to the stress required to produce a given elongation, which is a measure of the material stiffness (Lynch, 1978). The ultimate elongation of silicone rubber depends greatly upon processing parameters such as curing time. It can reach up to 1000%. Upon repeated stress cycling, some

silicon rubber vulcanizates demonstrate a decrease in modulus (Lynch, 1978). The resistance to compression set of silicone is excellent. This is the amount, in percent, by which a standard test button fails to return to its original thickness after being subjected to a compressive stress for a prolonged period of time. Hardness of silicone rubbers depends on the molecular characteristics or the fillers. Using a Shore A instrument, hardnesses are found in between 25 and 75 (Lynch, 1978). Silicone rubber shows vibration damping properties.

Flexibility

The molecule of silicone rubber has the ability not only to change spatial arrangements by rotations around its skeletal bonds (dynamic flexibility) but also to be compact when in the form of a random coil (equilibrium flexibility). Long skeletal bonds, small side groups and an open Si-O-Si bond angle explains the high flexibility (Mark, 1990). The glass transition temperature, T_g, is the lowest glass transition temperature recorded for a polymer: $\simeq -125°C$.

Surface properties

Silicone rubbers are known for their outstanding release characteristics. This explains their use as coating in machinery which handle sticky materials such as candy or even adhesives. Critical surface tension is a measure of the surface activity of materials (Meyer et al., 1994; Baier and Meyer, 1986). Siloxane-based materials, polydimethylsiloxane in particular, have a very low surface energy: depending on its molecular weight, the liquid surface tension for polydimethylsiloxane ranges from 16 to 21 mN/m at room temperature (Owen, 1990). This is the result of the combination of a flexible backbone and low surface energy side groups: the flexible backbone allows the low surface energy pendant groups to be presented at a surface. In polydimethylsiloxane, intermolecular forces between methyl groups are low. As a result, polydimethylsiloxane behaves differently with low- and high-surface-energy substrates. The polydimethylsiloxane molecule is known to interact with a given substrate through two types of interactions:

1. London dispersion forces from the induced dipoles in the methyl groups, and
2. permanent dipoles in the partially polar siloxane backbone.

Interaction energies involving permanent dipoles are stronger than dispersion forces associated with methyl groups (Owen, 1990). With significantly polar substrates such as glass, polydimethylsiloxane interacts through its siloxane backbone with polar entities on the sub-

Table 2.3 Properties of the General Electric RTV11 silicone and the Wacker's Silgan® J-500 silicone compound

	RTV11	Silgan® J-500
Cure condition	RT	RT
Curing agent	Tin based	Moisture
Mix ratio[1]	200:1	
Silicone content	100 %	variable
Viscosity at 25°C	12,000 cP	1,000 – 20,000 cP
Specific gravity	1.18	
Hardness, Shore A	45	75
Tensile strength	350 lbs/in^2	500 lbs/in^2
Elongation	150 %	60 %
Tear resistance (die B)	20 lb/in	
Tear strength		35 lbs/in^2
Service temperature	-54 to 204 °C	125 °C
Release properties	Excellent	Fair
Drying time	1 – 12 hours	1 – 4 hours

[1]base to curing agent, by weight

strate surfaces, whereas with nonpolar substrates such as polymers or oils, interaction will happen through methyl groups by London dispersion forces. Liquid polydimethylsiloxane can readily spread over any high-surface-energy substrate such as metals, silica and alumina (Owen, 1990).

Bonding of silicone rubber occasionally can be facilitated by the use of primers. The primer, when applied to a substrate, tends to form new chemical species, which will then react with the silicon rubber molecule, facilitating its bonding (Lynch, 1978; Griffith, 1995).

RTV11 and Silgan® J-501 compounds A list of properties of the GE RTV 11 and the Silgan® J-501 silicone compounds is given in table 2.3.

The class of Silgan elastomers combine the excellent low viscosity and ease of handling properties of PDMS-based silicones with high tensile and tear strengths associated with organic polymers such as epoxies and polyurethanes. They cure at room temperature with low shrinkage and demonstrate superior low temperature flexibility and resistance to corrosion, moisture and harsh environments (Lynch, 1978).

Table 2.4 Characteristics of fillers used for silicone-based duplex coatings according to Lynch (1978).

Filler	Specific gravity	Particle size mean diameter (nm)	Surface area (m^2/g)
Fumed silicas	2.20	10 – 15	250 – 325
Calcium Carbonate	2.65	30 – 50	32

The role of fillers Fillers can be added to a material to achieve specific properties. For example, the thermal conductivity of silicone rubbers tends to increase with introduction of fillers. The properties of typical fillers used in fouling release coatings, fumed silicas and calcium carbonate, are listed in table 2.4.

Fumed silicas are highly reinforcing fillers. They are reconstituted from silicon and have a very large surface area (Lynch, 1978). Isolated hydroxyl groups present on the surface of the filler slowly form bonds with the polymer at room temperature, resulting in strong rubbers with high elongation. As the number of filler-polymer bonds increases, the material becomes stiffer. This is called creep-hardening and is accompanied by absorption of the polymer by the silicas, or wetting of the filler.

Calcium carbonate fillers are extending fillers. Their primary use is to reduce the cost of the silicone rubber compound. However, they do reinforce to some extent the compound to which they are added.

Screening tests

As standard tests developed for metallic based paints (Preiser and Halpern, 1983) are no longer suitable, performance criteria for coating evaluation have been redefined for the needs of novel fouling release coatings.

While some tests are custom designed for fouling release coatings, others are standard tests. The testing matrix includes accelerated laboratory tests, short term and long term field tests, which can either be standard test methods or custom designed methods for fouling release coatings.

Pre-exposure testing At the very initial stage of coating development, numerous tests are conducted and allow initial screening. For example, physical properties of candidate

coatings are monitored such as critical surface tension (Baier and Meyer, 1986, 1992), pseudo-biological adhesion (Swain et al., 1997), and resistance to brush abrasion (Meyer et al., 1995).

Field tests Field tests at multiple immersion sites around the world follow the initial screening process. The primary purpose of field tests is to measure antifouling or fouling release properties (Meyer et al., 1994; Swain and Schultz, 1996) as well as to study their resistance to mechanical damage.

Post-exposure testing Following panel immersion, additional laboratory or short-term field tests can be conducted to re-evaluate fouling release properties (Swain and Schultz, 1996) or cleanability (Meyer et al., 1994, 1995).

2.3 Tribology of elastomers

Evaluation of the wear resistance of novel coatings is a very crucial part of the program. As the best candidate to date are silicone-based elastomers, we will review the broad topic of the tribological behavior of elastomers and more specifically the wear of elastomers.

2.3.1 General considerations

Many reviews and studies of the friction, wear and lubrication of polymers have been published in the literature as early as in the 1950's (Lancaster, 1990; Briscoe, 1982).

Wear Wear is defined as the loss of material from the interface of two bodies when subjected to relative motion under load. It depends on the combination of a multitude of random and interactive factors such as the nature of the materials in contact, the geometry of the contact, the environment, and the operating conditions. Wear can be explained by a combination of mechanical, thermal and mechano-chemical processes. The main wear processes are adhesive, abrasive, fatigue and corrosive mechanisms (Lancaster, 1990; Rabinowicz, 1995; Eiss Jr., 1991; Arnell et al., 1991). In adhesive wear, the loss of material is due to the formation of adhesive bonds and the subsequent fracture during relative motion. Abrasive wear is the process in which a hard (and sharp) indenter is pressed into the surface of a softer material and plows a groove, thereby resulting in the removal of material from

the softer surface. Fatigue wear refers to the generation of wear debris from cyclic stress variation. Corrosive wear is a process in which a chemical reaction with the environment predominates. Other wear mechanisms such as erosive wear, fretting wear or cavitation wear are considered minor forms of wear. In a practical situation, all types of wear are likely to occur. This explains why studying wear mechanisms can be very complex if simple processes can not be isolated.

Wear and friction are not necessarily proportional. However, they are connected and interrelated: understanding the mechanism of friction sometimes helps understanding the mechanism of wear for a given system.

Friction and energy dissipation The friction force generated between two sliding bodies can be represented as the sum of two quantities: the adhesion and deformation terms (Bowden and Tabor, 1950), which are respectively considered surface and bulk phenomena, the latter showing its ultimate effect at the surface:

$$F = F_{\text{adh}} + F_{\text{def}} \tag{2.1}$$

While Ludema and Tabor (1966) treated them as separate and independent processes, Johnson (1980) presents models which show a strong interaction between adhesion and deformation.

The adhesion component of the friction force may be attributed to molecular bonding of exposed surface atoms in both members, according to a stretch, break and relaxation cycle of events. Moore (1983) describes the adhesion term as a thermally-activated, molecular stick-slip mechanism which occurs readily as a flexible surface "flows" against the texture of a rigid surface. Indeed, during relative motion of an elastomer and a hard surface, the separate chains in the surface layer attempt to link with molecules in the hard base, thus forming local junctions. Sliding action causes these bonds to stretch, rupture and relax before new bonds are made, so that effectively the elastomer molecules jump a molecular distance to their new equilibrium position (Moore, 1972). This explains the stick-slip process on a molecular level.

The deformation term is due to a delayed recovery of the elastomer after indentation by a particular asperity. The bulk deformation effect within the rubber-like material contributes to the hysteresis term of friction. It is dependent on the presence of distinct

asperities on a macroscopic scale. As an asperity deforms the rubber-like material under sliding conditions, the pressure distribution in the region of contact is unsymmetrical due to the inertia effect exhibited by the material which accumulates in front of the asperity and shows a delayed recovery from the indentation effect behind each asperity. Work is therefore done within the forward zone of contact (leading edge) in deforming and deflecting the rubber-like material, whereas within the rearward contact zone (trailing edge) almost all of this work is returned. The difference between work expended and that returned is the energy loss which gives rise to frictional forces (Moore, 1983; Uetz and Fohl, 1978).

Since the work of friction is dissipated in the polymer (Eiss Jr., 1994), the loss tangent is expected to correlate with friction. Indeed, on a macroscopic level, both adhesion and hysteresis can be attributed to the viscoelastic properties of the elastomer (Moore, 1983; Barquins, 1992; Briscoe, 1980; Bueche and Flom, 1958/59; Ludema and Tabor, 1966). The ratio of energy dissipated (whether in the stretch and rupture cycle of individual bonds in the molecular adhesion model, or in the deformation and recovery cycle associated with hysteresis) to the energy stored per cycle is defined as the loss tangent such that:

$$\tan \delta = \frac{E''}{E'} \tag{2.2}$$

where E' is the storage modulus and E'' is the loss modulus. E^* is the complex modulus defined by $E^* = E' + jE''$. Briscoe (1980); Bueche and Flom (1958/59) and Ludema and Tabor (1966) define a deformation frequency, close to the contact frequency or the sliding frequency, which affects an element beneath the surface. It is equal to the ratio of the sliding speed to the average diameter of the indenter. Since frictional work is equivalent to the energy lost beneath the contact, the frictional force corresponds to the loss tangent, $\tan \delta$, at a given temperature and frequency. Briscoe (1980) reviewed how the viscoelastic nature of friction might influence the mechanism of wear.

The concept of energy dissipation within the surface is of great importance in understanding the mechanism of wear as well. Several researchers have shown that there is a relation between wear of materials and energy expended (Uetz and Fohl, 1978; Heilmann and Rigney, 1981; Qiu and Plesha, 1991; Jahanmir, 1978; Zhang, 1992). Indeed, macroscopic or microscopic surface deterioration occurs as a consequence of the energy transfer mechanism. When a given element moves through a distance, the friction force results in the generation of work, the frictional work, which can be dissipated as heat through the

bulk of the material (Eiss Jr., 1991). Figure 2.3 represents the various mechanisms of energy dissipation in the case of a rigid asperity sliding on a polymer and in the case of a polymer sliding on a smooth surface.

The mechanisms of the adherence and of the sliding and rolling friction of rubber-like materials has been extensively studied. In the early fifties, the phenomena of waves of detachment was described by Schallamach (1952b). Since then, the mechanism has been extensively studied (Schallamach, 1953, 1968, 1971; Barquins, 1992). The waves observed in this mechanism do not damage the surface of the material. It simply constitutes a replacement of the phenomenon of true sliding. The abrasion pattern described by Schallamach (1952b) is caused by the repetitive passes of a slider on a surface where viscoelastic ridges have not completely disappeared as explained in the following section on wear of elastomers.

Elastomers behave differently than most glassy polymers. Elastomers usually exhibit a low surface energy. Therefore, forces between the elastomer surfaces are limited to weak Van der Waals bonds, rather than strong cross-linking bonds found in the bulk material. With such materials, the separation usually occurs at the interface as the work of adhesion is low. However, pull-off forces can be high due to viscoelastic hysteresis losses arising from the deformation of the elastomer. As no transfer of material can be observed, no true sliding occurs but the phenomena of Schallamach waves where the frictional work equals the work of adhesion and the pull-off work does (Arnell et al., 1991). Schallamach waves disappear and true sliding takes place when the cross-linking or the mechanical strength increase while the interfacial forces remain constant. In lubricated conditions, the adhesion and associated viscoelastic losses decrease and friction is proportional to the deformation losses. According to Briscoe (1980), Schallamach waves are removed in a fully lubricated contact.

2.3.2 Wear of elastomers

Many (Schallamach, 1952b; Moore, 1972, 1983; James, 1967; Barquins, 1992) have worked extensively in the area of friction, wear and lubrication of elastomers. Moore (1972) and Lancaster (1990) identified three main classes of wear modes for elastomers, which are dependent upon surface roughness: abrasion (or tearing), fatigue and roll formation. The most severe wear mode which is more likely to happen on a rough surface is abrasion. It is caused by a sharp texture in the base surface (two-body abrasion). Micro-cutting

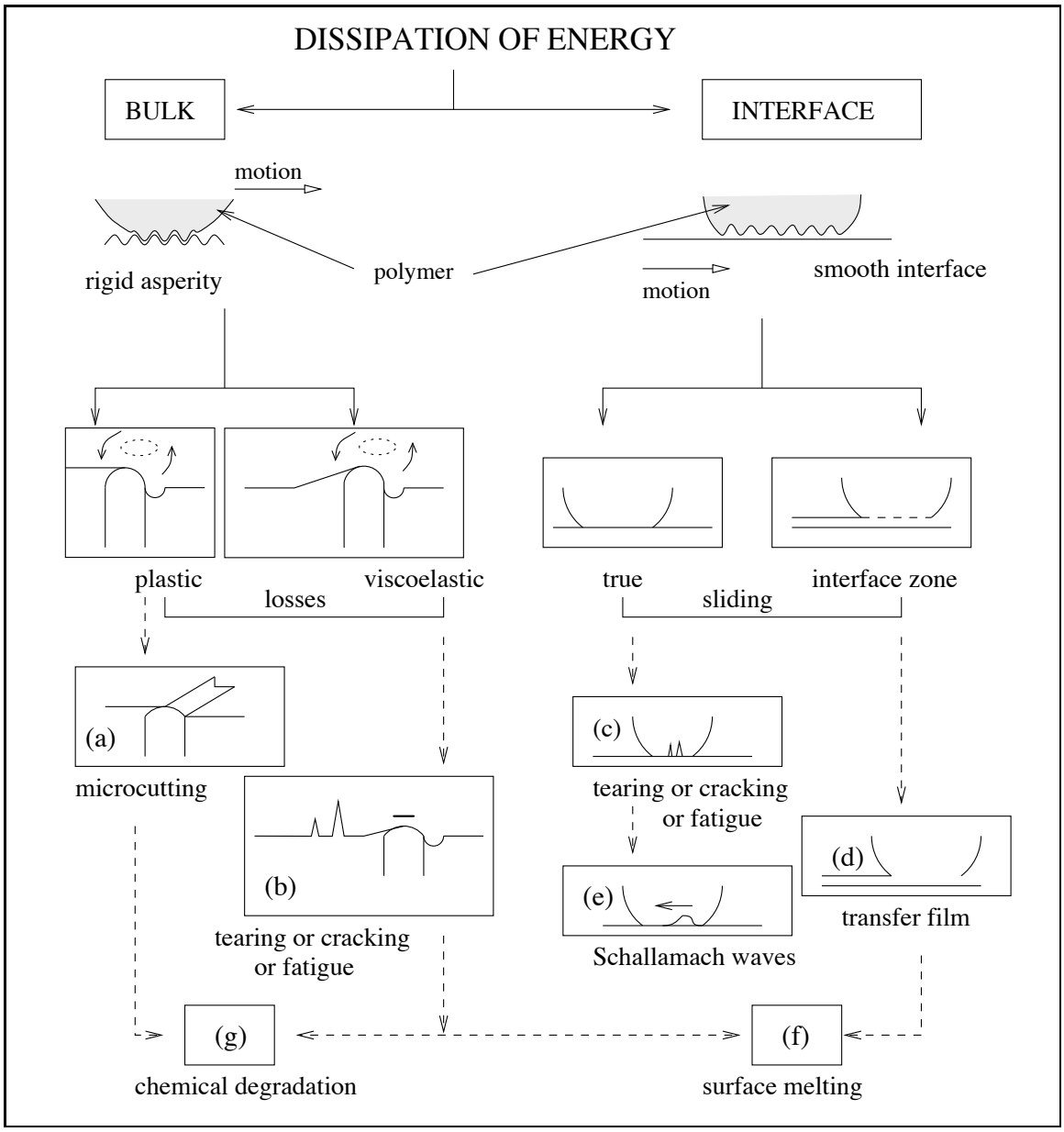

Fig. 2.3 Mechanisms of dissipation of energy and associated wear for polymers as introduced by Briscoe (1982).

and longitudinal scratches are observed. Fatigue wear, which is milder, happens also on rough surfaces when the asperities of the base surface are blunt. The cyclic deformation of the elastomer leads to fracture as a result of fatigue. Finally, a severe wear mode which occurs with smooth and highly elastic surfaces exhibiting high friction is roll formation. Rolls are formed at the sliding interface and eventually torn away. In a study published by James (1967), the mechanism of wear of rubber is treated as a twofold mechanism which combines frictional and abrasive effects. Abrasive mechanism results from micro-cutting by solid projections on the surface of the abraded body and frictional mechanism results from the forces of friction created by projections which deform the surface layers of the elastic material many times and separate them off. Longitudinal lines are formed under the action of abrasive wear whereas transverse ridges appear under the action of frictional wear. Briscoe (1980), in his review of friction of polymers, shows how the viscoelastic properties of a polymer plays a role in the deformation component of friction. The phenomenon of nascent grooving dominates when no permanent deformation is observed. However, if the contact pressure is increased to the point where it exceeds the flow stress of the polymer, depending on the response of the polymer, plastic grooving or tearing and transverse cracking appear. The latter form of damage was documented by Schallamach (1958) where isolated stress concentrations accounted for the formation of tears transverse to the sliding motion and perpendicular to the surface. Under the action of interfacial (adhesional) friction, cohesive failure of the polymer may lead to the transfer of a thin layer of polymer on the surface which ultimately affects frictional conditions (Briscoe, 1980). This might be related to the work done by Gent and Pulford (1983) who have identified a different wear mode for rubbers: mechano-chemical decomposition. Also, when high level of adhesion prevails, Barquins (1992) has evidenced the onset of adhesive wear under low loads and low sliding speeds.

As a result of viscoelastic properties, Briscoe (1980) reported that the contact area decreases with increasing sliding velocity because the rubber tends to stiffen.

In most practical cases, combination of these wear behaviors occur and it is difficult to isolate the contributions of one versus another.

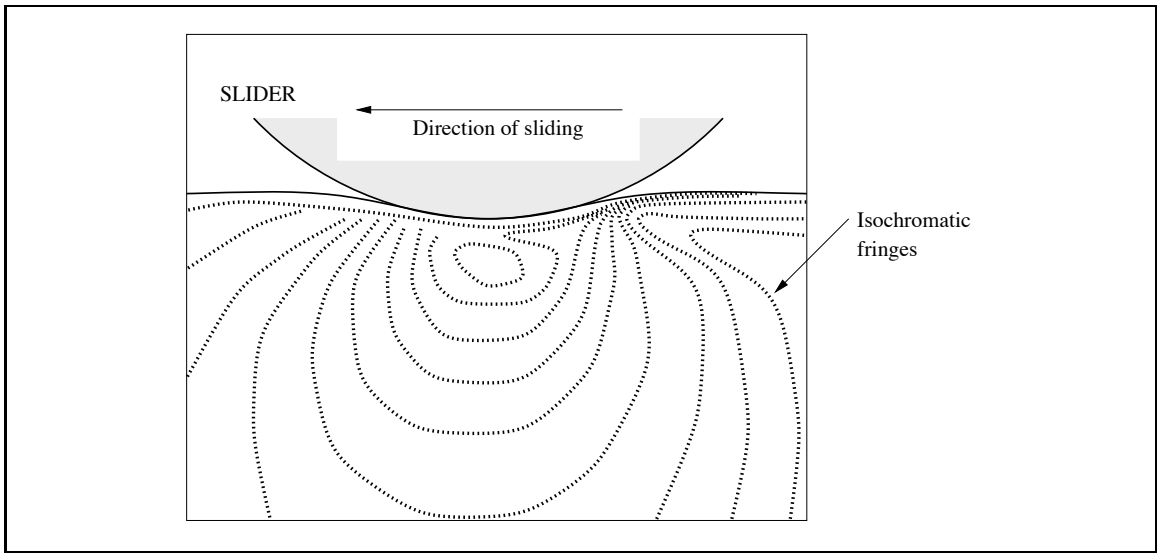

Fig. 2.4 Photoelastic stress distribution in transparent rubber from Schallamach (1954)

Theory of abrasive wear

Experimental observations In order to identify the wear mechanisms, Schallamach (1954) conducted experiments in which a 1 mm-diameter hemisphere (blunt asperity) and a sharp needle (sharp asperity) were slid across an elastomeric surface.

In the case of the hemisphere, under high load, discontinuous series of tears were evidenced across the track. Their periodicity suggests a mechanism of stick-slip during sliding: adhesion between the hemisphere and the rubber is followed by the stretching of rubber in the direction of sliding until the elastic restoring force exceeds the limiting friction at which point the rubber snaps back. Spacing between the tears and the size of the tears themselves is proportional to the hardness of the material. This has been explained by the stress distribution in rubber as evidenced by figure 2.4: the close spacing of isochromatic fringes indicates stress concentration at the rear of the contact area where the rubber is in tension.

In the needle test, larger damage such as tearing and subsequent detachment of rubber particles is caused by interlocking and higher tractive forces (Schallamach, 1952a). Figure 2.5 shows the distortion of the reference line and the evidence of concentration of stress at the vicinity of the needle. The curves shown are originally equidistant reference lines marked on the surface of the rubber at a right angle to the direction of motion. Contrary to the test with the hemisphere, the tear occurs at the point where the rubber

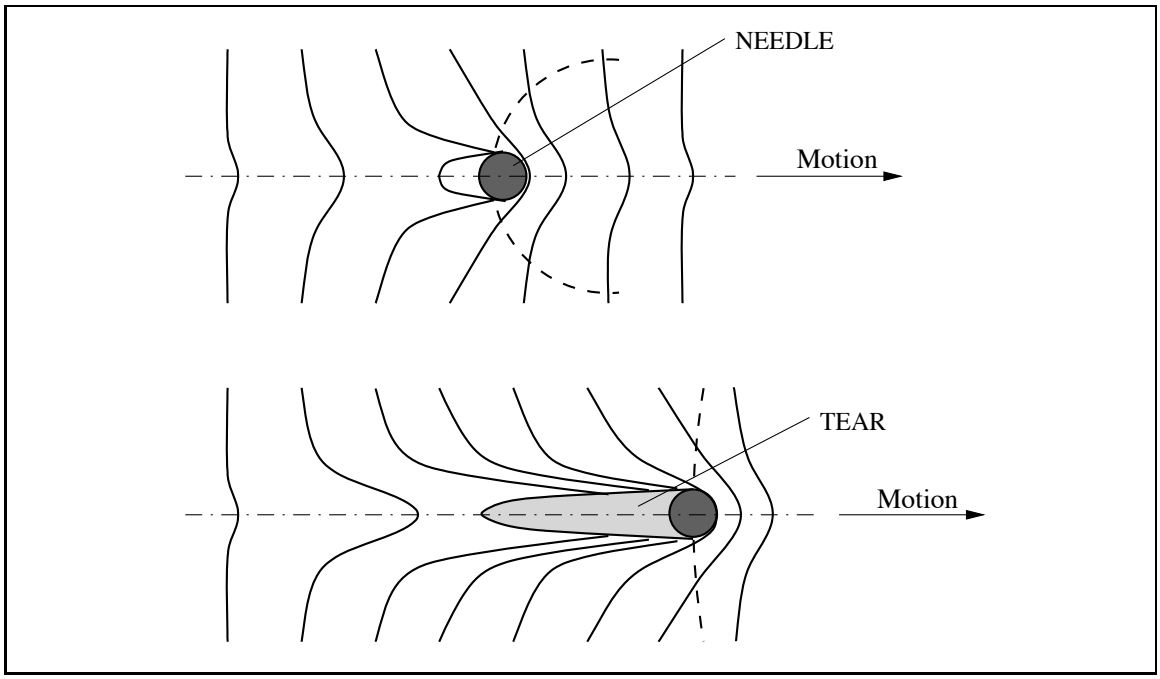

Fig. 2.5 Two stages in the deformation and tearing of a rubber surface by a needle based on experimental observations by Schallamach (1952a).

first loses contact with the needle and the tear happens laterally as represented by the dashed line on figure 2.5.

Moore (1972) concludes that frictional adhesion as well as mechanical interlocking are responsible for the abrasion phenomena. Once a tear is formed, it propagates at right angles to the direction of sliding, and successive passes will lead to the formation of wear particles at tearing sites as confirmed by Schallamach (1954) and Grosch and Schallamach (1966).

Theoretical considerations Based on the experimental observations, Grosch and Schallamach (1966) developed a theory of abrasive wear with the following assumptions:

1. the tear length is proportional to the width of contact between the abradant and the elastomer, and

2. the volume of a detached rubber particle is proportional to the cube of the length of the original tear.

Figure 2.6 illustrates the contact conditions. The volumetric wear rate, K_v, is defined as the ratio of the volume layer removed to the sliding distance multiplied by the apparent

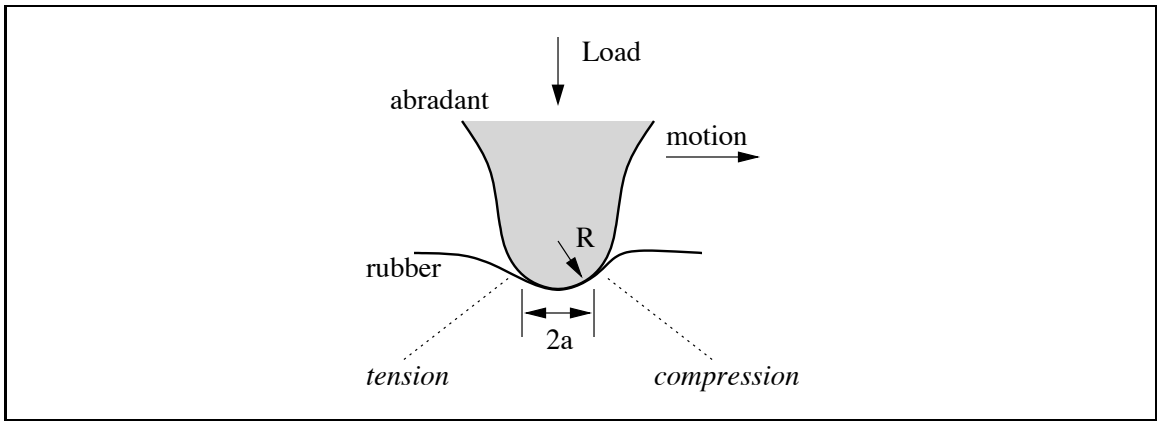

Fig. 2.6 The interaction of a rubber surface and an abradant during sliding proposed by Moore (1972).

area, such that:

$$K_v = \text{constant}_2 \left(\frac{W_{\text{tot}} R}{G} \right) \tag{2.3}$$

where K_v is the volumetric wear rate , $2a$ is the mean diameter of the area of contact of an asperity, W_{tot} is the applied normal load per unit area, R is the average radius of curvature at the tip of the abrasive asperity, and G is the elastic constant characterizing the rubber. According to equation 2.3, rubber abrasion increases linearly with increasing normal load. This is confirmed by the experimental work conducted by Grosch and Schallamach (1966).

Pattern abrasion One characteristic of rubber abrasion is the pattern developed at the surface upon sliding. When motion is unidirectional, ridges at right angle to the direction of sliding are formed: these ridges are called "abrasion patterns" (Schallamach, 1952b). A cross-section of the abrasion pattern in the direction of sliding shows that a saw-tooth profile is opposed to the direction of abrasion. According to Grosch and Schallamach (1966) and Moore (1972), as the abradant moves, the teeth are bent backward, exposing their underside to the action of the abradant. Simultaneously, part of their surface is protected from abrasion at the rear. This is called the under-cutting effect. Teeth wear thinner until the crests are worn away, leaving blunt edges. In the mean time, ridges continue to grow out from the bulk material, and the pattern is self perpetuating.

Later work by Fukahori and Yamazaki (1994a) led to a better understanding of the fundamental processes leading to the formation of the abrasion pattern. Indeed, two types of periodic motions observed constitute the sources of the mechanism of wear: stick-slip

oscillations on one hand and micro-vibrations generated during frictional sliding of rubber. Initial micro-cracks are induced in the slip phase of the stick-slip oscillation by micro-vibration with the natural frequency of rubber. Propagation of these micro-crack leading eventually to abrasion patterns is driven by the stick-slip oscillation. While initial cracks are observed in the slip region of rubber surfaces, the propagation of cracks is excited in the stick region.

Fukahori and Yamazaki (1994a) demonstrated experimentally that the origin of abrasion patterns, a series of parallel ridges perpendicular to the sliding direction, is produced after the first contact between the slider and the surface. The distance between the initial cracks (micro-ridge spacing) is small and increases proportionally to the velocity. The micro-cracks continue to grow in depth and ridge spacing with the number of contacts until the pattern spacing eventually reaches a critical value set by the correlation between the period of stick-slip oscillation and the sliding velocity. Once the critical value is reached, the spacing of the ridges remains constant thereafter regardless of the number of contacts. It is believed that the small parallel cracks coalesce in the normal direction and finally merge into the main large ridges. The initial formation of micro-ridges is sometimes referred to as the intrinsic abrasion while the final critical ridges are called the abrasion pattern. Further analysis revealed that the crack propagation in rubber abrasion can be divided into two categories:

- the first category is the propagation which takes place at the root of the large ridges governed by the adhesive force in stick-slip motion, and
- the other is that of small cracks or small ridges which occur on the surface of the large ridges in the slip phase of stick-slip motion, driven by micro-vibration

Subsequently, abraded particles formed in the abrasion of rubber follow a bimodal size distribution (Fukahori and Yamazaki, 1994a; Gent and Pulford, 1983): fine particles ($\simeq 10\,\mu$m or less) originate from micro-vibration and coarse particles (several hundred μm) are generated by stick-slip motion. 95% of the total weight loss due to abrasion is thought to be due to the larger particles (Fukahori and Yamazaki, 1994a).

Gent and Pulford (1983); Schallamach (1958); Grosch and Schallamach (1966) showed that the abrasion pattern is related to the rate of wear. The intensity of the abrasion pattern increases with coarseness of the track and with a decrease in the stiffness of the compound (Grosch and Schallamach, 1966).

The spacing between the ridges, s, is assumed proportional to the diameter of contact 2a, the mean particle size is inversely proportional to the square root of the number of abrasive particles per unit area $(1/n)$, then:

$$s \simeq \left(\frac{W_{\text{tot}} R\ d^2}{G}\right)^{1/3} \simeq d^{2/3} \tag{2.4}$$

This proportionality between the spacing of the ridges and the mean particle size d of the abradant has been experimentally verified. Further on, by modeling the abrasive surface as closed packed hemispheres such that $d = 2R$, the volumetric wear rate, K_v, is proportional to the spacing of the pattern:

$$\frac{K_v}{s} \simeq \left(\frac{W_{\text{tot}}}{G}\right)^{2/3} \tag{2.5}$$

Equation 2.5 shows that the proportionality between the wear rate and the spacing between ridges depends on the ratio of the applied pressure and the elastic properties of the material. As the pressure increases or as the stiffness decreases, the influence of frictional force on the development of patterns increases. The following empirical equation relating the pattern spacing to the rate of abrasion loss $(\overline{V})$ was proposed by Schallamach (1952a) and James (1967) and is a generalization of equation 2.5:

$$\overline{V} = ks^n \tag{2.6}$$

where k and n are constant. This relationship was experimentally verified by Fukahori and Yamazaki (1994a) and confirmed that the pattern spacing can be a measure of the rate of abrasion in natural rubber.

The abrasion process is therefore explained by tensile failure of the elastomer as illustrated by figure 2.5. Detachment of molecules of elastomer from the bulk is caused by catastrophic tearing behind the sharp asperities in the track, following high rates of strain. According to Lancaster (1990), the tearing during successive contacts can be modeled as a propagating crack.

The appearance and non-appearance of the waves of detachment in a given sliding situation is a manifestation on a macroscopic level of the fundamental and underlying molecular-kinetic, stick-slip adhesional phenomenon that applies to all situations where at least one of the sliding bodies is a rubber-like material (Moore, 1983). James (1967) concludes that the presence of transverse ridges is characteristic of the abrasion of elastic polymers.

Theory of fatigue wear When repeated compression, tension, expansion and reversed shearing stresses within a surface layer of an elastomer are caused by rounded and blunt asperities, fatigue wear leads to failure. It is milder than abrasion and it can be classified as a bulk rather than a surface effect. It becomes significant when cyclic stresses are present over long periods of time, when the adhesion is relatively small and when the applied stresses are below the yield stress of the material. Moore (1972) developed a theory of fatigue wear which shows that the ratio of the factor of abrasion resistance, β, to the coefficient of friction, f, depends uniquely on the normal load for a given rubber or elastomer: as the load increases, $\frac{\beta}{f}$ decreases. This can be interpreted as a simultaneous increase of the contribution of abrasive wear in the overall wear mechanism.

Theory of roll formation Abrasion and fatigue are wear mechanisms typically observed on rigid surfaces exhibiting macro-roughness. On smooth and highly-elastic surfaces when the friction is high, roll formation is observed (Moore, 1972). This wear mechanism is explained by internal failure of the elastomer following severe deformation before slippage takes place at the interface. When such failure occurs, the surface layers are in a state of maximum strain and a crack may appear perpendicular to the direction of attempted sliding. Subsequent growth of these cracks doesn't result in immediate wear particle generation. The elastomer gradually tears to allow relative movement in the contact area without complete slippage. This is achieved when the layer of rubber separated off during tearing winds into a roll. Rolling friction governs the relative motion, along with continuous tearing of elastomer and accumulation of the separated shred in the form of a roll. Figure 2.7 illustrates the gradual stages of roll formation. The force which causes elongation depends on the resistance to tearing of the material at the place where the shred separates off. Failure at the shred occurs when the elongation reaches a critical maximum value, resulting in detachment of the rolled shred.

Specific external conditions combined to specific properties of the elastomer are necessary for the onset of wear by roll formation. It is more likely to happen with elastomers with low tear strength exhibiting high friction with the counterface. The energy involved in peeling the elastomer away from the contact area during the detachment wave formation accounts for a large part of the frictional energy dissipation (Moore, 1983). Temperature affects tear strength. In certain cases, as the temperature increases under sliding conditions,

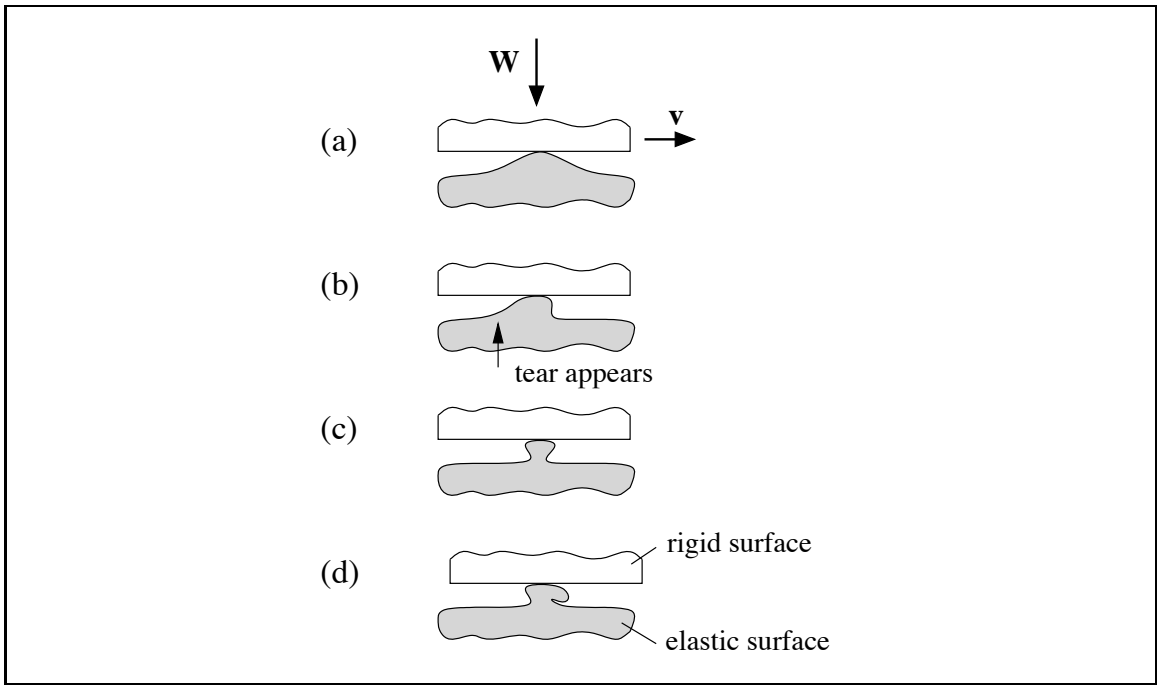

Fig. 2.7 Gradual changes in the formation of a roll according to Moore (1972).

the subsequent increased tackiness of the elastomer results in the increase of the frictional coefficient. The coefficient of abrasion resistance, β, is dependent on the tear energy of the elastomer, the elastic modulus, the dynamic resilience, as well as the average values of thickness, width and radius of the shredded roll. The wear pattern formed is very similar to the ridge formation obtained by Schallamach for rough surfaces (Schallamach, 1968).

Mechano-chemical decomposition of rubber Gent and Pulford (1983) identified two competing processes in the wear of rubber under unlubricated conditions: the abrasion wear previously described and a mechano-chemical decomposition of the rubber surface. The latter is caused by local heating during sliding; oxidative deterioration, possibly accelerated by local heating; and mechanical rupture of the molecular network to form a low-molecular weight material. It is sometimes described as smearing of the surface.

Dependence of wear on operating conditions

The effect of operating parameters such as applied load, sliding speed, temperature and environment has been extensively studied for various plastic and elastomeric materials. Their roles can be of crucial importance in determining the form of the predominating wear

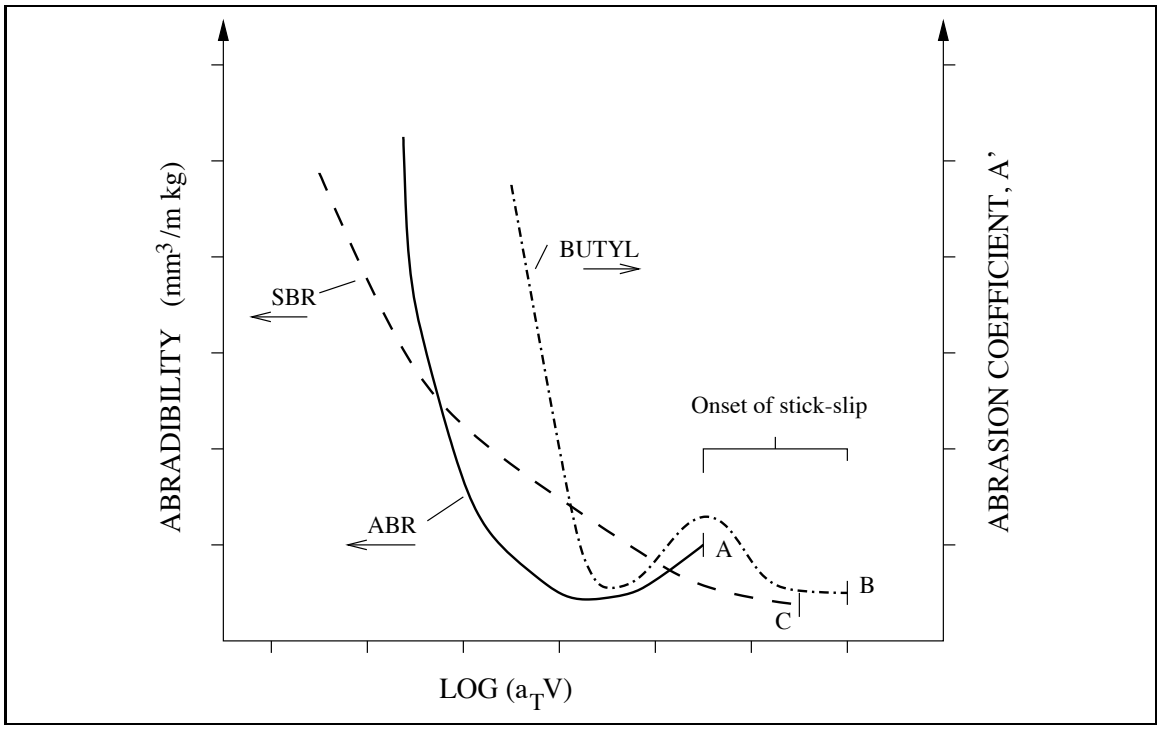

Fig. 2.8 Master curves obtained experimentally by Grosch and Schallamach (1966) for the abrasion of three unfilled rubbers: acrylonitrile butadiene, styrene butadiene and butyl rubbers.

mechanism.

Viscoelastic aspect of abrasion: effect of sliding speed Friction can be considered as a viscoelastic phenomenon based on the established viscoelastic nature of adhesion and hysteresis. The mechanism of abrasion, as it is related to the frictional behavior of the materials in contact, shows distinct viscoelastic properties as well. Figure 2.8 illustrates the abradibility γ as a function of the sliding velocity for three rubbers. The abradibility is defined by Grosch and Schallamach (1966) and Schallamach (1968) as:

$$\gamma = \frac{\text{abraded volume}}{\text{work of friction}} = \frac{1}{\beta} = \frac{A'}{f} \tag{2.7}$$

where A' is the abrasion factor, β is the factor of abrasion resistance, and f is the coefficient of friction. A' is defined as the volume abraded per unit normal load and unit sliding distance. β is defined as the work of friction, FL, divided by the abraded volume ΔV. One or more minima in the abradibility are observed and it can be easily explained using the variation of the friction force with sliding speed represented in figure 2.9.

Indeed, as shown by figure 2.9 (a), the total coefficient of friction, which is assumed

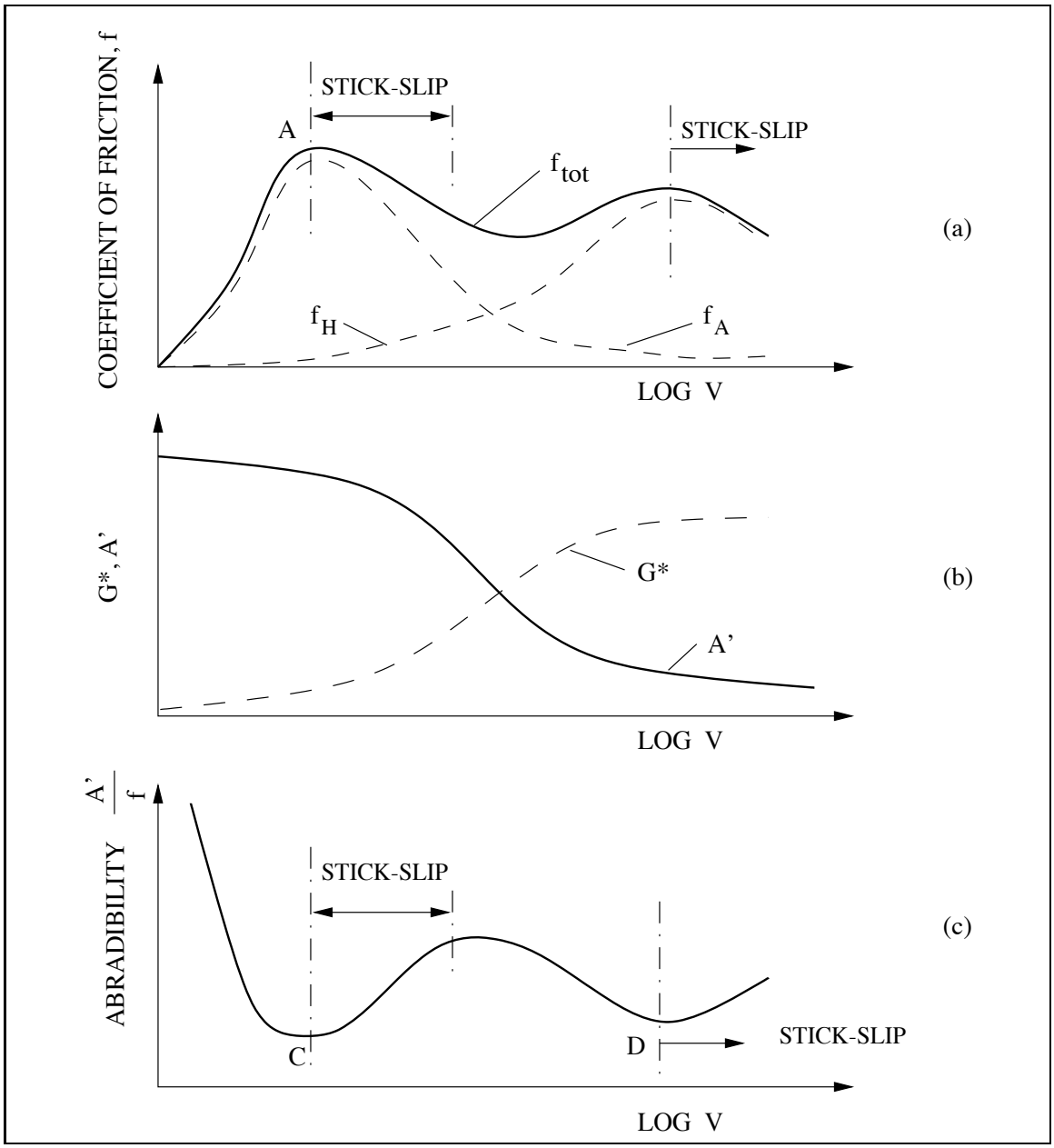

Fig. 2.9 The viscoelastic nature of abrasion: analogy between the mechanisms of friction and wear from Moore (1972)

equal to the sum of the coefficient of friction due to adhesion and to the coefficient of friction due to hysteresis, shows two maxima in its variation with the sliding velocity. Figure 2.9 (b) represents the variation of the elastic modulus with speed and establishes the inverse relationship between elastic modulus and A', the abrasion factor (Moore, 1972). Therefore, the variation of A' with sliding speed can be obtained from the variation of $G*$ with sliding speed. Finally, using equation 2.7, the abradibility coefficient γ can be plotted as a function of sliding speed as shown on plot (c) of figure 2.9. Two distinct minima can be observed: they correspond to the maxima observed in the friction-velocity curve (curve (a)). Peaks C and D are therefore respectively referred to as adhesion and hysteresis minima. Grosch (1963) experimentally proved that peak C could be reduced by placing powder between the elastomeric surface and the abradant, hence reducing adhesion. One important observation is that stick-slip is observed to happen on the onset of a positive slope in the abradibility curve (curve (c)) or, respectively the onset of a negative slope in the friction curve (curve (a)). In the previous discussion, Moore (1972) establishes a broad analogy between friction and abrasion. Other authors (Gent and Pulford, 1983) have later shown that the rate of abrasion depends upon the frictional force, in a similar way as the rate of crack growth depends upon the magnitude of the tearing force applied intermittently.

Viscoelastic aspect of abrasion: effect of temperature Grosch and Schallamach (1966) and Schallamach (1968) studied the effect of temperature on the friction force F, the abrasion factor A' and the abradibility γ of elastomers at constant sliding speed and found evidence that abrasion has distinct viscoelastic properties. Frictional data can be used to estimate the extent of abrasion.

According to James (1967), wear resistance of a material is affected by temperature in two competitive ways. On one hand, an increase in temperature results in a reduction in strength and hardness, leading to a decrease in wear resistance. On an other hand, the increase in temperature leads to a sharp increase in the breaking elongation, which tends to increase wear resistance.

Effect of load on wear of elastomers The effect of the applied load on the abrasion of elastomers has been extensively studied (Moore, 1972; James, 1967). The effect of load on the volume of abrasion is established by equation 2.3 on page 22, for the case of an

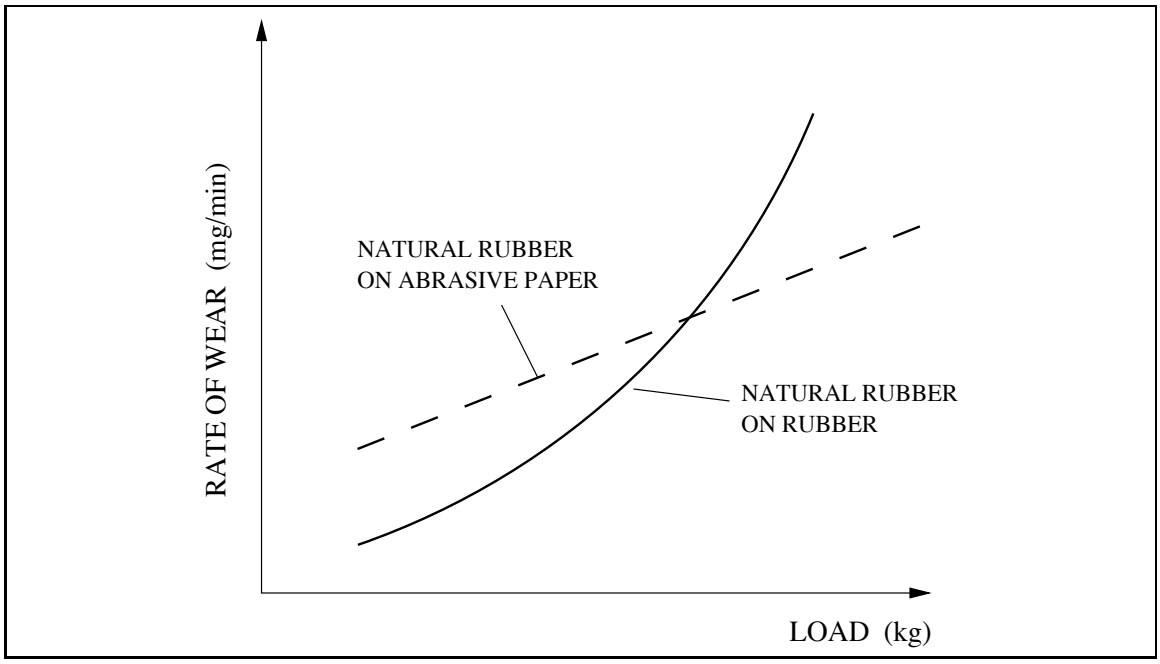

Fig. 2.10 Load dependence of wear rate for natural rubber from Moore (1972)

elastomer sliding on a rough texture surface. It can be generalized as follows:

$$K_v = Cp^{\alpha} \tag{2.8}$$

where K_v is the abraded volume per unit area and sliding distance (cm^3/cm^2 m), C is a constant, and p is the interfacial pressure (N/cm^2). C and α are specific to the texture of the abrading surface (Moore, 1972) and α varies with elastomer composition: addition of fillers increases α while swelling decreases it. Equation 2.8 clearly demonstrates the effect of the asperity shape on the volume of abrasive wear. As the projections become sharper, p increases and so does K_v.

Fukahori and Yamazaki (1995) demonstrated that the initial pattern spacing is independent of normal load since its width is only determined by the natural period of the rubber and the mean sliding velocity (Fukahori and Yamazaki, 1994b,a). However, the final critical spacing depends strongly on the normal load, i.e the higher the normal load, the larger the pattern spacing. It has been previously established that the pattern spacing is determined by the mean sliding velocity as well as the period of the stick-slip oscillation (Fukahori and Yamazaki, 1994b,a). Therefore, as the normal load increases, the period of stick-slip oscillation increases proportionally, leading to the increase in the critical spacing.

Effect of material composition and characteristics Various attempts have been made to relate the wear of elastomers to their physical and mechanical properties such as Shore hardness or tensile strength (James, 1967; Schallamach, 1958). Empirical relationships have been proposed but have limited applicability due to the extent of degradation observed at the surface of an elastomer, degradation leading to the formation of surface layers whose properties are different from those of the bulk materials.

For example, James (1967) established a qualitative relationship between the resistance to wear of a material and its mechanical characteristics:

$$V \simeq \frac{f}{\mathrm{H}\ \sigma\epsilon} \tag{2.9}$$

where f is the coefficient of friction, H the hardness, σ the strength, ϵ the breaking elongation and V, the decrease in volume or dimensions of the body per unit distance traveled. James (1967) observed that the ratio of frictional to abrasive wear depends on the elasticity of the material being abraded and the sharpness of the solid projections on the abrading surface.

Schallamach (1954) showed that the chemical composition of rubber has little effect in the case of sharp asperities. On one hand, the addition of inactive fillers increases the hardness but not the strength or the wear resistance (James, 1967). On an other hand, according to Furukawa (1996), a filler such as carbon black improves the abrasion resistance by its reinforcing ability. This resistance is enhanced by the increase in the content, specific surface area and adhesion ability of carbon black. Fukahori and Yamazaki (1994b) investigated the effect of fillers on the fundamental processes believed to be responsible for the formation of the abrasion pattern. It was shown that the magnitude of stick-slip oscillation is independent of the materials. However, the micro-vibration, which are believed to be the source of initial small cracks (Fukahori and Yamazaki, 1994a), and particularly its attenuation when it spreads over the surface of rubber as a surface wave is observed to be strongly dependent on the dynamic properties of the material, hence on the content of fillers. As a consequence, as the filler content increases, the smaller the initial spacing is, the slower it propagates and the lower critical value it reaches. As the rate of abrasion is believed to be proportional to the critical ridge spacing, the rate of abrasion is therefore smaller as well.

The resistance to wear is proportional to the strength and inversely proportional to the coefficient of friction. The limiting deformability, i.e. the breaking elongation, plays a

fundamental role in the process of fatigue wear. The act of wear as a separation of particles occurs only when the elongation brought about by the abradant exceeds the breaking elongation of the material, in conditions where the surface is in tension (James, 1967). Other characteristics such as the variation of the material with depth strongly affect the mechanism of wear as well as its severity (Lancaster, 1982).

Effect of wear debris and transfer films Wear debris generation is inherent to the phenomenon of wear. Its consequence on the overall wear rate can be either beneficial or detrimental depending on the nature of the wear debris and the application. If the wear particles formed are hard, then they will be abrasive and increase the wear rate. If the wear particles formed are soft, then they will redistribute the normal load over a larger area and will decrease the overall wear rate via a reduction of the stresses (Eiss Jr., 1991). Wear debris are representative of the wear behavior. When collected and analyzed, they can help identify the wear modes acting in a given system. For example, Gent and Pulford (1983) identified two wear modes based on the microscopic observations of collected debris.

Under certain sliding conditions, formation of surface layers is observed: they affect the contact conditions and therefore the wear behavior of the system under study. These layers are composed of consolidated wear debris as observed for polymer-based composites on both the slider and the counterface (Lancaster, 1982).

Parameters such as the size of the apparent surface area, its degree of conformity, the initial surface area, the nature of environmental contamination, the load, the sliding speed, the type of motion as well as the amount of solid lubricant within the composite itself influence the formation of transfer films and wear debris.

Effect of the environment: lubrication A distinct elastohydrodynamic effect is observed when a lubricant is added at the interface of an elastomer and a rigid rough surface. Moore (1983) developed a simple theory of hydrodynamic separation for rubber-like materials sliding and slipping against a macro-texture in lubricated conditions. Elastohydrodynamic lubrication applies to a particular form of lubrication between engineering surfaces which tend to deform under load. Since rubber-like materials deform more likely than metallic surfaces, elastohydrodynamic lubrication is more likely to occur. Moore (1983) differentiates between macro-elastohydrodynamic and micro-elastohydrodynamic effects which

occur readily depending on the scale of roughness. The contact between surfaces in relative motion is affected by these effects. When the macro-elastohydrodynamic effects prevail, contact between the surfaces is limited whereas, as the surface roughness increases and asperities become sharper, dry contact occurs due to the breaking of the lubricant film by the sharp asperities. Abrasion wear follows. As the asperities are rounded following wear, the hydrodynamic film may form again leading to lubricated contact. In the case of road tire, this effect can be very detrimental as traction is lost (Moore, 1983). However, in a reverse situation where a reduction of friction is by far not important, this previous effect might be considered as positive in term of wear reduction. Sliding speed is known to affect the thickness of the lubricant film. As the speed is increased, the thickness increases proportionally. In the former case, if the film thickness exceeds the value of roughness of the surface, dry contact and the associated wear will decrease significantly up to the ideal case of perfect hydrodynamic lubrication where no wear occurs! Moore (1983) also incorporates in his work the elastic response of viscoelastic materials to applied pressure. Indeed, the scale of surface texture is related to the flexibility of the rubber-like material. The frequency of indentation of the rubber-like surface is inversely proportional to the scale of surface texture. If the frequency of indentation increases, the rubber-like material tends to stiffen in response and to behave like a rigid body.

Moore (1972) shows how the properties of a surface in terms of wettability may affect the lubrication conditions (and the adhesion between surfaces in contact). By definition, a hydrophobic surface tends to reject water and prevent complete wettability. The adhesion force is then greater than it would be with a hydrophilic surface. Wettability is a time-dependent phenomena as the hydrophobic characteristic of a given surface tends to change towards hydrophilicity. In the case of a rough surface, adhesion increases compared to that with smooth surfaces.

Typically, through the formation of a low shear strength film between surfaces, fluid lubricants can reduce friction and wear in three ways (Arnell et al., 1991):

- reduction of adhesion,
- cooling of surface by reducing input of frictional energy and by removing heat, thus decreasing deleterious thermal effects as surface softening, and
- carrying away detrimental debris in recirculating systems.

The latter point however can also be lead to an increase in wear. Indeed, the presence of

a lubricant can prevent the formation of surface films of consolidated wear debris – third bodies – in distributed areas in the case of soft debris (Lancaster, 1982). The fluid may even penetrate into surface cracks and pores and hydrostatic stresses developing during contact would facilitate the disruption of the surface layer. This supports the theory that the presence of voids tends to adversely affect wear properties.

2.4 Experimental analysis of wear

Development of sliding wear tests to assess and enhance the performance of bulk materials or coatings is necessary for the ultimate selection of the best system. There is no better way to test a given system than to test it in real service conditions or in a very close laboratory simulation. However, when results are needed quickly or when such real-life simulations are expensive, short-term accelerated laboratory-scale tests are valuable, particularly in the first stage of material selection such as a comparative study. Accelerated laboratory wear tests usually involve single and concentrated contacts (Lancaster, 1982) such as a sphere on a rotating disk. Accelerated laboratory wear tests present the following advantages:

- initial screening of candidate systems, limiting the amount of full-scale testing,
- identification of key parameters, material and functional, that will be most likely to affect friction and wear behaviors, and
- assistance in the further development of systems with enhanced performance.

However, even with simplified wear tests, wear computation can be complicated by the low sensitivity of wear measurements, which implies long tests or by contact non-uniformity, which may ultimately lead to a premature failing of a given system caused by stress concentrations.

2.4.1 Laboratory devices for wear testing

A extensive description of laboratory devices for the measurement of friction and wear can be found in the literature (James, 1967; Eiss Jr., 1991; Payne and Bayer, 1991). For a given application, the selection of wear tests is based on the observed damages in service operation. As an example, for a clear coated plastic (such as plastic used for windows), separate standard methods can be utilized to study the rubbing action of cleaning and maintenance operations, the effect of the impacts by moving particles, scratching and penetration, and

the effects of changes in the environment caused by excessive moisture, heat or exposure to chemicals (Haluska, 1982). When available, standard tests, such as ones developed to rank materials subjected to abrasive wear, are used. A detailed listing of ASTM wear tests can be found in Eiss Jr. (1991, 1994).

A tribometer is an apparatus whose principal purpose is to measure friction and wear. It is characterized by the following 4 elements (Eiss Jr., 1991):

1. the geometry of the contacting element (point, line or area contact),
2. the normal load application (dead weight, pneumatic or hydraulic cylinders),
3. the relative motion (reciprocating or unidirectional) and the contact ratio, as well as
4. the component and measurement interaction.

When the contact is either of line or area type, a problem of misalignment between the two elements arises. This usually leads to a period of transient wear or running-in as illustrated on figure 2.11 (Eiss Jr., 1994, 1991). The misalignment causes a point contact instead of a line or area contact. As the test begins, the contact area developed by the point contact is much smaller than that would be achieved under the theoretical line/area contact. The stresses can therefore exceed the yield strength of the material, leading to an initially high wear. This phenomena continues until the contact reaches the line/area contact where the nominal stresses are much lower. Transient wear can also be observed as a result of frictional heating, dynamic response of the system as it is set in motion, or even as a result of the deflection of the element due to the friction force (Eiss Jr., 1991). If the transient wear is followed by a steady-state wear, then the reported value should be that of the steady-state wear.

2.4.2 Measurement of wear

Wear can be quantified with various methods (Eiss Jr., 1991; Rabinowicz, 1995):

- Weighing method:
  - Weight measurement of the specimen sample before and after a test,
  - Weight measurement of the wear debris collected.
- Mechanical Gaging method:
  - Dimensional change measurement (due to a loss of mass),
  - Change in surface roughness (Zahavi and Schmitt Jr., 1982).

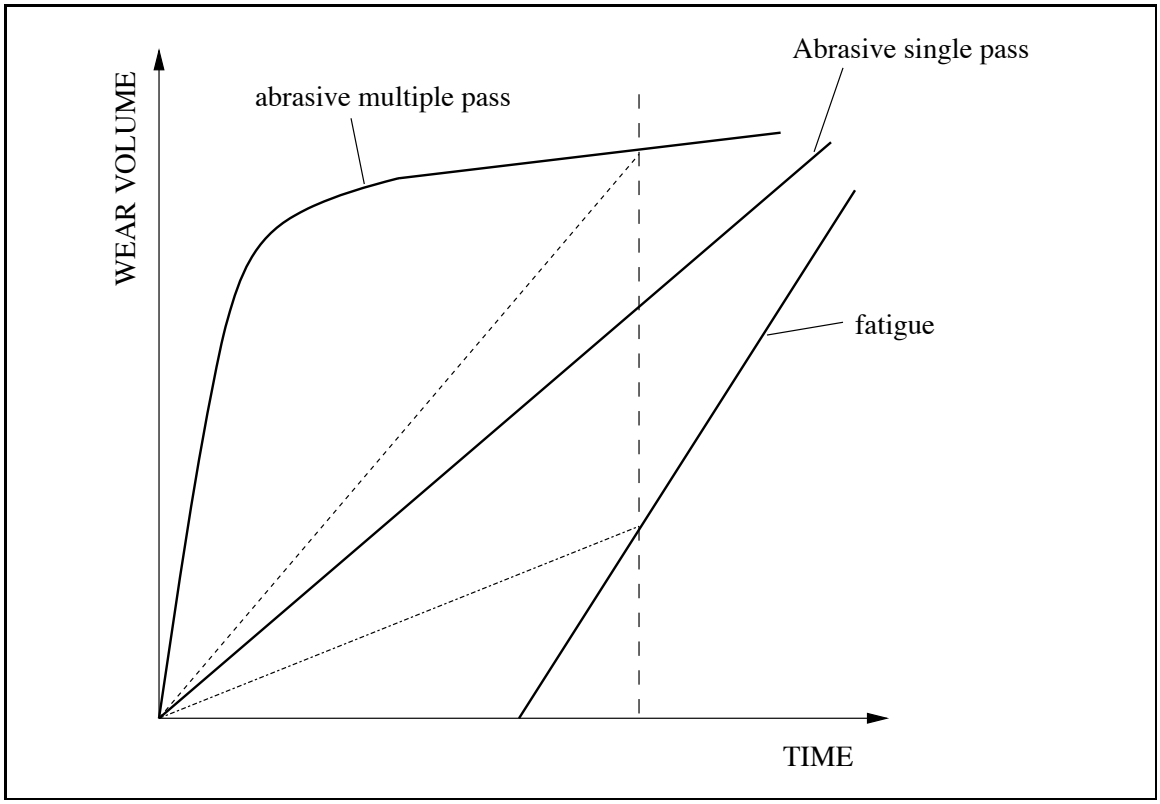

Fig. 2.11 Transient wear and steady-state wear according to Eiss Jr. (1994)

- Optical method:
  - Transmittance loss to visible and non-visible light (for transparent materials),
  - Scanning electron microscopy (SEM), electron spectroscopy for chemical analysis (ESCA) and Auger electron spectroscopy (AES).
- Radioactive tracers.

Weight loss measurement is a very common and widely spread method to measure wear. Dimensional changes are used to calculate the volume change, i.e. the volume of wear. In particular, when a sliding element makes a repetitive path over another element (assuming that the former does not wear), a groove is formed in the surface of the wearing element (Eiss Jr., 1991). This technique is used for thin coatings, for which the method of the weight loss is not applicable due to the fact that the weight of the material lost is much smaller than that of the overall sample. The wear volume can then be calculated from the average of the measurements of the area of the groove in several places along the track multiplied by the length of the groove. A profiler is used for these measurements. The accuracy of the former method depends on the shape of the groove formed, the accuracy of the method used to calculate the area from the profile data, but also on the variation of the groove area along its length (Eiss Jr., 1991).

Procedures to measure wear are of two kinds. In the first procedure, the test is run for a finite period of time and wear is measured once the elements are removed from the test apparatus. Then, they can be placed back in the testing apparatus and the test can be carried on with he same elements. In the second procedure, the test is run continuously until a wear measurement is made. After that, the elements are not reused. Instead, a new set of elements is placed in the test for a longer period of time and so on. In both procedures, a value for the wear rate can be obtained. The wear rate is defined as the volume (or mass) of material lost per unit of time. In cases where the relative sliding velocity is constant, then the sliding distance is used and the wear rate becomes the volume (or mass) of material lost per unit of sliding distance. Other wear parameters can be found in the literature: the specific wear rate (the wear rate divided by the normal load) and the wear coefficient (the specific wear rate multiplied by the hardness). In the special case of the measurement of the groove area as mentioned previously, the wear rate is expressed as the groove sectional area per revolution of the element (Eiss Jr., 1991).

2.4.3 Wear testing applied to coatings

Wear tests have been developed specifically for coatings. They are generally designed to work for a given combination of material and operating conditions. Indeed, a wear test developed to study thin metallic film may need to be altered for the study of soft, elastomeric, and thick coatings. In general, the methodology can be altered to fit a given situation (Saltzman, 1982).

Bunshah (1982) covers the topic of the selection and use of wear tests for coatings and reviews adhesive, abrasive, fatigue and erosive wear tests for coatings. Not only is wear a very diversified phenomena but coatings are very different and more complicated than monolithic and uncoated materials. Characterization of the coating as well as the coating/substrate interface is essential in order to fully understand the tribological behavior of a coated system. There are probably almost as many wear tests available as there are possible combinations of wear mode and coatings characteristics. Wear tests of coatings are usually accompanied by characterization tests of the coating/substrate and coatings properties (Bunshah, 1982). The characterization tests include:

- characterization of the chemical composition, stoichiometry, phases present, preferred orientation, residual stress, micro-structure, and surface topography,
- adhesion tests (indentation tests, scratch tests, blade tests), and
- tests of mechanical properties such as hardness, bend strength and fracture toughness.

The way wear is evaluated is linked to the identification of the requirements for the coatings while in use and to the identification of possible failure modes. Typical modes of failure identified are:

- loss of adhesion to substrate, eventually resulting in peeling off,
- formation of cavities and/or cracks, leading to local removal of material, and
- loss of original properties such as loss of transmittance for transparent coatings.

The mechanism of wear is characterized by a series of processes. As a result of these processes, a definite pattern is formed, an analysis of which helps to assess the mechanism of wear.

2.4.4 Durability tests for elastomeric fouling release coatings

As previously stated, evaluating the durability of novel coatings is an essential part of the evaluation process. A coating system can be considered durable on a direct level and an indirect level. The direct level of durability refers to its ability to resist mechanical or physical damage whereas the indirect level refers to its ability to retain other initial characteristics or properties. For example, a durable coating is such that its physical characteristics are unaltered (same thickness, same hardness etc.) as well as its chemical properties (fouling release properties, or transmittance for transparent coatings).

Damage of marine antifouling coatings has been evaluated following normal operation (ASTM D4938 - 89, 1989; ASTM D3623, 1993; ASTM D4939 - 89, 1989) and following maintenance cleaning with brushes. The procedure was primarily based on subjective observation of the hull and comparison to pre-defined states (NAVSEA, 1989). The methodology has to be refined for the evaluation of soft elastomeric coatings developed for use in the marine environment. Figure 2.12 lists the sources of mechanical damage encountered by coated systems and establishes a strategy for accelerated laboratory evaluation.

To date, the evaluation of the resistance to mechanical damage has been conducted with controlled, basic and systematic scratch and scrape tests at the N.R.L. (Kohl et al., 1997), at the Naval Surface Warfare Center (N.S.W.C.C.D.) (Haslbeck et al., 1997) and with simulative rotating brush abrasion tests at SUNY-Buffalo (Meyer et al., 1995).

Studies of durability under controlled single contact conditions

Dr. I. L. Singer at the N.R.L. studies fouling release coatings durability with three apparatus: a continuous indentation tester, a scratch tester and a blade scrape adhesion tester. The combination of the three techniques leads to the correlation of mechanical properties and coating durability, the determination of failure modes under basic contact conditions and the screening of candidate coatings.

Continuous indentation tester A Fisherscope Model H100 indents a specimen surface with a 1-mm diameter steel ball (or Vickers diamond) at a controlled rate. The applied force and displacement of the surface are recorded. Typical results include modulus of elasticity, hardness, elastic energy recovery and creep of coated systems.

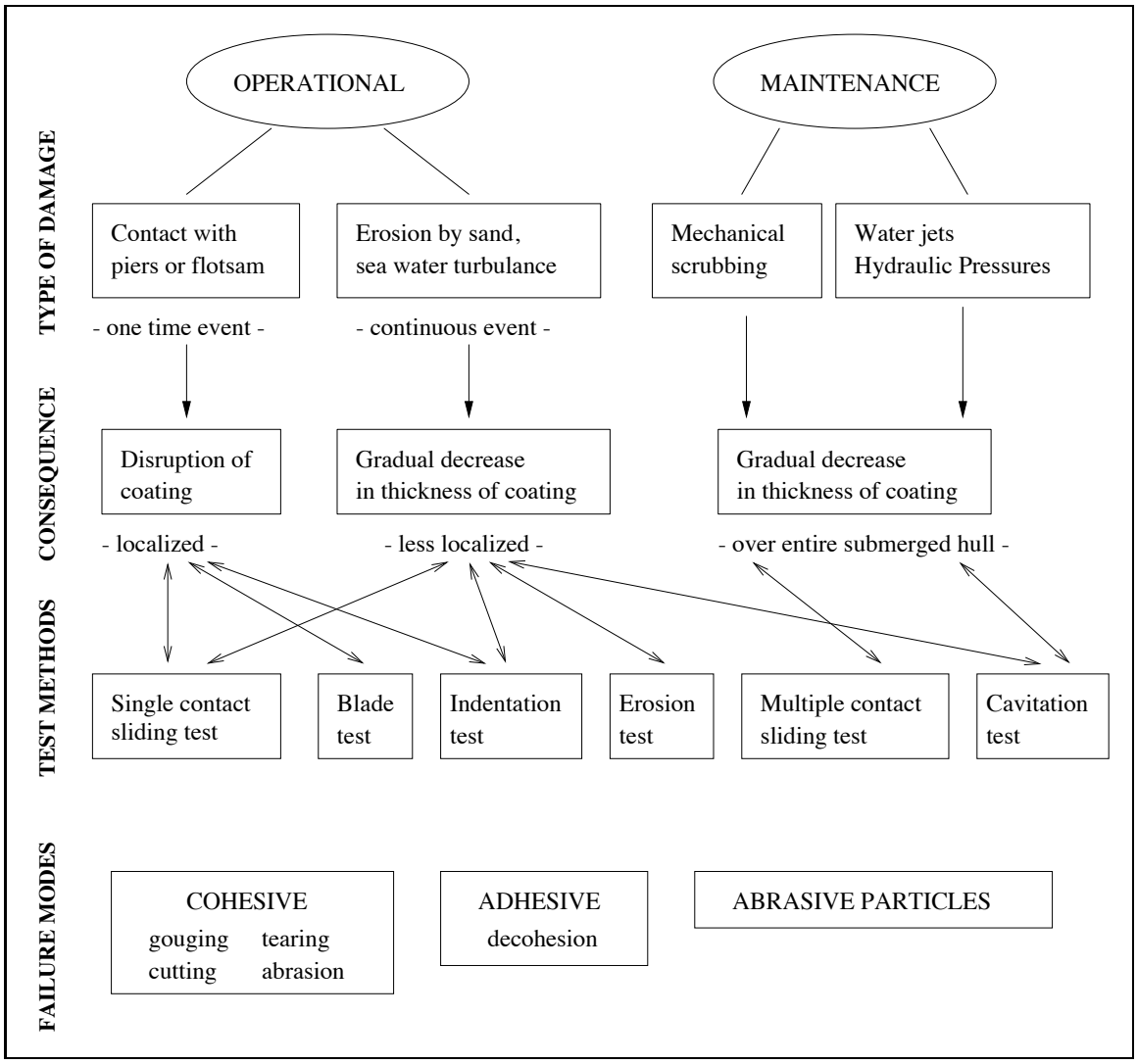

Fig. 2.12 Evaluation of coatings durability

Scratch tester Scratch tests are commonly used to evaluate the durability of hard coatings. The tests can be easily adapted for use with soft elastomeric coatings. The device consists of a stylus sliding at constant speed (5 mm/min) on the surface of a specimen sample under either constant normal load or constant normal loading rate (97 N/min) (Kohl et al., 1997). The stylus shape is well defined: it can be hemispherical (steel, 1.6 mm radius) or conical with varying angles (diamond, 120°, 0.8 mm tip radius). The tangential force and the normal load are recorded leading to the determination of the critical load to failure.

Microscopic observations following single pass scratch tests show typical failure mechanisms for various coating formulations. Typical mechanisms of failure under these testing conditions are tearing, cracking or delamination of the coating from the substrate.

Blade scrape adhesion tester or hesiometer The instrument drives a blade at an angle into the moving coating, causing it to peel. The force and displacement are recorded leading to the determination of the interfacial adhesion energy of the coating.

Rotating brush abrasion testing

The methodology used at SUNY-Buffalo is characterized by multi-contact design. Brush abrasion tests are conducted on pre-exposure coupons. The apparatus is a customized toothbrush tester. As pictured on figure 2.13, it consists of four brushes fixed to the outer perimeter of a rotating wheel. The brushes intermittently contact a sample coupon which is loaded with a fixed normal mass of 290 g. A reservoir which contains the test liquid of interest is located on the path of the brushes and collects coatings fragments and other test residues. The rotational speed of the wheel is equal to 67 RPM, resulting in a brushing rate of approximately 250 brush strokes per minute. A counter records the total number of brush strokes and the test is stopped at four intervals, respectively after 20,000 brush strokes, 50,000 strokes, 90,000 strokes and 145,000 strokes, allowing qualitative and quantitative data analysis.

The wear resistance is quantified through the measurements of the depths of wear of the specimen samples with a depth gauge. Multiple attenuated internal reflection infrared spectroscopy (MAIR-IR) is utilized to analyze pressure-transfered residues and chemical signature exudates. Comprehensive contact angle measurements are collected to evaluate loss or retention of fouling release properties following the abrasion tests. Further details

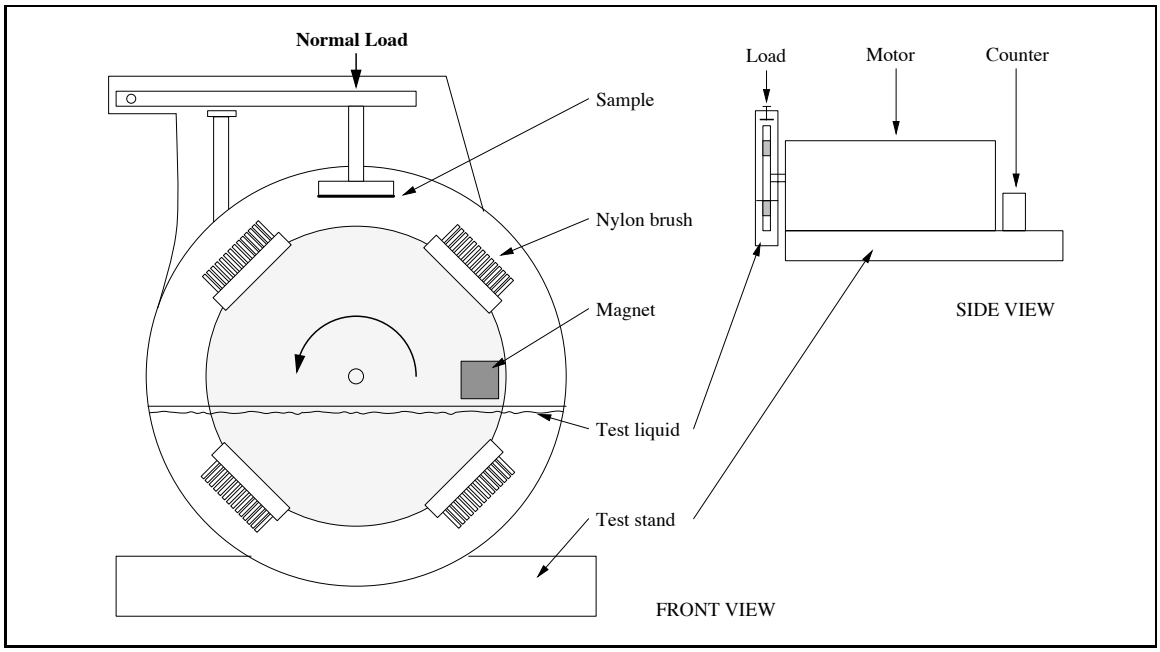

Fig. 2.13 Rotating brush abrasion apparatus developed at SUNY-Buffalo from Baier et al. (1997)

about the apparatus and procedures can be found in Meyer et al. (1994, 1995); Meyer and Baier (1997).

The apparatus developed by SUNY-Buffalo is a very efficient device. However, some design features neglect basic tribological principles. In order to characterize the wear mechanism of the candidate coatings in addition to quantifying the volume of wear, i.e. the durability, a new apparatus has been designed.

Chapter 3

Description of experiments

3.1 Materials and experimental apparatus

3.1.1 Materials

The materials under study are multi-layered systems called "duplex coatings". They are typically composed of one or more anti-corrosion (AC) layers, one intermediate layer and one top layer. The purpose of the intermediate layer is to promote the adhesion of the top layer onto the AC layer. Its chemical composition was formulated in such a way that it also toughens the top layer without affecting its properties. The intermediate and the top layers are respectively called the tie (bond) and release coats in reference to their respective properties. The cross-section of a coated sample can be seen in figure 3.1.

Two series of duplex samples were supplied for testing: the NRL series and the EXS series. Samples from the EXS series are duplex coatings originally developed by General Electric (Carroll et al., 1997). Samples from the NRL series are duplex coatings originally developed by Griffith (1997) of the Naval Research Laboratories. Table 3.2 briefly summarizes the principal constituents for the samples.

The thicknesses of the different layers of a duplex coating may vary widely. Table 3.1 lists the ranges of thickness per type of coating layer according to the patent description (Griffith, 1995). The supplied coatings were available in variable ratios of the top coat thickness to the bond coat thickness: 0/20, 5/15, 10/10, 15/5 and 20/0. The total thickness of the bond and top coat was theoretically maintained constant and equal to 20 mils. In the case of the NRL series, the first number indicates the thickness of the top coat expressed

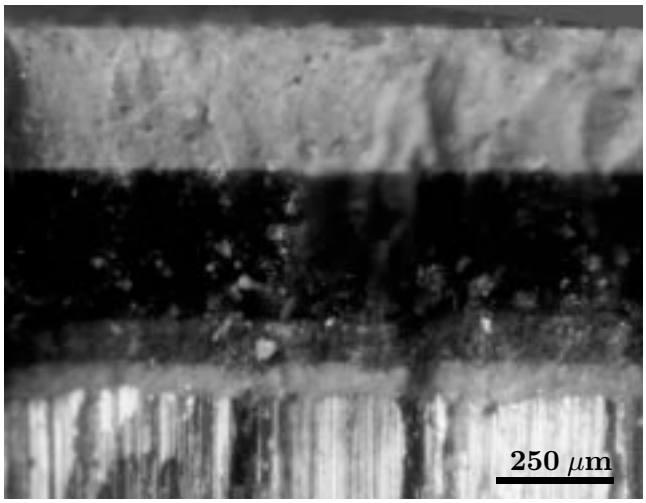

Fig. 3.1 Cross-section of a duplex coated system (NRL 10/10) showing the steel substrate, the anti-corrosion layers, the bond and the top coats.

Table 3.1 Layer thicknesses of the duplex coatings according to Griffith (1995)

		NRL series	EXS series
Anti-corrosive coat	μm (mil)	non-specified	100 – 750 (4 – 30)
Bonding layer	μm (mil)	25 – 250 (1 – 10)	100 – 750 (4 – 30)
Release layer	μm (mil)	50 – 1000 (2 – 40)	250 – 750 (10 – 30)

in mils, whereas the second number represents the thickness of the bond coat in mils as well. However, for the EXS series, the numbers indicated are reversed; the first and second numbers respectively indicating the bond coat and the top coat thicknesses. We chose not to change this designation for ease of comparisons of results with other laboratories. In other words, a EXS 20/0 label refers to a specimen sample with NO top coat and a 20 mil bond coat.

It is important to note that many other candidate coatings have been developed as fouling release coatings and they are not all "duplex" coatings as some of them consist of a single layer applied to multiple anti-corrosion layers.

NRL coatings The present series of samples is labelled "NRL" in this project. However, these samples constitute only a few of the many samples that the Naval Research Laboratories have developed.

Table 3.2 Composition of the duplex coatings

	NRL series	**EXS series**
Top layer	G.E. grey RTV11	G.E. Exsil® 2200
Bonding layer	Wacker Silgan® J-501	Wacker Silgan® J-501
Anti-Corrosion layers	Epoxy	Epoxy
Substrate	Steel	Steel

Table 3.3 Composition of the release layer of NRL samples

Weight %[1]	Component	Example
90–99	Organopolysiloxane with terminal Si-bonded hydroxyl groups	PDMS
0.1–5	Alkyl silicate	
0.1–5	Curing agent	Tin based catalyst
10–300	Fillers	Calcium carbonate

[1]based on the weight of the release layer

Release layer Typically, for NRL samples, the release layer is composed of three components (Griffith, 1995) as indicated in table 3.3. One representative product is the silicone rubber commercialized by General Electric Company: the Room Temperature Vulcanized RTV11. It is a non-toxic two-part, room temperature vulcanized, condensation cured polydimethylsiloxane filled with calcium carbonate. Before curing, it is a white fluid, like paint. The curing agent provided is dibutyl tin dilaureate. Some of its properties (Harper, 1992; Griffith, 1995) are listed in table 2.3 on page 14.

The coatings available to us were coated with a grey top layer which seem different from the commercial RTV11. They have been labelled RTV11 in their shipment. We will refer to the top coat of the samples from the NRL series as "grey RTV11" in order to distinguish them from the commercial white RTV11 compound.

Bonding layer The weight composition of the bonding layer is described in table 3.4 (Griffith, 1995).

One compound frequently used as a bonding layer is Wacker's Silgan® J-501 which is a product of Wacker Silicones Corporation. It is a fluid paint which cures at room temperature on contact to atmospheric moisture and which can liberate s-butylanine naphtha (Griffith, 1995). Its properties are listed in table 2.3 on page 14.

Table 3.4 Composition of the bonding layer

Weight %[1]	Component	Example
10–80; 25–60	Organopolysiloxane with terminal Si-bonded hydroxyl groups	PDMS
30–80; 40–70	Polymerizable vinyl aromatic compound: monofunctional polymer and polyfunctional polymer	Styrene Butyl Acrylate
0.05–3	Curing agent	
0.1–20	Free radical initiator	Organic peroxide
Variable	Fillers	Metallic oxides; Si-based

[1]based on the weight of the bonding layer

EXS coatings The duplex coating formulation of the General Electric Company is very similar to that of the Naval Research Laboratories coating formulation. The release layer is General Electric Exsil® 2200, which is a tin catalyzed, condensation cured fumed silica filled RTV silicone. The bonding layer is generally based on organopolysiloxane chemistry. Wacker's Silgan® J-501 as well as GE silicones SF1708 and SF1927 are used. The anti-corrosive materials, which inhibits corrosion or degradation of the substrate due to reaction with its environment, include a two-component system with an epoxy functionalized base material and a curing catalyst (Carroll et al., 1997). Researchers are trying to simplify the duplex coating technology by combining the anti-corrosive materials with the bonding materials in one layer (Carroll et al., 1997).

Sample preparation Most of the samples tested in this study were obtained through the State University of New York at Buffalo. The detailed procedure for the preparation of the NRL samples is included in Appendix A. A steel plate is initially coated with several layers of epoxy to ensure corrosion protection of the steel substrate. Then, two layers of silicone-based elastomers are one at a time applied onto the epoxy-covered steel substrate. In between each application, the samples are left at room temperature in ambient air allowing sufficient time to ensure partial curing and good adhesion to the previously coated substrate. The silicone-based layers are applied with a Doctor's blade. The Doctor's blade controls the thickness of uncured materials as they are deposited onto the substrate. Upon curing, the thickness of the films tends to decrease due to shrinkage of the material. The percentage shrinkage of a given material is unknown. Instead, an estimate has been made based on

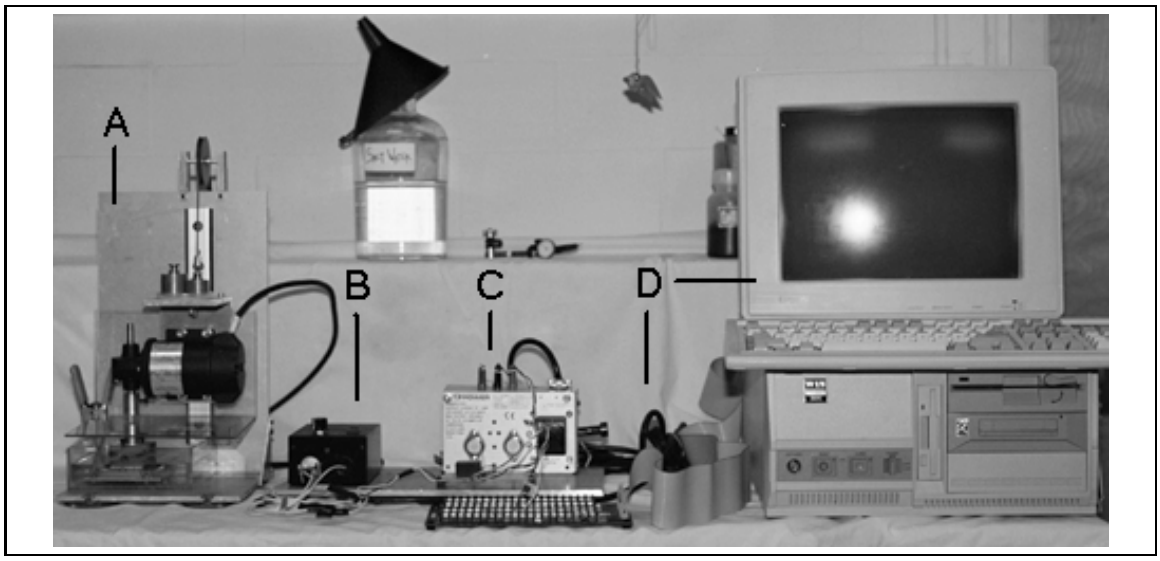

Fig. 3.2 Overview of the experimental set-up where A = wear tester, B = speed control box, C = current sensor circuit, D = data acquisition system.

Table 3.5 Variable test parameters

Parameter	Range
Load	100 g - 300 g - 1000 g
Speed	125 - 395 RPM
Brushes	Flat head toothbrush
	Variable stiffness
Environment	Salt water
Duration	Variable,
	proportional to brush strokes

previous observations. Therefore, for the same setting of the Doctor's blade, the thickness of the dry film may vary significantly. The thickness of the completely dried films, the nominal dry-film thickness, needs to be measured once the coated system is cured completely.

3.1.2 Experimental apparatus: the wear tester

In order to study the action of cleaning brushes on specimen samples, a dedicated and simulative testing apparatus was designed and built. The experimental set-up can be seen in figures 3.2 and 3.3, and a schematic of the wear tester is shown in figure 3.4. This section describes the main apparatus, which will thereafter be called the "wear tester", and its various accessories.

The wear tester has been designed for the specific needs of the current project,

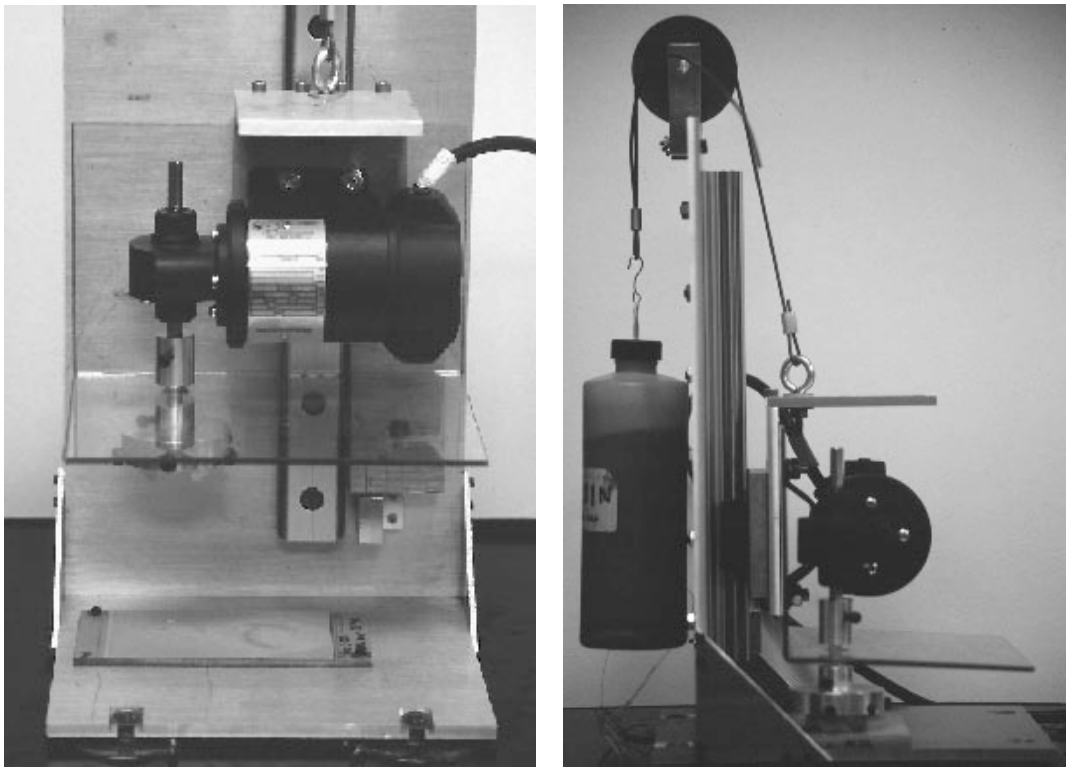

Fig. 3.3 Front and side views of the wear tester

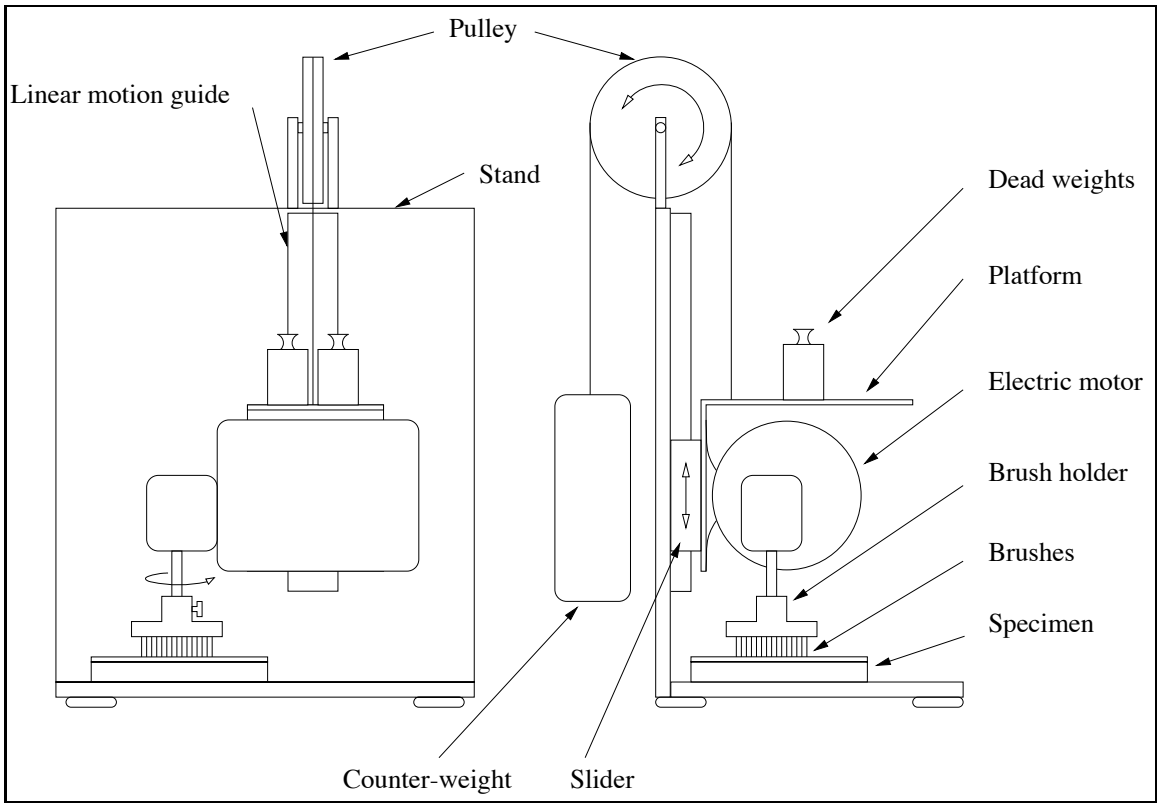

Fig. 3.4 Schematic diagram of the wear tester

i.e. to allow the variation of specific testing parameters as shown in table 3.5. The major variables are the rotational speed of the brushes and, in some way, the applied load. Indeed, the rotational speed is determined by the electric motor, which has an theoretical operating range of 0–416 RPM. In practice however, the speed range is 40–400 RPM. The upper value for the applied load is limited by the types of brushes used. Indeed, when soft brushes are used, an excessive load may cause the tufts to buckle and fail. The other test parameters can be easily varied: brush type, environment or duration of the tests, rendering the apparatus quite versatile.

As seen in figure 3.4, brushes are fixed on a holder, thereafter referred to as the brush holder, which is fastened onto an electric motor shaft. The electric motor is placed on the slider of a Techno Isel linear motion guide allowing vertical motion of the motor. The overall system (electric motor + various shields + brush holder + brushes) is counter-weighted with lead shot and a pulley. The linear motion guide, the counter-weight system, and therefore, the electric motor and other platforms and shields, are fixed on an aluminum L-shaped frame, thereafter called the stand.

Load is applied by placing dead weights directly onto a platform above the electric motor, the former platform being fastened to the slider of the linear motion guide as well.

A specimen sample is mounted either directly on the stand base as seen in figure 3.3a or to a holder which is then attached to the stand. Both sample mounting procedures ensure that the sample is properly aligned with the motor shaft.

To conduct tests in submerged conditions, either the whole testing apparatus can be placed in an aquarium (Fig. 3.5), or the sample and sample holder are fixed in a small container which is in turn attached to the test stand (Fig. 3.6).

Electric motor

A 1/25 HP electric DC gear motor manufactured by Baldor is utilized. A DC control box (SCR) controls the variation of the rotational speed of the shaft to speeds up to 412 RPM. A strobotac was used to calibrate the motor speed (Appendix B). The motor speed is controlled with the percentage on the control device. Most of the tests carried out in this study were run at a low and a high level of speed, which are set, respectively, at 40% and 100%. Using the calibration curve, these levels correspond to (125 ± 5) RPM for the low setting and (395 ± 5) RPM for the high setting.

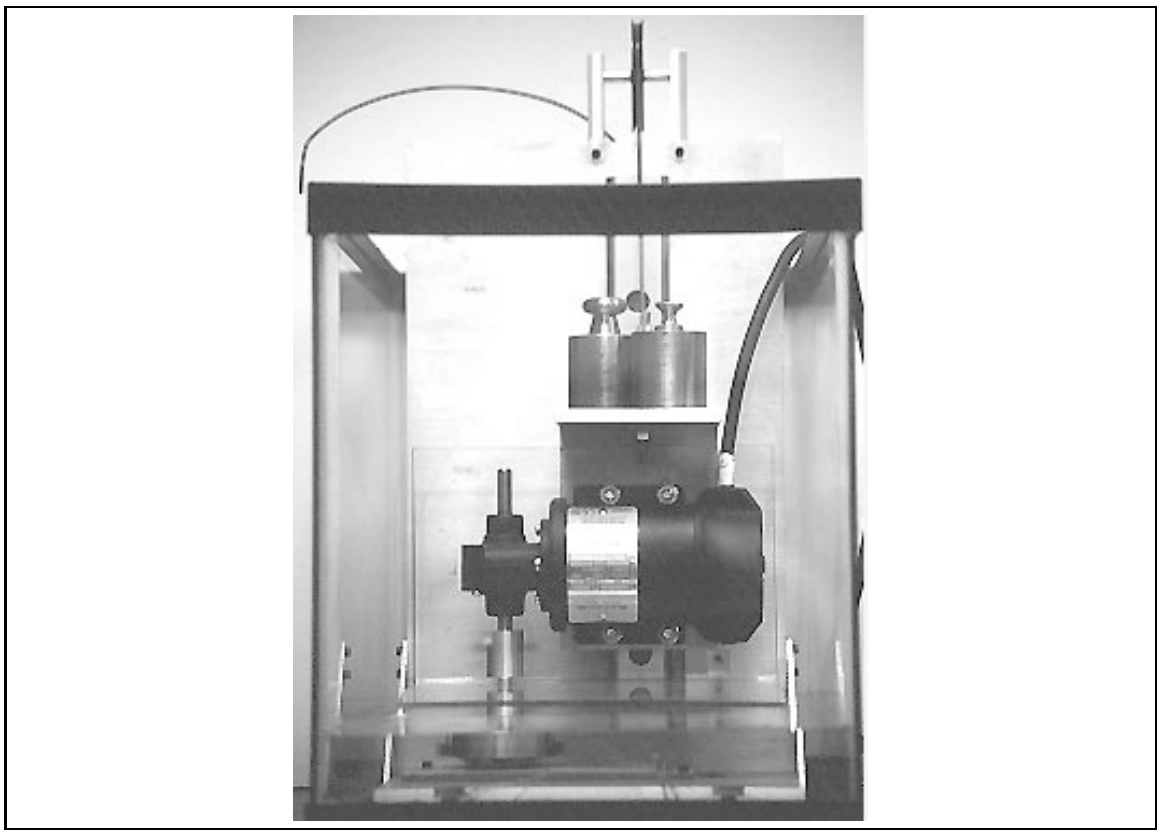

Fig. 3.5 Front view of the testing apparatus partially immersed in water in an aquarium

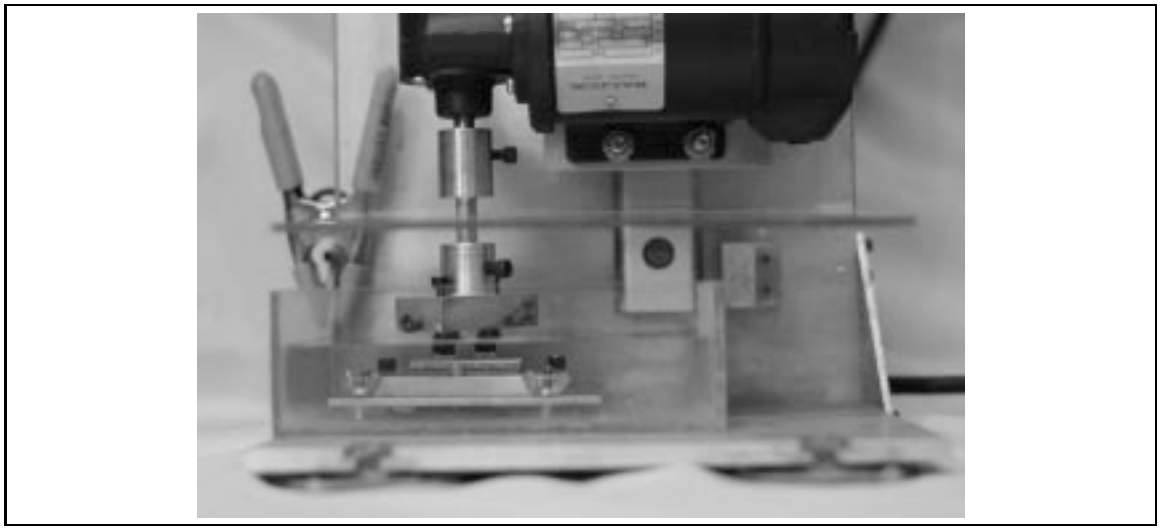

Fig. 3.6 Close-up view of the specimen sample immersed in water

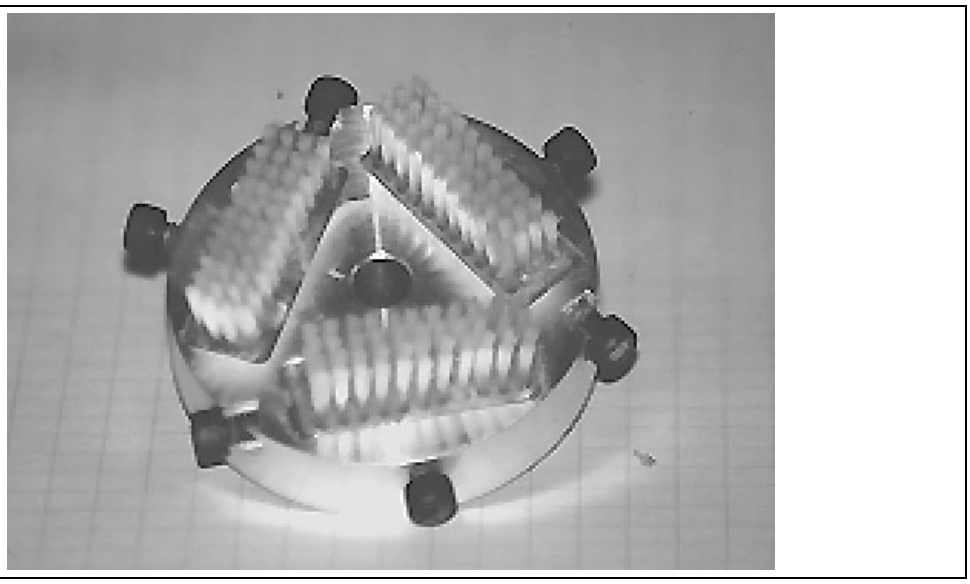

Fig. 3.7 Initial design of the toothbrush holder

Brush holder

Several brush holders were designed and built. The initial design made with aluminum accommodated three brushes. It can be seen in figure 3.7. This holder is used for large samples. For smaller samples, the former holder is not appropriate due to the large circumference of the brushing path. An alternate brush holder which accommodates a single brush was designed and built. The center of the brush matches the axis of rotation as indicated in figures 3.9 and 3.13 by the letter C.

Brushes

The brushes used are commercial toothbrushes, chosen for their low cost, their availability and their consistent high quality. Also, researchers at the State University of New York at Buffalo used commercial toothbrushes for their tests. The commercial toothbrushes used were Colgate Classic flat head, medium stiffness. The stiffness of a commercial toothbrush is typically achieved by changing the geometrical characteristics of the brush. The number of bristles per tuft, number of tufts per head as well as spatial arrangement of the tufts on the head of the brush are parameters typically varied in toothbrush design (Rawls et al., 1990) to achieve a desired stiffness while maintaining the overall cleaning efficacy. The geometry of the toothbrush head is detailed in figure 3.9. The shape and dimensions of the wear scar are critical for the analysis of wear in this study. The classical wear quantification

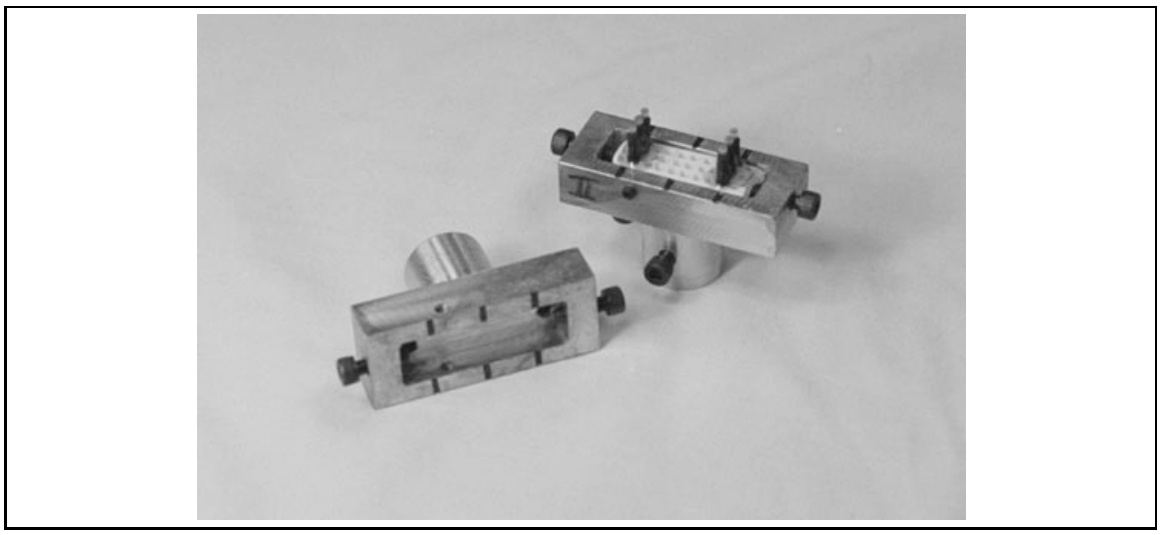

Fig. 3.8 Single brush holder

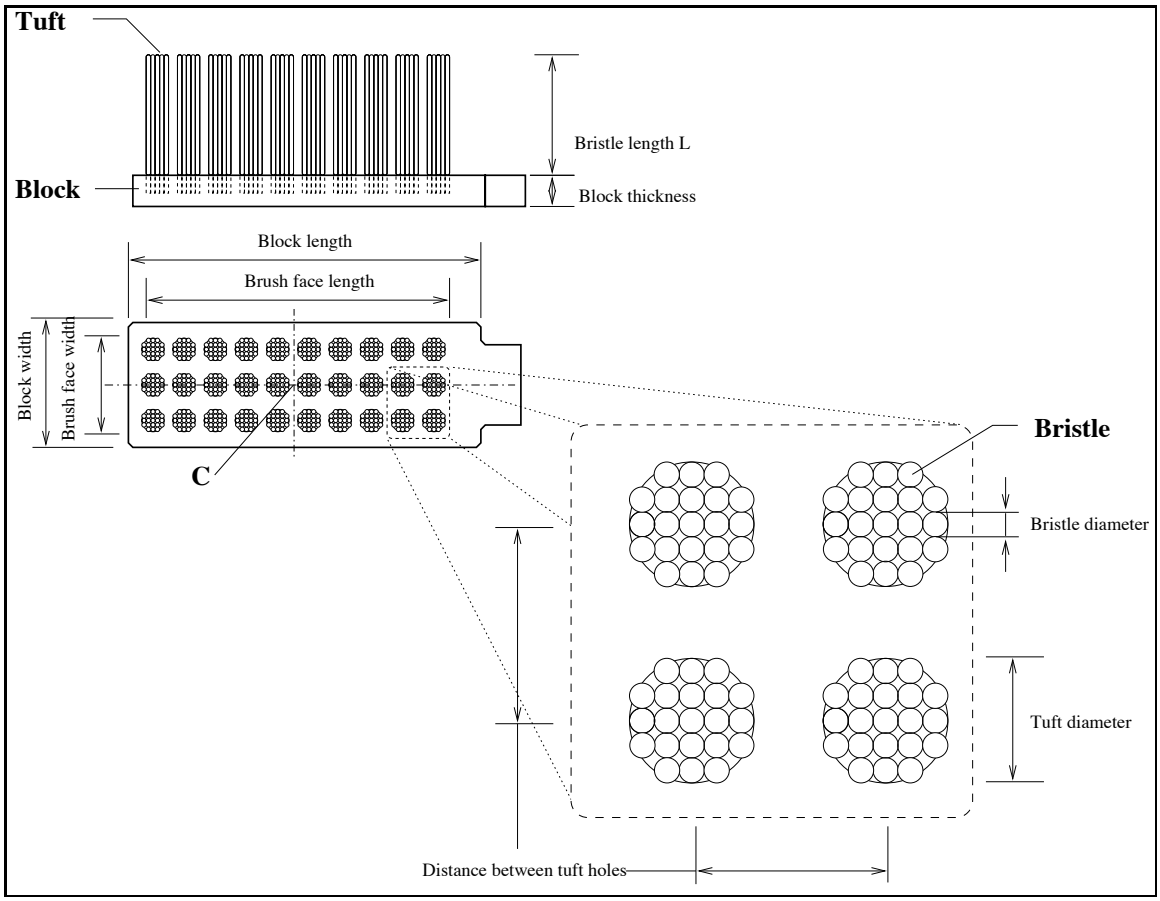

Fig. 3.9 Terminology of a toothbrush head

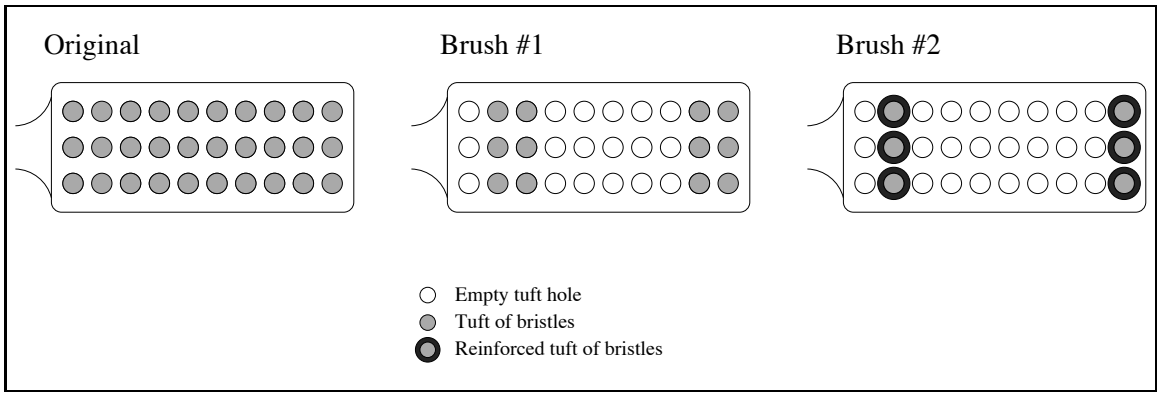

Fig. 3.10 Three brush design: original toothbrush head, altered head (#1) and altered-reinforced (#2)

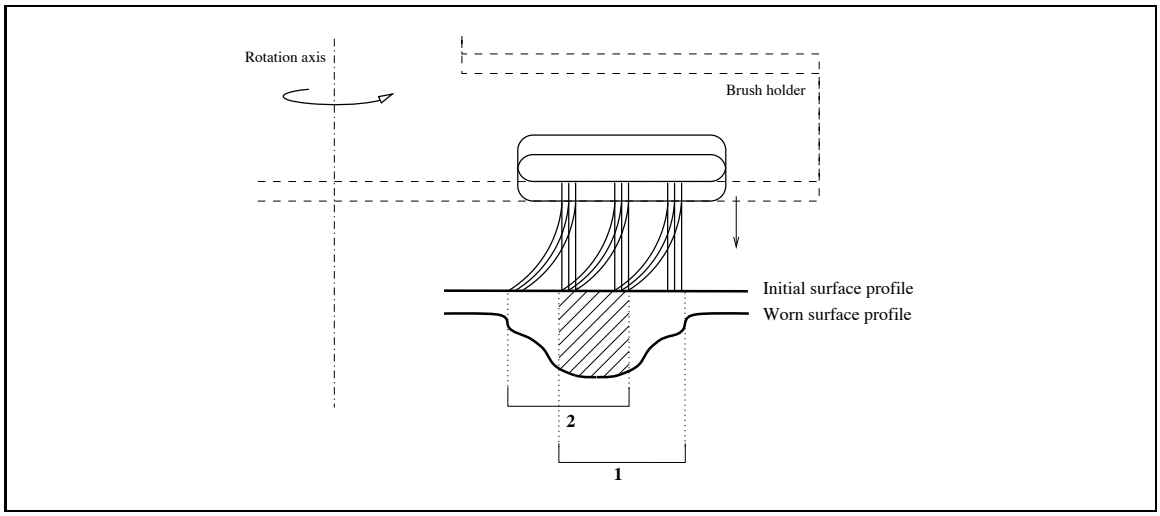

Fig. 3.11 Error in the profile of the wear track induced by bending of the bristles. Region 1 and region 2 respectively represent the initial and final positions of the bristles on the sample. The shaded region is subjected to brushing throughout the whole test.

method through weight measurements can not be utilized because the mass loss is below the resolution of the balance which can weight the specimen mass. Instead, a profiler was used. The latter (section 3.1.3) has a 10 mm limit for the length of a scan. As a consequence, the width of the wear scar had to be restrained. If the original toothbrush head is rotated around its center C, the wear scar is circular, with a diameter slightly larger than the brush face length. In such a configuration, the profiler can not be utilized as well. To obtain a ring-shaped scar within the limits set by the profiler used, tufts were removed from the brush head in a way that the single brush head can be considered as two brushes of three tufts each. This new brush design is called the design #2 and is shown in figure 3.10.

One additional problem inherent to the use of commercial toothbrushes is the low bending stiffness of the bristles. Indeed, the combination of the bristles small diameter and the properties of nylon leads to bending of the bristles in the course of a given test. As a consequence, as the bristles bend during the test, the wear track tends to widen. This is a problem since a given point of the wear track will be brushed more or less depending on its location across the track. As the bristles bend towards the center of the track, the outer and inner locations across the wear track will be subjected to a lower number of brush strokes than the center part of the scar as illustrated in figure 3.11. As we have no way to rapidly characterize the bending rate and the extent of bending of the bristles, it is incorrect to characterize the given wear track in terms of one given number of brush strokes.

In order to limit the bending of the brushes, the brushes can either be substituted by custom designed brushes, using different material, different dimensions and characteristics, or they can be altered in such a way that the brush stiffness increases. According to the model developed by Rawls et al. (1990), reducing the length of the bristles increases brush stiffness. This is accomplished by immobilizing the base of the tufts as seen in figure 3.12. Heat shrinkable electric tubing was used for this purpose. Small 9 mm (0.35 in) long tubes were positioned around each tuft of bristles. As heat is applied using a cigarette lighter, the tubes shrink around the nylon bristles. Extra care was used not to melt the nylon bristles. Once each tuft was constrained by the tubing material, extra-strength and quick-set Master Mend® epoxy resin (manufactured by Duro) was deposited around the base of the tubes to fix them. The epoxy used is clear, waterproof, solvent-resistant, and sets in 4–6 minutes. The design was successfully tested under the working loads, speeds and duration of the wear tests. According to the stiffness equation developed by Rawls et al. (1990) (equation G.11 in Appendix G), the brush stiffness was multiplied by a factor of 17. The achieved stiffness value of the brush is half that of an equivalent steel brush. Figure 3.13 illustrates the details of brush design #2. The characteristics of the brushes used for each design illustrated in figure 3.10 are summarized in table 3.6. The brush face length, d, is approximately 25 mm, resulting in average sliding speeds of 8.56 cm/s at 395 RPM and 2.7 cm/s at 125 RPM.

The tips of the bristles have been studied and even though they are rounded off during the manufacture of the brush, they can be quite irregular as shown in figure 3.14.

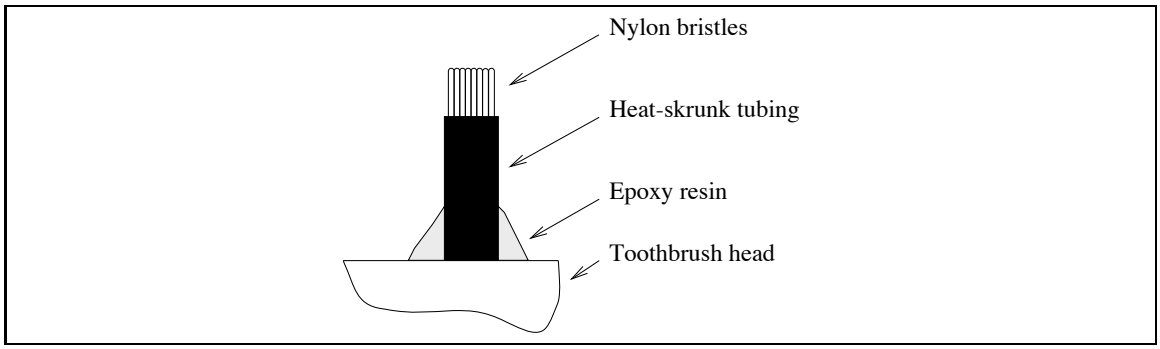

Fig. 3.12 Stiffening of a toothbrush tuft

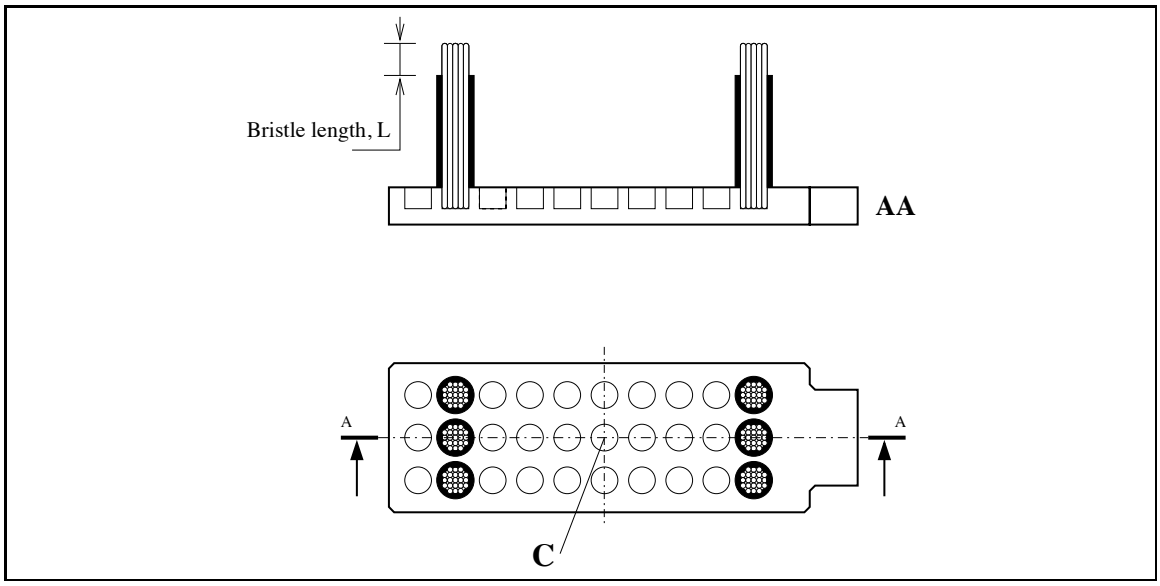

Fig. 3.13 The altered toothbrush head (design #2)

Table 3.6 Characteristics of the brushes used as seen in figure 3.10

	Brush design		Original	# 1	# 2
Bristle	Material[1]		Nylon 612	Nylon 612	Nylon 612
	Diameter[2], D_b	(mm)	0.290	0.290	0.290
	Length[2], L	(mm)	11	11	2.5
Tuft	Base diameter[2], D_{base}	(mm)	2.12		
	Top diameter[2], D_{top}	(mm)	2.34		
	Diameter[3], D_T	(mm)	2.23		
	Number of bristles[4]		38		
Brush	Number of rows		3	3	3
	Number of columns		10	4	2
	Number of tufts, N_T		30	12	6
	Number of bristles, N_b		1140	228	228
	Calculated stiffness[5], N/m		438.5	175.4	7470.0

[1]Source Colgate-Palmolive

[2]Measured by microscopic observation on TV monitor

[3]Average of base and top diameters

[4]Average of all tufts (microscopic observations)

[5]Per Rawls et al. (1990), modeled as 2 separate brushes

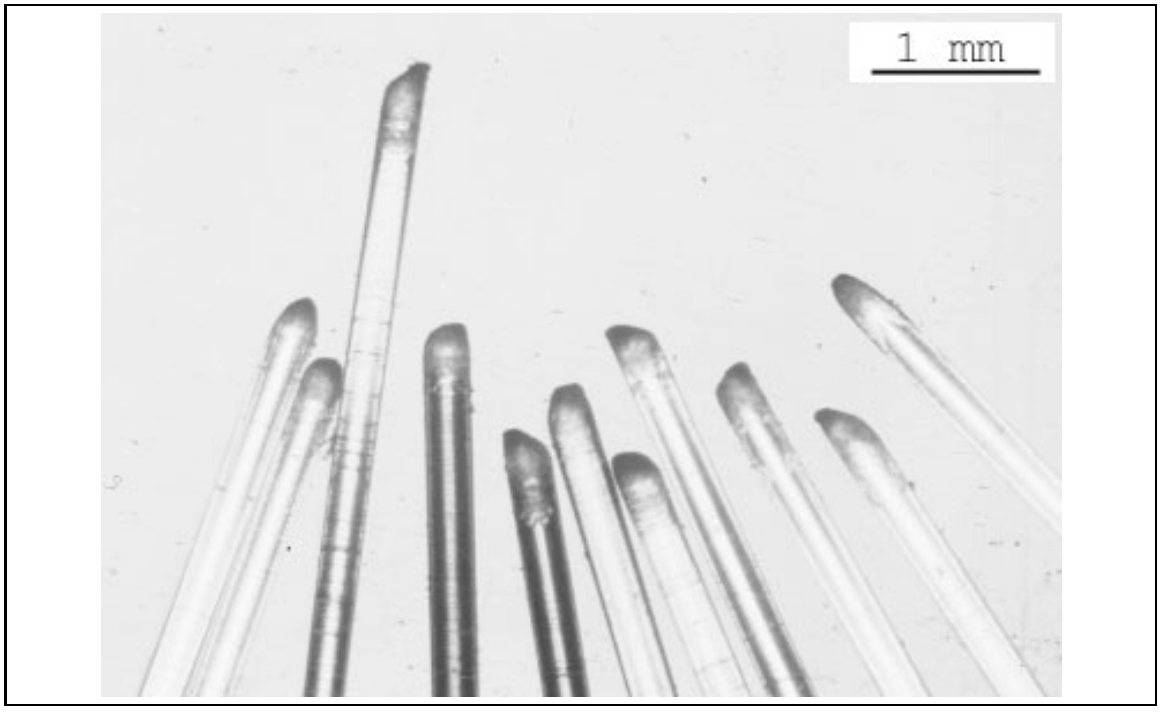

Fig. 3.14 Tips of nylon bristles

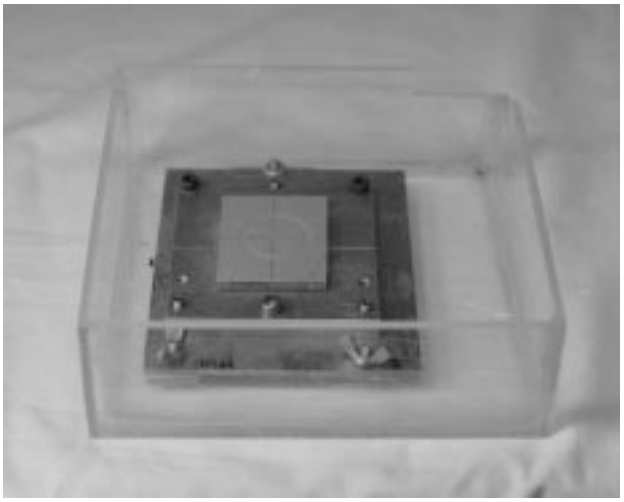

Fig. 3.15 View of the sample holder device in the container for running test in submerged conditions.

Sample holder

Various methods for securing the specimen samples in the test rig have been used depending on the sample substrate material, size or other design specifics. However, throughout the tests, one design was used primarily. The samples are fixed on a sample holder with epoxy glue (Duro Master Mend®) or silicone glue (General Electric Silicone Clear, General Purpose Glue and Seal). The sample holder consists of a 1/4 in thick aluminum square which was designed to fit accurately on the stand base. The sample holder has alignment ticks which facilitated, accelerated and rendered more accurate the positioning of the specimen samples, hence the alignment with the electric motor shaft. The sample holder also has three so-called alignment screws which permit the alignment of the sample surface with the plane of rotation of the tips of the brushes. A picture of the sample holder can be seen in figure 3.15.

Environment control

Tests can be run under submerged conditions by either placing the apparatus in a aquarium or by placing the sample and sample holder in a small Plexiglas container with approximately 500 ml capacity. The later container is, in turn, attached to the test stand. With the latter design, the sample holder is attached directly to the container with stainless-steel screws and brass wing nuts. In the course of one test, the holder can be easily removed for

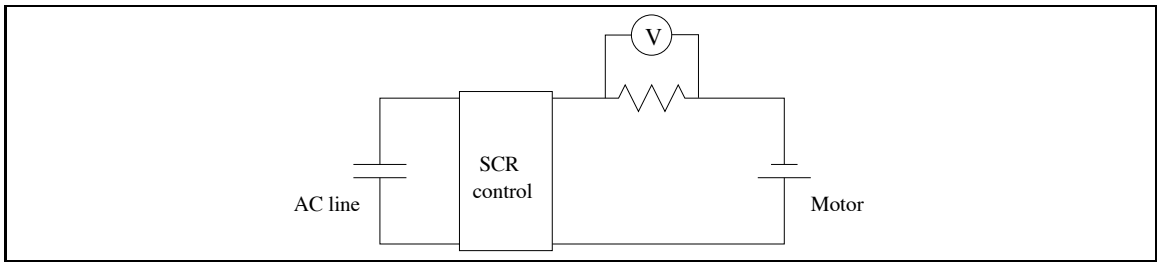

Fig. 3.16 Conventional voltage measurement

data collection and placed back for further testing. The latter design was preferable as a smaller quantity of water was used and could therefore be filtered to collect wear debris. It also facilitated controls and eventual interventions while a test was running. The small container is pictured in figure 3.15. It is made out of 1/8 in thick Plexiglas sheet, assembled with super glue and sealed with silicone glue. Salt water is synthesized with Instant Ocean synthetic sea salt.

When the test is run in the small Plexiglas container, the test fluid can be collected and filtered using filter paper (FisherBrand, qualitative P8, coarse porosity, fast flow rate) in between each phase or at the end of the test. The fluid was systematically filtered after each test to collect wear debris and the filter was placed in a sealed plastic bag for further analysis.

Data Acquisition

In order to monitor the torque of the electric motor, the voltage input in the electric motor was monitored during the tests. Knowing the torque of the motor provides information on the level of friction between the brushes and the surface. Ideally, we were hoping to observe changes in the voltage either as a consequence of debris formation or as a consequence of the removal of the top layer.

Current sensing electrical circuit The SCR phase control does not provide isolation between the electric motor and the AC power line. Therefore, the traditional reading of the voltage across a resistor placed in series (Fig. 3.16) is not possible because of the presence of a ground loop which is larger than the operational voltage range of the data acquisition board used (30 volts).

In order to insulate the data acquisition board from the circuit, a closed loop Hall

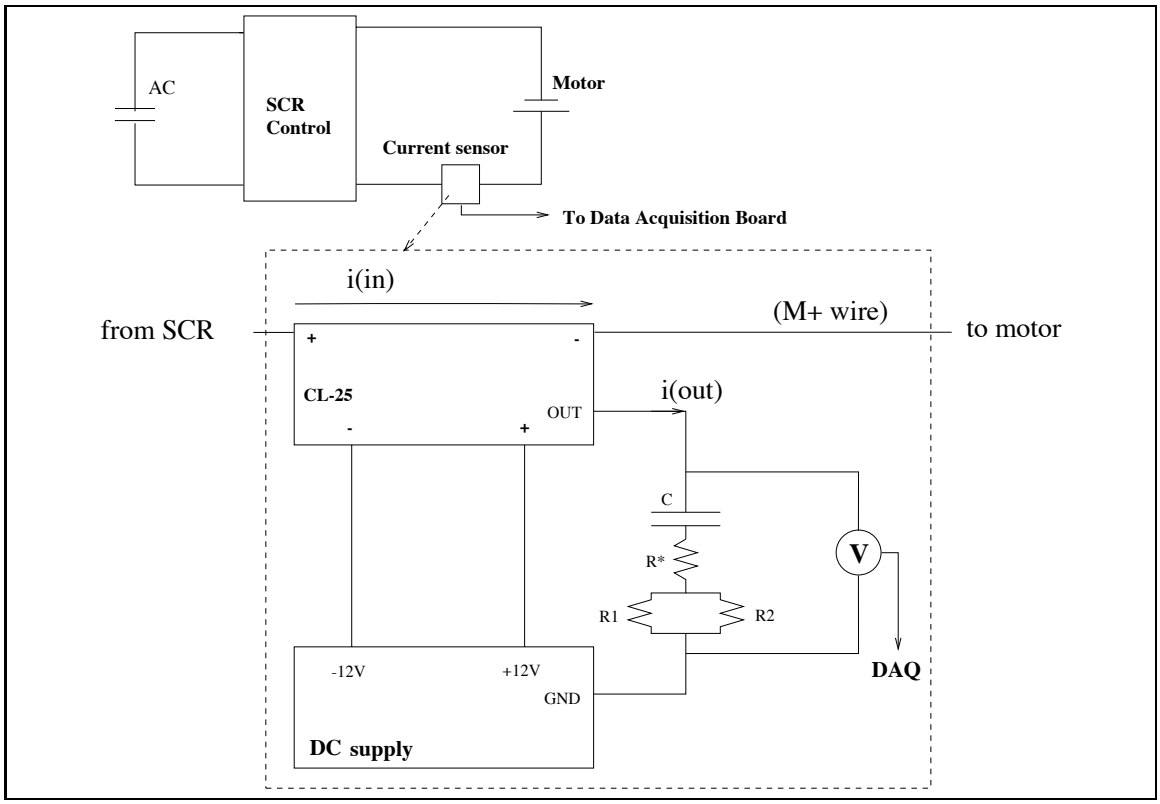

Fig. 3.17 Voltage measurement with a custom designed circuit

effect current sensor was connected to the system as shown in figure 3.17.

Its principle is shown in figure 3.18. It consists of a coil wound around a magnetic core, a Hall generator placed in the gap of the core and an amplifier which drives the coil. The current in the coil sets up a magnetic field which opposes the field produced by the current carrying conductor placed through the aperture of the sensor. The output of the sensor is a current proportionate to the current through the aperture. It measures AC and DC currents accurately and provides electrical isolation between the current carrying conductor and the output of the sensor. Therefore, the output of the sensor can be connected to a data acquisition board.

The sensor used is a F. W. Bell sensor, CL-25, operated by an International Power bipolar DC power supply ($\pm$12 V at 0.4 A) with adjustable outputs. The turns ratio is set as 1:200.

Data acquisition A DT-2801 A/D board is used. A data acquisition program was initially written in Basic by Frank Caldwell and further modified by the author. A complete

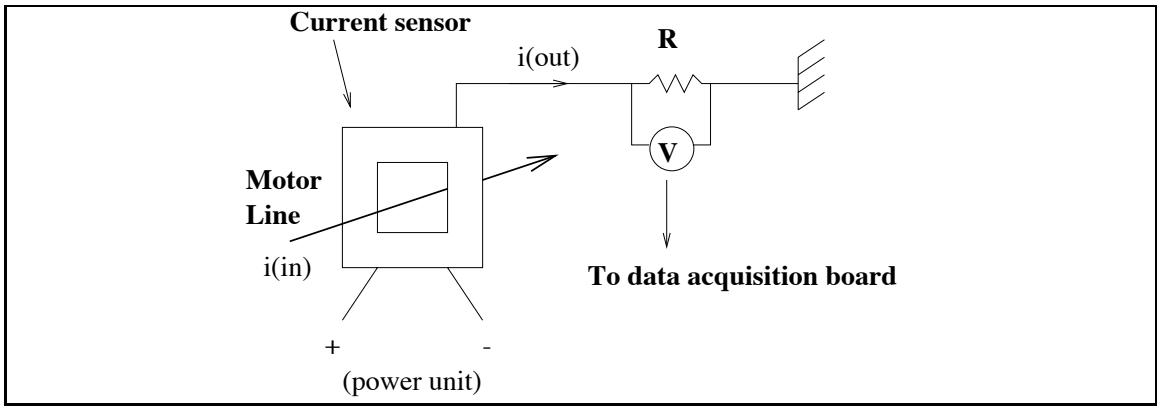

Fig. 3.18 Principle of the closed-loop Hall effect sensor

listing of the data acquisition program can be found in Appendix C.

3.1.3 Experimental techniques: collection of wear data.

Back-reflected light microscope

A Wild Makroscope with a magnification range from 1.5× to 128× and with a 5 to 1 zoom lens is equipped with a 35 mm Polaroid camera, as well as a video camera and a TV monitor. It is used in this study to observe the surface condition during and after the wear tests. It is also used the characterization of toothbrush bristles, the determination of the sample thickness or for various alignment procedures.

Tencor Alpha-Step 500 profile meter

Theory of operation The primary method used to quantify wear through the volume of lost material is profilometry with a Tencor Alpha-Step 500 profiler. It is a computerized, high-sensitivity instrument which characterizes a surface by scanning it with a diamond stylus. The resulting trace is a cross-sectional view of the surface. It can be used to measure the cross-section area of grooves worn by indenters in a sample, leading to the evaluation of wear.

The Alpha-Step 500 has an inductive sensor which registers the vertical motion of the stylus. The stylus assembly is attached to an arm that rotates about a flexure pivot, ensuring smooth and stable movement across the scan length. It features the ability to measure micro-roughness over short distances as well as waviness over a full, 10 mm (0.4 in.) scan. Vertical features ranging from under 100 $\mathring{\text{A}}$ (0.4 μin.) to approximately 0.3 mm (12 mils)

can be measured with a vertical resolution of 1 or 25 Å (0.004 or 0.1 μin.). A variety of materials can be profiled with the instrument. Samples of up to 150 mm (6 in.) wide and 15 mm (0.59 in.) thick can be accommodated. A Manual Precision XY Stage is used to position samples for scanning. An attached 80486DX computer offers measurement control, data storage, and analysis. The scanner assembly moves the 12.5 μm radius stylus across sample surfaces to collect profile data. The stylus force is manually adjustable in the range of 1.0–99.9 mg. A given stylus force is recommended by the manufacturer for a given scan speed. The stylus drop speed can be set by the user. A very low setting is required for very soft samples, or for styli with radii below 5 μm.

Surface analysis fields include many general purpose parameters such as the area of peaks, of valleys, the profile length, the average roughness, the RMS roughness or the average waviness.

Recipe setting The recipe contains scanning instructions, as well as settings for surface analysis. The maximum scan length is 10 mm (0.4 in.), and the maximum scan time is 100 s. Scan speeds range from 2 to 200 μm/s. The sample rate is the nominal rate at which data is collected. It can be set to 50, 100, or 200 Hz for all scan speeds. Setting the scan speed and the sample rate will determine the horizontal resolution.

Figure 3.19 shows the recipe used for collection of profiles in this study. For the tests run with the altered brushes (design #2), as the wear scar width is approximately 3 mm, the selected scanning length is set at 5 mm. The scanning speed is set at 200 μm/s, then the scan time is automatically 25 seconds. The sampling rate selected is 50 Hz, leading to a horizontal resolution (or sampling interval) of 4 μm. The total number of data points collected in a profile is approximately 1250.

The high scanning speed lowers the sampling interval, hence the horizontal resolution. However, such a high speed was chosen because, in the case of polymeric materials, it has been shown that a high traveling speed reduces the stylus penetration in the specimen material. Gilliam (1985) showed that for polymeric materials the stylus indentation decreases with faster traversing speeds. Further investigation has been done by the author as well (Appendix F).

The stylus force selected is 15 mg. The instrument manufacturer recommends the use of stylus force ranging from 12 to 40 mg (Tencor Instruments, 1994) for a 200 μm/s scanning

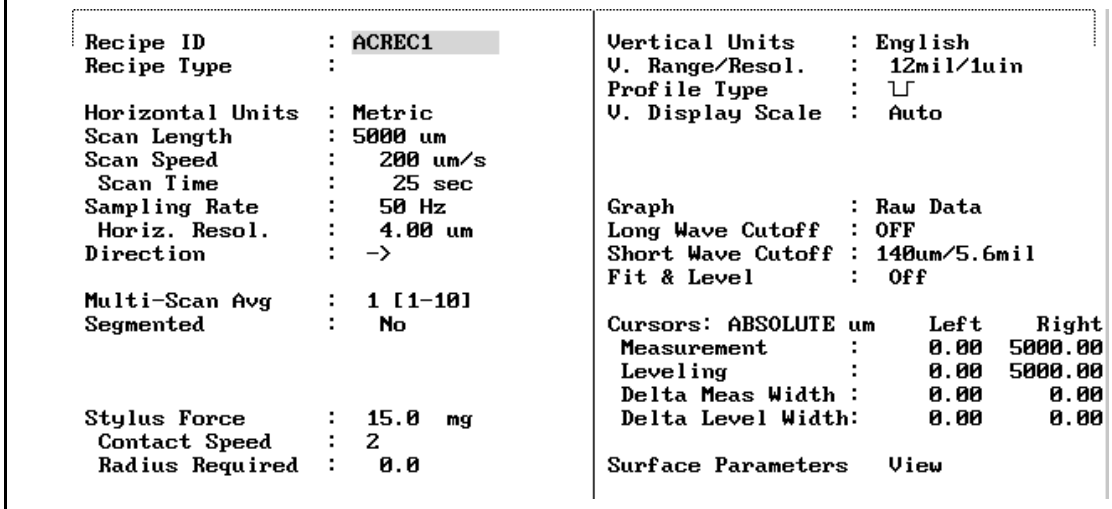

Recipe ID	: ACREC1	Vertical Units	: English
Recipe Type	:	V. Range/Resol.	: 12mil/1uin
		Profile Type	: ⊔
Horizontal Units	: Metric	V. Display Scale	: Auto
Scan Length	: 5000 um		
Scan Speed	: 200 um/s		
Scan Time	: 25 sec		
Sampling Rate	: 50 Hz	Graph	: Raw Data
Horiz. Resol.	: 4.00 um	Long Wave Cutoff	: OFF
Direction	: ->	Short Wave Cutoff	: 140um/5.6mil
		Fit & Level	: Off
Multi-Scan Avg	: 1 [1-10]		
Segmented	: No	Cursors: ABSOLUTE um	Left Right
		Measurement	: 0.00 5000.00
		Leveling	: 0.00 5000.00
		Delta Meas Width	: 0.00 0.00
Stylus Force	: 15.0 mg	Delta Level Width	: 0.00 0.00
Contact Speed	: 2		
Radius Required	: 0.0	Surface Parameters	View

(a) Main page of the recipe

SURFACE ANALYSIS

TIR	Tot Ind Runout	No	ROUGHNESS PARAMETERS:			
Avg	Average Height	Yes	Ra	Average	Display	
Slope	Slope	No	MaxRa	Maximum Ra	No	
Rad	Radius	Yes	Rq	RMS	Display	
Area+	Area of Peaks	Display	Rp	Peak	No	
Area-	Area of Valleys	Display	Rv	Valley	No	
Area	Total Area	Yes	Rt	Peak/Valley	Yes	
ProfL	Profile Length	No	Rz	10pt Height	No	
MaxHt	Maximum Height	Display	R3z	6pt Height	No	
MinHt	Minimum Height	Display	Rh	Roughness Height	Yes	
Edge	Distance to Edge	No	WAVINESS PARAMETERS:			
StpWd	Width of Step	No	Wa	Average	No	
StpN	Number of Steps	No	Wq	RMS	No	
StpMn	Mean Step Height	No	Wp	Peak	No	
StpSD	Std Dev Step Ht	No	Wv	Valley	Yes	
			Wt	Peak/Valley	Yes	
EDGE TYPE:	UpEdge		Wh	Waviness Height	Yes	

(b) Surface analysis page of the recipe

Fig. 3.19 Recipe parameters for the collection of surface profiles.

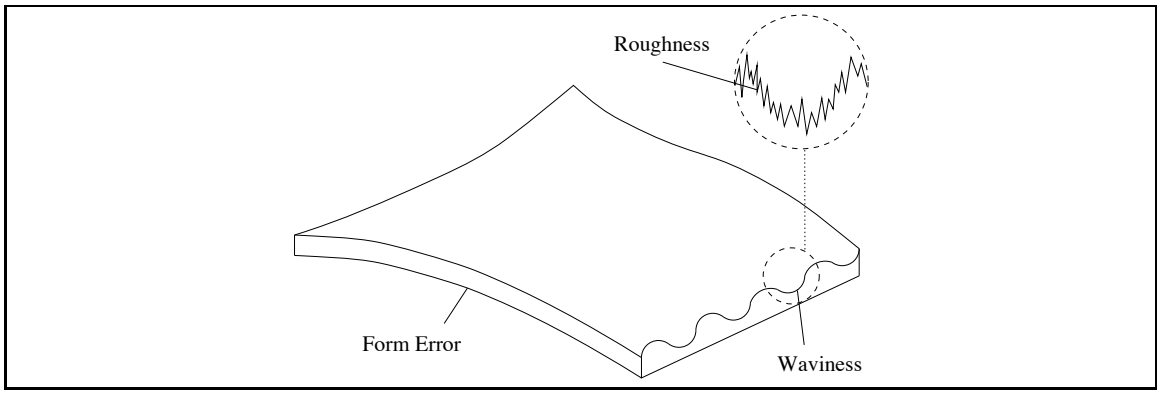

Fig. 3.20 Three types of surface texture parameters

speed. Since the samples tested are soft materials, a low stylus force was recommended as well as a low stylus contact speed.

The vertical range is set at its maximum: 300 μm (12 mils), with a vertical resolution of 25 $\mathring{\text{A}}$ (1 μin). The profile type selected for our measurements is a valley bias which is appropriate for measuring grooves. The wavelength cut-off allows one to separate readings of roughness, waviness and form error. The roughness is regarded as the fine grain texture of a surface. Coarser irregularities, with 30 to more than 100 times the wavelength of the roughness, constitute waviness. With a high pass filter, waviness can be removed from the trace. Form error is defined as the deviation from a perfect realization of a nominally specified shape (flatness as an example). These concepts are illustrated in figure 3.20.

Figure 3.19 also displays the Surface Analysis window of the recipe. It allows the user to select the surface analysis parameters which are calculated following recording of the height data. The following parameters are displayed on the profile window: the area of peaks, Area +; the area of valleys, Area -; the maximum height, MaxHt; the minimum height, MinHt; the average roughness, Ra; and the Root-Mean-Square (RMS) roughness, Rq. The following parameters were recorded in the data summary: the average height, Avg; the distance from the center of curvature of the profile arc to the profile, Rad; the sum of the area of peaks and area of valleys, Area; the vertical distance between the highest peak and the lowest valley in the sampling length leveled on the mean line, Rt; the difference in height in the roughness profile, Rh as well as waviness parameters such as Wt, and Wh. The area of valleys, Area -, is equal to the total area bounded by the leveled baseline and the profile where it descends below the baseline within the sampling length. The area of peaks,

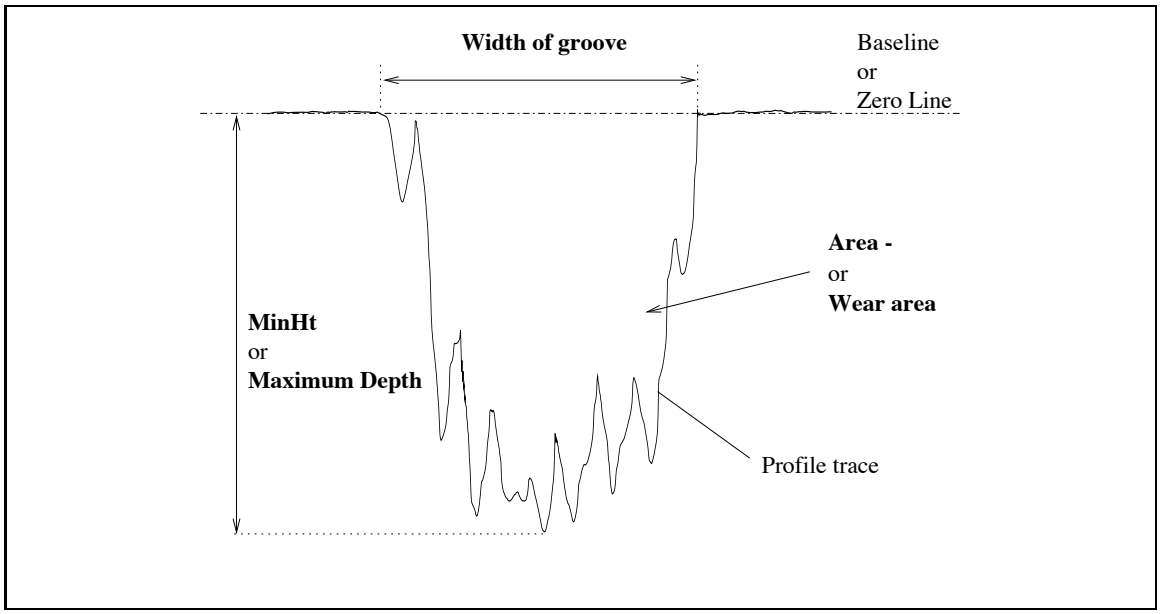

Fig. 3.21 Details of the computation of the wear data from a surface profile.

Area +, is equal to the total area bounded by the leveled baseline and the profile where it rises above the baseline within the sampling length. MaxHt and MinHt are respectively the maximum and the minimum height of the trace relative to the zero line within the sampling length. Ra and Rq were defined previously. The wear data collected in this study includes the wear area (which is equivalent to the area of valleys, Area -), the maximum depth of the wear track (which is equivalent to the minimum height of the profile, MinHt) and the track width as seen in figure 3.21 for a given surface profile.

3.2 Experimental procedures

3.2.1 Pre-wear tests

Sample preparation

1. The samples are cut to a square size of 1.5 inch by 1.5 inch with a band saw. Prior to cutting, special care is taken to protect the surface of the coatings from the metal burrs by applying a thin plastic film on the surface of the sample and securing it with tape.

2. A thickness gauge for ferrous substrates, the Minitest type F102 by Electro-Physik, Inc., is used to measure the total thickness of the multiple layers, including the anti-

corrosion, the tie and the top layers. The measurement of the thicknesses of each individual layer was done with the microscope (section 3.1.3 on page 62). A total of 12 measurements is collected and averaged for each layer. Results are reported in Chapter 4.

3. After the thickness of the candidate samples is recorded, a thin coat of silicone glue is applied to the sides of the samples on the steel substrate to inhibit corrosion. Samples are rinsed off with salt water to remove dust or any loose debris from the surface.

4. Samples are then closely examined under the microscope and defects or unusual features are reported prior to running the wear test.

5. The samples are fixed on a sample holder with general purpose silicone glue (General Electric Silicone Clear, General Purpose Glue and Seal) and are placed in the fume hood overnight.

Brush preparation

1. Brushes are prepared according to the design chosen. Tufts are removed off and the remaining tufts are stiffened according to the procedure previously described. Once the brush is prepared, the handle is cut off and quality control is done with the microscope.

2. To limit the influence of changes in the properties of the nylon fibers upon water absorption, brushes are soaked for 24 hours minimum in salt water.

Brushes and samples alignment Since the brush bristles tips form a plane which is in contact with the plane of the specimen sample, the geometry of the contact is flat-on-flat. This is leads to difficulties to align the brushes with the sample surface. The alignment procedure is critical. Indeed, if the contact conditions deviate from the ideal flat-on-flat contact conditions, then the contact stresses are much higher than predicted, leading to variations in the volume of wear, potentially changes in wear mode and even premature and unexpected failure.

As aligning the brushes with the sample is critical in the wear test, a very careful alignment procedure is followed. Once the sample is secured on the sample holder and once

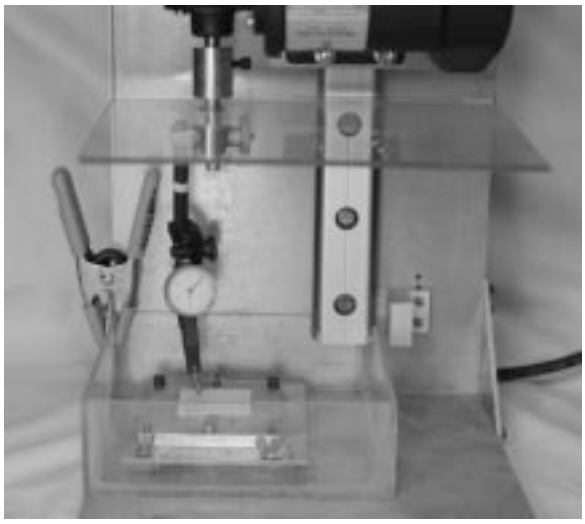

Fig. 3.22 Dial indicator located on the motor shaft to level off the sample

the holder is placed in the testing container, a dial indicator with an accuracy of 0.0005 in is attached to the shaft of the electric motor, and its probe is located on the sample surface as shown in figure 3.22. As the motor is turned on at low speed, the variation in height, hence the deviation from perpendicularity can be read on the dial indicator. The position of the sample is then adjusted until the dial indicator readings are nearly constant.

The brush is then aligned in the brush holder using of the microscope.

Finally, the brush holder is fixed to the electric motor shaft in place of the dial indicator and visual check of the alignment is performed.

This alignment procedure is developed to reduce the scatter in the computed wear data.

3.2.2 Wear tests

The wear test is conducted once the preliminary operations are completed. The electric motor is warmed up for an hour prior to beginning of the test. Profiles of the initial surface are collected. These profiles are thereafter called "blank" profiles.

The wear tests are ran according to an experimental program. A full description of the author's experimental program is included in section 3.4.

3.2.3 Post wear tests

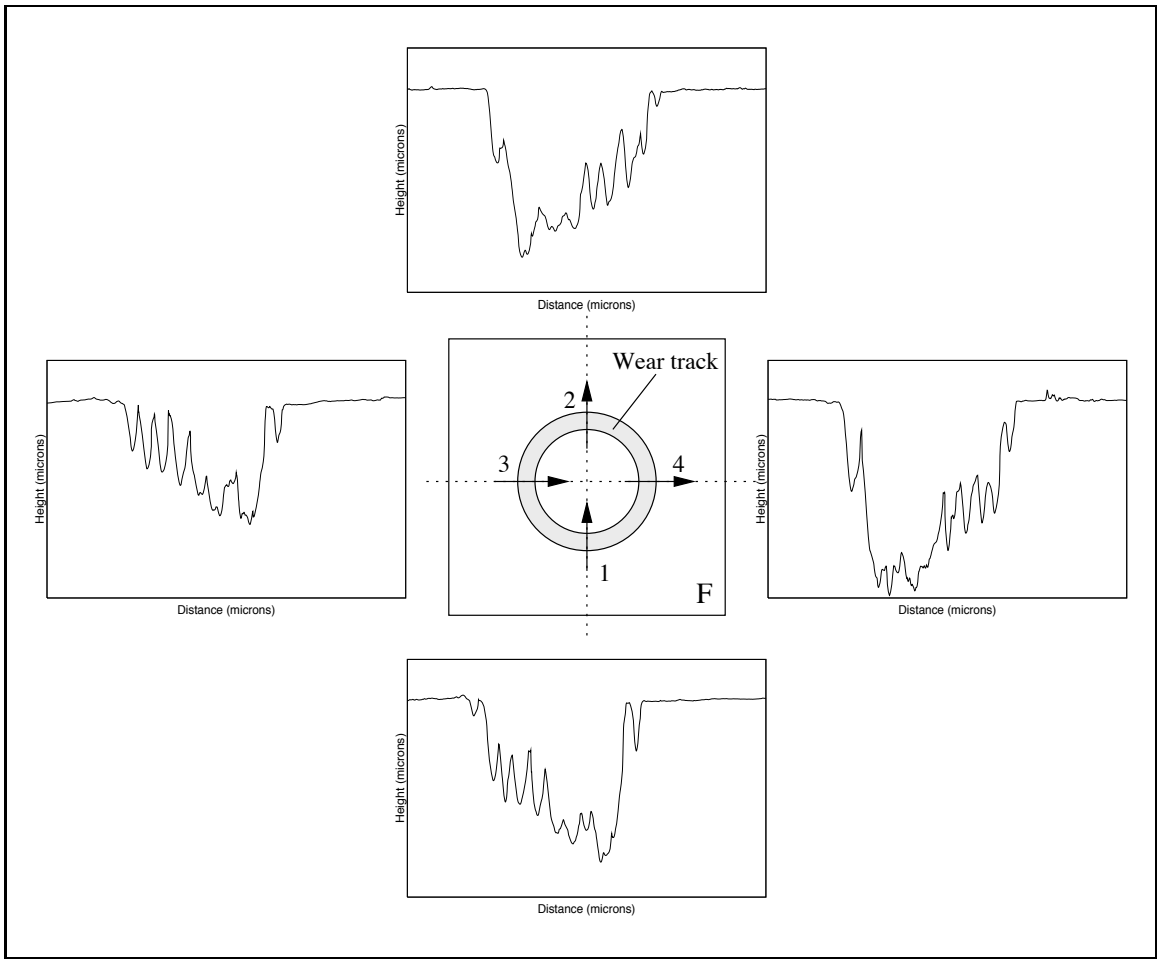

Fig. 3.23 Illustration of the locations where surface profiles are collected. The numbers refer to the location number utilized throughout the report. The letter "F" is used for identification of the Front of the sample. Arrows represent the scanning direction.

Wear data collection Wear measurements on the coated specimen are made intermittently by removing the samples and collecting profiles of the groove using the profilometer. Average values of the wear depth and wear area are computed from four different profiles. Figure 3.23 illustrates the four equidistant locations where the cross-section of the groove is recorded with the profiles. The arrows on figure 3.23 illustrate the direction of scanning, i.e. for scans gathered from locations 1 and 3, the direction of scanning is set from the outer perimeter towards the center of the ring formed by the wear scar whereas for locations 2 and 4, the scanning direction is reversed.

To sum up, computation of the wear data consists of the collection of the wear area, maximum wear depth and wear scar width (profiler), the computation of the wear rate, and the microscopic pictures of the specimen samples, of the brushes, and of the wear debris.

This data is used to report results of the tests in Chapter 4.

3.3 Other characterization techniques: material science

3.3.1 Texture analyzer

The "Minimat" is a miniature materials tester developed by Polymer Laboratories (Thermal Science division). It is located in Dr. Kander's laboratory at Virginia Tech. It is a tensile testing machine which has the ability to clamp small samples, powered by a computer equipped with adapted software. The instrument has three modes of testing: stress/strain, relaxation and creep.

For the purpose of this study, the stress-strain mode is used to determine the modulus of elasticity of the nylon bristles as well as the stress-strain behavior of free films of RTV11. Plots of either the load versus the extension or the engineering stress versus the strain can be obtained. Results are presented in Chapter 4.

3.3.2 Dynamic Mechanical Analyzer (D.M.A.)

A computerized Perkin-Elmer Dynamic Mechanical Analyzer (D.M.A. 7) was used to measure the dynamic properties in tension over a range of frequency and temperature. In a D.M.A., a sample undergoes repeated small amplitude strains in a cyclic manner. Molecules perturbed this way store a portion of the imparted energy elastically and dissipate a portion in the form of heat. The measured quantity is the loss tangent, $\tan\delta$, which is equal to the

ratio of the Young's loss modulus to the Young's storage modulus. δ is the angle between in-phase and out-of-phase components of the cyclic motion.

Forces up to 800 mN can be applied in a frequency range of 0.1–50 Hz. Free films of samples, when available, were tested. Sample dimensions are 15 mm long and approximately 3 mm wide. The sample thickness varied from sample to sample. The NRL samples were 0.51 mm (20 mil) thick while the EXS samples were 0.40 mm (15.7 mil) thick. The initial static force applied is variable and the corresponding dynamic force is set 20 % smaller than the static force. A typical plot is included in Appendix E.

3.3.3 Differential Scanning Calorimetry (D.S.C.)

A Perkin - Elmer Differential Scanning Calorimetry (DSC) instrument is used for morphology analysis, in particular for determining the glass temperature, T_g, of the materials.

Calibration for sub-ambient operation is done with n-decane (T_f = -29.7°C and ΔH_f = 202.25 J/g) and acetone (T_f = -94.82°C). An aluminum pan containing 9 to 12 mg of sample and an empty aluminum pan are placed in the DSC . The empty pan serves as a reference to monitor the amount of heat flow necessary to heat the sample at a linear heating rate. All experiments were performed at a heating rate of 1°C/min, from -120°C to 100°C. Each experiment is replicated once with the same sample to monitor any permanent and irreversible changes caused by heating. DSC results are presented in Appendix E.

3.4 Experimental program

This section describes the experimental program of the present study. Three groups of tests were conducted.

3.4.1 Preliminary Tests

Purpose

Preliminary tests were performed to evaluate the testing rig, calibrate it and make necessary adjustments. A series of tests was conducted with brushes of design #1. The analysis of these wear tests is difficult as the width of the wear scar nearly exceeds the maximum scan length set by the profiler (section 3.1.3). Also, the damage to the coatings is minimum and it is therefore difficult to assess the amount of wear which occurred in the course of

the tests. The results for these tests, which are qualitative rather than quantitative, are included in Chapter 4.

Samples

The samples studied are samples from the EXS series and the NRL series, with top-to-bond coat thicknesses 15/5, 10/10 and 5/15.

Test conditions

Table 3.7 summarizes the testing conditions.

Table 3.7 Variable test parameters for the preliminary tests

Parameter	Range
Load	300 g
Speed	395 RPM
Brushes	Flat head toothbrush Design #1
Environment	Salt water
Duration	4 phases

Data collected

Profiles of the surface at the end of the test phases were collected. Collecting wear data was difficult and erroneous due to the large width of the wear scar and due to the fact that the measured depths of wear are comparable to the waviness of the surface. Microscopic pictures were taken and are useful to understand the wear behavior of the candidate coatings.

3.4.2 Rate Tests

Purpose

The purpose of the rate tests is to investigate the wear behavior of the candidate coatings investigated in the load-speed matrix under one combination of load and speed levels and with constant phase duration. These tests also evaluate the effect of the thickness of the coatings on their wear resistance.

Samples

The candidate samples tested in the rate group are from the NRL series and the EXS series. These coatings are available in four groups of top-to-bond coat thicknesses, as described in section 3.1.

Test conditions

Table 3.8 summarizes the testing conditions.

Table 3.8 Variable test parameters for the rate tests

Parameter	Range
Load	300 g
Speed	395 RPM
Brushes	Flat head toothbrush
	Design #2
Environment	Salt water
Duration	6 phases of equal duration

These tests are done at one set of load and speed combination, e.g. level 2 (high)-level 2 (high). They can be compared to load-speed tests conducted under the same conditions and under the same number of brush strokes. Data were collected at time intervals during the course of the rate tests. These tests phases are kept constant as shown in table 3.9. Brushes were cleaned between phases.

Table 3.9 Duration (hours:min) and number of brush strokes per phase for the rate tests

Phase #	Per Phase Duration	Brush strokes	Cumulative Duration	Brush strokes
1	00:15	11,850	00:15	11,850
2	00:15	11,850	00:30	23,700
3	00:15	11,850	00:45	35,550
4	00:15	11,850	01:00	47,400
5	00:15	11,850	01:15	59,250
6	00:15	11,850	01:30	71,100

Figure 3.24 shows the correspondence between the number of strokes of the load-speed tests at high speed and the number of strokes of the rate tests. We observe that the number of brush strokes for phase 2 for the rate tests and phase 1 for load-speed tests are

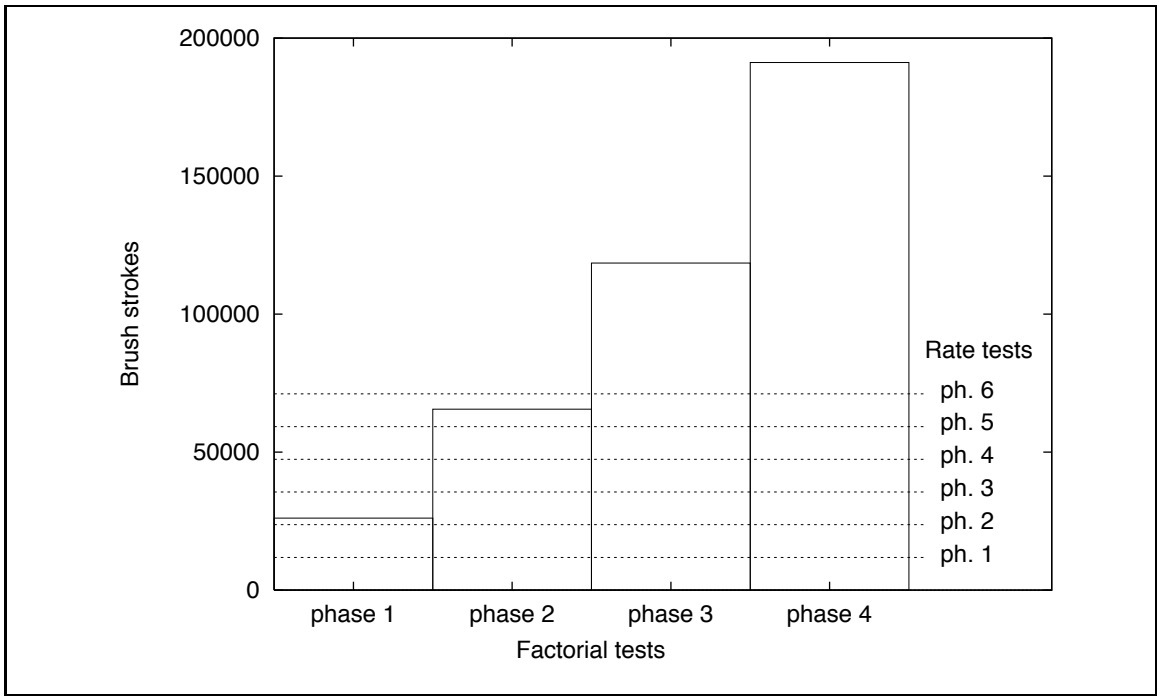

Fig. 3.24 Comparison of the brush strokes number for load-speed tests and rate tests

similar (10% more strokes in load-speed tests) and data collected at these particular phases can be compared.

Data collected

Similarly to the load-speed tests, the data collected includes surface profiles, microscopic pictures, voltage measurements and wear debris.

3.4.3 Load-Speed Tests

Purpose

The purpose of the load-speed tests is to evaluate the wear resistance of the candidate coatings under various levels of speed and load combined. These are called factorial experiments in statistical analysis. Candidate samples can also be compared.

Samples

The candidate samples evaluated in the load-speed group are from the NRL series and the EXS series. The samples are all 10/10 specimens, i.e. the ratio of top-to-bond coat

thicknesses is equal to 1. The total thickness is theoretically equal to 20 mils. However, in practice, the total thickness deviates significantly from this value.

Test conditions

Table 3.10 summarizes testing conditions. Data was collected at four intervals or phases during the course of the load-speed tests. Table 3.11 summarizes the duration and corresponding number of brush strokes per phase for low and high speed tests. The total number of brush strokes per phase (or duration) increases with the phase number. The ratio of the number of brush strokes for a given phase to the number of brush strokes for the first phase is plotted versus the phase number in figure 3.25. The duration or number of brush strokes is multiplied by a factor of 1.3 – 1.5 at each phase change. This is important if the duration of the phase has an effect on the wear rate of some candidate samples. Because of a miscalibration of the electric motor speed, the duration of each individual phase does not match the duration of phases of the brush tester operated at the State University of New-York at Buffalo, as originally intended.

Table 3.10 Variable test parameters for the load-speed tests

Parameter	Range
Load	100 g, 300 g
Speed	125 RPM, 395 RPM
Brushes	Flat head toothbrush Design #2
Environment	Salt water
Duration	4 phases

The number of brush strokes differs slightly between low and high speed tests. Figure 3.26 is a plot of the number of brush strokes for the high speed tests versus the number of brush strokes for the low speed tests. There is a deviation from the ideal 1:1 correlation. A sample tested under high speed will be exposed to approximately 1.05 the number of brush strokes a sample would be exposed to if tested under low speed.

Since the number of brush strokes is kept constant between the low and high speed tests, the duration of the test phases is larger for low speed tests. The total duration of a low speed test is 12 hours and 5 minutes whereas, to achieve the same number of brush strokes, the duration of a high speed test is approximately 4 hours.

Table 3.11 Duration (hours:min) and number of brush strokes per phase for the load-speed tests

Phase #	Per Phase Duration	Brush strokes	Cumulative Duration	Brush strokes
Low speed				
1	01:40	25,000	01:40	25,000
2	02:30	37,500	04:10	62,500
3	03:20	50,000	07:30	112,500
4	04:35	68,750	12:05	181,250
High speed				
1	00:33	26,070	00:33	26,070
2	00:50	39,500	01:23	65,570
3	01:07	52,930	02:30	118,500
4	01:32	72,680	04:02	191,180

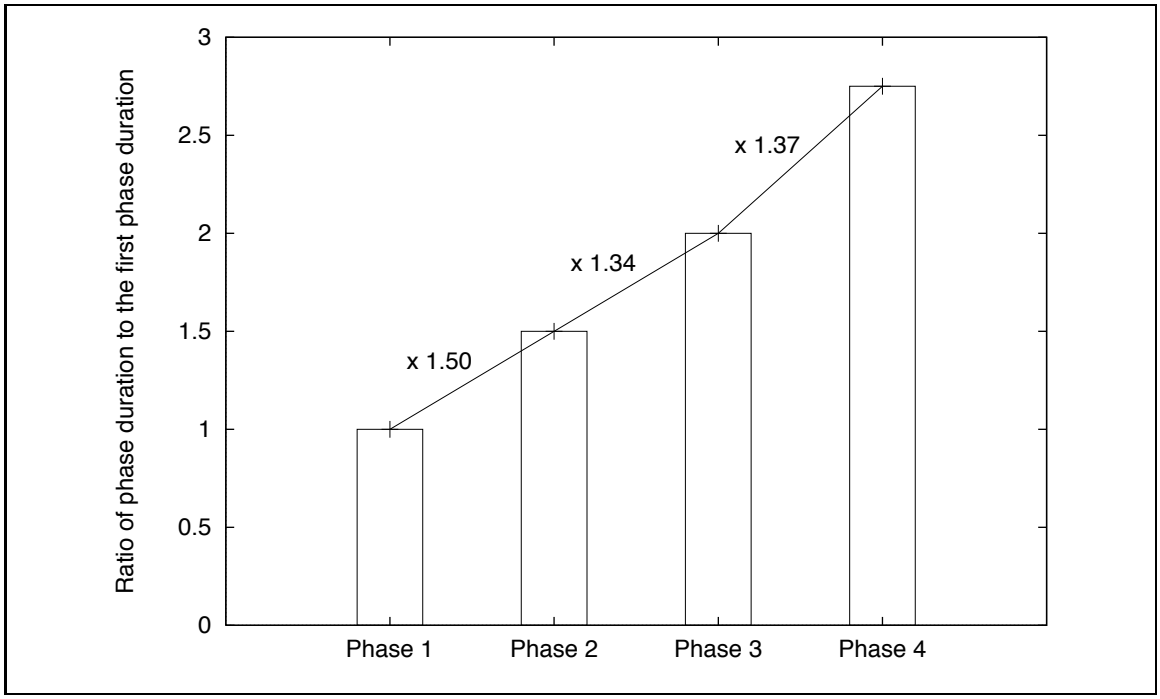

Fig. 3.25 Ratio of the phase duration to the duration of the first phase showing the rate of duration increase per phase.

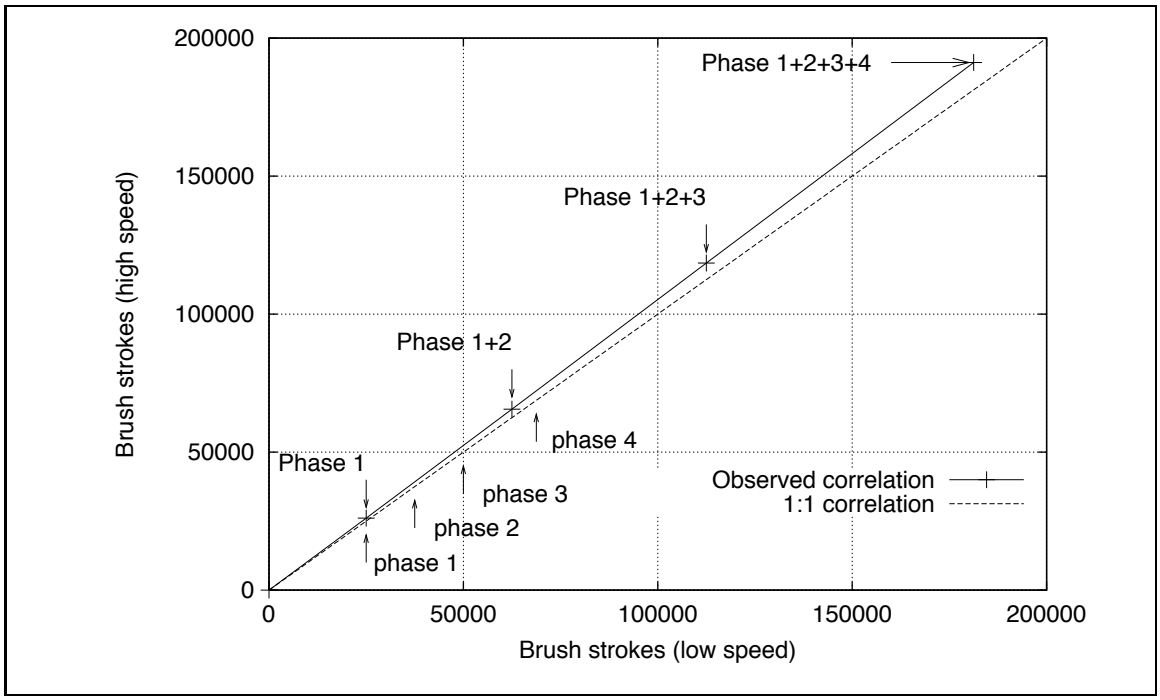

Fig. 3.26 Correspondence between the number of brush strokes between high and low speed tests

Data collected

The data collected consists of surface profiles at each test phase, microscopic pictures of the wear scar, voltage data for motor input torque monitoring and wear debris collected with the filtering procedures.

Chapter 4

Results

4.1 Thickness measurements

The thicknesses of the individual layers which are part of the duplex coatings are measured using the back-reflected light microscope. Four measurements per sample side are taken, i.e. a total of 16 data points per sample. Table 4.1 summarizes the results.

Figures 4.1 (a) and 4.1 (b) illustrate the measured thicknesses in mils for the NRL and the EXS samples. We can see that the total thickness of the EXS samples varies while that for NRL samples is nearly constant. Furthermore, we observe that the NRL 10/10 and NRL 15/5 samples have very similar layer thicknesses. Based on the thickness measurements, similar wear behaviors for these two samples can be expected. Similarly, EXS 10/10 and EXS 5/15 are very similar in terms of thickness. However, they are much thinner than the corresponding NRL samples.

Figures 4.2 (a), 4.2 (b) and 4.2 (c) are plots of the ratios of the top coat to the bond coat thicknesses. Figure 4.2 (a) is the nominal thickness ratio. Figure 4.2 (b) shows the ratio of the measured dry film thicknesses for NRL samples while figure 4.2 (c) shows the ratio of the measured dry film thicknesses for EXS samples. We can see that the thickness of the EXS films follow the nominal ratios initially set whereas thicknesses of the NRL films deviate slightly more.

In these two samples series, the relative thickness ratios are fairly similar. However, the total thicknesses of the samples are different. The deviation from the nominal values are large particularly for the EXS samples.

Table 4.1 Dry-film thickness for the NRL series and EXS series samples, top coat, tie coat and anti-corrosion (AC) coat.

Nominal dry film thickness (DFT) (mils)					
top	0	5	10	15	20
tie	20	15	10	5	0
AC	n/a	n/a	n/a	n/a	n/a
	NRL 0/20 [a]	**NRL 5/15** [a]	**NRL 10/10** [a]	**NRL 15/5** [a]	**NRL 20/0** [a]
top	0	3	12.5	16.5	23.5
tie	21.5	18	11.5	12.5	0
AC	8.5	7	7	8	5.5
top+tie	21.5	21	24	29	23.5
top+tie+AC	30	28	31	37	29.5
	EXS 20/0 [b]	**EXS 15/5** [b]	**EXS 10/10** [b]	**EXS 5/15** [b]	**EXS 0/20** [b]
top	0	5.5	7.5	9	18.5
tie	6	18	7.5	4.2	1
AC	7	9.5	11	8.5	7
top+tie	6	23.5	15	13.5	19.5
top+tie+AC	13	33	26	22	26.5

[a] top coat thickness/tie coat thickness.

[b] tie coat thickness/top coat thickness (opposite of NRL samples).

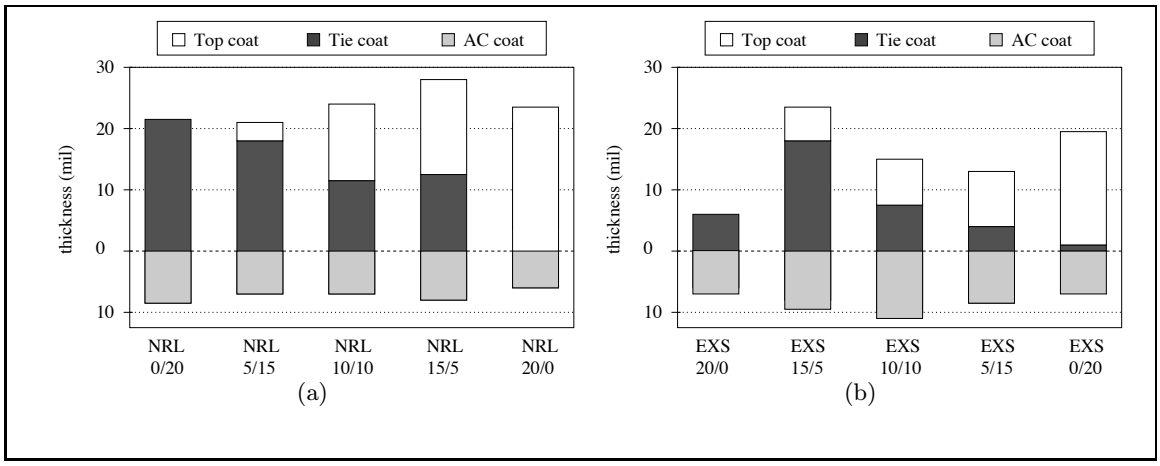

Fig. 4.1 Absolute thicknesses (mil) for the (a) NRL samples and (b) EXS samples. The zero line is offset and matches the position of the interface between the anti-corrosion layer and the bond coat, for easy visualization of the (bond+top) coats total thickness.

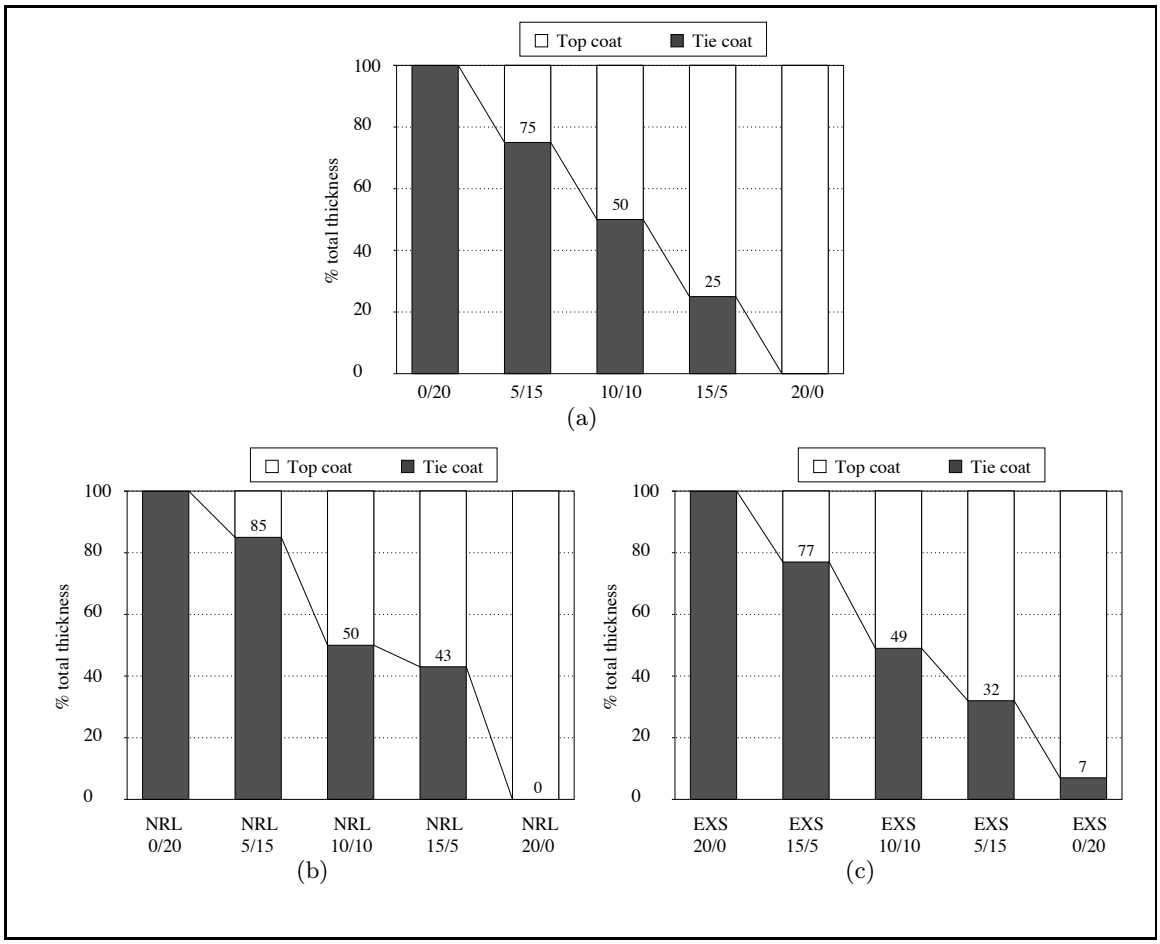

Fig. 4.2 Variation of the relative thicknesses of the top and the bond coats for (a) ideal nominal case, (b) NRL samples and (c) EXS samples.

4.2 Rate tests

The purpose of the rate tests is to compare samples with variable initial thickness ratios, and to evaluate the wear rate of NRL and EXS samples.

The tests are conducted in salt water under high load and high speed. The rate tests are divided into six phases of 15 minutes each. The duration of each phase is kept constant and is proportional to 11,850 brush strokes because an increase in the number of brush strokes might lead to a variation in the wear rate between phases. Indeed, when debris are formed, they accumulate in the brushes, modify the contact conditions and therefore the wear rate. The same brush is used for all tests conducted per sample group. Brushes are cleaned between phases and all debris removed from the tuft. Four samples from the NRL series and the EXS series are tested, respectively 0/20, 5/15, 10/10 and 15/5.

4.2.1 NRL samples

The top coat of the NRL samples is the grey RTV11 except for the 0/20 sample which is only coated with Silgan® J-501. The thicknesses of the NRL specimen samples hereby tested are listed in table 4.2.

Table 4.2 Dry-film thicknesses (mil) of the top and bond coats for the NRL samples

Thickness ratio	**0/20**	**5/15**	**10/10**	**15/5**
Top coat (mil)	0	3	12	15
Tie coat (mil)	21.5	18	11.5	12.5

Figure 4.3 illustrates the variation of the wear area and the maximum depth of the wear scar as a function of the number of brush strokes for NRL samples. Figure 4.4 illustrates the variation of the wear rate as a function of the number of brush strokes. The wear rate is equal to a hundred times the slope of the wear area versus brush strokes curve. This is equivalent to an average wear area (in mil^2) occurring as a result of a 100 brush strokes (b.s.).

The grey RTV11 top coat is less wear resistant than the Silgan® J-501 coat: wear areas and wear depths for the RTV11 coating are much larger than those obtained for Silgan® J-501 coatings. The wear areas measured for the Silgan® J-501 sample do not exceed 50 mil^2/100 b.s. after 71,100 brush strokes. In contrast, the wear areas of the samples

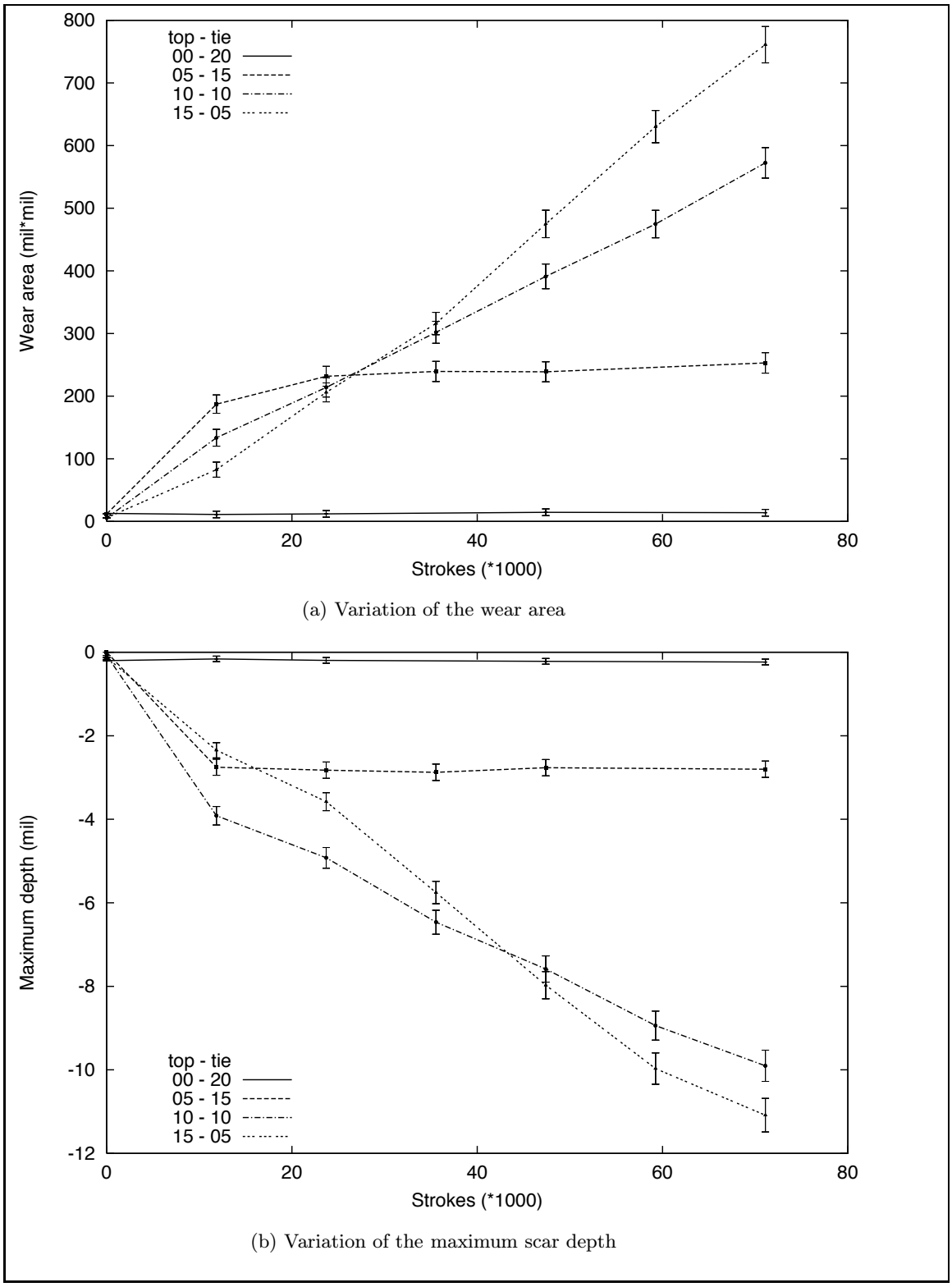

(a) Variation of the wear area

(b) Variation of the maximum scar depth

Fig. 4.3 Variation of the wear area and variation of the wear depth as a function of the number of brush strokes for NRL samples with variable initial thickness ratio. The measurement error on the wear data is plotted as error bars

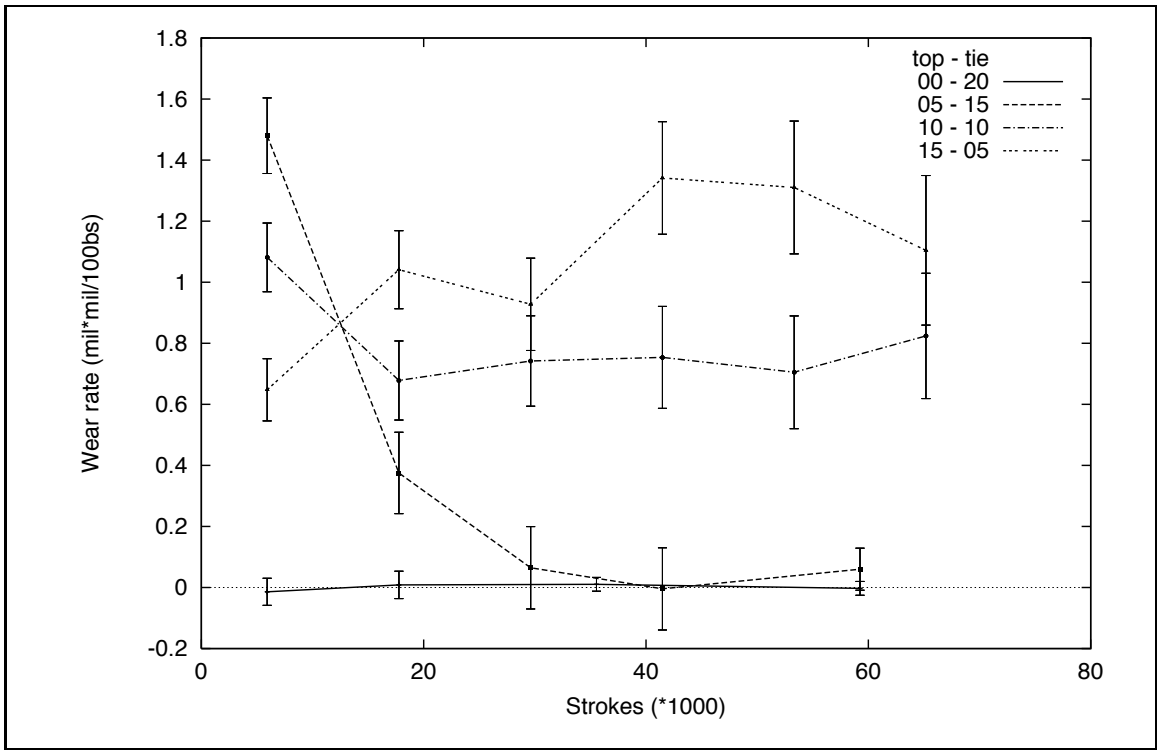

Fig. 4.4 Variation of the wear rate as a function of the number of brush strokes for NRL samples with variable initial thickness ratio. The measurement error on the wear data is plotted as error bars

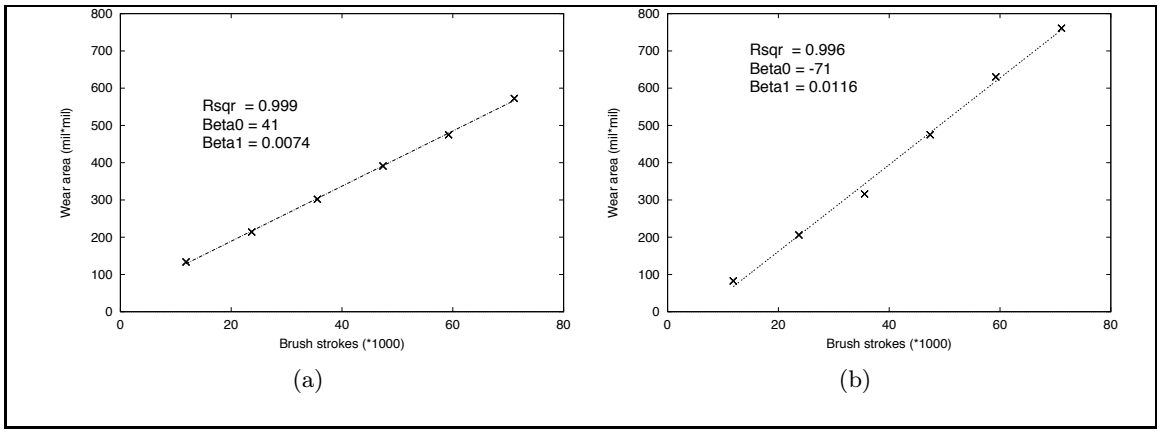

Fig. 4.5 Regression analysis of the average wear area versus the number of brush strokes for (a) NRL 10/10 and (b) NRL 15/5.

coated with grey RTV11 exceed 100 mil^2/100 b.s. following 23,700 brush strokes (phase 2). Similarly, as seen on figure 4.4, the wear rate of the Silgan® J-501 coatings is very low compared to the wear rate of the three samples coated with modified RTV11. The analysis of the results obtained for the Silgan® J-501 coatings can be found on page 90. It is treated separately from the RTV11 since it is a different coating which does not exhibit fouling-release properties.

In the case of NRL 5/15, the brushes removed the top coat completely during phase 1, leading to the direct contact of the brushes with the bond coat. Therefore, for phases 2 through 6, the wear data reported is representative of the bond coat and no longer of the top coat. This explains the decrease of the wear rate for NRL 5/15 observed on figure 4.4. As a consequence, only the wear data obtained for phase 1 can be utilized to compare the NRL 5/15 sample to NRL 10/10 and NRL 15/5 samples.

The top coats of the NRL 10/10 and NRL 15/5 were not removed by the action of the brushes after 71,100 brush strokes. Therefore, the data reported here reflect contact conditions with the top coat, with variable initial thickness ratio. The variation of the wear area and the maximum wear depth with the number of brush strokes for NRL 10/10 and NRL 15/5 samples is very similar.

A linear regression analysis of the variation of the average wear area with the number of brush strokes is plotted on figure 4.5 for NRL 10/10 and NRL 15/5. Rsqr, Beta1 and Beta0 are included on the plots. Rsqr, or R^2, is the coefficient of determination. It measures how well the regression equation fits the data. Beta0 and Beta1 are, respectively, the slope

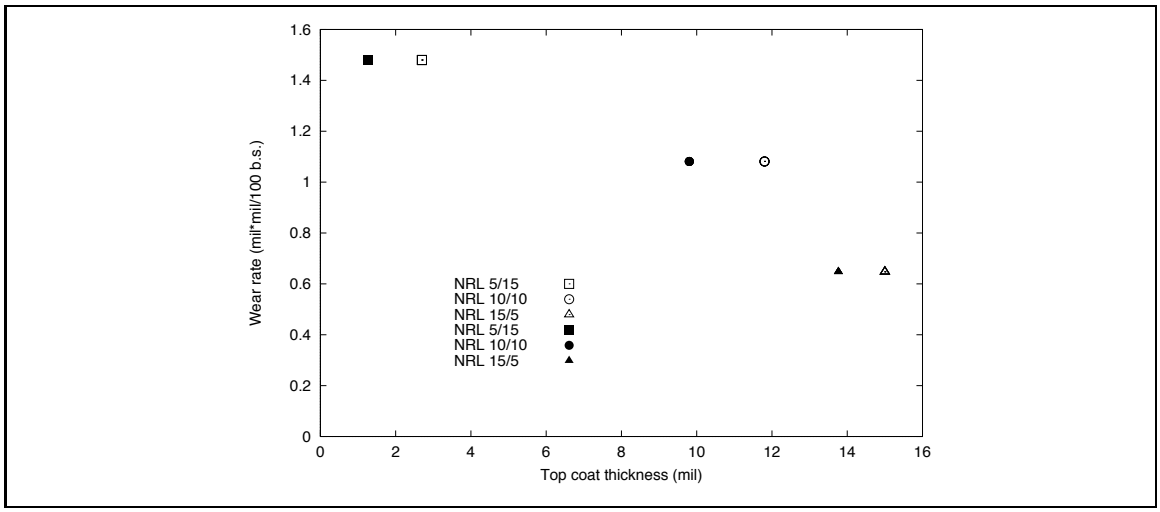

Fig. 4.6 Variation of the initial wear rates for NRL samples as a function of the specimen initial top coat thickness (empty bullets) and the average top coat thickness (filled bullets).

and the intercept of the regression line. The estimated slopes are, respectively, 0.0074 ($R^2 = 0.999$) and 0.0116 ($R^2 = 0.996$). The corresponding estimated wear rates are: 0.739 $\text{mil}^2/100$ b.s. and 1.163 $\text{mil}^2/100$ b.s. Even though the wear areas for the two samples appears very much alike, the rates at which each sample wears out are different. This is explained by the variation of the wear rate during the first phase. From the results of the rate experiments, it appears that the thickest sample wore out faster than the thinnest sample. The 95% confidence interval (CI) for the intercepts are 41.4 $\pm$ 10.6 for NRL 10/10 and -70 $\pm$ 12 for NRL 15/5. While a higher wear rate is observed during phase 1 for NRL 10/10, a lower wear rate is observed during phase 1 for NRL 15/5, suggesting that fatigue might play a role in the case of a sample with a thick top coat with respect to the bond coat.

Since the total amount of wear for the former samples is influenced by the output of the initial test phase, the wear rates for all samples during the first phase are analyzed. As seen in figure 4.4, the initial wear rates of the NRL samples tested differ. Figure 4.6 shows the initial wear rate for the NRL samples versus the initial thickness of the top coat and the average top coat thickness. As the brushes wear the coating, its thickness decreases. The average top coat thickness is the average of the values for the thickness before and after a given phase. We observe that the initial wear rates of the NRL samples decreases with increasing initial top coat thickness. This is contradictory to the theory which states that the bond coat strengthens a thin top coat. Statistical analysis of the data is necessary in order to conclude whether or not there is a significant difference between the samples.

Unfortunately, these tests were not replicated due to the lack of samples and therefore, statistical analysis can not be conducted.

To compare the influence of the thickness ratio on the wear resistance of the candidate coatings, data for the initial phase of the test is important. With the present apparatus, it is very difficult to evaluate the wear data for the initial conditions. As debris are formed instantaneously, the thickness of the top coat decreases and the initial thickness ratio changes accordingly. An alternative method for studying the influence of the thickness of the samples on their wear resistance is proposed later in the chapter (page 92).

4.2.2 EXS samples

All samples tested, except EXS 20/0, are coated with Silgan® J-501 and Exsil® 2200 with variable thickness ratios. The EXS 20/0 is coated with Silgan® J-501 only. Similarly to the NRL samples previously described, the EXS samples tested have different thickness ratios as presented in table 4.3.

Table 4.3 Dry-film thicknesses (mil) of the top and bond coats for the EXS samples

Thickness ratio[a]	**0/20**	**5/15**	**10/10**	**15/5**
EXS labels[b]	20/0	15/5	10/10	5/15
Top coat	0	5.50	7.50	9.00
Tie coat	5.86	18.15	7.40	4.20

[a]top coat thickness/bond coat thickness.

[b]The EXS labels are reversed compared to that of NRL samples: the thickness of the bond coat is indicated prior to the top coat for EXS samples.

Figure 4.7 illustrates the variation of the wear area and the maximum depth of the wear scar as a function of the number of brush strokes. Figure 4.8 illustrates the variation of the wear rate as a function of the number of brush strokes.

The wear data measured for samples coated with Exsil® 2200 are larger than the wear data measured for the Silgan® J-501 sample.

The wear rates of the samples coated with 10 and 5 mil Exsil® 2200 are equal within the experimental error as shown on figure 4.8. The wear rate of the sample with the thickest top coat is not only much larger than for the former two, but it also fluctuates.

A regression analysis of the variation of the wear area with the number of brush strokes (figure 4.9) leads to the following estimated rates of wear:

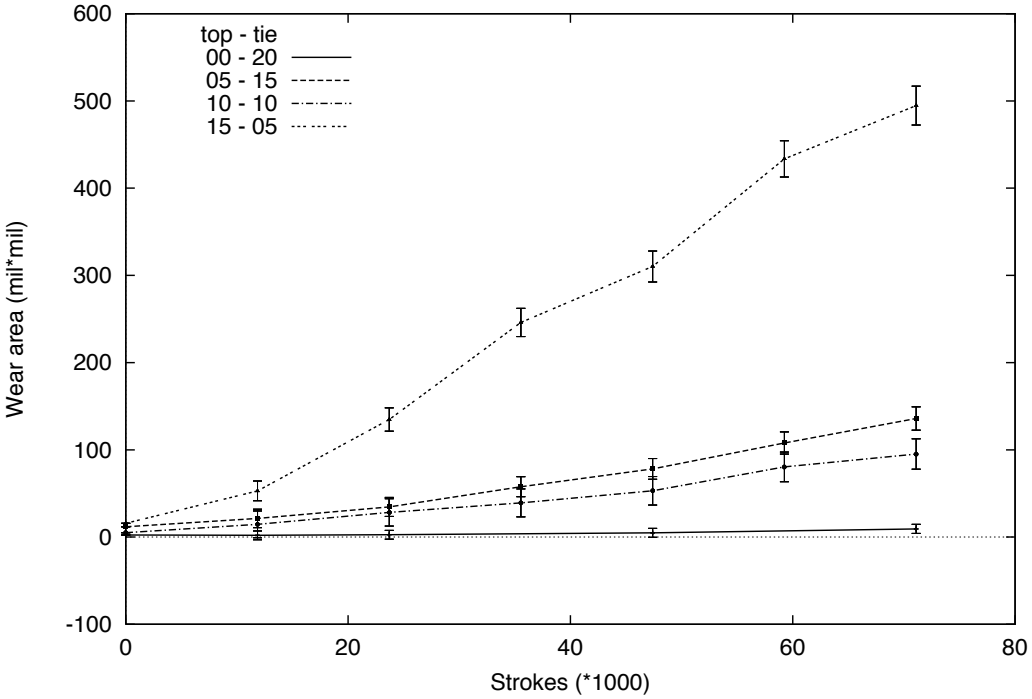

(a) Variation of the wear area

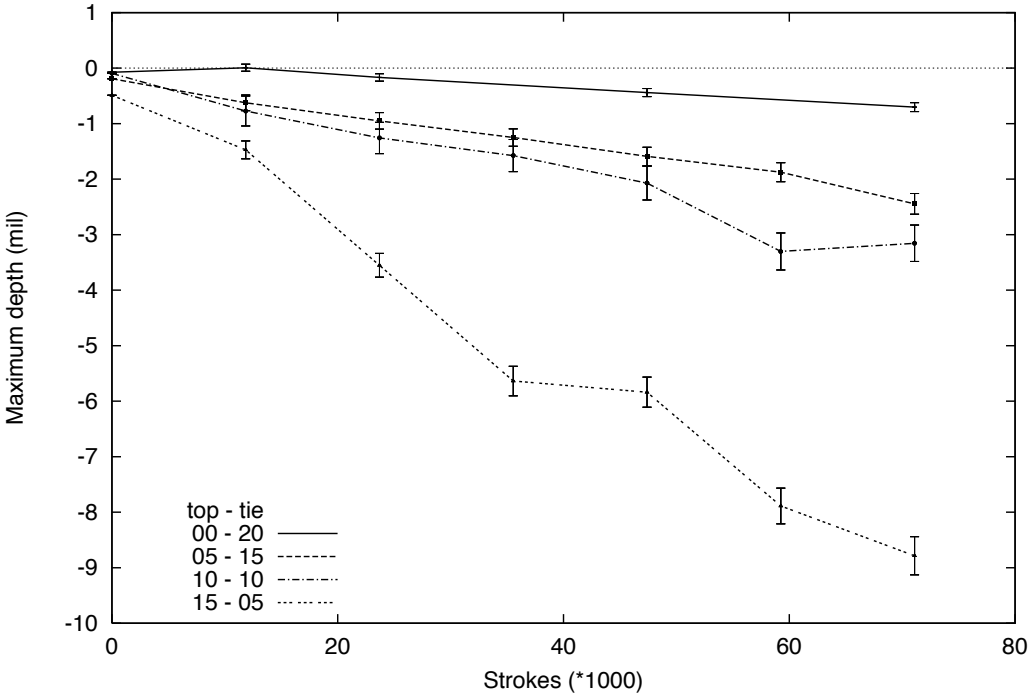

(b) Variation of the maximum scar depth

Fig. 4.7 Variation of the wear area and wear depth as a function of the number of brush strokes for EXS samples with variable initial thickness ratio. The measurement error on the wear data is plotted as error bars

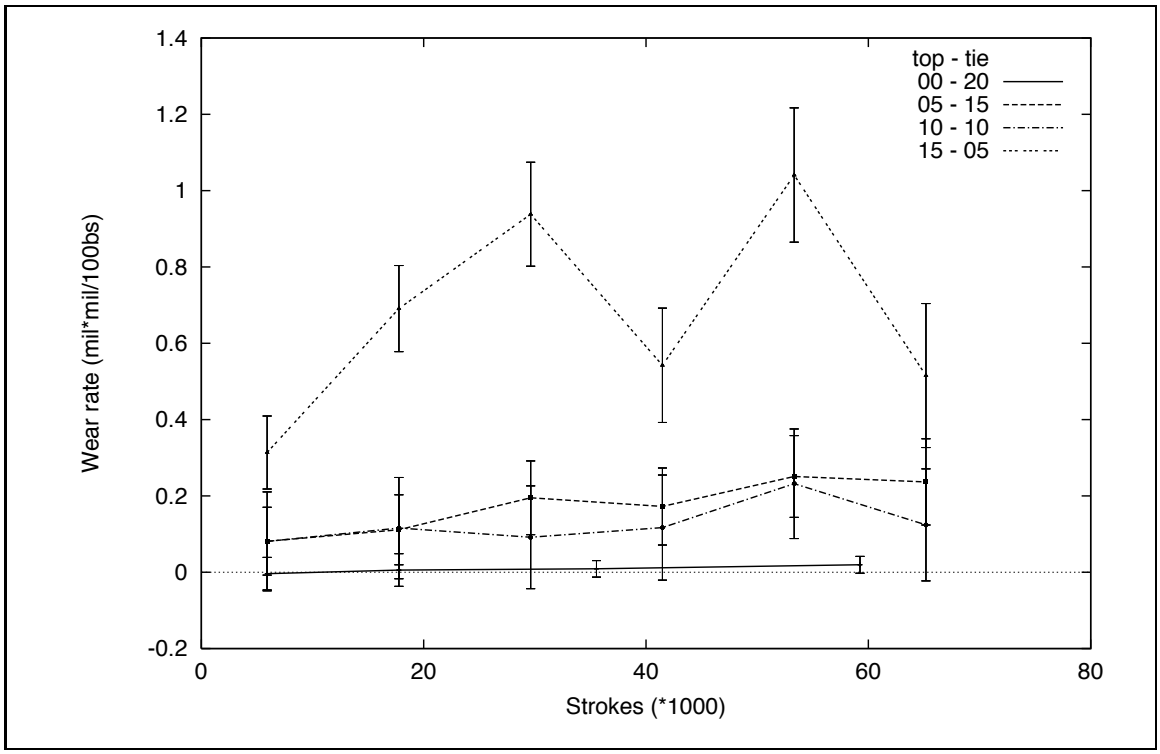

Fig. 4.8 Variation of the wear rate as a function of the number of brush strokes for EXS samples with variable initial thickness ratio. The measurement error on the wear data is plotted as error bars

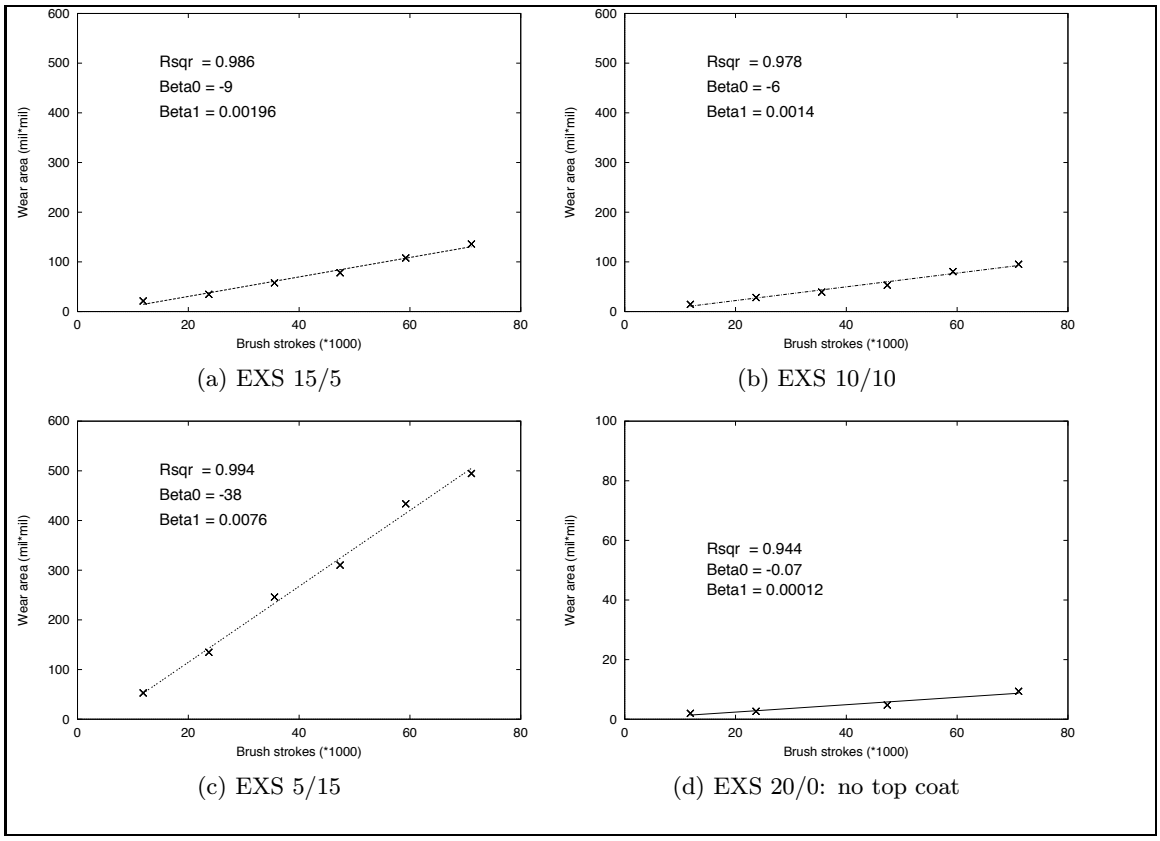

(a) EXS 15/5 (b) EXS 10/10

(c) EXS 5/15 (d) EXS 20/0: no top coat

Fig. 4.9 Regression analysis of the average wear area versus the number of brush strokes for EXS samples.

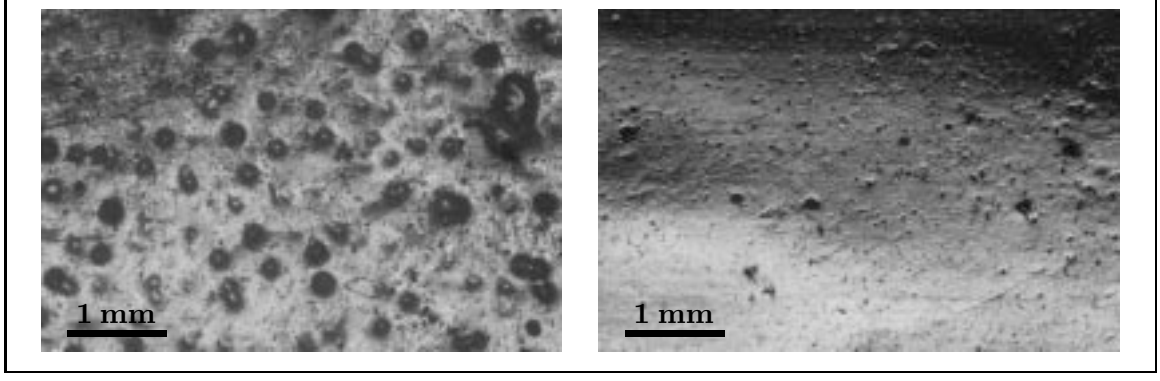

Fig. 4.10 Microscopic pictures of the Exsil® 2200 top coat for (a) EXS 5/15 and (b) EXS 10/10 or EXS 15/5.

Sample	**Wear rate** (mil^2/100b.s.)	$\mathbf{r^2}$
EXS 20/0	0.0123	0.944
EXS 15/5	0.1960	0.986
EXS 10/10	0.1383	0.978
EXS 5/15	0.7641	0.994

The intercepts of the linear regressions fall within the 95% CI for all EXS samples except for the EXS 5/15 for which the intercept is negative. Similarly to NRL 15/5, it suggests that fatigue might play a role for a sample with a tich top coat with respect to the bond coat.

Microscopic observations of the sample revealed that the top coat of the thickest coating, EXS 5/15, differs from the top coat of the other two coatings, EXS 10/10 and EXS 15/5. Microscopic pictures can be seen in figure 4.10. One possible explanation is entrapment of air bubbles during curing in the EXS 5/15 samples. As a consequence, formation of wear debris is facilitated and the wear resistance of the top coat is lowered.

4.2.3 Silgan® J-501 specimen samples

Figure 4.11 illustrates the results obtained for Silgan® J-501 samples. We observed that the Silgan® J-501 coatings are more wear-resistant than the RTV11 or Exsil® 2200 based coatings. The amount of wear generated by the brushes on the Silgan® J-501 coatings is very low. On the surface profiles collected, it is difficult to isolate features due to wear from features due to the initial surface condition or defects, which explains why negative wear rates can be measured.

Even though the sample issued from the NRL series is 21 mil-thick whereas the sample from the EXS series is only 6 mil-thick, no difference in the wear resistance of the two specimens can be seen.

A linear regression analysis of the data for the wear area is shown on figure 4.12. The slope of the regression lines gives an estimate of the wear rate, 0.00517 mil^2/100 b.s. and 0.0123 mil^2/100 b.s. respectively. The difference observed between the two replicates is within the experimental error.

Also, when the brushes remove the top coat completely, then the wear data measured is representative of the bond coat. Indeed, as shown on figure 4.4, the wear rate of the

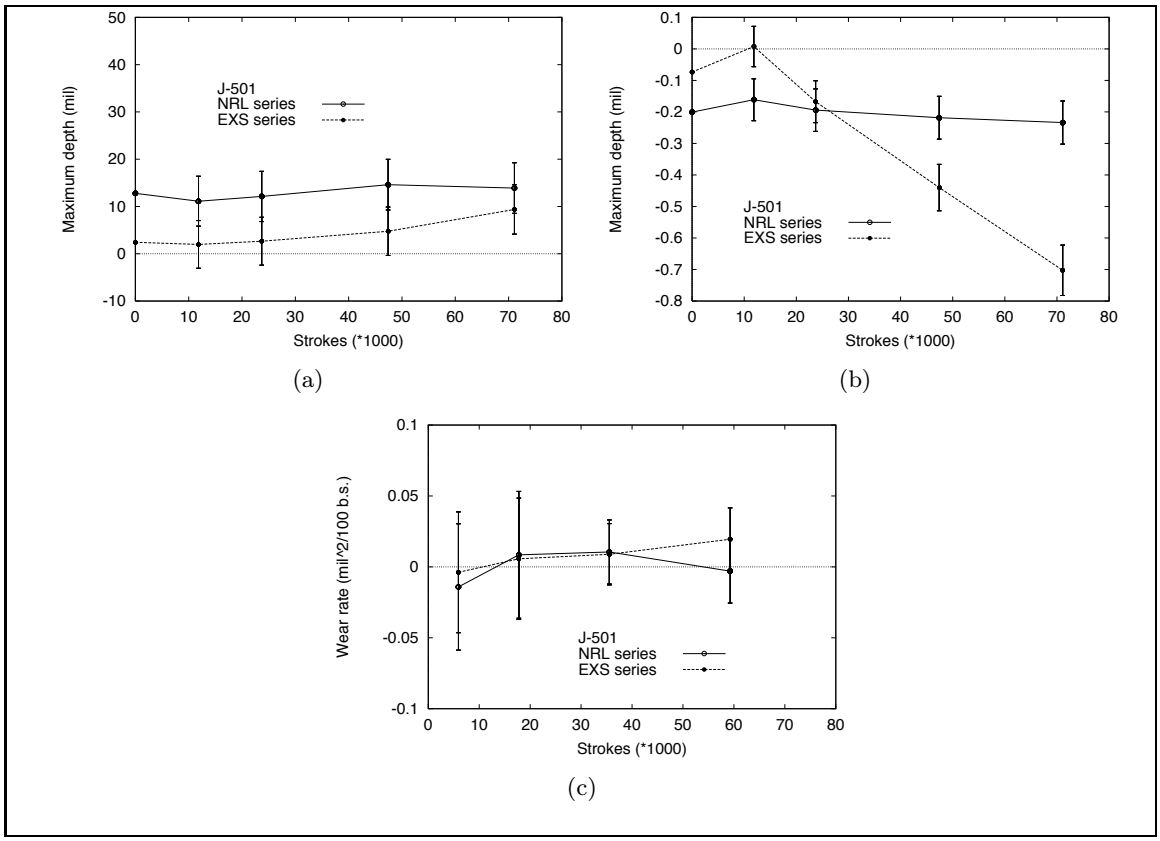

Fig. 4.11 Variation of the (a) wear area, (b) maximum wear depth and (c) wear rate as a function of the number of brush strokes for samples coated with Silgan® J-501. The measurement error on the wear data is plotted as error bars

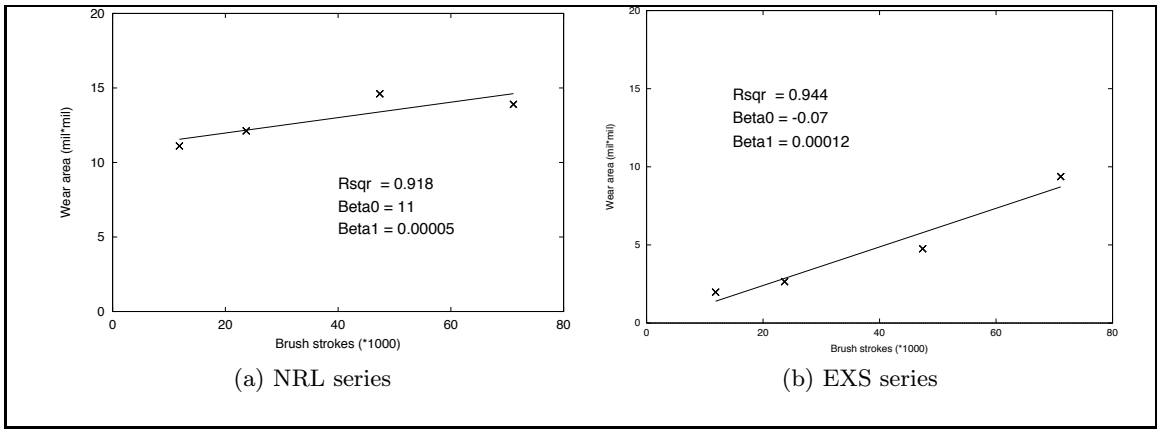

Fig. 4.12 Regression analysis of the wear area versus the number of brush strokes for Silgan® J-501 specimen coatings.

NRL 15/5 sample fell down to the values representative of the NRL 0/20 sample, i.e. Silgan® J-501 coating, after removal of the top coat.

4.2.4 NRL and EXS samples

Figures 4.13 and 4.14 show the wear data for the NRL and EXS samples which retained their top coat throughout the tests, i.e. NRL 10/10, NRL 15/5, EXS 15/5, EXS 10/10 and EXS 5/15.

The wear resistance of the EXS samples is greater than the wear resistance of the NRL samples, except for the thickest EXS samples, which, as previously described, wore out faster than the other EXS samples due to surface defects. The wear behavior of the thickest EXS sample is similar to the wear behavior of the NRL sample.

The Exsil® 2200 and RTV11 top coats are both dimethylsiloxane based materials, with different fillers. RTV11 contains calcium carbonate whereas Exsil® 2200 contains fumed silicas. The two sample series differ by means of their physical characteristics: the NRL samples are overall much thicker than the EXS samples. Indeed, as shown in table 4.1 on page 79, the total thickness (i.e. the top+bond coat thickness) of the coatings for NRL 10/10 and NRL 15/5 is 24 and 27 mil respectively whereas it is 15 and 13 mil for EXS 10/10 and EXS 5/15.

Analysis of the effect of thickness of the wear rate of the NRL and the EXS samples When the top coat is continuously removed, its thickness decreases. The initial thickness of the coatings is not representative when the top coat is being removed during the tests. The thickness of the coatings at the end of each phase is equal to the initial thickness minus the measured maximum depth of the wear scar. Using the depth measurements, the true average thickness is computed after each test phase. The average wear rate can be plotted as a function of the true average thickness of the coating.

NRL samples Figure 4.15 shows the variation of the average wear rate with the sample true average thickness for NRL 10/10. The initial thicknesses of the top and bond coats are both approximately 12 mil. The initial wear rate at larger top coat thicknesses is larger than the following wear rates obtained for smaller top coat thicknesses. Similar results have been obtained for NRL samples with differing initial top/bond coats thicknesses.

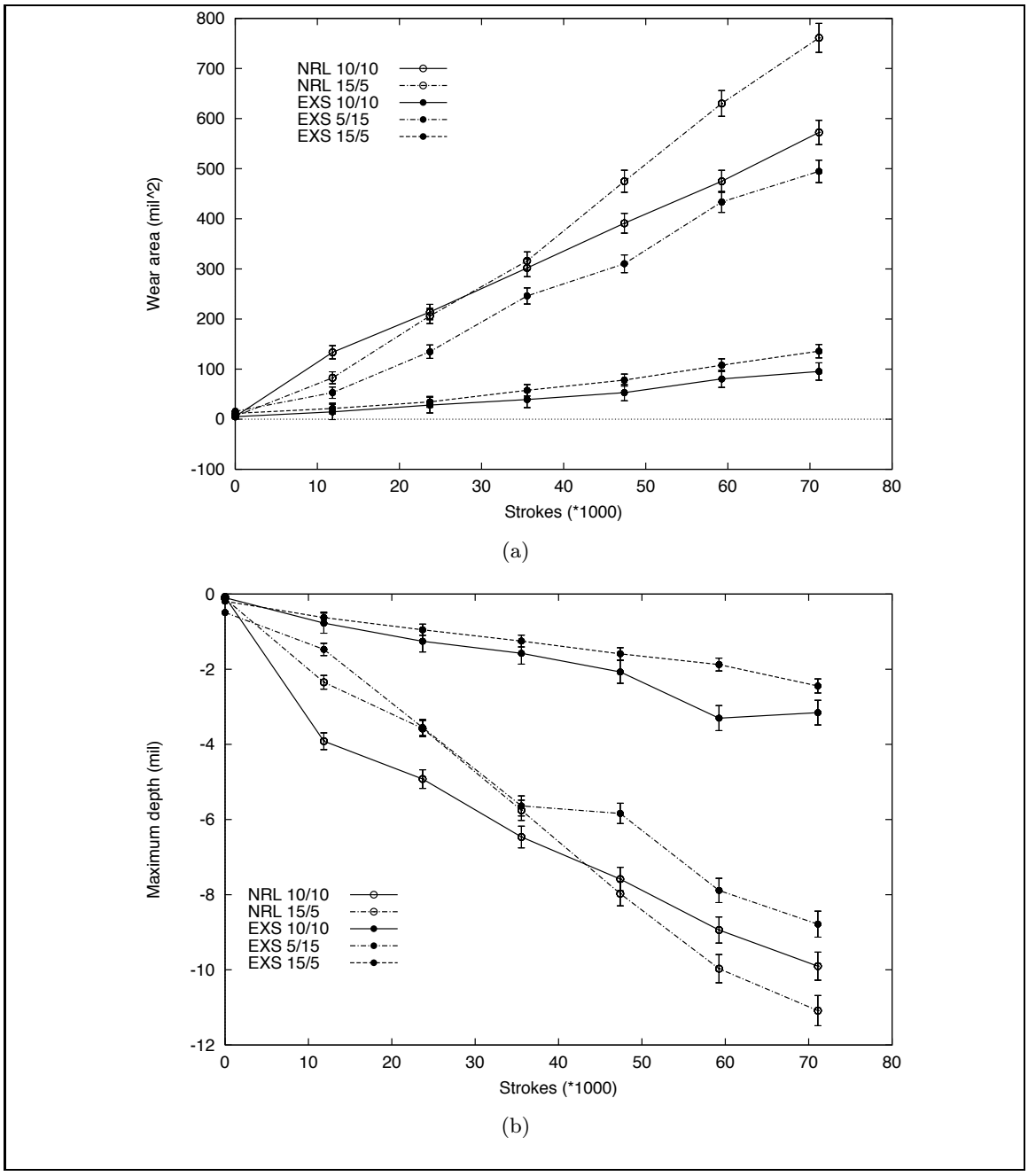

Fig. 4.13 Comparison of the wear area and the wear depth for NRL samples (open circles) and EXS samples (filled circles). The measurement error on the wear data is plotted as error bars

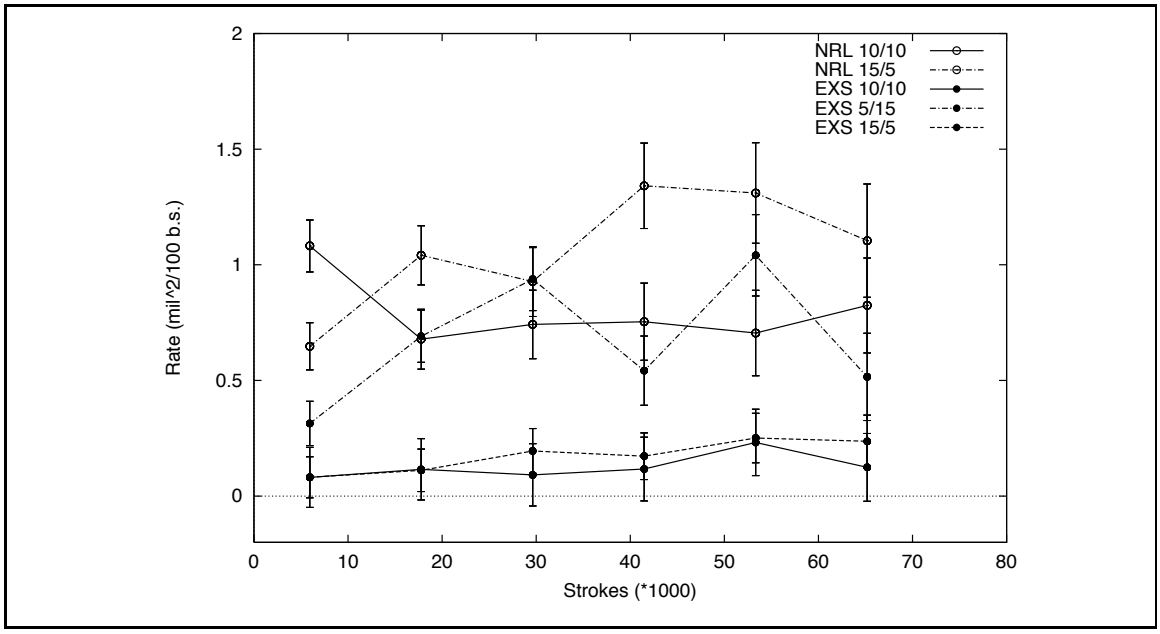

Fig. 4.14 Comparison of the wear rate for NRL samples (open circles) and EXS samples (filled circles). The measurement error on the wear data is plotted as error bars

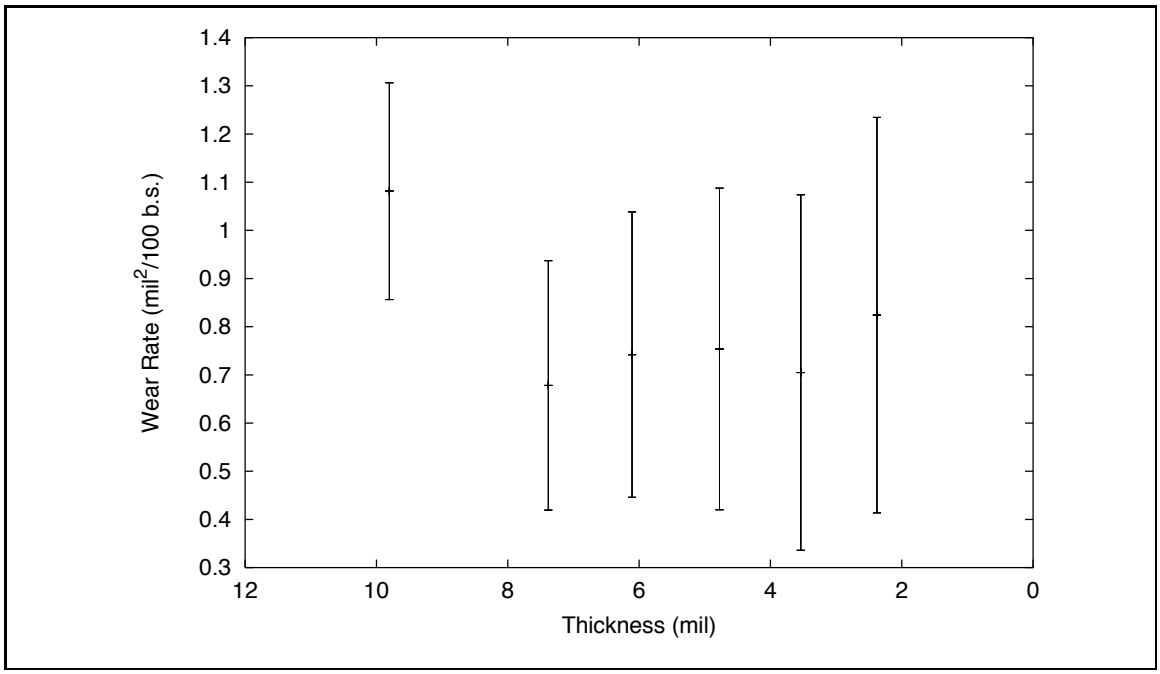

Fig. 4.15 NRL 10/10: Variation of the average wear rate as a function of the average thickness. The measurement error on the wear data is plotted as error bars.

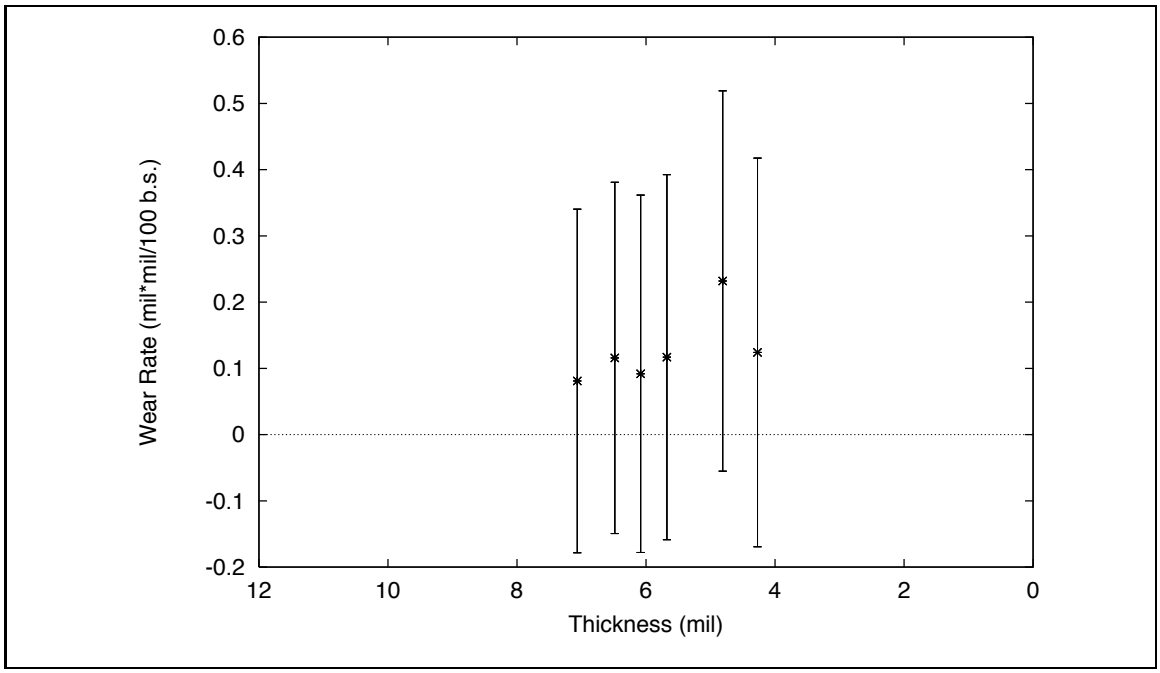

Fig. 4.16 EXS 10/10: Variation of the average wear rate as a function of the average thickness. The measurement error on the wear data is plotted as error bars.

The wear rate of NRL samples under the action of stiff brushes appears to be independent of the thickness of the top coat of the samples.

EXS samples Figure 4.16 shows the variation of the average wear rate with the sample true average thickness for EXS 10/10. The initial thicknesses of the top and bond coats are approximately 7.5 mil.

The wear rate of the EXS samples is independent of the thickness of the top coat as well, for a given bond coat thickness. Assessing the influence of the thickness of the bond coat on the wear resistance on the present coatings is difficult. Indeed, samples with top coats of constant initial thickness and bond coats with varying thickness were not available.

In conclusion, the thickness of the top coat does not appear to have an effect on the wear rate of neither the NRL nor the EXS samples. However, within the range of thicknesses of the candidate coatings tested here, a sample with a thicker top coat would be preferable to a sample with a thinner top coat since it would last longer.

4.3 Load-Speed testing

When the effects of two or more factors on a response y (i.e. wear rate) are of interest, a matrix of tests can be designed in which the levels of main factors vary. The simplest case is encountered when two main parameters take one low value (level 1) and one high value (level 2). This design was used in the present test matrix. As seen in table 4.4, two factors, the load, w, and the speed, v, each with two levels, were studied.

Wear data was collected as described in the experimental procedure for each individual test. Wear area, maximum depth and calculated wear rate are used to study the effect of load and speed, as well as cumulative number of brush strokes (proportional to time), on the measured and calculated data. Further analysis leads to the comparison of the wear behavior of different specimen samples.

Table 4.4 Example of a 2×2 matrix for testing the effects of two levels of two independent factors (A and B) on n replicates

		Factor Load	
		Low	High
Factor Speed	Low	$w_1 \times v_1$ (rep. 1, n)	$w_2 \times v_1$ (rep. 1, n)
	High	$w_1 \times v_2$ (rep. 1, n)	$w_2 \times v_2$ (rep. 1, n)

4.3.1 NRL samples

In this section are presented the results of tests conducted for the load-speed tests for the NRL samples.

NRL samples were tested according to the matrix seen in table 4.4, with 2 replicates (n). Since it was demonstrated previously that the wear rate of the NRL samples was independent of the sample thickness, and the ratio of the top coat thickness to the bond coat thickness, two series of NRL samples were used, NRL 10/10 and NRL 15/5. Tests were randomized.

Wear data

Wear area and maximum wear depth Figures 4.17 and 4.18 illustrate the variation of the wear area and the maximum depth of the wear scar as a function of the number of brush strokes for both replicate samples under low and high speed, and constant load, respectively low and high.

At low load (figure 4.17), it can be seen that replicate sample 1 (indicated by hollow triangles) wore more than did replicate sample 2 (indicated by filled triangles). This effect is more pronounced at low speed, except for results collected after the final test phase. We observe on figure 4.17 that for phase 4, at low speed, the wear area for replicate sample 1 is then lower than that for replicate sample 2. This is explained by the difference in thickness of the top coat. The top coat thickness is larger for replicate sample 2 than it is for replicate 1. Under low load, it was observed that the brushes wore through the top coat of the sample used for replicate sample 1 whereas they barely did in the case of replicate sample 2. The plot of the maximum depth of the wear scar in figure 4.17 shows this phenomenon. Indeed, for sample replicate 1, the curve levels off quickly by the end of the second phase. However, top coat material is still being removed and the wear area increases accordingly. This shows that, within the course of the third phase, the brushes wore through the top coat. As the bond coat is tougher than the top coat, it is believed that the bristles splayed more and material was removed from the sides instead of from the bottom of the scar. This explained a nearly constant maximum depth with an increasing wear area. In the course of phase 4, most of the material was removed from the sides of the scar and the wear area did not increase as much as in the previous phases. Another factor playing a role in this trend is the limitation of the instrumentation. Indeed, the maximum groove depth which can be measured by the profiler is about (300 ± 20) microns. If the brushes form a groove in the sample deeper than this limit, then wear data, particularly depth data, will level off and will no longer representative. The decrease of the wear rate is then not due to the influence of the bond coat through the thin top coat but to the bond coat itself and to the limit set by the measuring device. This effect is not observed under high speed as the brushes did not wear though the top coat in the course of the test. Further observations of the surface profiles provide an additional way to determine the reasons of the levelling off. We observed that the outer side of the groove is worn about twice as deep as the inner side after phase 2. The maximum depth recorded is accordingly high and will remain close to this value throughout the rest of the test. Observation of the variation of the wear area

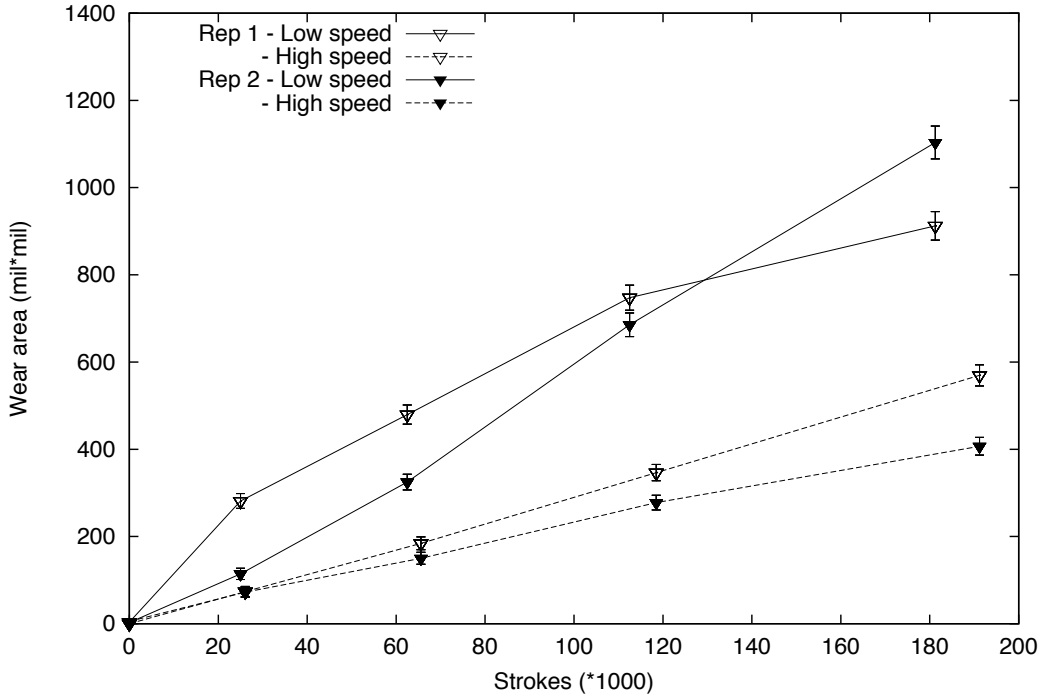

(a) Variation of the wear area under low load

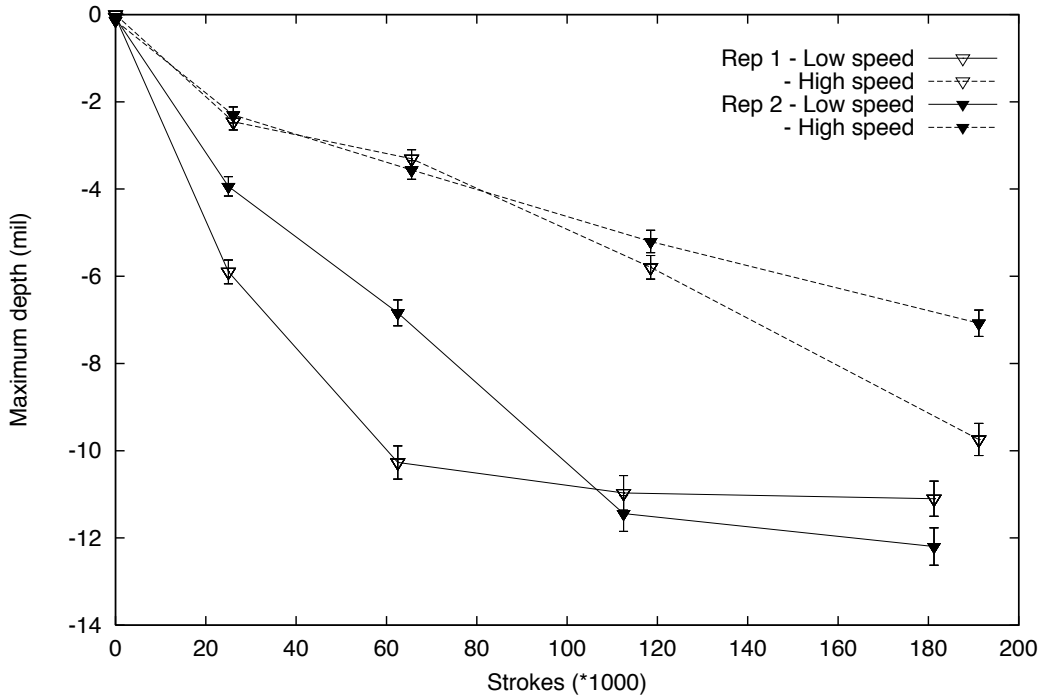

(b) Variation of the maximum scar depth under low load

Fig. 4.17 Variation of the wear data as a function of the number of brush strokes. Data for replicates 1 and 2 of NRL samples, at low load, low and high speed, are plotted. The measurement error on the wear data is plotted as error bars.

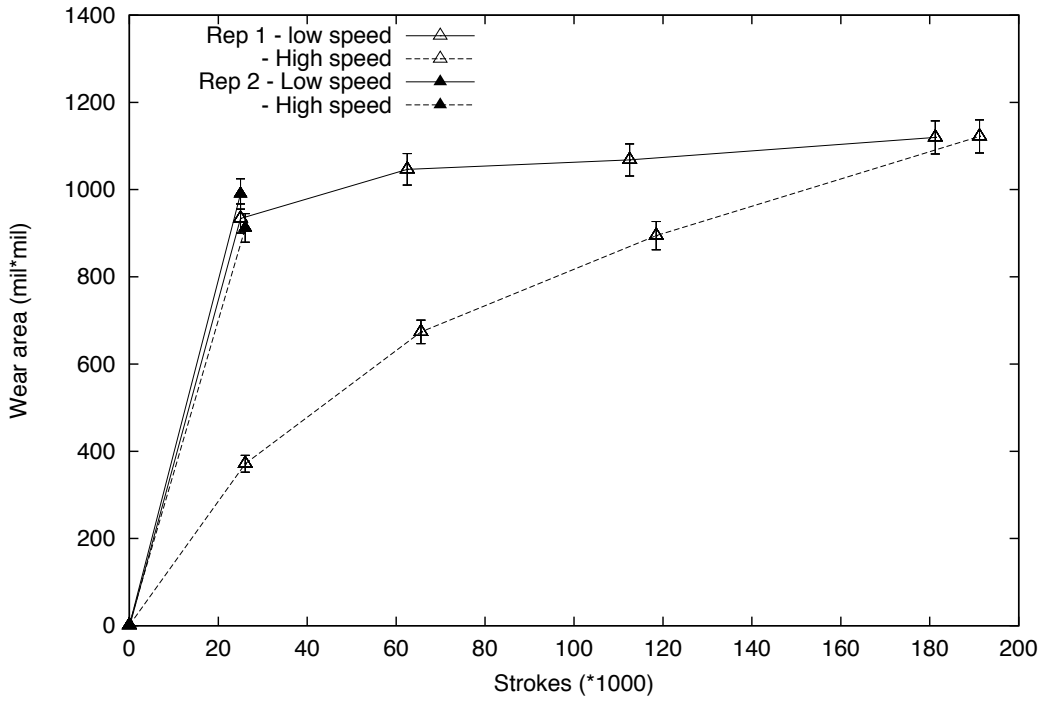

(a) Variation of the wear area under high load

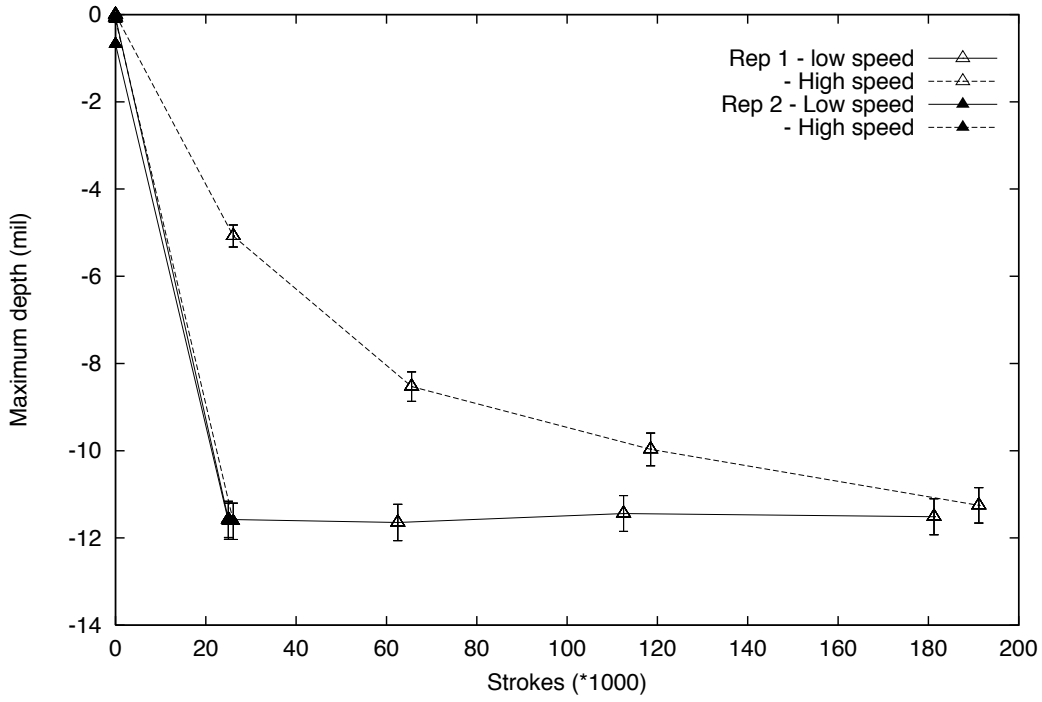

(b) Variation of the maximum scar depth under high load

Fig. 4.18 Variation of the wear data as a function of the number of brush strokes. Data for replicates 1 and 2 of NRL samples, at high load, low and high speed, are plotted. The measurement error on the wear data is plotted as error bars.

throughout the rest of the test is crucial to understand the situation as material is still being removed from the inner side of the track. The observed irregularity is believed to be inherent to the brushes used, if some bristles are slightly longer than the rest of them. This can also account for the discrepancy between replicate samples.

At high load, only limited data is available in the case of the second replicate sample. Indeed, in both cases, the brushes wore through the top coat immediately, and consequently, the tests were stopped at the end of phase 1. Intermediate data was collected during phase 1, corresponding to a number of brush strokes of 1250, 2500, 7750, and 25000 for high speed settings and 7900 and 26070 for low speed settings. In the case of replicate sample 1, it is observed that brushes wear through the top coat within phase 1 under low speed. When the rotational speed of the brushes is increased, in the case of replicate sample 1, the brushes wear through the top coat at a much lower wear rate. For replicate sample 2, as brushes wore through the top coat immediately, no speed effect is detected.

In both the low and high load cases, it has been showed that the wear area and the maximum depth data are complementary to each other and that they contribute to the understanding of the process of wear. We observed a load effect: as the load is increased, the amount of wear generated by the brushes increases regardless of the speed level. Within the measurement error, the level of speed does also appear to have an effect on the wear area and the maximum depth of the wear scar, especially for low load experiments. In all cases where the brushes remain in contact with the top coat, the wear area shows a linear increase with time or number of brush strokes.

Wear rate Figure 4.19 illustrates the variation of the wear rate as a function of time for both replicates under low and high speed, and under constant load, respectively low and high. The wear rate is equal to a hundred times the slope of the wear area versus brush strokes curve. This is equivalent to a wear area (in mil^2) occurring as a result of a 100 brush strokes.

The level of the speed appears to have an effect on the wear rate of NRL samples. For both replicate samples under low load, the wear rate is higher under low speed than it is under high speed. For replicate 2, the high initial wear rate can be explained by a phenomenon of transient wear whereas the low final wear rate can be accounted by the effect of the bond coat as described in the previous section. At high load, the wear rate

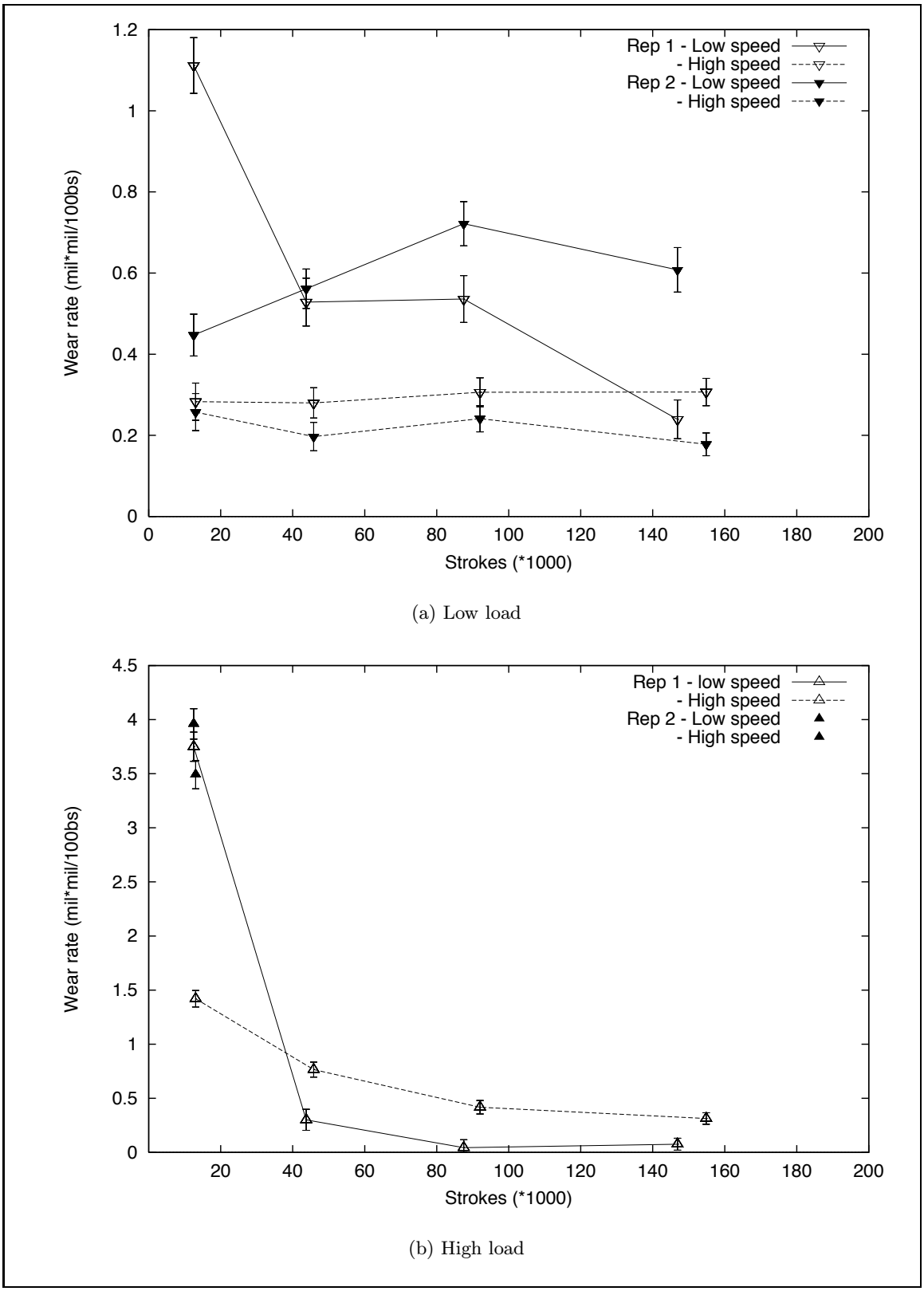

(a) Low load

(b) High load

Fig. 4.19 Variation of the wear rate versus number of brush strokes. Data for replicates 1 and 2 of NRL samples at low and high speed, are plotted for (a) low load (b) high load. The measurement error on the wear data is plotted as error bars.

data is hardly representative of the top coat material as brushes immediately wear through it. This explains the high initial value of the wear rate and its immediate decrease to lower values.

In order to illustrate the combined effect of load and speed levels, the previous wear area and wear rate data was plotted separately for each replicate sample as seen in figures 4.20 and 4.21. High load data is represented by upward triangles whereas low load data is represented by downward triangles. Low speed results are plotted with a solid line and high speed data with a dashed line. We can see that increasing the applied load while keeping the speed constant results in an increase in the wear area whereas increasing the rotational speed while keeping the load constant results in a decrease in the wear area. This trend is observed for the wear rates calculated for phase 1 as seen on figure 4.21. Wear rates calculated for phase 2 (without taking into account phase 1) follow the same trend but not as distinctively. The wear rate for high load and low speed falls down to values comparable to wear rates under low load. This is explained by the fact that the wear rate reported there is that of the bond coat, no longer that of the top coat. Wear rates under the other three treatment combinations follow the trend described previously for phase 1. The effect of the treatment combination on the wear rates for phase 3 and 4 can no longer be seen as the brushes wore through the bond coat in the most severe cases. In the case of replicate sample 2, the effect of the load level is clearly seen. However, the effect of the speed level is overcome by that of the load.

Another interesting point is that, for replicate sample 1, as seen in figure 4.20, the wear area obtained under high load – high speed is comparable to the wear areas obtained under low load – low speed. We could tentatively conclude that the load and the speed affect the area of the wear scar in a comparable manner: in terms of the area of the wear scar, reducing the load by a factor of 3 is nearly equivalent to increasing the speed by a factor of 3.

Statistical analysis is essential in determining whether or not there is sufficient evidence to conclude about the effect of the treatment combinations on the wear data of NRL samples.

Statistical analysis The experimental design described previously was chosen to fit the statistical design known as "repeated measures in a factorial design in a completely ran-

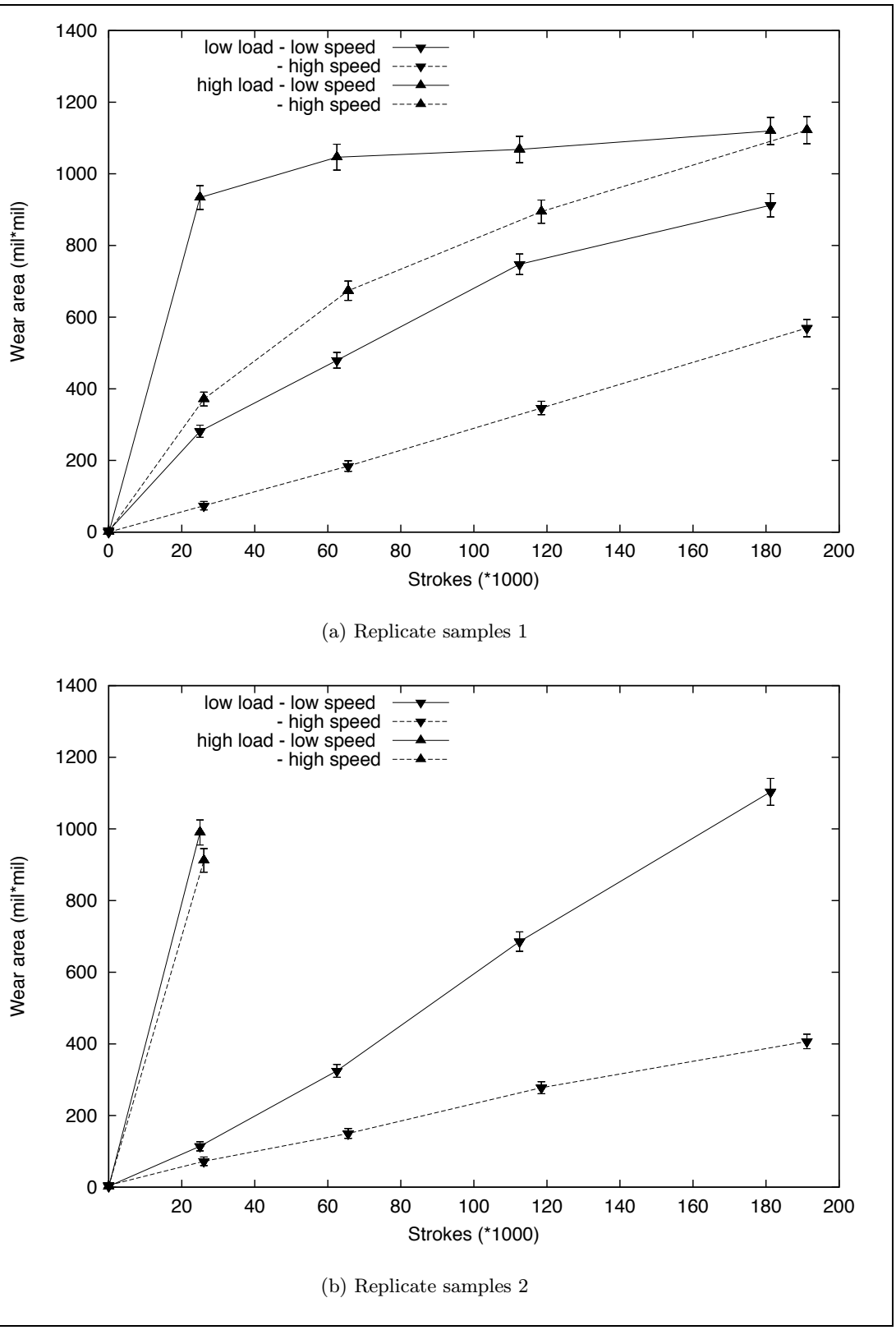

(a) Replicate samples 1

(b) Replicate samples 2

Fig. 4.20 Variation of the wear area as a function of the number of brush strokes. Data at low and high load combined with low and high speed are plotted for (a) replicate sample 1 (b) replicate sample 2. The measurement error on the wear data is plotted as error bars.

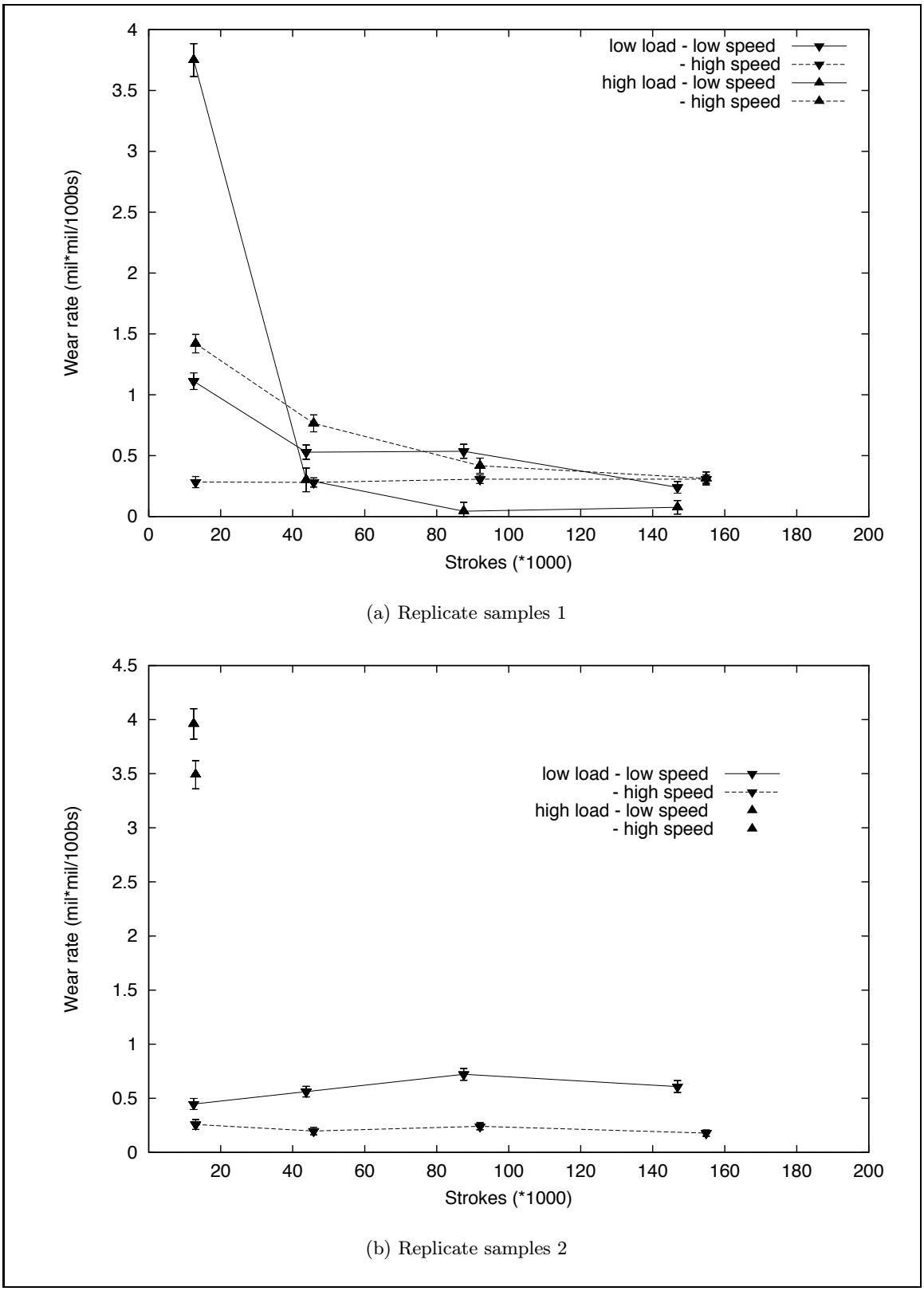

(a) Replicate samples 1

(b) Replicate samples 2

Fig. 4.21 Variation of the wear rate as a function of the number of brush strokes. Data at low and high load combined with low and high speed are plotted for (a) replicate sample 1 (b) replicate sample 2. The measurement error on the wear data is plotted as error bars.

domized design with sub-sampling". Repeated measures design accounts for the progressive collection of data as a function of time. The current design used is a 2×2 factorial design as described in Appendix D.

Figure 4.22 shows interaction plots for the average initial wear rate for phase 1 and the average wear rates for phase 2. The average wear rate is plotted versus the speed of the brushes for two load levels. After phase 1, we can easily see that increasing the load increases the initial wear rate. The effect of speed is well illustrated at high load level but is not quite as obvious at low load level. However, based on such a plot, we can tentatively say that for NRL samples, increasing the rotating speed can result in a decrease of the wear rate. This is observed after phase 2 as well as seen on figure 4.22 except for the high load tests. High load-low speed data is altered by the fact that the contact conditions are different since the top coat is missing and the wear rate reported is that of the bond coat. The increase of the wear rate upon speed increase is therefore not conclusive.

Figure 4.22 shows that there is no interaction between the load and the speed factors. Saying that two factors do not interact is equivalent to saying that the effect of one factor is the same for both levels of the other factor.

Further analysis was done using `SAS`. A listing of some of the `SAS` codes used is available in Appendix D.

Test of load and speed effect on the initial wear rate In a first time, `SAS` was used to test whether or not the data presented above give sufficient evidence that the load and speed factors affect the wear rate of NRL samples. Wear rate data obtained for phase 1 for both replicate samples was introduced in the statistical code with 4 observations per treatment combination and per replicate, leading to a total of 32 observations.

The statistical design is a 2×2 factorial experiment with sub-sampling with 2 replicates, and 4 observations per treatment combination. The linear model for a statistical analysis of the data can be written as:

$$(\text{rate})_{ijkl} = \mu_{\text{rate}} + w_i + v_j + wv_{ij} + \epsilon_{ijk} + \eta_{ijkl} \tag{4.1}$$

where rate_{ijkl} is the wear rate obtained for the lth observation (l = 1,2,3,4) for the kth replicate (k = 1,2) at the ith level of load (w) factor and jth level of speed (v) factor (i, j = 1,2). ϵ_{ijk} and η_{ijkl} are, respectively, the random and the observational errors. Table 4.5 summarizes the hypotheses tested with the 2 x 2 factorial design.

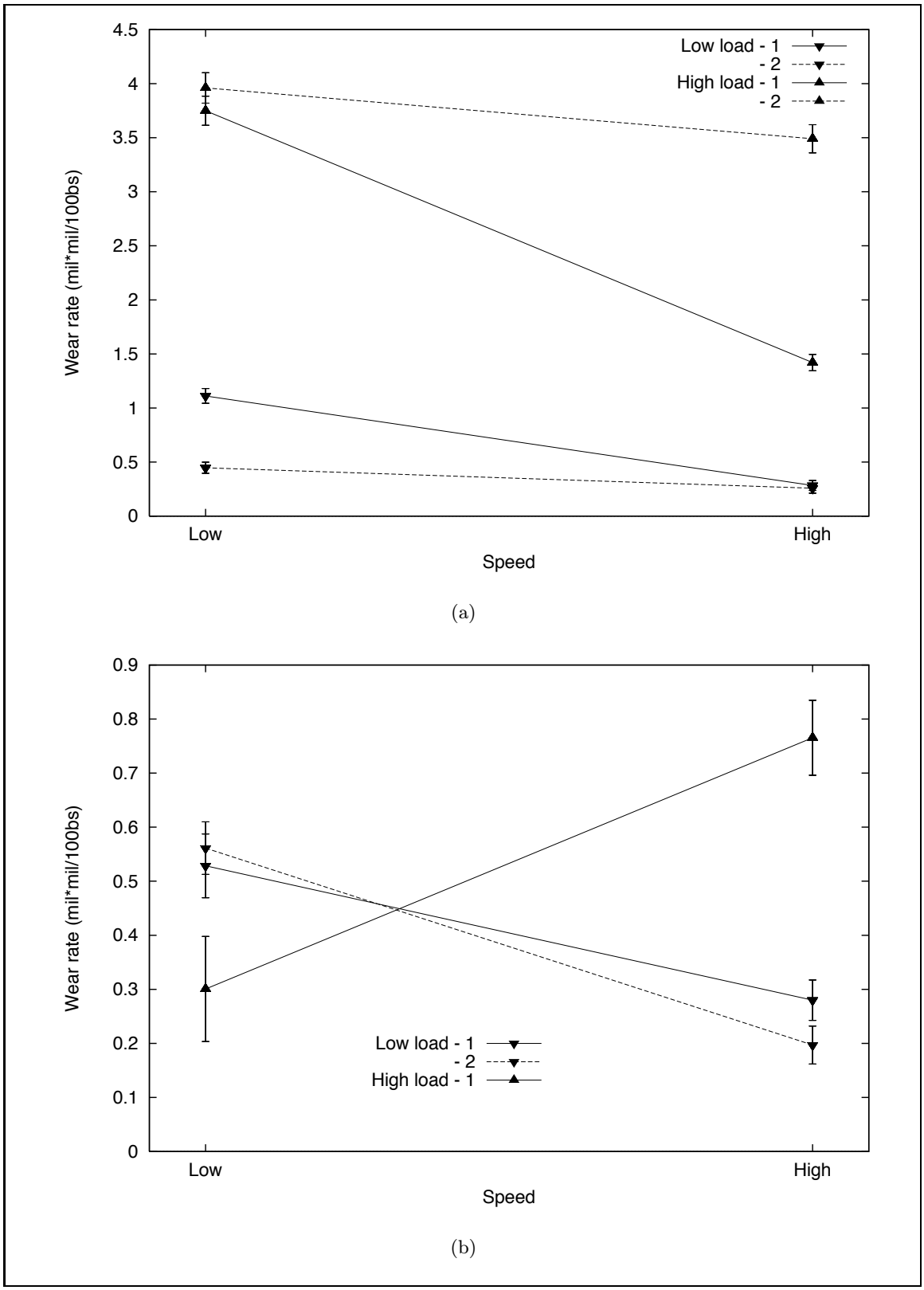

Fig. 4.22 Variation of the wear rate of NRL samples versus speed level as a function of the load level for (a) phase 1 and (b) phase 2. The measurement error on the wear data is plotted as error bars.

Table 4.5 Testing hypotheses for a 2×2 factorial design where the tested factors are load, w and speed, v.

Interaction between factors?	Null hypothesis, H_0	$wv_{11} = wv_{12} = wv_{21} = wv_{22}$
	Alternative hypothesis, H_a	at least one wv_{ij} differs, i.e. there is no interaction between factor level combinations
Load effect?	Null hypothesis, H_0	$w_1 = w_2$
	Alternative hypothesis, H_a	$w_1 \neq w_2$, i.e. there is a load effect
Speed effect?	Null hypothesis, H_0	$v_1 = v_2$
	Alternative hypothesis, H_a	$v_1 \neq v_2$, i.e. there is a speed effect

Table 4.6 Results of the tests of fixed effects with `MIXED` procedure

Source	**NDF**	**DDF**	**Type III F**	**Pr > F**
Load	1	4	45.42	0.0025
Speed	1	4	11.46	0.0276
Load × Speed	1	4	3.04	0.1561

The results for the test of fixed effects are listed in table 4.6. Since the p-value for the interaction term "Load × Speed" is larger than $\alpha = 0.05$, we accept the null hypothesis H_0 and conclude that there is no interaction between the levels of factors load and speed. Since there is no interaction between the two factors of interest, we can test the effect of the main factors, load and speed, separately. As seen in table 4.6, the p-values for the load and speed factors are both less than $\alpha = 0.05$. There is therefore sufficient evidence to reject the null hypotheses described in table 4.5.

In conclusion, for NRL samples, during phase 1, the speed and load levels do not significantly interact with each other. The factors load and speed do have an effect on the mean values of the wear rate as observed in figures 4.21 and 4.22, with levels of significance 0.0025 and 0.0276, respectively.

Test of speed and time effect on the wear area and wear depth Another study was done on the wear and the depth data to study the speed and time (or brush strokes number) factors with a repeated measures in a completely randomized design. A factorial design as used previously could not be utilized as we can not incorporate data

Table 4.7 Results of the tests of fixed effects with `MIXED` procedure for two responses: the wear area and the maximum wear depth

Response	**Source**	**NDF**	**DDF**	**Type III F**	**Pr > F**
Wear area	Speed, v	1	8	52.91	0.0001
	Time, t	3	8	36.94	0.0001
	$v \times t$	3	8	3.95	0.0534
Linear contrast	Time	1	48	57.94	0.0000
Wear depth	Speed, v	1	8	44.84	0.0002
	Time, t	3	8	20.17	0.0004
	$v \times t$	3	8	1.47	0.2936
Linear contrast	Time	1	48	110.35	0.0000

collected for high load tests. Indeed, the data obtained for phases higher than phase 1 was not representative of the top coat. A total of 64 observations were used.

The linear model for a statistical analysis of the data can be written as:

$$(\text{wear})_{ijkl} = \mu_{\text{wear}} + t_i + v_j + vt_{ij} + \epsilon_{ijk} + \eta_{ijkl} \tag{4.2}$$

where wear_{ijkl} is the wear rate obtained for the lth observation (l = 1,2,3,4) for the kth replicate (k = 1,2) at the ith level of time (t) factor (i = 1,2,3,4) and jth level of speed (v) factor (j = 1,2). ϵ_{ijk} and η_{ijkl} are, respectively, the random and the observational errors.

Table 4.7 summarizes the results of the analysis. For the wear area response, the p-value for interaction testing is close to 0.05. One may or may not reject the null hypothesis depending on a given application. It is believed that the low p-value obtained (0.0534) is due to the fact that the wear does not increase as significantly during the last test phase as the brushes started wearing through the top coat. This will come out of the statistical analysis as interaction between the two factors even though it is not. Therefore, in this study, we will conclude that there not enough evidence to reject the null hypothesis and therefore, the speed and time levels do not interact with each other.

The p-values obtained for the test of main factors effects are all well under 0.05 as seen in table 4.7. Therefore, we can conclude that the time and the speed at low load do have an effect on the wear data collected, i.e. wear area and wear depth, with a level of significance 0.0001. Statistical analysis of the results obtained for the maximum depth response lead to the conclusion that there is no interaction between the levels of the factors

speed and time ($p = 0.2936$), and that both factors, time and speed, are significant with levels of significance $p = 0.0002$ and $p = 0.0004$, respectively.

A contrast analysis was conducted to study the relationship between the response versus the factor levels. Such a study was conducted to study the variation of the wear area and the maximum wear depth as a function of the number of brush strokes. The linear contrasts are highly significant with p-values equal to 0.0000 in both cases. This shows that, indeed, the wear area and the maximum wear depth varies with the time level according to a linear relationship.

Test of speed and time effects on the wear rate Time factor was introduced in a study of the wear rate response at low load, similarly to the previous statistical study. A total of 64 observations were used in the design.

The linear model for a statistical analysis of the data can be expressed by equation where wear_{ijkl} is now rate_{ijkl}.

Table 4.8 Results of the tests of fixed effects with `MIXED` procedure for the wear rate

Source	**NDF**	**DDF**	**Type III F**	**Pr > F**
Speed	1	8	11.40	0.0097
Time	3	8	0.67	0.5925
Speed × Time	3	8	0.46	0.7186

Table 4.8 summarizes the results of the analysis. We can not reject the null hypothesis stating that there are no interaction since p is equal to $0.7186 \gg 0.05$. The speed factor is significant with a p-value of 0.0097. However, the time factor is not significant as p equals $0.5929 \gg 0.05$. Therefore, we may conclude that there is no time effect on the wear rate of the NRL samples. This is in agreement with the former statistical analysis on the wear area response which showed that there is a linear effect in the wear area as a function of time.

4.3.2 EXS samples

In this section are presented the results of load-speed tests conducted on the EXS samples.

EXS samples were tested according to the matrix seen in table 4.4 on page 96, with 2 replicates. The samples used are EXS 10/10 (replicate 1) and EXS 5/15 (replicate 2).

The thicknesses of the top and bond coats for EXS 10/10 are 7.60 mil and 7.36 mil, and for EXS 5/15, 9.10 mil and 4.20 mil.

Wear data

Wear area and maximum wear depth Figures 4.23 and 4.24 illustrate the variation of the wear area and the maximum depth of the wear scar as a function of the number of brush strokes for both replicate samples under low and high speed, and constant load, respectively low and high.

Under low load, it is observed that replicate samples 2 (represented on figure 4.23 by filled triangles) wore more than replicate samples 1 (represented on figure 4.23 by hollow triangles), regardless of the level of speed. As indicated by figure 4.23 (b), the brushes did not wear through the top coat in any case under low load. Indeed, the maximum wear depth after completion of phase 4 does not exceed 3 mil for replicate samples 1 and 6 mil for replicate samples 2. This is also confirmed by microscopic observations. As indicated previously, the thicknesses of the top coat of the two replicates are respectively 7.5 and 9 mil. Under high load, as shown on figure 4.24 (a), replicate samples 2 wore out more than replicate samples 1, for a given level of speed. However, except for replicate sample 1 tested under high load and low speed conditions, the brushes did remove the top coat off the specimens by the end of all tests as evidenced by figure 4.24 (b).

Under low load settings, the tests conducted with replicate samples 1 and 2 show no evidence of a speed effect on the amount of wear generated by brushes. Indeed, the variation of the wear area with the level of speed is plotted on figure 4.23 for replicate samples 1 and 2 and does not show any difference significantly larger than the measurement error.

Under high speed settings, as shown on figure 4.24, there is evidence of a speed effect on the amount of wear measured for both replicate samples. However, in the case of replicate sample 1, increasing the speed under high load resulted in an increase in the wear area whereas in the case of replicate sample 2, increasing the speed under low load resulted in a decrease in the wear area. The effect of the speed is not clearly observed. However, there is a strong load effect: indeed, as the load is increased, the wear area increases as well, regardless of the speed level.

The wear area appears to increase linearly with the number of brush strokes under

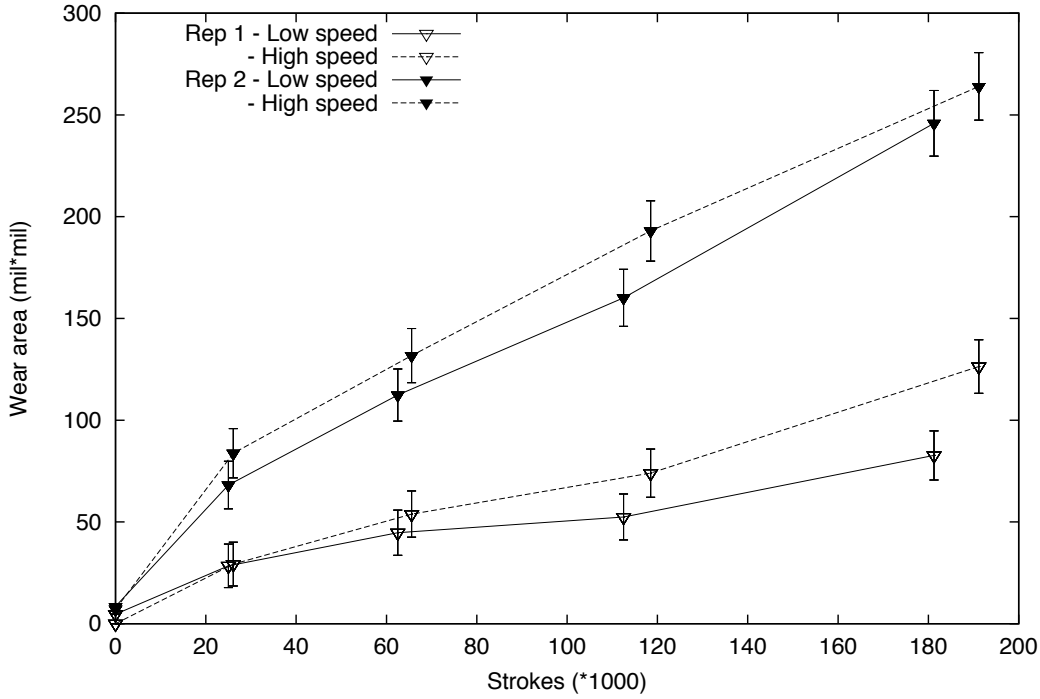

(a) Variation of the wear area under low load

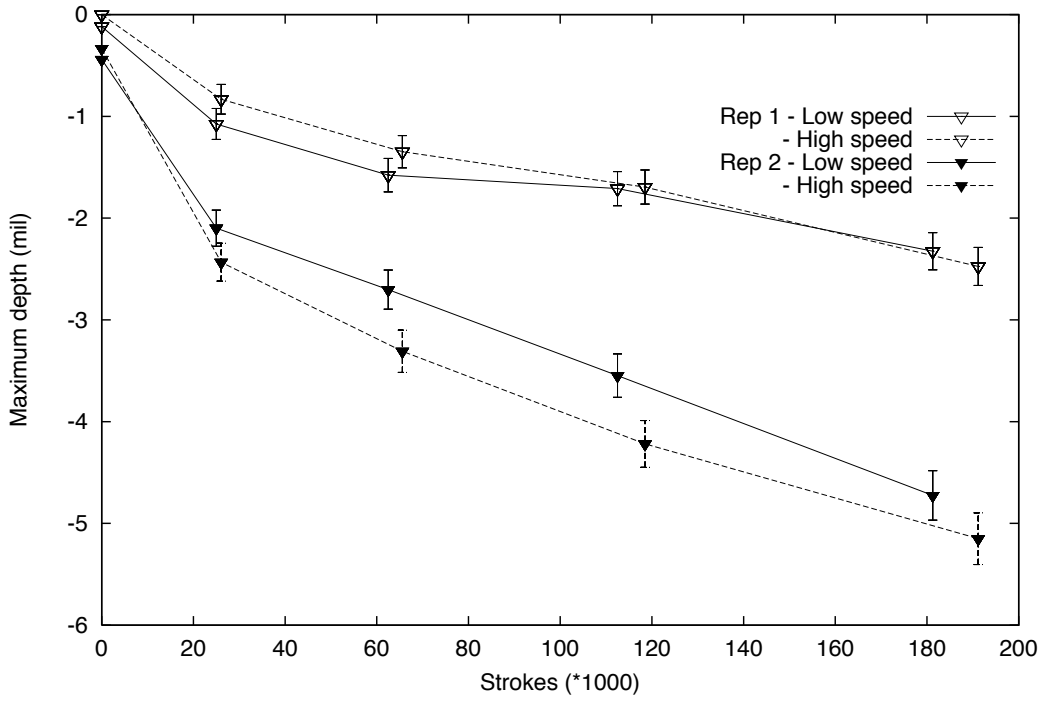

(b) Variation of the maximum scar depth under low load

Fig. 4.23 Variation of the wear data for EXS samples as a function of the number of brush strokes. Data for replicates 1 and 2, at low load, low and high speed, are plotted. The measurement error on the wear data is plotted as error bars.

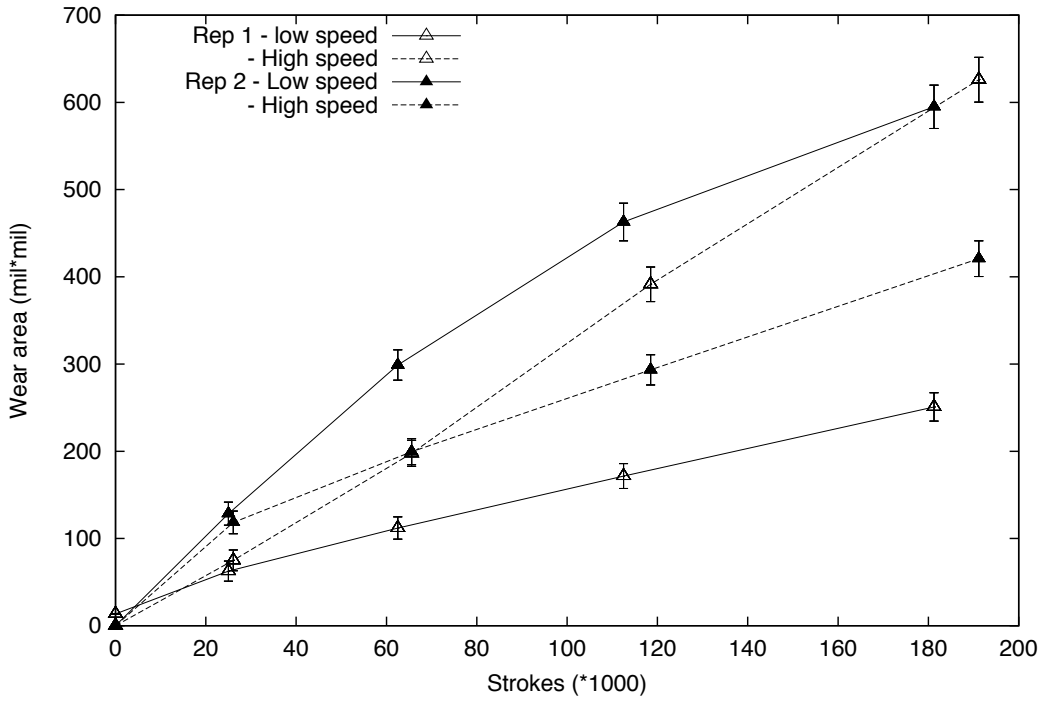

(a) Variation of the wear area under high load

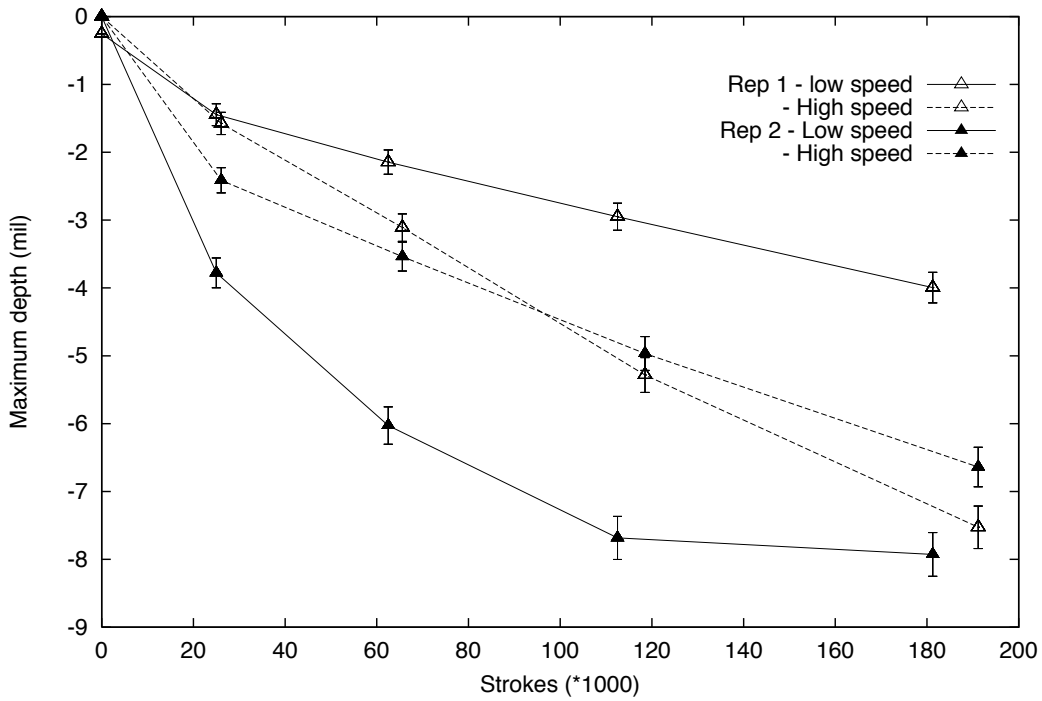

(b) Variation of the maximum scar depth under high load

Fig. 4.24 Variation of the wear data for EXS samples versus number of brush strokes. Data for replicates 1 and 2, at high load, low and high speed, are plotted. The measurement error on the wear data is plotted as error bars.

all factor combinations considered here.

Wear rate Figure 4.25 illustrates the variation of the wear rate as a function of the number of brush strokes for both replicates under low and high speed, and under constant load, respectively low and high. As previously, the wear rate is equal to a hundred times the slope of the wear area versus brush strokes curve. This is equivalent to a wear area (in mil^2) occurring as a result of a 100 brush strokes.

Under low load, the wear rate of the EXS samples is not affected by the level of speed. The wear rates for replicate samples 2 are larger than the wear rates for replicate samples 1, particularly for phase 1. However, the general variation of the wear rate with the total number of brush strokes is very similar for the two series of replicates. Indeed, the wear rate calculated for the initial phase is much higher than the wear rates calculated for the remaining tests phases, which remain constant within the measurement error.

Under high load, the wear rates are larger than those obtained under load load conditions. The variation of the wear rates with the number of brush strokes is scattered and difficult to explain at this point. In the case of replicate sample 1, the wear rates are fairly constant throughout the tests and wear rates for low speed tests are lower than than wear rates for high speed tests. In the case of replicate sample 2, under low speed, the wear rate continuously decreases with the increasing number of brush strokes. Under high speed, there is a large drop in the value of the wear rates: initially as high as wear rates obtained under low speed, and then dropping to values constant within the measurement error.

In terms of initial wear rates, we can conclude that there is no evidence of an effect of the speed level on the wear rates of EXS samples regardless of the load level.

In order to illustrate the combined effect of load and speed levels, the wear area and wear rate data are plotted separately for each replicate sample as seen in figures 4.26 and 4.27. High load data is represented with upward triangles and low load data is represented with downward triangles. Low speed results are plotted with a solid line and high speed data are plotted with a dashed line. Figure 4.26 confirms that increasing the level of load increases the wear area for EXS samples, regardless of the speed level. However, no conclusive remarks can be made concerning the effect of the level of speed on the wear area of the EXS samples hereby tested.

Statistical analysis is essential to determine whether or not there is sufficient evidence

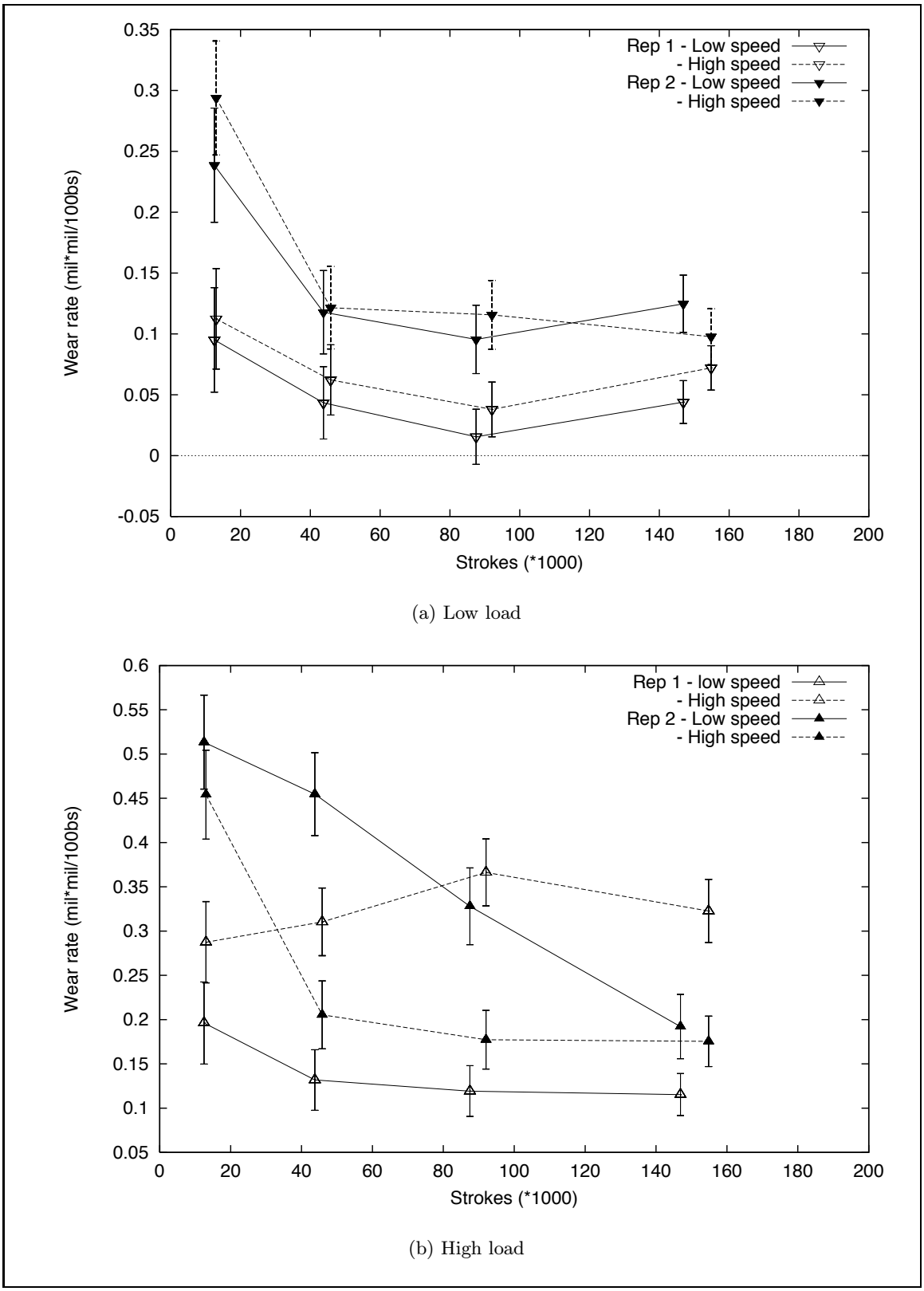

(a) Low load

(b) High load

Fig. 4.25 Variation of the wear rate for EXS samples as a function of the number of brush strokes. Data for replicates 1 and 2 at low and high speed, are plotted for (a) low load (b) high load. The measurement error on the wear data is plotted as error bars.

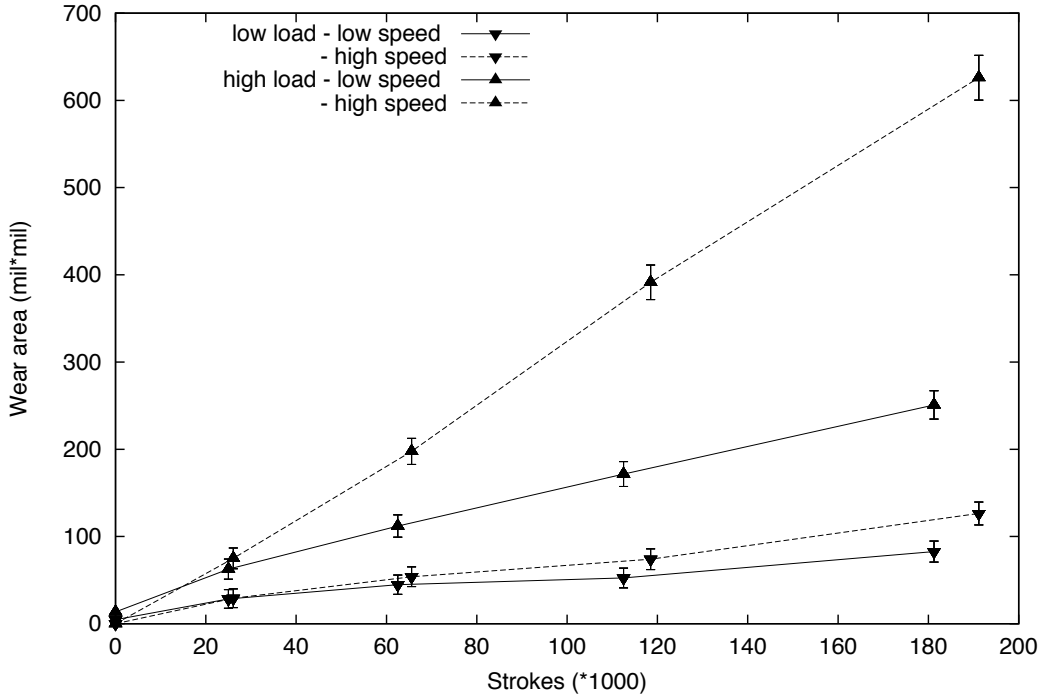

(a) Replicate sample 1

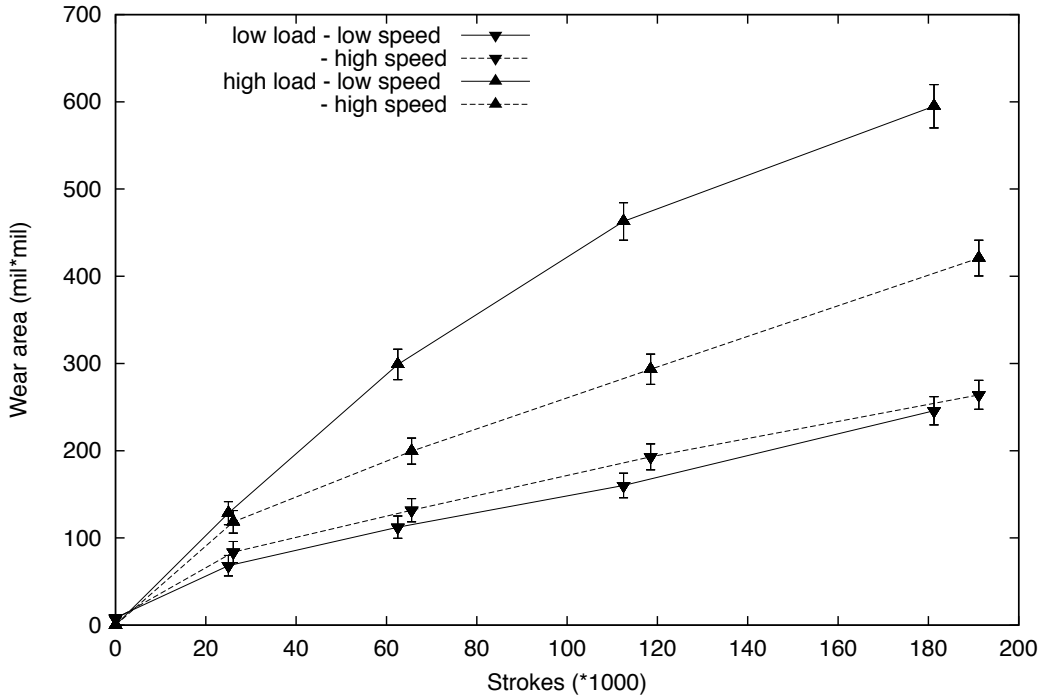

(b) Replicate sample 2

Fig. 4.26 Variation of the wear area for EXS samples as a function of the number of brush strokes for (a) replicate sample 1 and (b) replicate sample 2. The measurement error on the wear data is plotted as error bars.

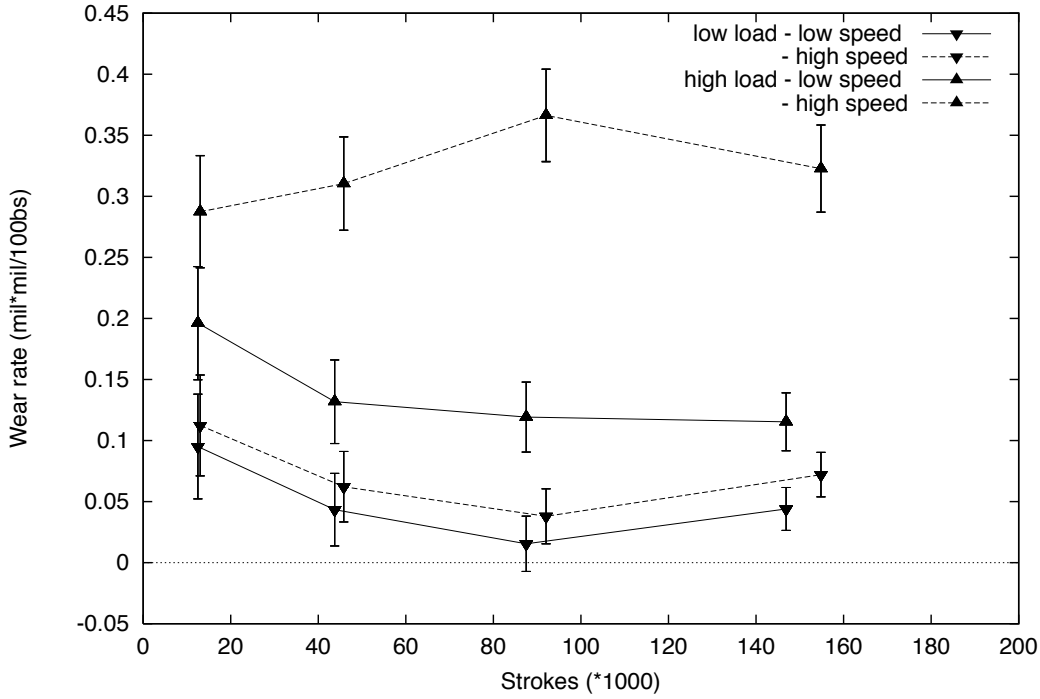

(a) Replicate sample 1

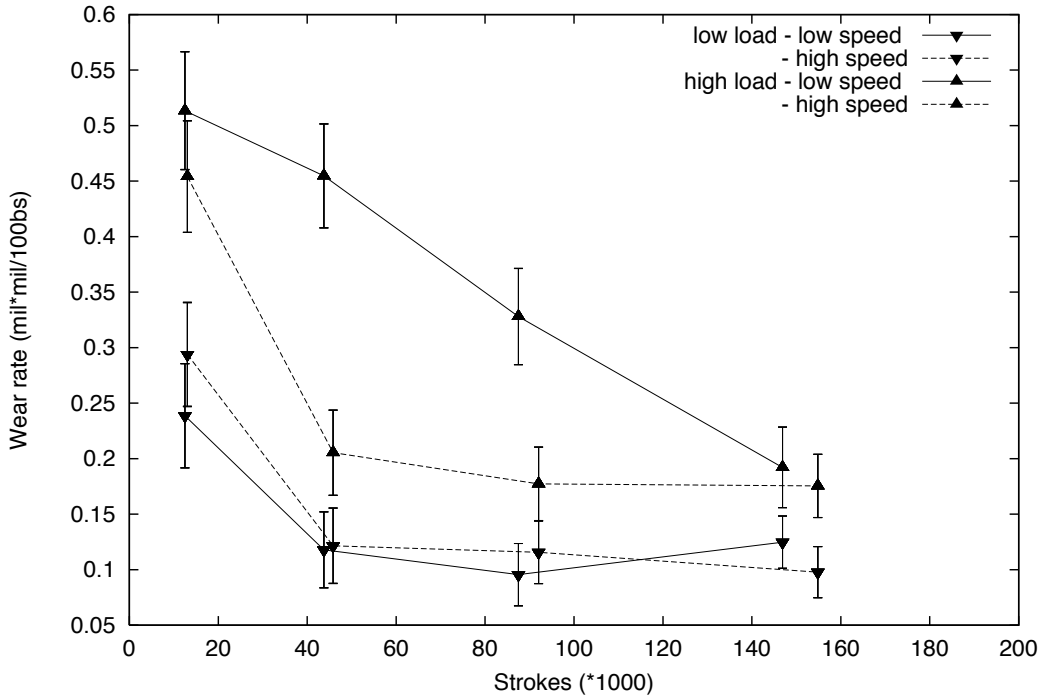

(b) Replicate sample 2

Fig. 4.27 Variation of the wear rate for EXS samples as a function of the number of brush strokes for (a) replicate sample 1 and (b) replicate sample 2. The measurement error on the wear data is plotted as error bars.

about the load effect and to study the relationship between the wear area, or the wear rate, and the number of brush strokes.

Statistical analysis As previously utilized for the analysis of the wear data of the NRL samples, the statistical design known as "repeated measures in the factorial design in a completely randomized design with sub-sampling" is utilized for the wear data of the EXS samples.

Figure 4.28 shows interaction plots for the average initial wear rate for phase 1 and the average wear rates for phase 2. The average wear rate is plotted against the speed of the brushes for the two load levels. After phase 1, this plot clearly shows that increasing the load results in an increase in the wear rate regardless of the speed level. Again, the effect of speed is not conclusive at this point. The same observations are still valid after the completion of test phase 2.

Further analysis was done using `SAS`.

Test of load and speed effects In a first time, SAS was utilized to test whether or not the data reported previously give sufficient evidence that the load and speed factors affect the wear rate or EXS samples. The wear data utilized is the wear rate. In the present case, for a majority of the tests, the surfaces in contact remained brush-top coat. Therefore, wear rate data obtained for all phases could be introduced in the statistical code, leading to a total of 128 observations.

The statistical design is a 2×2 factorial experiment with sub-sampling with 2 replicates, and 4 observations per treatment combination. The linear model for the statistical analysis can be written as:

$$(\text{rate})_{ijklm} = \mu_{\text{rate}} + w_i + v_j + wv_{ij} + t_k + wt_{ik} + vt_{jk} + wvt_{ijk} + \epsilon_{ijkl} + \eta_{ijklm} \qquad (4.3)$$

where rate_{ijklm} is the wear rate obtained for the mth observation (m = 1,2,3,4) for the lth replicate (l = 1,2) for time kth (k = 1,2,3,4) at the ith level of the load (w) factor and jth level of the speed (v) factor (i, j = 1,2). ϵ_{ijkl} and η_{ijklm} are, respectively, the random and the observational errors.

The results for the test of fixed effects are summarized in table 4.9. The p-values for the three- and two-factor interactions are larger than α=0.05. We can not reject the corresponding null hypotheses H_0. Therefore, we conclude that there is no interaction between

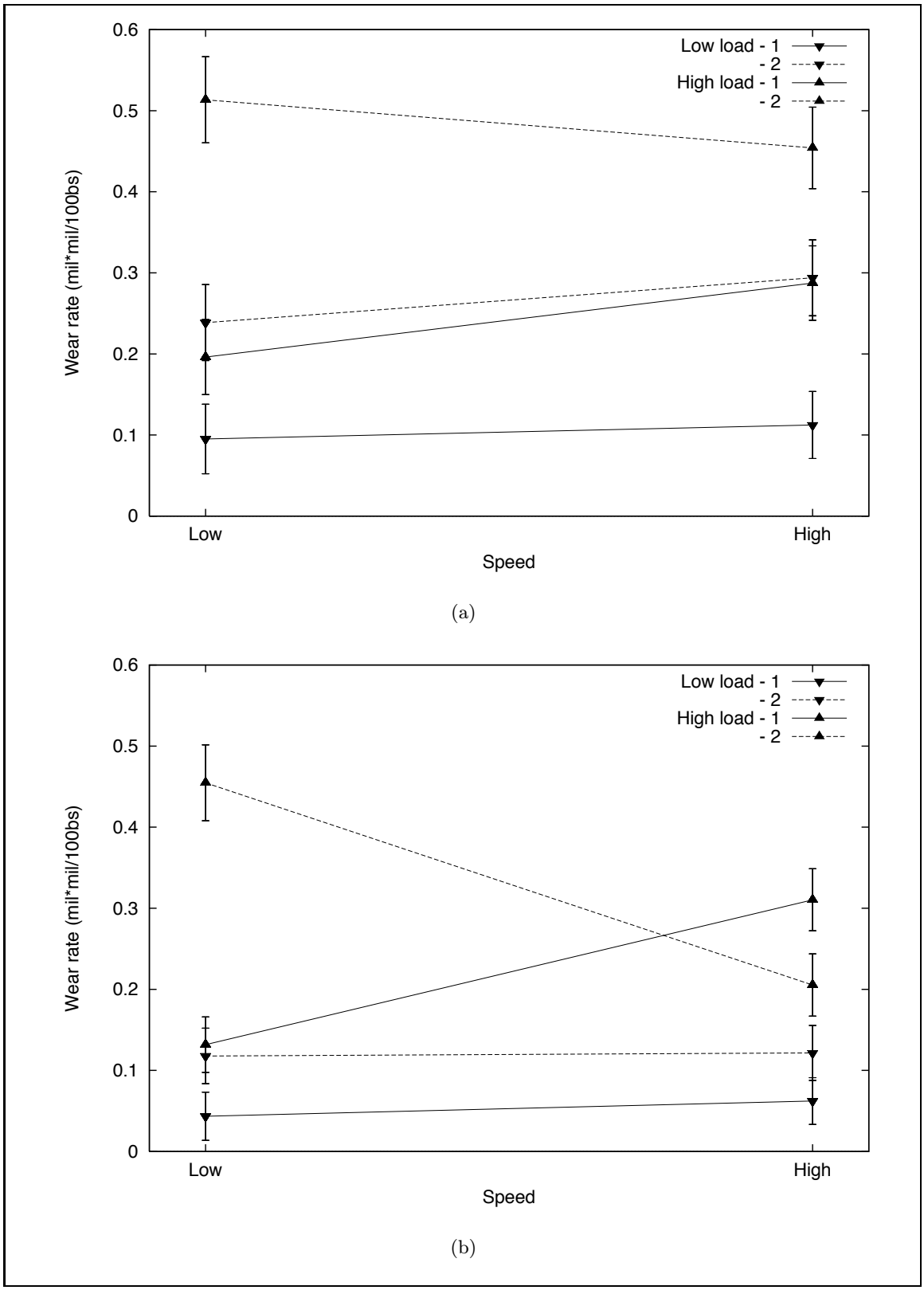

Fig. 4.28 Variation of the wear rate for EXS samples versus speed level as a function of the load level for (a) phase 1 and (b) phase 2. The measurement error on the wear data is plotted as error bars.

Table 4.9 Results of the tests of fixed effects with `MIXED` procedure

Source	**NDF**	**DDF**	**Type III F**	**Pr > F**
Main factor tests				
Load, w	1	4	5.93	0.0716
Speed, v	1	4	0.13	0.7411
Time, t	3	12	4.92	0.0187
Two-factor interactions				
$w \times v$	1	4	0.01	0.9251
$w \times t$	3	12	0.40	0.7585
$v \times t$	3	12	0.24	0.8699
Three-factor interaction				
$w \times v \times t$	3	12	0.34	0.7963

the factors load, speed and time. The p-values for the load, speed and time individually are, respectively, 0.0716, 0.7411 and 0.0187. We can not reject the null hypothesis H_0 defined as $H_0 : v_1 = v_2$. There is therefore insufficient evidence for an effect of the speed factor on the wear rate data of the EXS samples. The factors load and time, in comparison, are significant. Therefore, this analysis confirms that the level of factor load does affect the wear rate of the EXS samples regardless of the level of speed. The time has an effect on the response as well. This is due to the scatter which can be observed in the rate data.

Test of load and speed effects per test phase When the tests are severe enough, the top coat is completely removed from the specimen samples by the end of phase 3. We chose to test the effects of the two factors of interest for each individual phase separately. This eliminates the error due to the change in the contact conditions.

The results for the test of fixed effects are summarized in table 4.10. For phases 1 through 4, the factor load is highly significant whereas the factor speed is not significant.

Test of speed and time effect on the wear area and wear depth under constant load Under high load, one of the replicate sample did wear out faster and towards the final phase of the test, the contact conditions were altered in the sense that the brushes were no longer in contact with the top coat but with the bond coat. Therefore the previous statistical matrix was divided into smaller statistical groups. The analysis of this paragraph is related to the effect of speed and time for low load level on the wear area and

Table 4.10 Results of the tests of fixed effects per phase with `MIXED` procedure

Source	**NDF**	**DDF**	**Type III F**	**Pr > F**
Phase 1				
Load, w	1	28	6.34	0.0178
Speed, v	1	28	0.14	0.7142
Load × Speed	3	28	0.02	0.8865
Phase 2				
Load, w	1	28	12.05	0.0017
Speed, v	1	28	0.05	0.8266
Load × Speed	1	28	0.18	0.6725
Phase 3				
Load, w	1	28	7.90	0.0089
Speed, v	1	28	0.29	0.5948
Load × Speed	1	28	0.04	0.8369
Phase 4				
Load, w	1	28	9.55	0.0045
Speed, v	1	28	1.61	0.2146
Load × Speed	1	28	1.58	0.2198

the maximum wear depth. A similar analysis of the wear rate is conducted in the following paragraph. The linear model is similar to that utilized in the statistical analysis of the NRL samples (equation 4.3.1 on page 109).

Results are listed in table 4.11. With p-values larger than 0.99 for the wear area and the wear depth responses, we can conclude that there is no interaction between the speed and the time factors. The p-values obtained for the tests of the main factors effects are larger than 0.05, particularly for test of the speed effect where $p = 0.5984$ and $p = 0.7693$, respectively for the wear area and the maximum depth. Even though it was observed that the wear area does increase as a function of time, the statistical analysis indicates that there is not significant time effect. This is due to the extent of the confidence intervals compared to the increase in the wear area.

A similar analysis was done for data under high load as well. In this case, the tests for the time effects were significant with p-values equal to 0.0215 and 0.0669, respectively for the wear area and the maximum wear depth.

Table 4.11 Results of the tests of fixed effects with `MIXED` procedure for two responses: the wear area and the maximum wear depth, under constant load level, respectively, low and high.

Response	Source	NDF	DDF	Type III F	Pr > F
Low load level, w_1					
Wear area	Speed, v	1	8	0.30	0.5984
	Time, t	3	8	2.19	0.1673
	$v \times t$	3	8	0.02	0.9955
Wear depth	Speed, v	1	8	0.09	0.7693
	Time, t	3	8	1.56	0.2736
	$v \times t$	3	8	0.01	0.9989
High load level, w_2					
Wear area	Speed, v	1	8	0.19	0.6710
	Time, t	3	8	5.74	0.0215
	$v \times t$	3	8	0.13	0.9399
Wear depth	Speed, v	1	8	0.01	0.9102
	Time, t	3	8	3.56	0.0669
	$v \times t$	3	8	0.20	0.8964

Test of speed and time effects on the wear rate A similar statistical study was performed on the wear rates of the EXS samples under low load in a first time and under high load in a second time. A total of 64 observations were fitted into the model according to equation 4.3.1 (page 109).

Table 4.12 summarizes the output of the statistical analysis. As for the wear area and wear depth data, under low or high load, we observe that the speed effect is negligible. We also conclude that the time effect is not significant, which is lead to the conclusion that, under a given level for the load, the wear rate of the EXS samples remains constant as long as the contact conditions are not altered during the course of the wear test.

4.3.3 NRL and EXS samples

Analysis of the wear behavior of the NRL and the EXS samples showed that there exists some differences between the two sample series. On one hand, the load and the speed both have a significant effect on the wear behavior of the NRL samples whereas exclusively the load have a significant effect of the wear behavior of the EXS samples. On an other hand, even though for both samples the area of the wear scar increases linearly with the number of

Table 4.12 Results of the tests of fixed effects with `MIXED` procedure for the wear rate, under constant load level, respectively, low and high.

Source	**NDF**	**DDF**	**Type III F**	**Pr > F**
Low load level, w_1				
Speed	1	8	0.23	0.6413
Time	3	8	2.25	0.1597
Speed × Time	3	8	0.05	0.9864
High load level, w_2				
Speed	1	8	0.18	0.6861
Time	3	8	0.84	0.5086
Speed × Time	3	8	0.14	0.9346

brush strokes, the rate at which it increases for a given treatment combination is different.

Figures 4.29 and 4.30 show the variation of the wear area and of the wear rates for the NRL and the EXS 10/10 samples versus the number of brush strokes for low and high load. Low speed results are plotted with solid lines and the high speed results are plotted with dashed lines. The data are the average of the data obtained for the two replicates presented in the previous sections, except for the high load data for NRL samples for which only limited data are available. For these tests, the results obtained for the first replicates are plotted instead. The data for NRL samples are represented with filled circles and the data for EXS samples are represented with open circles (average data) and upright crosses (replicate 1 data).

According to figure 4.29 (a), under low load, regardless of the level of speed, the wear area of the NRL samples exceeds that of the EXS samples. However, after phase 1, the wear area of the scar generated on the NRL samples under high speed and low load is comparable to the wear area generated on the EXS samples under low load. According to figure 4.29 (b), under high load, regardless of the level of speed, the wear area of the NRL samples is larger that that of the EXS samples, for all test phases.

According to Fig. 4.30, the wear rates of the NRL samples are larger than the wear rates of the EXS samples regardless of the load level. Under high load, for the initial test phase, the average wear rates of the NRL samples are approximately five fold that of the EXS samples. After phase 1, under high load, the low wear rates reported for NRL samples are no longer strictly representative of the top coat, but rather of the bond coat as well.

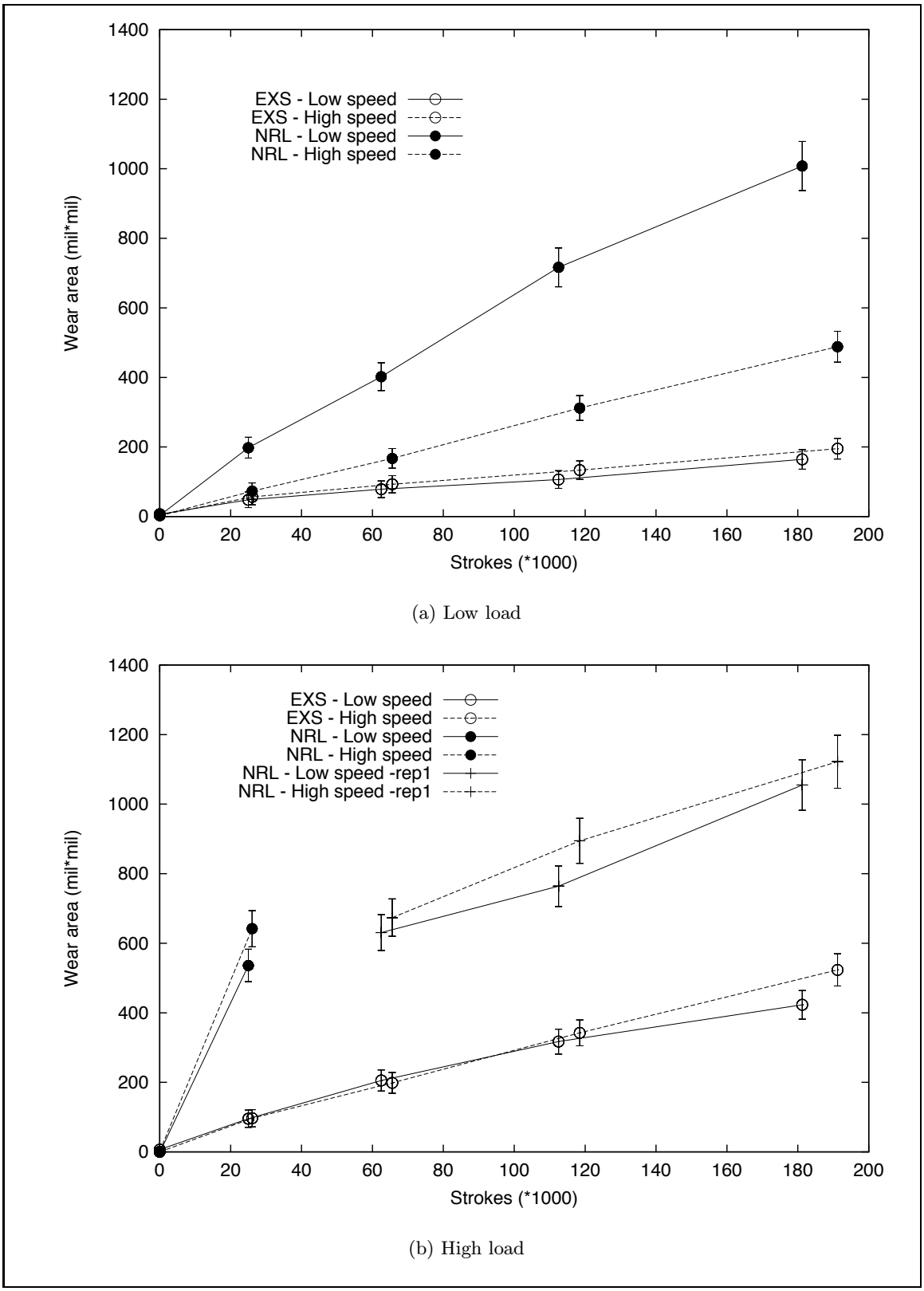

(a) Low load

(b) High load

Fig. 4.29 Variation of the wear area as a function of the number of brush strokes for NRL and EXS samples. The measurement error on the wear data is plotted as error bars.

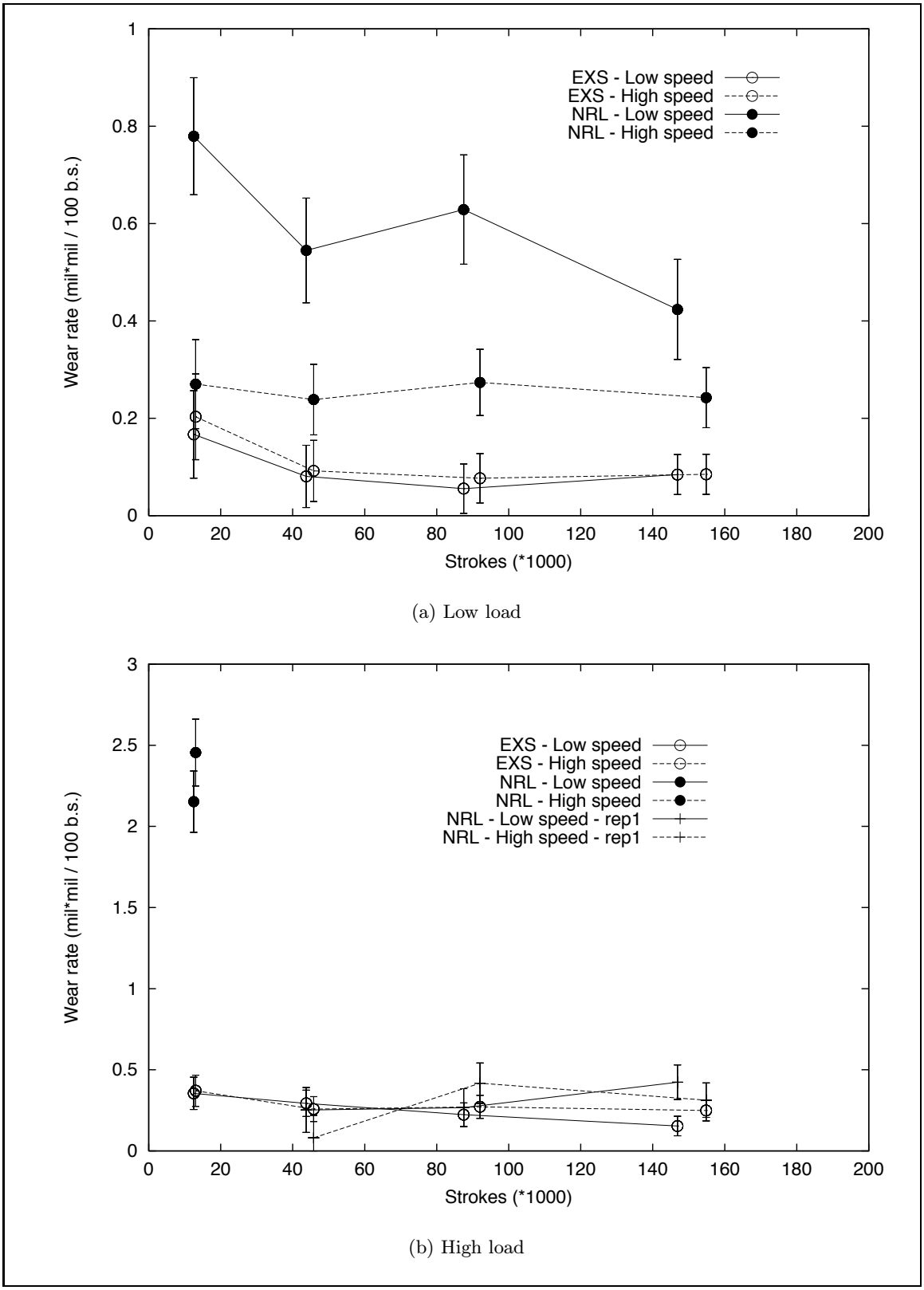

(a) Low load

(b) High load

Fig. 4.30 Variation of the wear rate as a function of the number of brush strokes for NRL and EXS samples. The measurement error on the wear data is plotted as error bars.

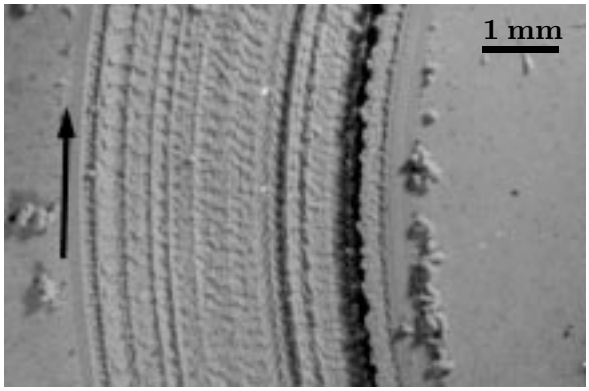

Fig. 4.31 Section of the wear scar of a NRL 10/10 specimen sample following $\simeq$ 26,000 brush strokes under high load and high speed. The arrow indicates the direction of sliding.

4.4 Microscopic study

Microscopic pictures of the wear scar and the brushes were taken at the end of each test, and, when possible, between each test phase.

4.4.1 NRL samples

Wear scar Figure 4.31 illustrates a section of the wear scar of a NRL 10/10 sample tested under high load and high speed after 26,000 brush strokes. We observe concentric scratches which match the path of the brush bristles.

Figure 4.32 is a representative profile of the wear scar of a NRL sample with concentric scratches, such as those seen in figure 4.31. Grooves can be detected from the profile.

Figure 4.33 represents a section of the wear scar of a NRL 15/5 sample tested under high load and high speed after 191,000 brush strokes. Transverse ridges perpendicular to the direction of sliding are observed. The spacing between the ridges vary slightly across the wear scar: ridges located near the outside perimeter of the wear track are spaced further apart from each other than ridges located near the inside perimeter of the wear track. Microscopic pictures of NRL samples tested under all treatment combinations are seen in figures 4.34 and 4.35.

The transverse ridges can be seen in all cases of figure 4.34. Pictures with higher magnification, shown in figure 4.35, show that the spacing of the ridges under low load and

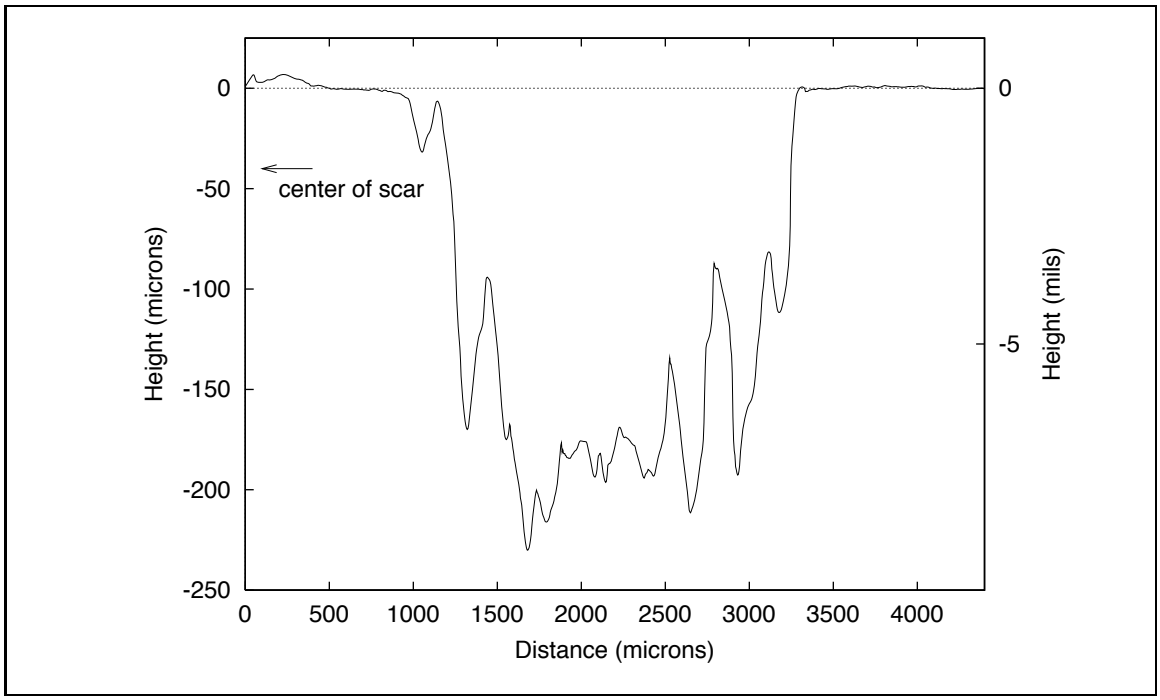

Fig. 4.32 Surface profile of a NRL specimen sample. The scanning direction is perpendicular to the direction of sliding.

speed is comparable to the spacing of the ridges under high load and speed. For cases (b) and (c), scratches disturb the regular pattern of the ridges and complicate the measurement of the spacing between ridges. Small, (c), and large, (b), tears can be seen parallel to the sliding direction. The saw tooth pattern discussed in Chapter 2 can be seen also.

Profiles were collected in the direction of sliding on surfaces with transverse ridges to measure the spacing between ridges. Figure 4.36 displays two representative examples of such profiles collected on NRL samples. The regular and periodic features of the abrasion pattern can be seen. The spacing between ridges is approximately equal to 90-165 μm with lengths ranging from 5 to 40 μm. This correlates well with microscopic pictures seen in figure 4.35.

Longitudinal scratches were not always present on the NRL samples as seen on figure 4.33. In contrast, transverse ridges are observed on all the NRL samples, regardless of the testing conditions, and even when longitudinal scratches seem to be the major form of damage. In the latter case, when the regularity of the pattern is disturb by scoring marks, the pattern seen in the scar is called a pseudo-abrasion pattern (Grosch and Schallamach, 1966).

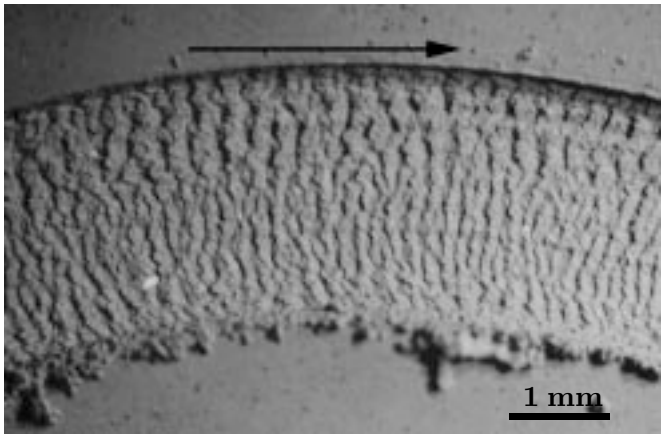

Fig. 4.33 Section of the wear scar of a NRL 15/5 specimen sample following $\simeq$ 191,000 brush strokes under high load and high speed. The arrow indicates the direction of sliding.

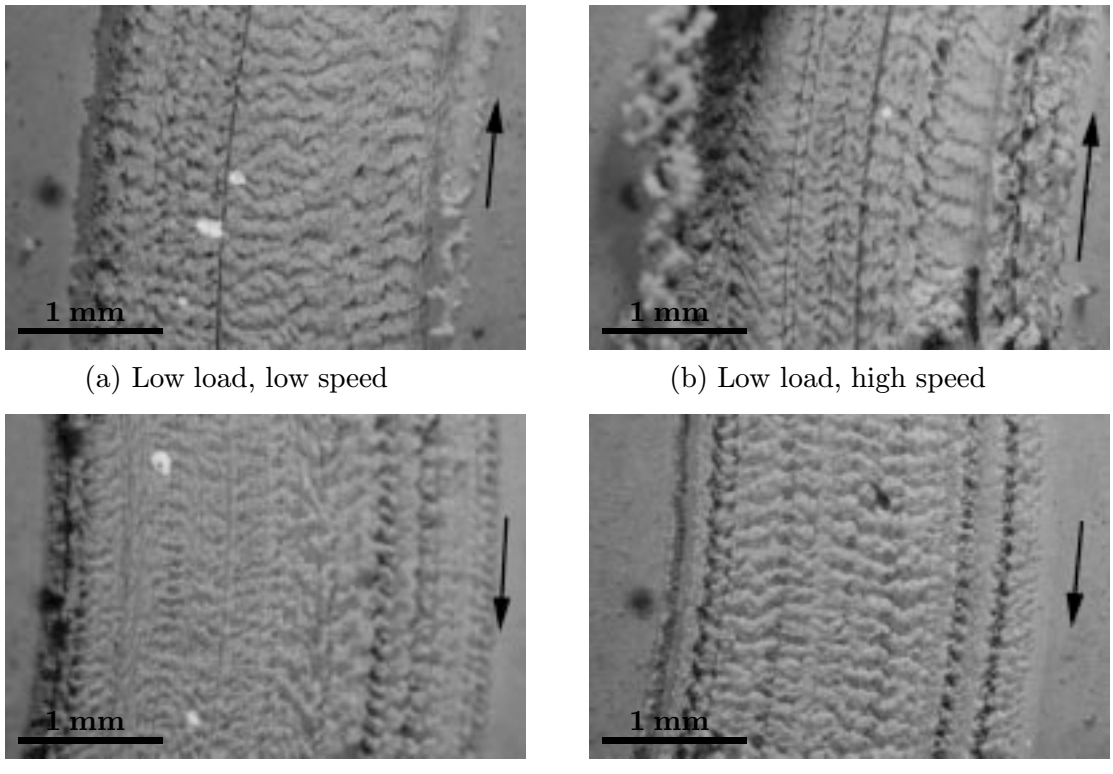

(a) Low load, low speed

(b) Low load, high speed

(c) High load, low speed

(d) High load, high speed

Fig. 4.34 Sections of the wear scars of NRL 15/5 specimen samples following $\simeq$ 191,000 brush strokes under (a) low load and low speed, (b) low load and high speed, (c) high load and low speed, and (d) high load and high speed. The direction of sliding is indicated by the arrow.

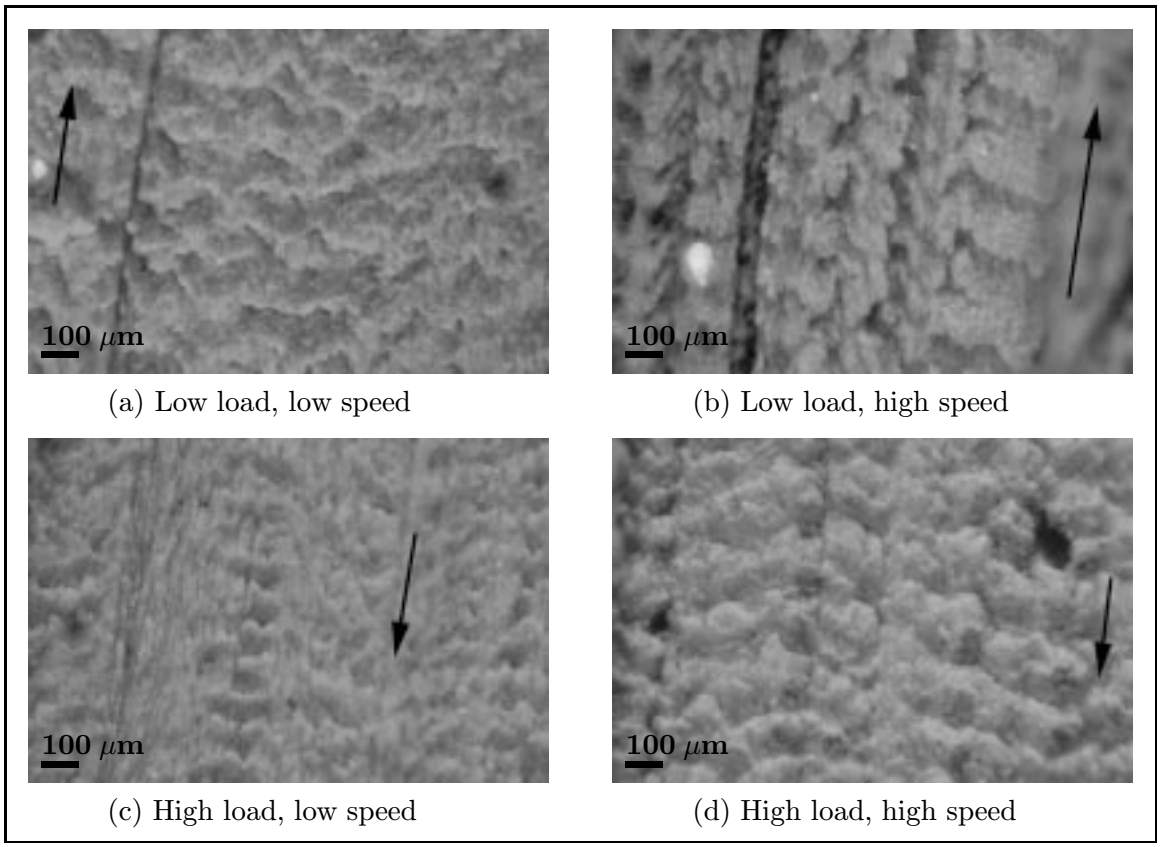

(a) Low load, low speed

(b) Low load, high speed

(c) High load, low speed

(d) High load, high speed

Fig. 4.35 Similar sections of the wear scars of NRL 15/5 specimen samples following $\simeq$ 191,000 brush strokes under (a) low load and low speed, (b) low load and high speed, (c) high load and low speed, and (d) high load and high speed. The direction of sliding is indicated by the arrow.

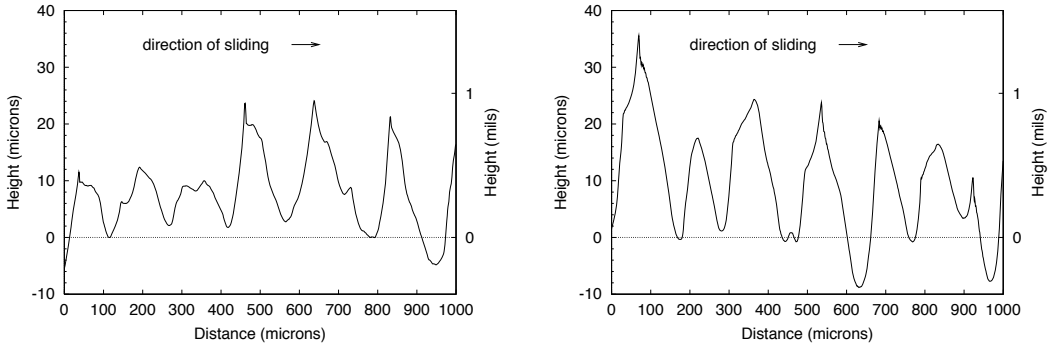

Fig. 4.36 Surface profiles of NRL 15/5 specimen samples showing the regular pattern of the transverse ridges. The scanning direction is parallel to the direction of sliding.

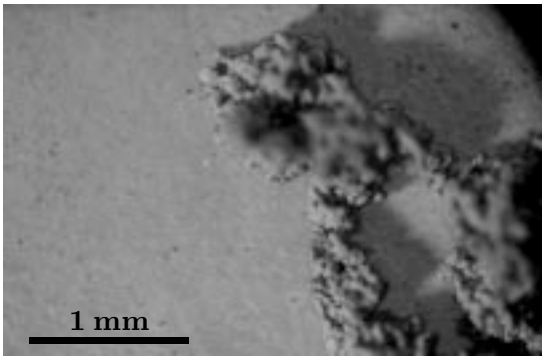

Fig. 4.37 Cluster of wear debris on a NRL specimen sample.

Debris Wear debris were formed immediately and gathered in clusters as shown on figure 4.37. The cluster is out of focus due to its large size. Individual particles can be seen as well, particularly at the edges of the wear track (Figs. 4.31 and 4.33).

Rolled debris have been observed on the brushes and also on the surface after a small amount of brushing. Figure 4.38 (a) illustrates the tips of the brush bristles at the end of a test conducted on a NRL 10/10 sample under low load and high speed. A rolled fragment as well as accumulation of debris can be seen. Figure 4.38 (b) is a microscopic picture of the surface of a NRL 10/10 sample tested under high load and speed after approximately 800 brush strokes. Limited damage to the surface can be seen. The wear debris visible in the wear track appear to be rolled debris. The true nature and the mode of formation of such debris is not understood. They might be debris which have been reshaped under the sliding motion of the brush. When microscopic observation of the surface is conducted after approximately 800 brush strokes, we observe not only rolled fragments but also small clusters of wear debris. Damage on the surface is observed and wear debris appear to be formed rapidly as seen in figure 4.39.

It is interesting to note that in the case of the rate tests, according to figure 4.40 the regular abrasion pattern previously observed can not be seen. In the rate tests, not only were the brushes cleaned between each test phase, but also the duration of the phases was shorter, hence limiting the amount of wear debris accumulated at the interface. This observation leads to the hypothesis that wear debris accumulated on the brush may play a significant role in the formation of the abrasion pattern.

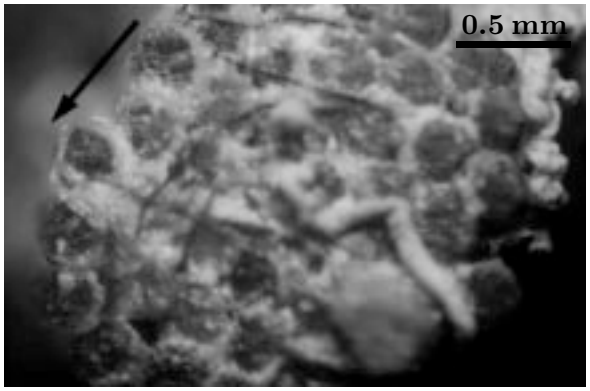

(a)

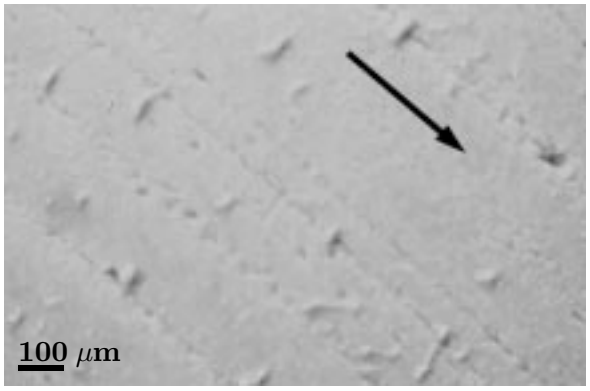

(b)

Fig. 4.38 Roll fragments (a) on a brush tuft after $\simeq$ 191,000 brush strokes under low load and high speed for a NRL specimen sample, (b) in the wear track of a NRL specimen sample after 800 brush strokes. The sliding direction is indicated by the arrows.

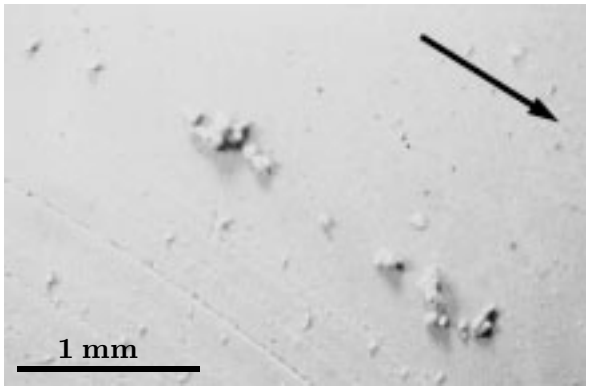

(a)

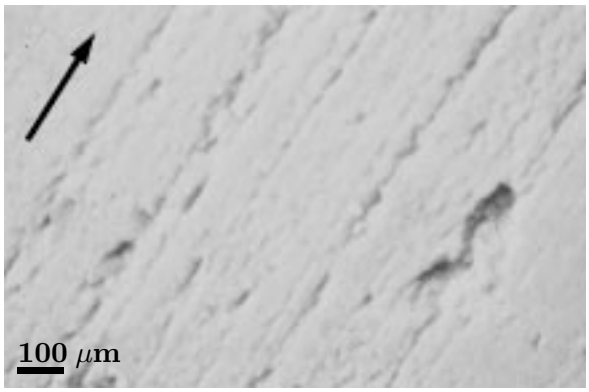

(b)

Fig. 4.39 NRL specimen sample following 800 brush strokes: (a) debris formed and gathered in clusters near the edge of the wear scar, (b) grooves and surface damage parallel to the direction of sliding. The arrows indicate the direction of sliding.

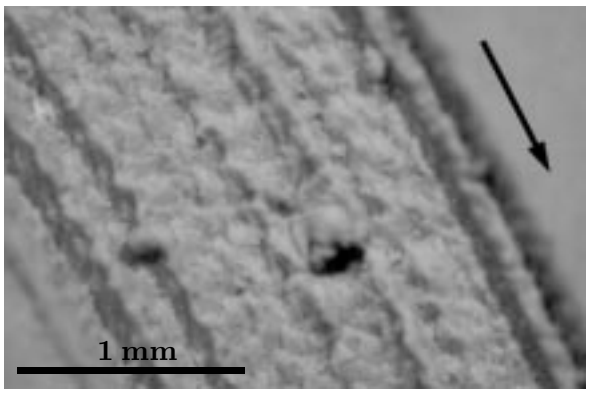

Fig. 4.40 Section of the wear scar of a NRL 15/5 sample following $\simeq$ 71,000 brush strokes under high load and high speed in the rate tests. The arrow indicates the direction of sliding.

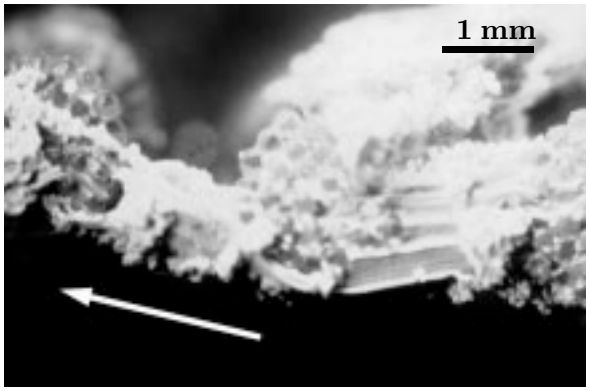

Fig. 4.41 Tips of brushes after $\simeq$ 26,000 brush strokes for a NRL 15/5 specimen sample under high load and high speed. The sliding direction is shown by the arrow.

Brushes Figure 4.41 illustrates the tip of the brushes at the end of the initial phase for a NRL sample tested under high load and high speed. Heavy accumulation of wear debris can be seen, in the form of clusters or larger particles which appear to be reshaped individual debris. Under low load conditions, as less wear debris are generated, fewer debris are accumulated on the brushes as seen in figure 4.38.

4.4.2 EXS samples

Wear scar On EXS samples, the brush bristles form circular grooves as shown in figures 4.42 and 4.43 as well as on the profiles collected perpendicularly to the direction of sliding (figure 4.44).

A well defined single scratch lies near the outer and inner perimeter of the wear scar shown in figure 4.42. This is caused by the spacial arrangement of the brush tufts. They are disposed in line and therefore, some of the bristles tend to form their own track as seen in figure 4.45. The single scratches may be the onset for wear debris formation, eventually leading to increased damage as observed in the center of the wear scar. On EXS surfaces which do not exhibit the air bubbles entrapment as EXS 5/15 does (figure 4.10), concentric scratches appear to be the predominant mode of damage.

It is not clear whether or not transverse ridges as previously seen on the surface of the NRL samples are observed on EXS samples. Figures 4.46 (a) and (b) are pictures of EXS samples tested under high load and high speed and low load and high speed, respectively. Features perpendicular to the direction of sliding can be seen for all treatment combinations.

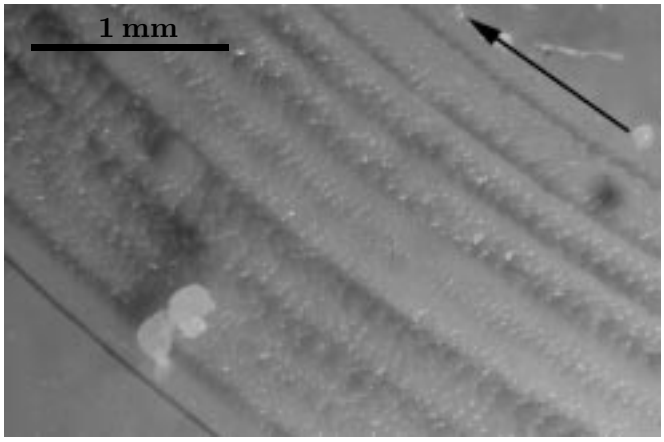

Fig. 4.42 Section of the wear scar of a EXS 5/15 specimen sample following $\simeq$ 62,500 brush strokes under low load and low speed. The direction of sliding is indicated by the arrow.

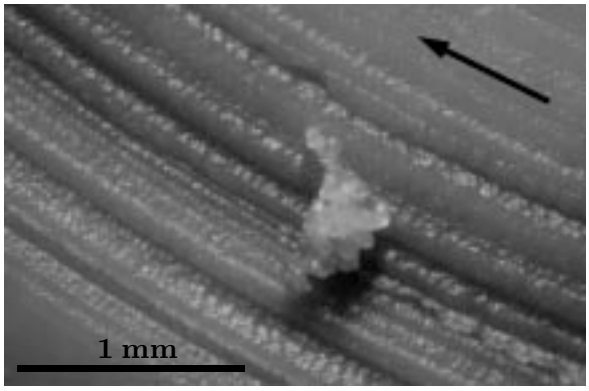

Fig. 4.43 Section of the wear scar of a EXS 10/10 specimen sample following $\simeq$ 181,000 brush strokes under low load and low speed. The arrow indicates the sliding direction.

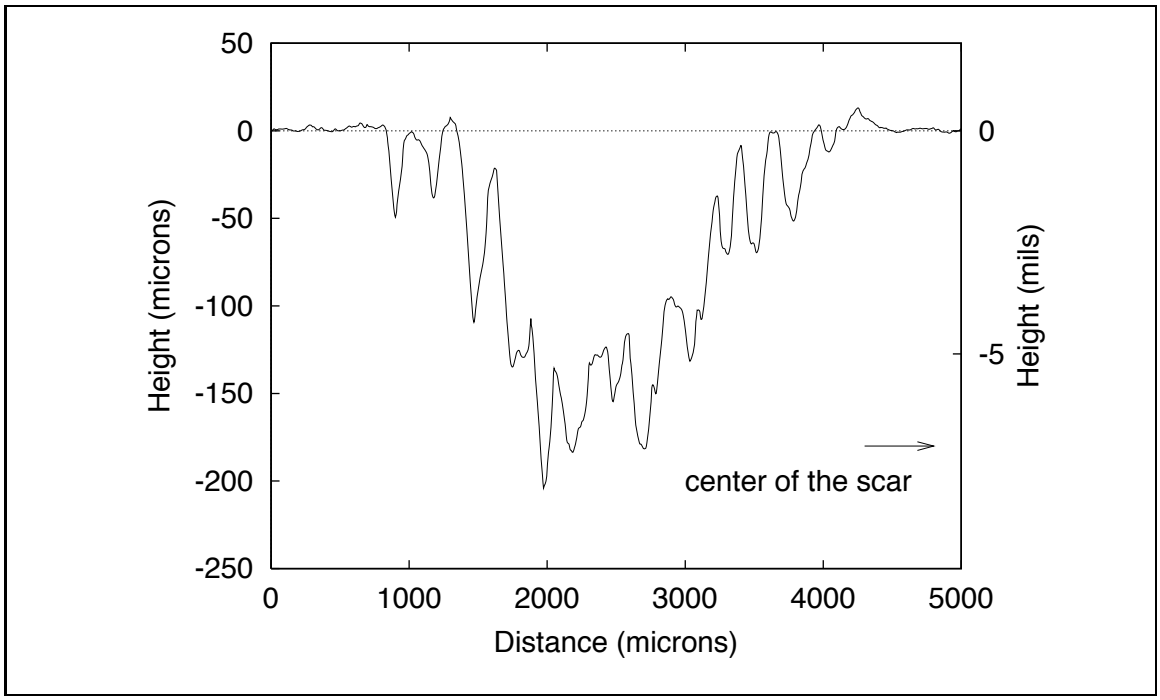

Fig. 4.44 Surface profile of a EXS sample. The scanning direction is perpendicular to the direction of sliding.

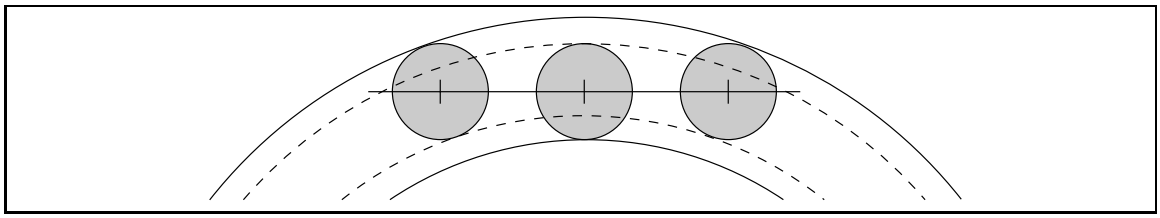

Fig. 4.45 Path followed by three brush tufts aligned with each other.

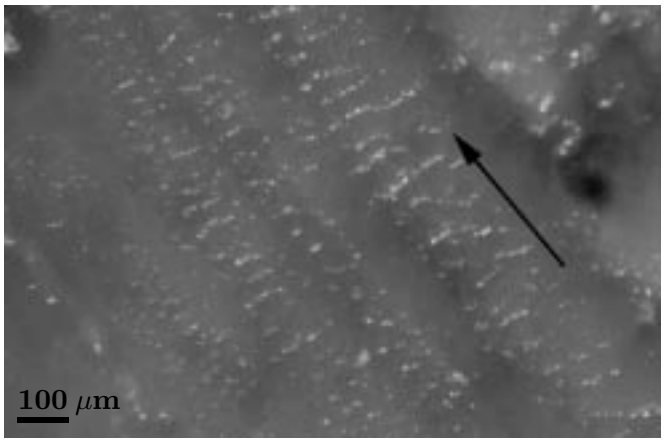

(a)

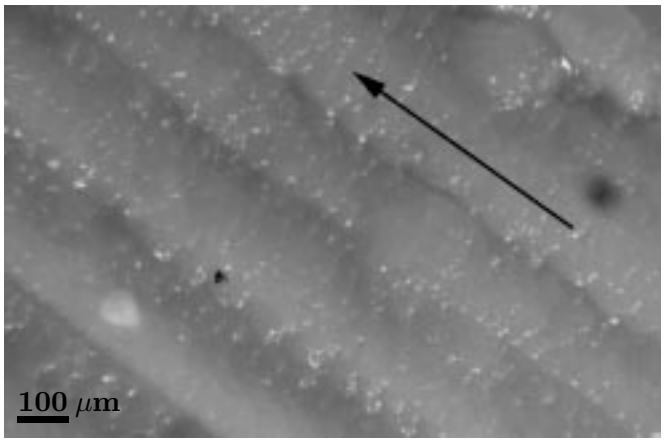

(b)

Fig. 4.46 Section of the wear scar for a EXS 5/15 specimen sample (a) following $\simeq$ 26,000 brush strokes under high load and high speed, and (b) following $\simeq$ 191,000 brush strokes under low load and high speed. The sliding direction is shown by the arrows.

They are not very regular. It is not known if they are transverse ridges due to abrasion or simply features inherent to the texture of the EXS samples.

Debris Wear debris, which are formed instantaneously, do not stick to the wear scar and tend to be evacuated fairly rapidly to the edges of the wear scar as seen on figures 4.42, 4.47 or 4.48. Figure 4.48 shows individual wear debris whereas figure 4.47 illustrates debris clusters which can be formed.

Brushes Figure 4.49 pictures the brushes at the end of a load-speed test conducted on the second replicate of the EXS samples, EXS 5/15. It can be seen that debris gather

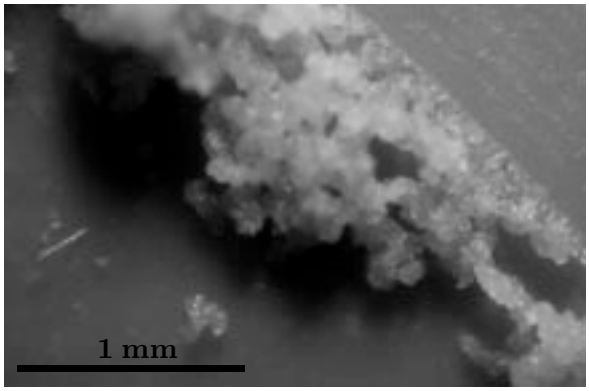

Fig. 4.47 Clusters of wear debris accumulated near the outer edge of the wear scar of a EXS 10/10 specimen sample following $\simeq$ 181,000 brush strokes under low load and low speed.

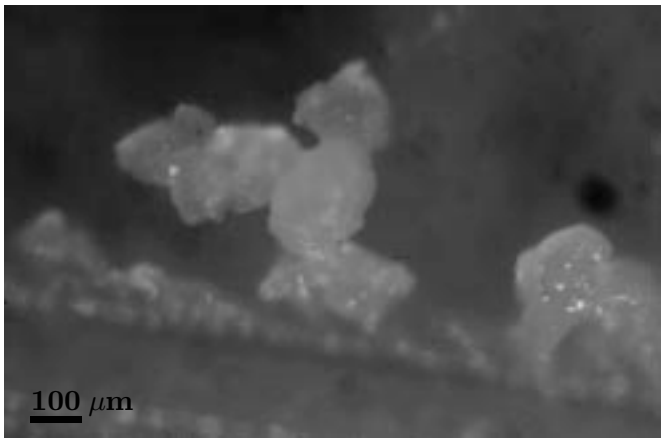

Fig. 4.48 Wear debris located near the outer edge of the wear scar of a EXS 5/15 specimen sample under low load and low speed.

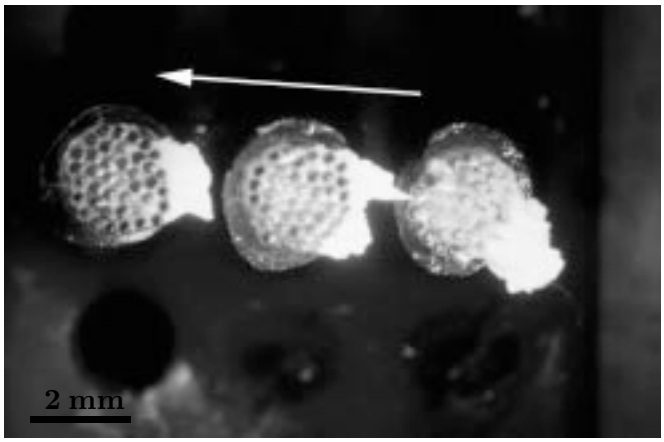

Fig. 4.49 Tips of the brushes after $\simeq$ 191,000 brush strokes on a EXS 5/15 specimen sample under high load and high speed, showing wear debris accumulation near the trailing edge of the brush tufts. The direction of sliding is indicated by the arrow.

in clusters at the trailing edge of each brush tuft. Under high load, as more wear debris are generated, more debris accumulate between the bristles of the brushes as seen on figure 4.50 (b) and (c). In this case, the average wear particle is large and no longer appears as a cluster of smaller particles. This is in contrast with low load tests where open gaps between the bristles, as seen on figure 4.50 (a), can be observed. However, in any case, even when debris accumulation is heavy, the tips of the brush bristles are not covered up with transfered material (figure 4.50 (b)). Exception is seen when some bristles are slightly shorter as in figure 4.50 (c).

4.4.3 Silgan® J-501 samples

Figure 4.51 illustrates a section of the wear scar of a EXS 5/15 sample after 62,500 brush strokes under high load and low speed. It shows that once the brushes removed most of the top coat, they were in contact with the bond coat which has better wear resistance than the top coat. The damage which occurs is limited and is in the form of concentric scratches. After multiple brush strokes, patches of the anti-corrosion epoxy layer can be seen as shown on figure 4.51.

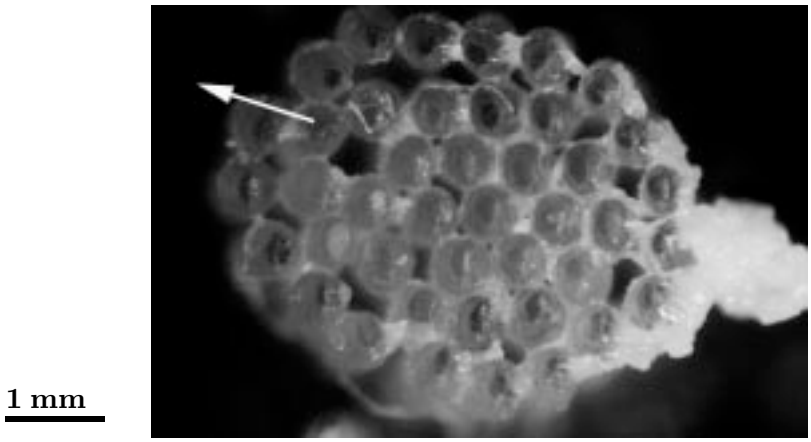

(a) Low load

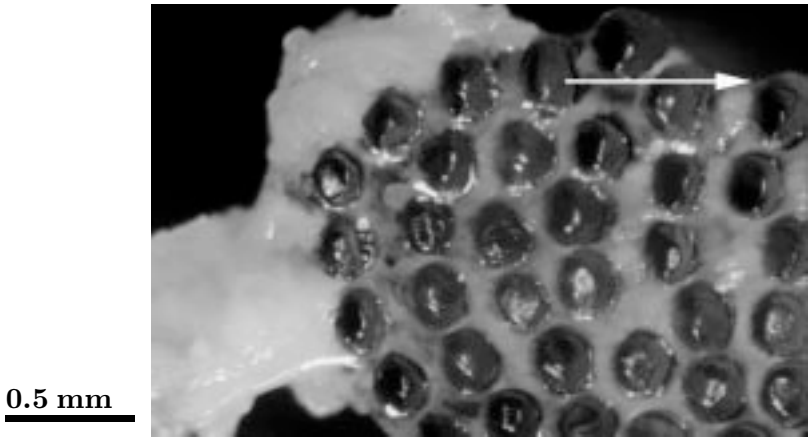

(b) High load

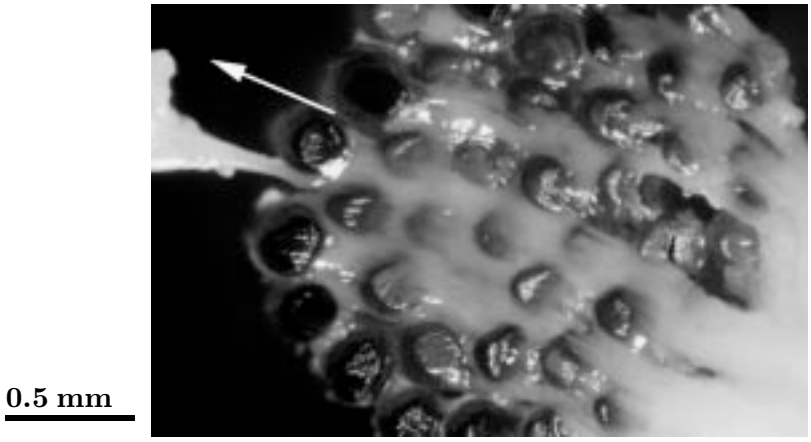

(c) High load

Fig. 4.50 Brushes after $\simeq$ 191,000 brush strokes on a EXS 5/15 specimen sample under high speed, showing (a) little wear debris accumulation between the brush bristles and at the trailing edge of the tuft, (b) heavy debris accumulation between the brush bristles and at the trailing edge of the tuft, and (c) bristles covered with debris. The arrows indicate the sliding direction.

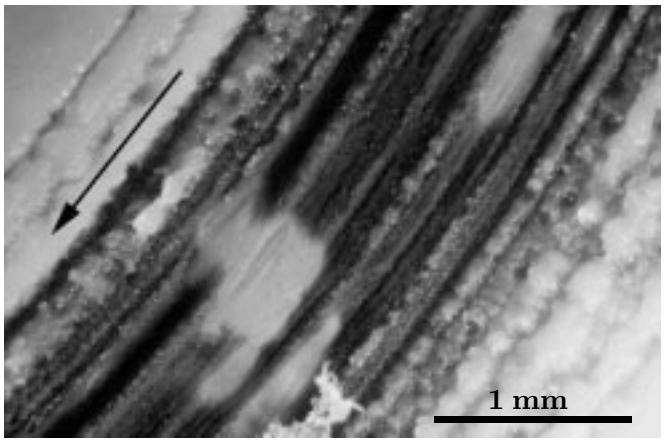

Fig. 4.51 Section of the wear scar of the EXS 5/15 specimen sample following $\simeq$ 62,500 brush strokes under high load and low speed. The sliding direction is shown by the arrow.

4.5 Voltage measurement

The voltage input in the electric motor was monitored in order to measure the load increase on the motor as a result of changes in the contact.

Figure 4.52 shows the voltage obtained under low and high speed with no load on the motor. It can be seen that the initial voltages are high and decrease to a steady-state value after approximately 1 hour for the high speed test and 1/2 hour for the low speed test. This decrease of the initial voltages was attributed to the resistance imposed as the motor is started, such as viscous forces in the gear box. In consequence, the motor was systematically warmed up for an hour prior to the start of a test, regardless of the speed. Between test phases, voltages were recorded under no load in order to provide a baseline to the voltage data.

Figure 4.53 represents typical curves of the voltage as a function of time for the low and high speed tests conducted on a EXS sample. The difference observed in the duration of the tests is linked to the fixed number of brush strokes per test, hence increasing the duration of a test for a low speed case.

Transition between phases can be seen by the large drop in the voltage for approximately 5 minutes at regular intervals. This provides a baseline from which the data can be substracted to obtain the increase in voltage due solely to the contact between the brushes and the sample. It can be seen that the increase in voltage is approximately the same inder

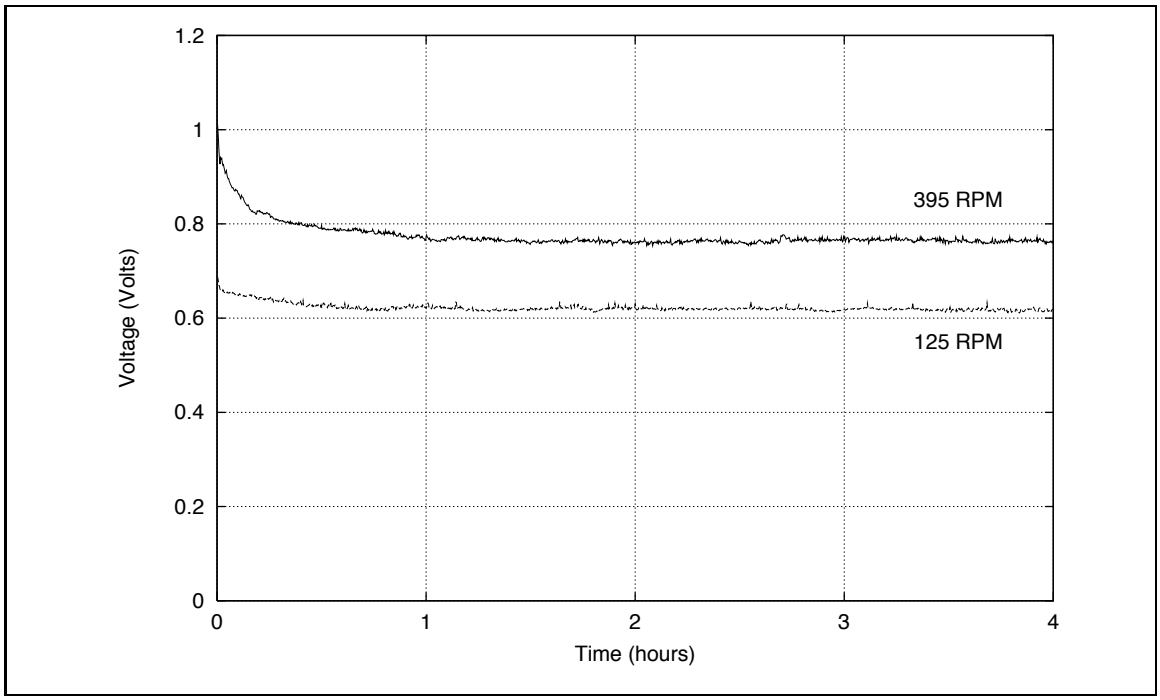

Fig. 4.52 Baselines for the motor operating at low and high speeds

low or high speed. This is expected as all other contact conditions are assumed similar. Even though the motor was turn on prior to the start of the test, a decrease of the initial voltage value is seen. This could be explained by the increase of the load on the motor as the brushes come into contact with the sample.

Figure 4.54 plots the voltage as a function of time for tests conducted under high speed and varying load. It can be seen that voltages are higher when the load is increased in the initial period of the phases. However, the voltages tend to decrease to values closer to that obtained under low load conditions. This phenomenum remains unexplained. If indeed the voltage provide a measure of the level of friction, then the friction would be decreasing towards a steady-state value as the test is conducted.

Finally, figure 4.55 represents the voltage curves obtained under low load and high speed for a NRL and a EXS sample. At first approximation, the voltages measured are slightly higher for the EXS sample than for the NRL sample. However, the difference observed might be due to external factors. For example, the level of water in the testing container could have an impact on the voltage.

In the three former plots, the irregular features which can be seen in the curves are unexplained at this time. Further calibration and analysis, including a Fourier Transform

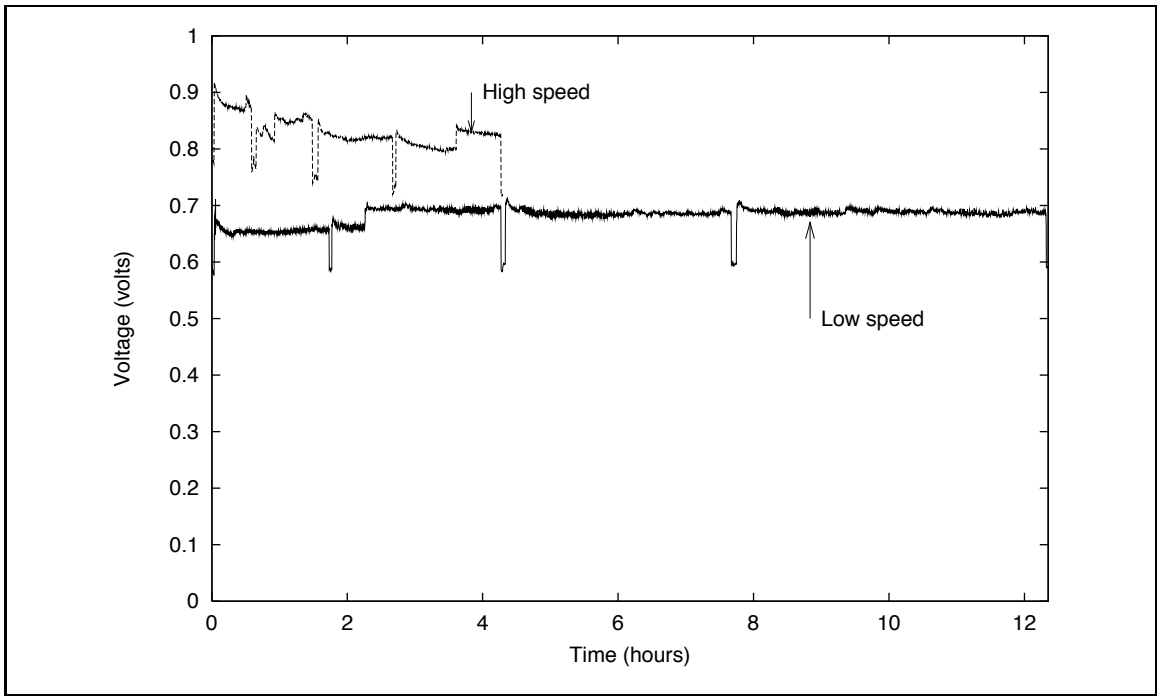

Fig. 4.53 Voltage versus time under low load and variable speed for a EXS sample

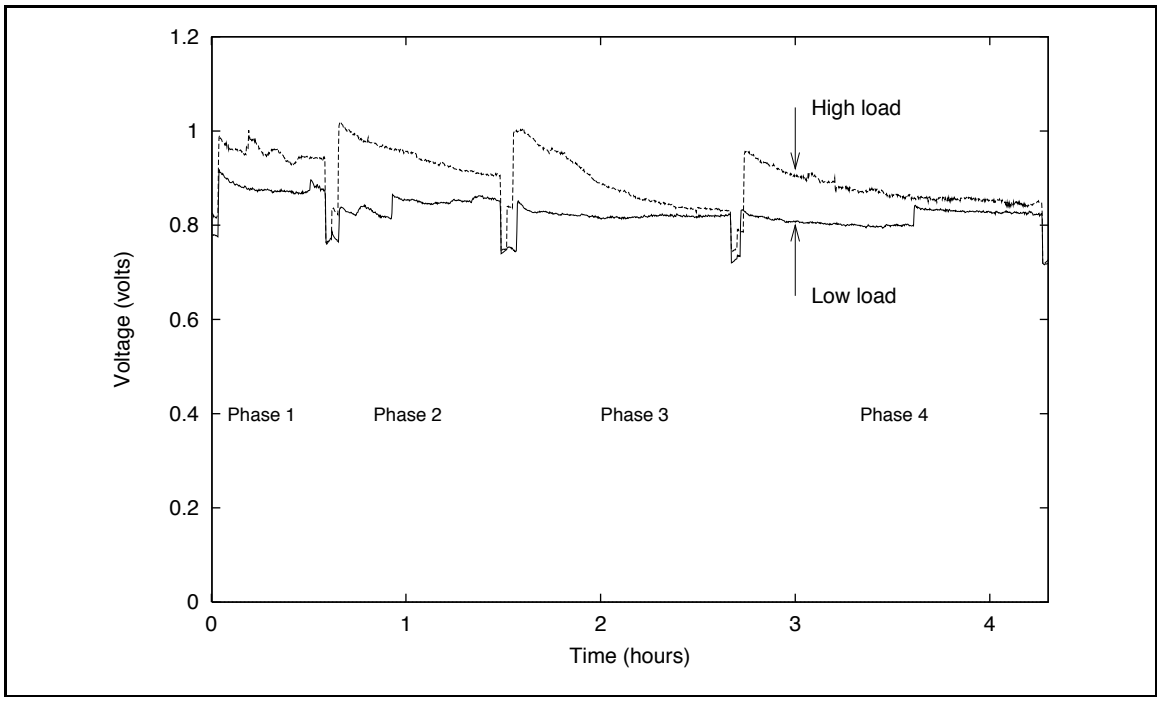

Fig. 4.54 Voltage versus time under high speed and variable load for a EXS sample

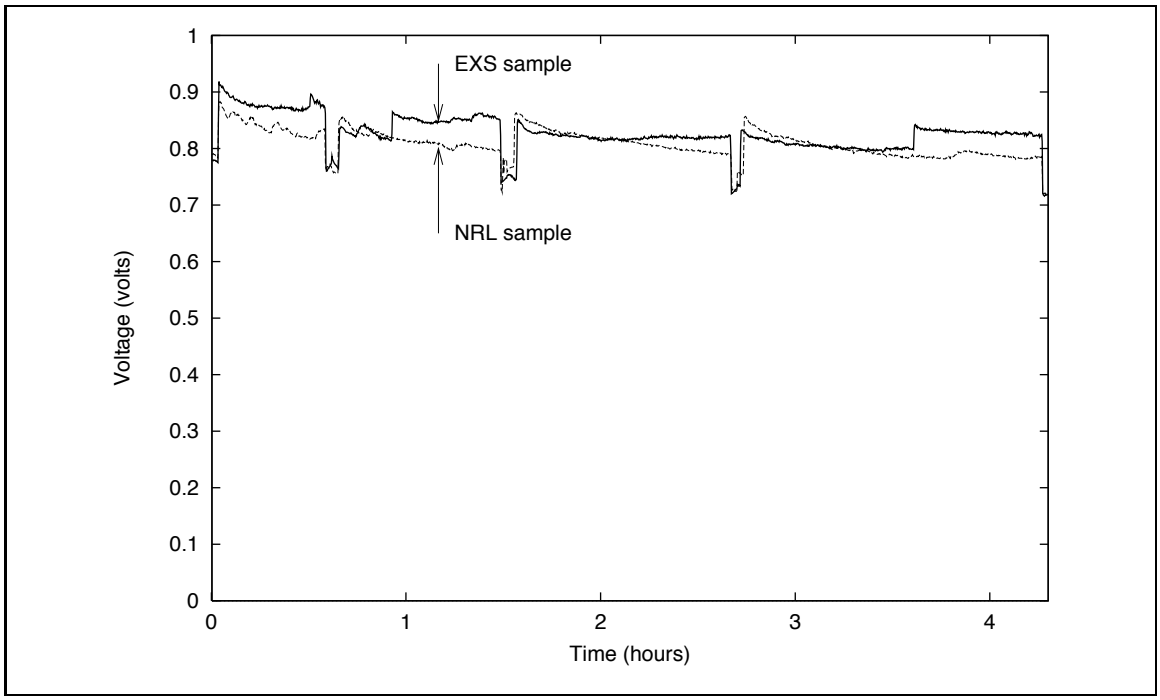

Fig. 4.55 Voltage versus time under low load and high speed for EXS and NRL samples

analysis, are necessary to correlate this data to the torque of the motor.

Chapter 5

Discussion

5.1 Results

Identifying the variables which affect wear as well as understanding their effects can contribute to better wear control.

5.1.1 Effects of operational variables

Operational variables such as sliding speed, applied load, temperature, test duration (sliding distance) or environmental conditions are very frequently significant to the wear process.

One of the objectives of the experimental work is to characterize the effects of two operational parameters, namely the sliding speed and the applied load. Other operational parameters whose effects may also be significant to the wear behavior of the present coatings are the the duration of the test, the stiffness of the brushes and the nature of the environment in which the tests are conducted, i.e. its chemical composition and its temperature.

Effects of the combinations of the levels of sliding speed and applied load on the wear rates for the NRL and the EXS samples are listed in tables 5.1 and 5.2. Regression data and average data are also included.

Effect of sliding speed

In the case of the NRL samples, the initial wear rates are dependent upon the sliding speed of the brushes and that for both levels of applied load. An increased sliding speed resulted in a decreased wear area.

Table 5.1 Wear rates (mil^2/100 brush strokes) per test phase for NRL samples for combined low and high levels of applied load and sliding speed. The data for two replicates as well as their mean are listed. The results of a linear regression analysis, the slope of the regression line, β_1 and the regression coefficient, R^2, are included as well.

	Low load		**High load**	
	Low speed	**High speed**	**Low speed**	**High speed**
Phase 1				
Rep. 1	1.11 ± 0.07	0.28 ± 0.04	3.74 ± 0.13	1.42 ± 0.07
Rep. 2	0.45 ± 0.05	0.26 ± 0.05	3.96 ± 0.14	3.49 ± 0.13
Mean	0.78 ± 0.07	0.27 ± 0.04	3.85 ± 0.14	2.46 ± 0.13
Phase 2				
Rep. 1	0.53 ± 0.06	0.28 ± 0.04	0.30 ± 0.10	0.76 ± 0.07
Rep. 2	0.56 ± 0.05	0.20 ± 0.03	n/a	n/a
Mean	0.54 ± 0.06	0.24 ± 0.04	n/a	n/a
Phase 3				
Rep. 1	0.54 ± 0.06	0.31 ± 0.03	0.04 ± 0.07	0.42 ± 0.06
Rep. 2	0.72 ± 0.05	0.24 ± 0.03	n/a	n/a
Mean	0.63 ± 0.06	0.27 ± 0.04	n/a	n/a
Phase 4				
Rep. 1	0.24 ± 0.05	0.31 ± 0.03	0.07 ± 0.06	0.31 ± 0.26
Rep. 2	0.61 ± 0.05	0.18 ± 0.03	n/a	n/a
Mean	0.42 ± 0.05	0.24 ± 0.03	n/a	n/a
Average for overall test (4 phases)				
Rep. 1	0.60	0.30	1.04[a]	0.73[a]
Rep. 2	0.58	0.22	n/a	n/a
Mean	0.59	0.26	n/a	n/a
Regression analysis: Steady-state wear rate				
Rep. 1 - β_1	0.53	0.30	n/a[a,b]	0.44[c]
- R^2	0.99	0.99	n/a	0.96
Rep. 2 - β_1	0.64	0.20	3.07	n/a
- R^2	0.99	0.99	1.00[d]	n/a
Rate tests				
NRL 15/5 - β_1	1.16		NRL 5/15 - β_1	n/a
- R^2	0.99		- R^2	n/a
NRL 10/10 - β_1	0.74		NRL 0/20 - β_1	0.005
- R^2	0.99		- R^2	0.72

[a]The bond coat was partially or totally visible during the test. The average data are not representative of the top coat only.

[b]Data are representative of Silgan® J-501 coat such that $\beta_1 = 0.11$ and $R^2 = 0.84$.

[c]Data for phase 2 are representative of top coat. $\beta_1 \approx 0.76$

[d]Two data points were used to calculate regression parameters.

Table 5.2 Wear rates (mil^2/100 brush strokes) per test phase for EXS samples for combined low and high levels of applied load and sliding speed. The data for two replicates as well as their mean are listed. The results of a linear regression analysis, the slope of the regression line, β_1 and the regression coefficient, R^2, are included as well.

	Low load		**High load**	
	Low speed	**High speed**	**Low speed**	**High speed**
Phase 1				
Rep. 1	0.09 ± 0.04	0.11 ± 0.04	0.20 ± 0.05	0.29 ± 0.05
Rep. 2	0.24 ± 0.05	0.30 ± 0.05	0.51 ± 0.05	0.45 ± 0.05
Mean	0.17 ± 0.05	0.20 ± 0.05	0.35 ± 0.05	0.37 ± 0.05
Phase 2				
Rep. 1	0.04 ± 0.03	0.06 ± 0.03	0.13 ± 0.03	0.31 ± 0.04
Rep. 2	0.12 ± 0.03	0.12 ± 0.03	0.45 ± 0.05	0.20 ± 0.04
Mean	0.08 ± 0.03	0.09 ± 0.03	0.29 ± 0.04	0.26 ± 0.04
Phase 3				
Rep. 1	0.02 ± 0.03	0.04 ± 0.02	0.12 ± 0.03	0.37 ± 0.04
Rep. 2	0.10 ± 0.03	0.12 ± 0.03	0.33 ± 0.04	0.18 ± 0.03
Mean	0.06 ± 0.03	0.08 ± 0.03	0.22 ± 0.04	0.27 ± 0.04
Phase 4				
Rep. 1	0.04 ± 0.02	0.07 ± 0.02	0.12 ± 0.02	0.32 ± 0.04
Rep. 2	0.12 ± 0.02	0.10 ± 0.02	0.19 ± 0.04	0.18 ± 0.03
Mean	0.08 ± 0.02	0.08 ± 0.02	0.15 ± 0.04	0.25 ± 0.04
Average for overall test (4 phases)				
Rep. 1	0.05	0.07	0.14	0.32
Rep. 2	0.14	0.16	0.37[a]	0.25
Mean	0.10	0.11	0.26	0.29
Regression analysis: Steady-state wear rate				
Rep. 1 - β_1	0.03	0.06	0.12	0.34
- R^2	0.97	0.99	0.99	0.99
Rep. 2 - β_1	0.11	0.11	0.29[a,b]	0.18
- R^2	0.99	0.99	0.96	0.99

Rate tests			
EXS 5/15 - β_1	0.76	EXS 15/5 - β_1	0.20
- R^2	0.99	- R^2	0.99
EXS 10/10 - β_1	0.14	EXS 20/0 - β_1	0.01
- R^2	0.98	- R^2	0.94

[a]The bond coat was partially visible during the last test phase, reducing the wear rate. The average data are not representative of only the top coat.

[b]Low R^2 due to bond coat influence – when last data point is removed from regression analysis, $\beta_1 = 0.44$.

In the case of the EXS samples, there is insufficient evidence that the initial wear rates are dependent on the sliding speed. Changes in the wear data upon increase of the sliding speed were below the measurement error, hence prohibiting any conclusions to be stated. Due to the variability observed in the top layer for EXS samples, additional tests should be conducted with enhanced accuracy.

The dependence of the wear area upon the sliding speed for the NRL samples is discussed in the following paragraphs. Several hypotheses explaining the effect of sliding speed on wear rate can be formulated. Understanding this phenomena may lead to an explanation of the lack of a similar relationship between the wear data and sliding speed for the EXS samples.

Hypothesis 1: Hydrodynamic lubrication All tests are conducted under flooded conditions. In this situation, hydrodynamic lubrication, also called fluid film lubrication, plays a significant role. Under this lubrication regime, the contact is governed by the bulk physical properties of the lubricant. Friction arises purely from shearing of the "viscous" lubricant and no contact occurs between the relatively moving solids. Several empirical models based on the Reynolds theory express the thickness of the fluid film, h_0, as a function of the relative velocity and the applied load with increasing levels of complexity. The simplest model, the classical theory model is

$$\frac{h_0}{R} = 4.9 \left(\frac{\nu U}{W} \right), \tag{5.1}$$

where W is the applied load per unit length, R is the effective radius of curvature, ν is the lubricant viscosity, and U is the average relative velocity.

As the sliding speed increases, the thickness of the fluid film increases proportionally. It can also be seen that, as the applied load increases, the thickness of the fluid film decreases to the point where its magnitude becomes of the order of magnitude of the surface roughness resulting in the loss of perfect lubrication regime since asperities between the two contacting surfaces begin to touch. In a state of ideal hydrodynamic lubrication, no wear is observed.

It is believed that in the present case, the regime might be pseudo-hydrodynamic lubrication. Indeed, the specific conditions required to reach the state of hydrodynamic lubrication are not satisfied. The geometry of the bristles lead to the hypothesis that the occurrence of hydrodynamic lubrication is not likely to be significant. If bending of the bristles is very important such as when the bristles buckle under load, then the contact radius is

greatly increased and the geometry of the contact will be more favorable to hydrodynamic lubrication.

Supplementary testing could be done to study the impact of fluid film lubrication, if any.

Hypothesis 2: Friction, bristle bending and debris entrapment Entrapment of debris within the brush bristles may explain the variation of wear with the sliding speed. When the bristles bend, then debris can accumulate between the bristles filling open space. As debris accumulates, the contact is altered. The area of contact may increase, leading to the decrease of the contact stresses and subsequent reduction in wear. Therefore, the reduction in wear upon increase the sliding speed for the NRL samples could be attributed to increased bending of the bristles when the speed is higher as a result of increased friction force. However, upon increase of sliding speed, it is generally expected that friction would decrease. Therefore, an alternate discussion relating the extent of bristle bending to the variation of wear with the sliding speed is proposed.

If the bristles bend, then the debris become trapped between the bristles and the surface area increases. The bristles are still in contact with the coating, resulting in contact of differing materials, i.e. A–B. When the debris stagger in the contact area, as in the case of limited bending, then similar materials are in contact (A–A instead of A–B as shown in figure 5.1). Since the bristle material is harder than the coating material, A–A contact results in reduced wear.

The conclusions of the two previous discussions contradict each other. Additional testing should be conducted to monitor friction in the system and to study the extent of bristle bending.

Hypothesis 3: Temperature softening Softening of the materials in the contact region as a result of frictional heating could be responsible for the decrease in wear. As the sliding velocity increases, the rate of energy dissipation increases accordingly. As a result, formation of hot spots in the contact area results in softening of the material, or melting in the most extreme cases. The contact area subsequently increases and the applied stress decreases. As a consequence, the wear rate decreases. In the case of melting, it has been previously reported that a lubricating effect is provided by the molten material, leading to a reduction

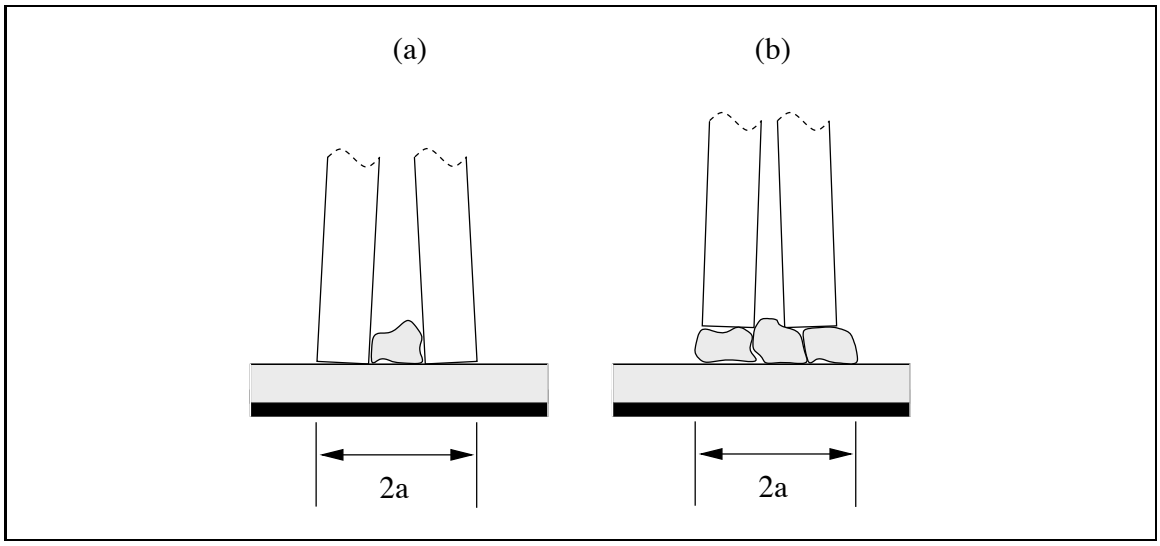

Fig. 5.1 Debris entrapment modes (a) A–B and (b) A–A contact. 2a is the diameter of the apparent contact area.

of friction and/or wear.

However, no trace of melting can be seen at the end of the test either on the track or on the bristles. Therefore, the decrease of wear of NRL samples upon increase of sliding speed is not likely to be due to temperature.

Hypothesis 4: Viscoelasticity Viscoelasticity is one of the most important properties of silicone rubber. The term viscoelasticity is commonly applied to materials which are neither ideal solids nor liquids, but possess characteristics which are typical of both. In the case of the classical theory of elasticity (Hooke's law), the stress is proportional to strain but not to the rate of strain. On the other hand, in the theory of hydrodynamics (Newton's law): the stress is directly proportional to the rate of strain, not to the strain itself.

Friction of elastomers has been related to their viscoelastic properties (Ludema and Tabor, 1966).

Increasing the deformation rate, which is proportional to increasing the speed, leads to an increase in the real modulus, E, as seen in Fig. 5.2. If the contact is assumed Hertzian, then the contact area is proportional to $E^{-\frac{2}{3}}$ (Hertz, 1896). Therefore, an increase of velocity results in a decrease of contact area. In conclusion, for a rubber, increasing the deformation rate reduces the area of contact, increases the strength and subsequently increases the resistance to damage.

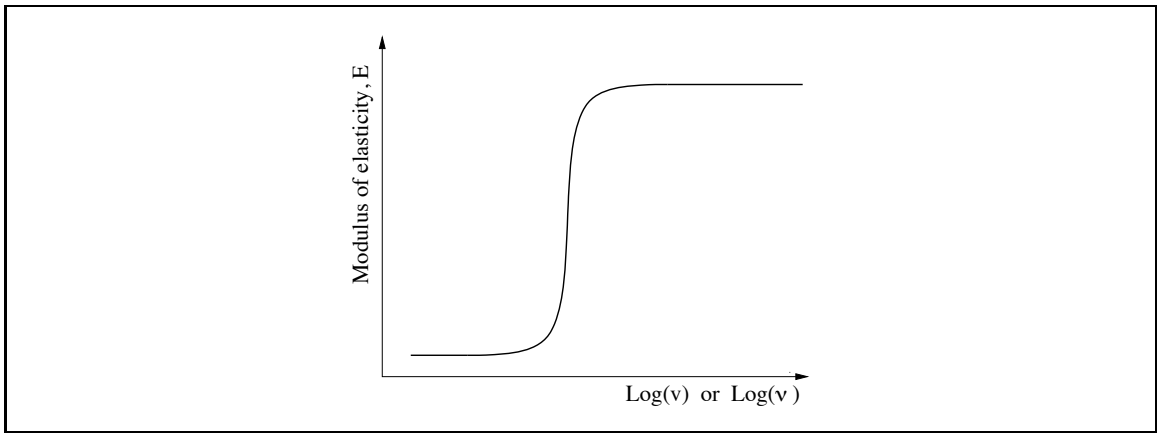

Fig. 5.2 Modulus of elasticity, E, versus the sliding speed, v, or the deformation frequency, ν, for a viscoelastic material

Sliding can be modeled as periodical loading and unloading. Ludema and Tabor (1966) assumed that the frequency of loading is equal to the ratio of the indenter velocity to the indenter diameter, i.e. equivalent to the time taken for the slider to traverse its own circle of contact. The rate of deformation is equivalent to the rate at which energy is stored and dissipated (Briscoe) and might match a specific frequency such as the natural or resonant frequency. The natural frequency of vibration of rubber is such that the total external mass exceeds the sample mass.

DMA analysis was conducted on the two samples series as a mean to identify relevant frequencies as well as to provide a comparison between the two groups of samples. DSC analysis was conducted in parallel in order to characterize significant transition temperatures such as the temperature of the glass transition. DMA and DSC results are presented in Appendix E. All samples (NRL, EXS, Silgan® J-501 and RTV11) exhibit a glass transition in the following temperature range: -50 to -40 °C. DMA analysis revealed no significant difference between the EXS and the NRL samples. The plot of the loss tangent as a function of temperature can be translated into a plot of the loss tangent versus the frequency when the Ferry transform applies (Ferry, 1961). Such a trace can be used in correlation with the frequency of vibrations measured in the material as the result of sliding of multiple indenters. Additional work is needed to further validate this promising method: a DMA trace could help predict the durability of an elastomeric coating when subjected to repetitive indentations by cleaning brushes or pulsating water jets. This would provide a controlled, standard and accelerated laboratory test. If the frequency of indentation is revealed as

Table 5.3 Apparent areas and corresponding contact stresses

	Original	Design #1	Design #2
Apparent area (mm^2)	75.3	30.1	15.1
Real contact area (mm^2)	37.6	15.1	7.5
Applied load (g)			
10 psi	263.5	105.4	52.7
50 psi	1317.7	527.1	263.5
Contact stresses (psi)			
100 g			18.9
300 g			56.7

being a significant variable then, modification of the bristle diameter, number of bristles per tuft, number of tufts per brush in conjunction with the sliding speed could help adjust and modify the wear behavior.

In conclusion, the speed effect has been studied and was shown to modify the wear behavior of the NRL samples. Further testing is needed to better further validate the hypotheses stated.

Effect of the applied load

The effects of a second operational parameter were studied for NRL and EXS samples. The applied load was varied by a factor of 3, i.e. from 100 g to 300 g. The effect of increasing the applied load was to increase the wear area for both NRL and EXS samples.

The applied load was selected based on similar tests conducted at SUNY-Buffalo. There, the static pressure was calculated using an estimated value of the real contact area.

Apparent area calculation and associated contact stresses Nominal contact stresses reported by SUNY-Buffalo were calculated assuming that the real area of contact is equal to half the apparent area of contact. A brush with N_b bristles can be modeled as an idealized rough surface with N_b spherical asperities of radius R_b, such that the apparent area, $A_{apparent}$, is

$$A_{apparent} = N_b \times \pi R_b^2. \tag{5.2}$$

Using the brush characteristics compiled in table 3.6 (page 58), the apparent and assumed real areas of the brushes are calculated. They are listed in table 5.3. The applied

loads associated with 10 psi and 50 psi contact stresses as well as contact stresses calculated for 100 g and 300 g dead weights are listed. For a brush with design #2, the maximum contact stresses are respectively 18.9 and 56.6 psi when the brushes are loaded with 100 g and 300 g dead weights.

True contact stresses (Hertzian theory) The true contact stresses can be better estimated using the Hertzian theory (Hertz, 1896), which predicts the real contact area as a function of the elastic modulus, E, Poisson's ratio, ν, the effective radius, R, and the applied load, W.

The modulus of elasticity of the nylon bristles has been experimentally determined elsewhere (Appendix F) and is assumed equal to 1.158 GPa. The Poisson's ratio is assumed equal to 0.4. The bristles are cylindrical with a 290 ± 5 μm diameter. The tips of the bristles are rounded off by the manufacturer. The surface indented by the bristles are RTV11 and Silgan® J-501. Their respective effective modulus of elasticity are 3 MPa and 23 MPa. They are assumed ideally flat ($R_{(2)} = \infty$). The effective radius, R' and the effective contact modulus, E', can be calculated according to

$$\frac{1}{E'} = \frac{(1-\nu_{(1)}^2)}{E_{(1)}} + \frac{(1-\nu_{(2)}^2)}{E_{(2)}}, \qquad \text{and}$$

$$\frac{1}{R'} = \frac{1}{R_{(1)}} + \frac{1}{R_{(2)}}.$$

In this study, E'_{RTV11} and $E'_{\text{J-501}}$ are respectively equal to 2.9935 MPa and 22.6226 MPa while R' is equal to the radius of the tip of the bristle, $R_{(1)}$.

The low load applied is 100 g, i.e. 0.98 N. The high applied load is 300 g, i.e. 2.9 N. For a brush of design #2, which has approximately 228 bristles, the low and high values of applied normal load per bristle are, respectively, 4.3×10^{-3} N/bristle and 12.9×10^{-3} N/bristle.

Ideally spherical bristle tips All bristles are idealized as illustrated by schematic A in figure 5.3. The tip of the bristles is spherical, with radius of curvature $R = 145$ μm. The Hertzian equations are utilized to calculate the radius of the contact area, a, the indentation depth, h, and the Hertzian maximum stress, p_o. Results are presented in table 5.4 for RTV11 and Silgan® J-501 under low and high loads.

Table 5.4 Radius of contact area, a, indentation depth, h, and maximum contact stresses, p_o, for ideally spherical bristles tips in contact with surfaces coated with RTV11 and Silgan® J-501

		RTV11		**Silgan® J-501**	
		Low load	High load	Low load	High load
a	(μm)	53.87	77.69	27.45	39.59
	(mil)	2.12	3.06	1.08	1.56
h	(μm)	10.39	22.57	2.6	5.51
	(mil)	0.41	0.89	0.10	0.22
p_o	(MPa)	0.7	1.0	2.7	3.9
	(psi)	106	153	409	590

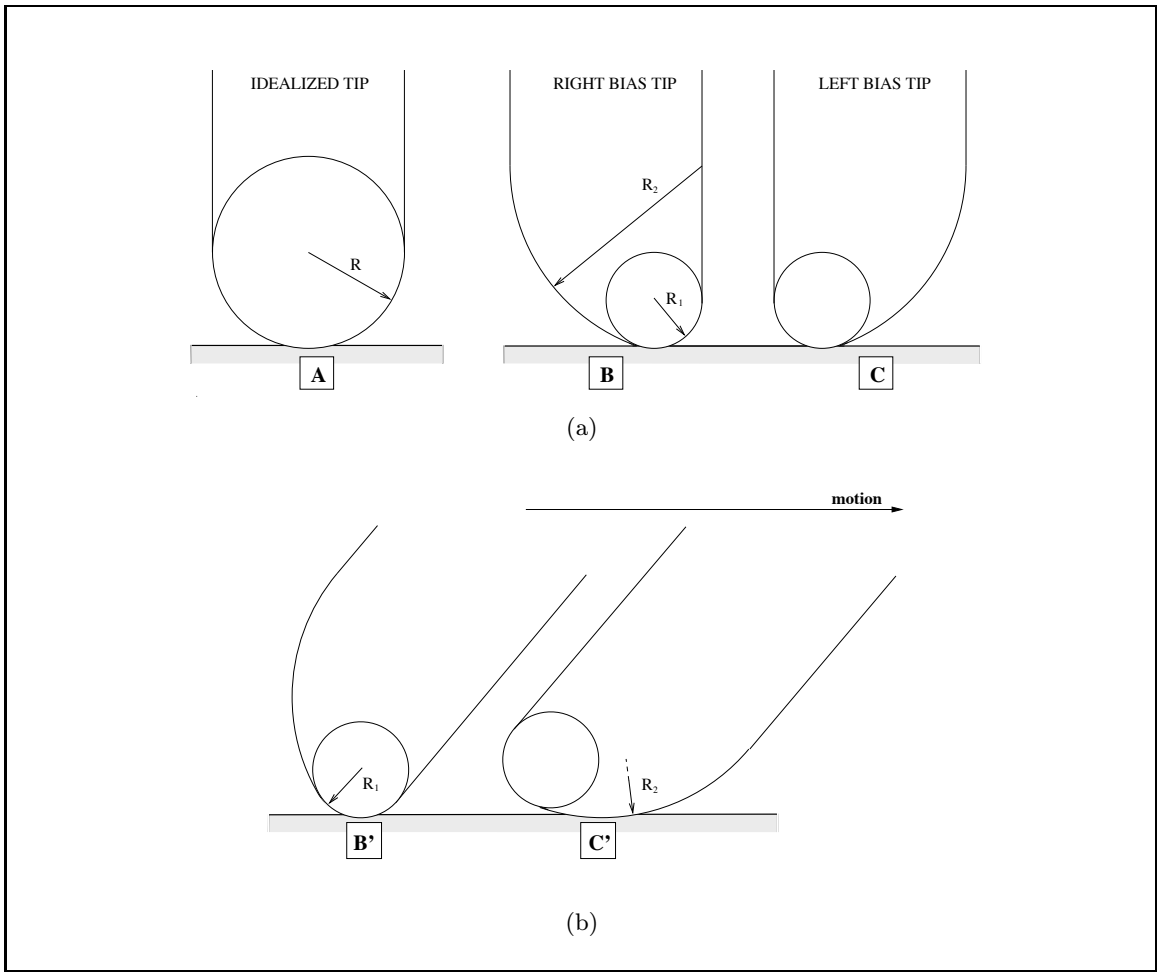

Fig. 5.3 Schematic representations of the brush bristles tips showing three ideal models, under (a) static and (b) sliding conditions.

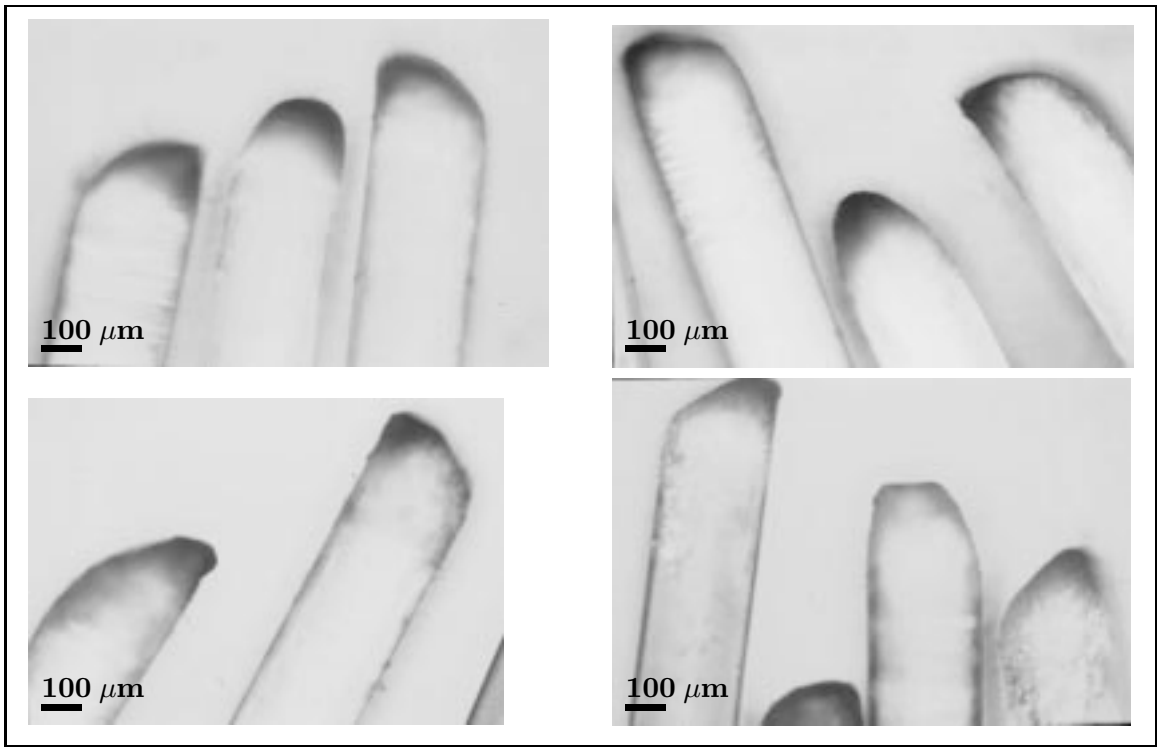

Fig. 5.4 Microscopic pictures of the tips of the bristles.

Irregular bristle tips The ideal case previously discussed underestimates the true contact stresses. As seen on figure 5.4, the shape of tips of the bristles is highly irregular.

In order to obtain a better estimate of the contact stresses, the tips are modeled as illustrated on figure 5.3. Three main groups of tips are identified and labelled types A, B and C. Type A refers to the idealized spherical tip with radius R discussed previously. Tips B and C are similar in shape and are referred to as "bias" tips. Bias tips are composed of two regions, each with a specific radius of curvature, respectively, R_1 and R_2, such that $R_1 \leq R$ and $R_2 \geq R$. The bias tips B and C have been differentiated in terms of their orientation with regards to the direction of sliding. Indeed, when the bristles bend as indicated on the lower schematic in figure 5.3, the region with low radius of curvature will contact the surface for tips of type B whereas the region with high radius of curvature will contact the surface for tips of type C. This situation results in different contact stresses. In order to calculate the contact stresses, a simple model was designed where $R_1 = \frac{1}{2}R$ and $R_2 = 2R$.

It is further assumed that all three types of tips are present at random: a% of tips of type A, b% of tips of type B and c% of tips of type C in any given toothbrush head. The total real contact area, A_r, is equal to the sum of the real contact area for each group of

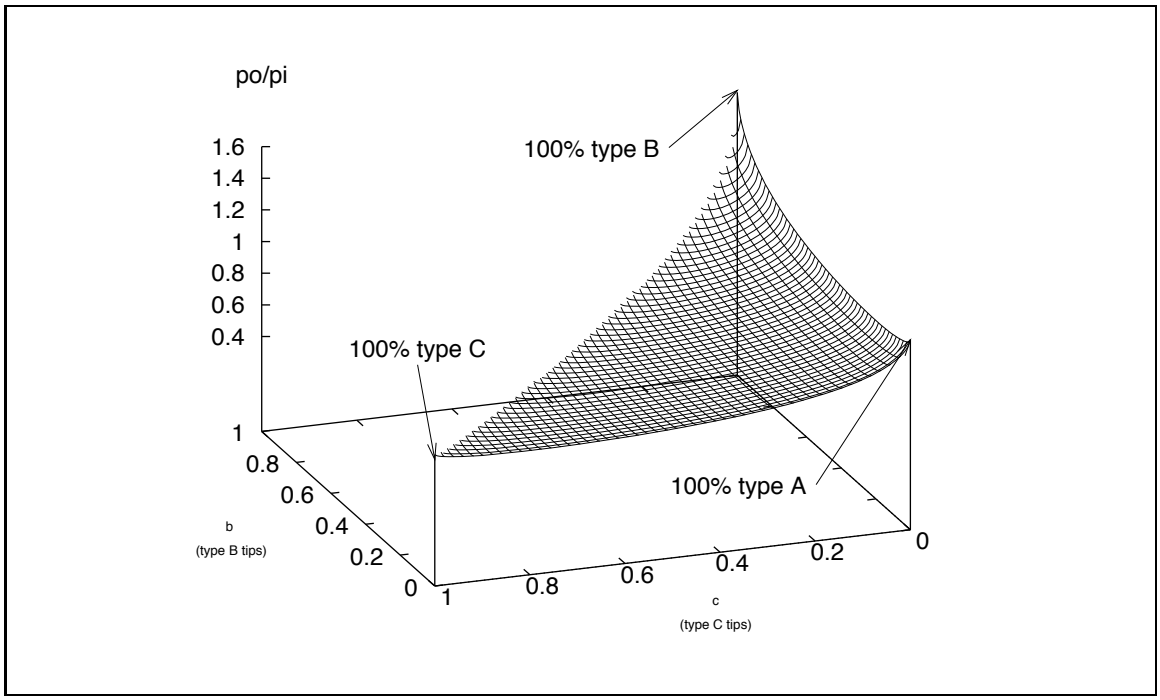

Fig. 5.5 Variation of $p_{\mathrm{o}}/p_{\mathrm{i}}$ as a function of the repartition of bristle tips.

bristles:

$$A_{\mathrm{r}} = A_{\mathrm{r}}^{\mathrm{A}} + A_{\mathrm{r}}^{\mathrm{B}} + A_{\mathrm{r}}^{\mathrm{C}}. \tag{5.3}$$

Using the Hertzian equations, the real area of contact and therefore the maximum contact stress is expressed in terms of the percentage of each type of bristles present in the brush head:

$$p_{\mathrm{o}} = p_i \times \left(\frac{1}{\left(\frac{\mathrm{a}}{100}\right)^{\frac{2}{3}} + \left(\frac{1}{2} * \frac{\mathrm{b}}{100}\right)^{\frac{2}{3}} + \left(2 * \frac{\mathrm{c}}{100}\right)^{\frac{2}{3}}} \right), \tag{5.4}$$

where $a + b + c = 100\%$. p_i is such that

$$p_i = \frac{1}{\pi} \left(\frac{6E'^2 W_{\mathrm{t}}}{R^2} \right)^{\frac{1}{3}}. \tag{5.5}$$

A surface plot of the ratio of p_{o} over p_i can be seen in figure 5.5. As expected, the contact stresses are the highest when all the bristles of the brush head are of type B. In this case, $p_{\mathrm{o}}/p_i = 2^{\frac{2}{3}} = 1.6$. When all the bristles are of type A, then $p_{\mathrm{o}}/p_i = 1$ and when all the bristles are of type C, $p_{\mathrm{o}}/p_i = (\frac{1}{2})^{\frac{2}{3}} = 0.63$.

If bristles of type B are present, then automatically bristles of type C will be observed as well. Unless the bristles do not bend at all, bristles of type C will reduce the contact

Table 5.5 Maximum contact stresses, p_o (psi), for RTV11 and Silgan® J-501 for various brush compositions under low and high load conditions

	RTV11		**Silgan® J-501**	
	Low load	High load	Low load	High load
100% type A	106	153	409	590
100% type B	168	243	649	936
100% type C	67	94	258	372
75% B & 25% C	89	133	356	513

stresses. 100% of bristles type C is not realistic. Using figure 5.5 and speculating on the relative proportions of each type of bristles, one may obtain an estimate of the level of contact stresses. Table 5.5 summarizes contact stresses obtained for various typical proportions of tips types in the case of RTV11 and Silgan® J-501.

The analysis is based on the assumptions that the indenter does not deform, that the regime of deformation is elastic at all times, that the contact area is the same under static or sliding conditions and that the brush bristles bend only slightly under the levels of applied loads (i.e. do not buckle). Within these assumptions, the analysis shows that simple variations in the shape of the bristle tips may lead to an increase or decrease in contact stresses. It is important to note that tips with irregularities, such as flat tips or pointy tips, were neglected in the calculation. This is far from being realistic since, if only one bristle has a very sharp tip, very high localized contact stresses will result and potentially lead to failure and formation of wear debris under the action of successive multiple indentations.

This is a complex problem. Indeed, the formation of wear debris which accumulate in the contact region will also contribute to either lower or higher contact stresses depending on their nature.

Effect of sliding distance The total sliding distance was kept constant. Data were collected at intermediate sliding distances. These data show that the wear volume varies linearly with sliding distance except for phase #1. This difference has been attributed to transient wear when the brushes and the surface are not aligned.

Effect of temperature and effect of the environment

The effect of temperature was not expected to be significant. No noticeable temperature rise was observed in the water during the tests.

The tests were conducted in salt water (500 ml) originally at room temperature. The mixing of the water by the rotating brushes was expected to result in a sufficiently high heat transfer coefficient to have prevented a significant difference between the temperature of the sample and the temperature of the water. Since the samples were thin, it was assumed that the temperature within the samples was approximately uniform. Thus, it can be concluded that if no significant temperature rise occurred in the water then there was likewise no significant temperature rise in the sample.

However, if abrasion of the elastomeric coatings is proven to be related to the viscoelastic nature of the materials, like friction (Briscoe, 1980; Ludema and Tabor, 1966), then all the information can be gained from simpler experiments at constant velocity and varying temperature by applying the Ferry transform (Ferry, 1961).

The effect of the environment can not be easily assessed since all the tests were conducted under similar conditions. Furthermore, blade tests conducted at the Naval Research Laboratories conducted in variable environments (air, water and silicone oil) showed that the failure mode was not dependent on the nature of the test liquid.

Effect of the brush stiffness

The stiffness of a brush affects its potential to splay, and subsequently its cleaning ability. Stiffness is related to design characteristics of the brushes as well as mechanical properties of the bristles as expressed in the mathematical model developed by Rawls et al. (1990). The stiffnesses of the brushes used in this study were calculated with this model. Results are included in Appendix G.

Derivation of the force from value of stiffness could be correlated to the brushing force. This could help design the desired brush based on the mathematical model by Rawls et al. (1990), and limiting the need of experimental testing of the cleaning ability of new brushes with apparatus such as the ones developed at F.I.T. by Wathen (1994) and Schumacher (1996) which allow a systematic measure of the cleaning ability of disk and cylinder brushes.

The stiffness of the altered brush, design #2, is approximately 17 times higher than that of the original toothbrush head but is half the value obtained for a steel brush with similar construction. This explains the high wear rate obtained in this study. A less stiff, hence less aggressive, brush would be sufficient to remove organisms from the surface and would lead to decrease damage.

However, the width of the wear scar may not exceed 10 mm because of the maximum scan length. This constraint dictated the stiffening of the brushes to limit bending. This resulted in the undesired increase of the stiffness and subsequent dramatic increase in wear volume.

This decreased the potential to apply the results of the accelerated tests to a real situation. However, the methodology is still valid since preliminary tests showed that the wear mode is the same with softer brushes as it is for stiffer brushes. The methodology was also proven satisfactory for comparing coatings as well as for studying tribological behavior under the action of multiple contacts.

Effect of friction

Current supplied to the motor was monitored in an effort to determine if changes in the current could be correlated to changes in the friction force. It has been reported that upon formation of wear particles, the friction force would be multiplied by a factor of three. It was suspected that this event could be seen in the current versus time data measured as the surface deteriorated. However, it was not possible to differentiate between the effects of several phenomena occurring simultaneously. Noise in the data further complicated the matter. A dynamometer suitable for the experimental apparatus was not available to measure the efficiency of the motor. Thus, the results obtained using this technique could not be used to make specific conclusions on the effect of friction.

5.1.2 Effects of coatings characteristics and properties

The coatings hereby under study were processed with a similar method. They are composed of multiple layers of compatible materials, each chosen for a specific purpose. Initial epoxy coats were deposited onto a steel substrate to provide corrosion control. Subsequent coatings were primarily based on silicone rubber. The so-called tie or bond coat is the intermediate layer whose functions are to provide adhesion of the final top coat to the epoxy-covered

substrate as well as to reinforce the soft top layer. The final layer is called the top layer as well as fouling release layer because its principal purpose is to allow easy release of any biological growths. The final layer is the most important in terms of fouling release ability for the coated system whereas the bond coat is the crucial component since it provides an overall more durable system.

The major differences between the two samples series lie within the formulation of the top layer. However, these differences in terms of the chemical compositions are not drastic and the mechanical behavior of the coatings is not expected to be drastically different. This is the investigation carried out in the present study.

Effects of coatings composition

As mentioned above, the only known difference in the chemical formulation of the two groups of samples is the top layer. It is a grey RTV11 silicone rubber in the case of the NRL samples and the Exsil® 2200 silicone rubber in the case of the EXS samples. General information can be found in the patents by Griffith (1995) and Carroll et al. (1997). The exact differences between the two is unknown at this time and further analysis is needed to identify the true nature of these two coatings.

Both formulations are based on silicone rubber technology, and more specifically on polydimethylsiloxane. The major known variant is the nature of the fillers used in the polymeric matrix. Fumed silicas can be found in the EXS samples while calcium carbonate is found in the NRL samples. Fumed silicas have a better reinforcing effect than calcium carbonate (Lynch, 1978). Therefore, it is expected that the fumed silicas filled samples (EXS samples) will have a better wear resistance to mechanical damage than the calcium carbonate filled samples (NRL samples). The results support this statement. Indeed, under the operating conditions selected in the laboratory tests, EXS samples have a enhanced wear resistance compared to that of the NRL samples. One EXS sample exhibited unusual wear behavior which has been attributed to the presence of large air bubbles, probably introduced upon curing.

The top coat of the EXS samples contains miscible oils. Similar samples were studied at SUNY-Buffalo and the results published on the analysis of the test fluid with MAIR-IR showed that traces of hydrocarbons were present in both the EXS and the NRL samples, therefore indicating that oils were present in both samples. Analysis of the test fluid after

the wear tests is necessary to confirm the presence of oil.

Samples only coated with the bond coat Silgan® J-501 were incorporated in the study as controls. Results showed that the wear rates were much smaller than that obtained for the NRL and EXS samples (with top coat).

A semi-circular crack perpendicular to the sliding direction was observed for RTV11 based coatings while decohesion or delamination was the failure mode identified for the Exsil® 2200 coated samples. Kohl et al. (1997) concluded that RTV11 coatings were more durable than the Exsil® 2200 samples.

Similarly to the scratch tests by NRL, the wear resistance of the RTV11 based coatings were higher than that of Exsil® 2200 based coatings, both series being the duplex series. Results showed that the wear resistance of the Silgan® J-501 coatings was less than that of the RTV11 and better than that of the Exsil® 2200 coatings. This result differs from the results of the present study since the Silgan® J-501 coated samples showed better wear resistance than any of the Exsil® 2200- or grey RTV11-coated samples.

Effect of coating thickness

The coatings were available in variable relative thicknesses as described in Chapter 3 for the purpose of evaluating the influence of bond thickness as well as top coat thickness on the wear resistance. Since the thicknesses of the bond and top coats were changed simultaneously, the effect of the thickness of each individual coat is difficult to isolate. Hence, the relative thickness ratio of the top coat to the bond coat rather than absolute thicknesses of the two layers was used for comparison.

The coatings were originally intended to be of equal (bond+top coats) thicknesses, i.e. 20 mils. Due to the difficulty to control shrinkage of the materials upon drying, the total thicknesses of the coatings differ from 20 mils. EXS samples are thinner than the NRL samples. However, the relative thickness ratios for the two sample series are similar (section 4.1).

The indentation tests conducted at the NRL showed that the thicker coatings recover more elastic energy than thinner duplex coatings. Therefore, the thicker coatings should have a better resistance to damage per unit load than thinner coatings.

The thickness of the coating might be relevant at the beginning of the test. Once the coating starts to wear out, its thickness continuously decreases. The wear rate is therefore

averaged out over a range of coating thicknesses and is independent of the thicknesses of the layers.

Scratch tests conducted on RTV11 at the NRL showed that the durability of the coating is dependent on the bond coat thickness and the total thickness for blunt indenters. However, the durability of the coating is not directly proportional to the total thickness directly. In the case of sharp indenters. the failure mode for RTV11 samples was tearing regardless of the bond coat thickness (Kohl et al., 1997). Similar studies conducted at the NSWCCD (Naval Surface Warfare Center, Carderock Division) on identical candidate samples showed no dependence of the durability on the thickness of the bond coat.

These results correlates well with the results of the present study, the bristles being sufficiently sharp indenters not to permit any discriminations amongst coatings with varying coat thicknesses.

5.1.3 Identification of wear behavior

The common and obvious features observed in the wear scars of the two samples series studied were longitudinal scratches. Additional features identified, very clearly in the case of the NRL samples, were the abrasion patterns similar to those described by Schallamach (1952a). Sets of parallel ridges are formed on the surface at right angle to the direction of sliding. Figure 4.33 on page 127 illustrates the abrasion pattern for a NRL sample under high load and high speed. In the case of the Silgan® J-501 coatings, only longitudinal scratches were observed, since the material is too stiff for abrasion patterns to develop.

Typically, the transverse ridges are associated with dry sliding, but Mok and Gorman (1995b) published some results for wet conditions as well. Under wet conditions, they observed that the spacing of the ridges increases as the test conditions change from constant to altered within the course of the same test. The purpose of conducting tests under varying conditions was evidently to try to better simulate actual service conditions. In the present experiments, the test conditions were not changed during the tests. As described in section 4.4, the spacing between the ridges is approximately 90 – 165 μm. Within the conditions of the tests, the speed and load did not have a significant effect on the ridge spacing. However, the pattern was best seen and more regular for the following two conditions: low load combined with low speed and high load combined with high speed. In these cases, for replicate 1, the variation of the wear areas as a function of number of brush strokes are

similar. It is now generally accepted that the abrasion rate of a rubber is proportional to the spacing of the ridges (Fukahori and Yamazaki, 1994b,a). Since no differences can be observed in the distance separating two ridges (figure 4.35), the wear rates are identical.

The lack of a regular pattern for the other two conditions, i.e. low load combined with high speed and high load combined with low speed, can be attributed to the presence of longitudinal scratches which disrupt the transverse ridges. Scratches can be attributed to irregularities in the brushes leading to dramatically increased contact stresses and subsequent premature failure of the coatings.

Grosch and Schallamach (1966) reported similar results. Indeed, observation of the same rubber surface with a different direction of incident light showed scoring marks across the ridges. The "pseudo-abrasion pattern" is formed as a result of the ridges being comparable in size with the dimensions of the abrasive grains. Hence, the size of the grain becomes important and ploughing through the ridges occurs.

The relative contributions of these two wear processes, i.e. abrasion pattern and tearing, influences the wear generated. Observation of the filtered debris with SEM could provide additional information on the contribution of each wear process to the overall wear behavior of the coatings. One hypothesis explaining the differences in the wear results reported is that the contribution of the abrasion pattern to the overall wear behavior is similar under all tests conditions, but the contribution of the longitudinal scratches varies. Eliminating completely one of the two wear processes can make it possible to evaluate which of the two processes is the most important. The abrasion pattern can be systematically studied as in the work of Fukahori and Yamazaki (1994b) where a single large and blunt indenter slides repetitively over a rubber specimen. The tearing process has been studied and characterized Kohl and Singer using scratch tests.

The influence of wear debris can not be neglected as it renders the bristles blunter and therefore favors the formation of abrasion pattern rather than longitudinal scratches.

The wear behavior of the EXS samples is dominated by longitudinal scratches rather than abrasion pattern. The hypothesis that oil is present in EXS sample would support the reduction in friction, which will then reduce the formation of the abrasion pattern. However, according to preliminary results, there is no dramatic changes in the voltage input into the motor between EXS and NRL samples. A systematic study of a nylon ball sliding on the candidate coatings would allow a comparison of the friction force.

These results agree with results by Bolster and Singer (1996) for the microscopic pictures of the damage of the top coat as a result of a blunt slider in the scratch tests: for RTV11, a semi-circular tear is seen perpendicular to the direction of sliding. For the Exsil® 2200 coatings, localized delamination was observed.

Fragments seen in Fig. 4.38 (pages 130) are not likely to be formed by the roll formation process described in section 2.3. Indeed, roll formation is expected to occur on elastomers with low tear strength exhibiting high friction at a smooth counter-face.

In conclusion, the principle modes of damage identified are circumferential tears and abrasion patterns. High rates of energy dissipation at the interface accompany the formation of micro-cracks and micro-tears, which are part of the overall modes of damage previously identified. Indeed, as described in section 2.3 (page 16), the formation of the abrasion pattern is composed of elementary tears at the base and at the crest of the ridges formed, hence rendering the abrasion pattern self-perpetuating.

5.2 Validation of the methodology

5.2.1 Apparatus

A methodology can be evaluated based on six criteria:

1. Reproducibility,
2. Precision,
3. Accuracy,
4. Versatility,
5. Ease of use, and
6. Accelerated test.

Reproducibility: are the tests reproducible?

In order to verify the repeatability of the tests, experiments under identical conditions were ran and results showed that the tests are indeed reproducible within the experimental error as long as tests conditions are maintained identical. Indeed, the effect of duration of the test phases on the wear rates was investigated. It was shown that the phase duration has to be large enough to minimize the contribution of high transient wear rates. Figure 5.6

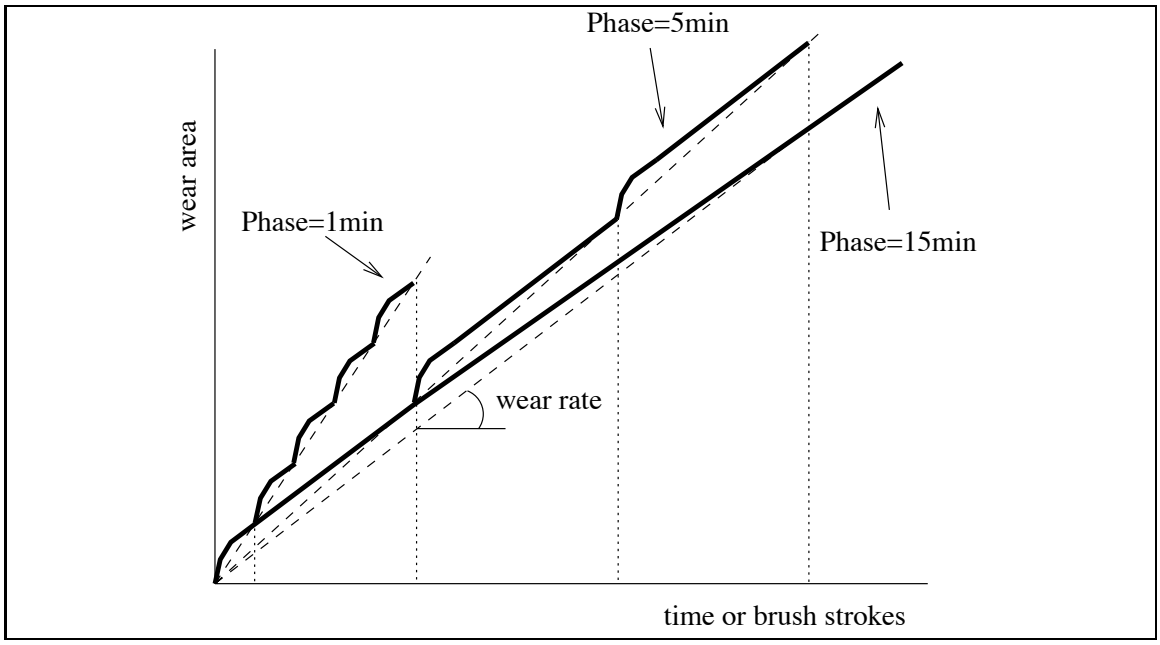

Fig. 5.6 Effect of the phase duration on the calculated wear rate, showing the influence of transient wear. The wear rate is equal to the slope of the dashed line.

illustrates the effect of reducing the duration of the test phases on the calculated wear rates when transient wear is considerable. Transient wear was attributed to the misalignment of the brushes with the sample surface as well as to wear debris accumulation at the interface. It can not be evaluated without monitoring the wear rate continuously, which with the current apparatus, can not be done. Limiting the misalignment will undoubtedly reduce transient wear.

Precision: is the variation of wear between similar samples reasonable?

The precision of the results was enhanced by the simultaneous collection of wear area and maximum wear scar depth. This is necessary to fully understand the conditions at the interface between the brushes and the specimen sample. Figure 5.7 illustrates the case of stiff brushes contacting a multi-layered specimen with a soft coating over a stiffer coat. Initially, as the brushes are in contact with the soft top coat, the depth of the wear scar as well as the area of the scar increase. This is true until the brushes have removed most of the top coat. At this point, the bristles can not longer break through the coating since the intermediate coat is stiffer than the top coat. Bristles start to bend under the applied load and speed and remove material from the sides of the scar. This results in the increase of

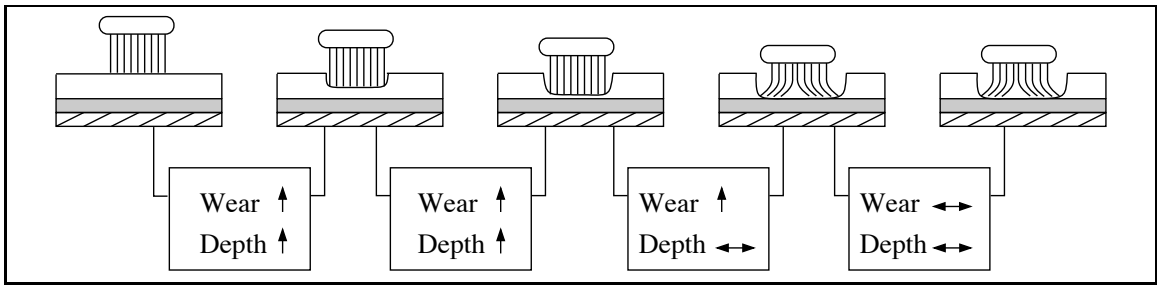

Fig. 5.7 Schematic showing the complementarity of the wear and depth data in the study of soft elastomeric duplex coatings

the wear scar while the maximum penetration depth remains fairly constant. Finally, when most of the top coat material is removed, the variation of both the depth and the area of the wear scar are smaller as the brushes are now in contact with the stiffer bond coat.

Accuracy: Is the wear mode in the tests similar to application wear mode?

Limited information is available for the wear mode of the new candidate coatings while in service conditions. Even though the tests conducted with the apparatus are intended to be simulative, they are only closer to being simulative with respect to tests such as pin-on-disk on scratch tests. Indeed, the samples are clean and undamaged as the wear tests are started. The presence of fouling will obviously alter the results as well as pre-existing damage as a result of impacts or biological and chemical degradation.

Versatility: Can a wide range of materials be studied? Can the wear mode be altered?

A wide range of samples of any size, thickness and materials can be tested with the wear tester. The brush holder can easily be altered to accommodate any custom designed brushes.

Ease of use: are the tests easy to run? Are they time and cost efficient?

The wear tests are very simple to run. The methodology described in Chapter 3 should be followed carefully for consistency. Tests are cost-efficient since commercial toothbrushes are used and the duration of the tests as well as other operational parameters can be adapted to fit one's need.

Accelerated results: Can the test method furnish results in a accelerated fashion?

Comparison with field cleaning is difficult because the U.S. Navy is in the process of redefining the cleaning requirements specified by NAVSEA (1989). However, the brushes are similar to those used with the SCAMP® machine, as well as to the brushes of type A authorized for use by the U.S. Navy (NAVSEA, 1989). The limitation of the present apparatus is that it does not allow for a transverse movement. It is also crucial to remember that the present tests were conducted on clean and undamaged samples. The presence of fouling organisms, particularly hard macro-foulers, will modify and possibly accelerate the wear process observed here.

5.2.2 Analysis techniques

Profilometry Our primary method for wear quantification is profilometry. As we have seen previously (section 3.1.3), this is a contacting method where a diamond stylus travels on the surface of a sample to record its topographic features. The contact between the stylus and the surface is affected by various parameters such as the specimen material, the contact force or the stylus shape and radius. In the case of soft surfaces, the diamond stylus is likely to indent the surface of the specimen sample. If the stylus plastically deforms the surface by ploughing through the material, then the sample will be damaged and the trace will incorrectly measure the topography of the sample. If the stylus elastically deforms the surface, the damage of the specimen will be limited and the traces might be also misleading. It is necessary to evaluate to which extent the stylus indents the specimen samples. This can be done with theoretical and experimental approaches.

These calculations are conducted to ensure that the profiler stylus did not indent and deform the surface to such an extent that the profile collected would no longer be representative of the surface. Theoretical analysis and experimental verifications of the depth of penetration are included in Appendix F. The results show that the maximum indentation depth predicted by the Hertzian theory of contact stresses is $6.4\,\mu$m under sliding conditions for RTV11. This is equivalent to a maximum of 5% of the thickness of the top coat.

The purpose of the following section is to characterize the consequences of the pen-

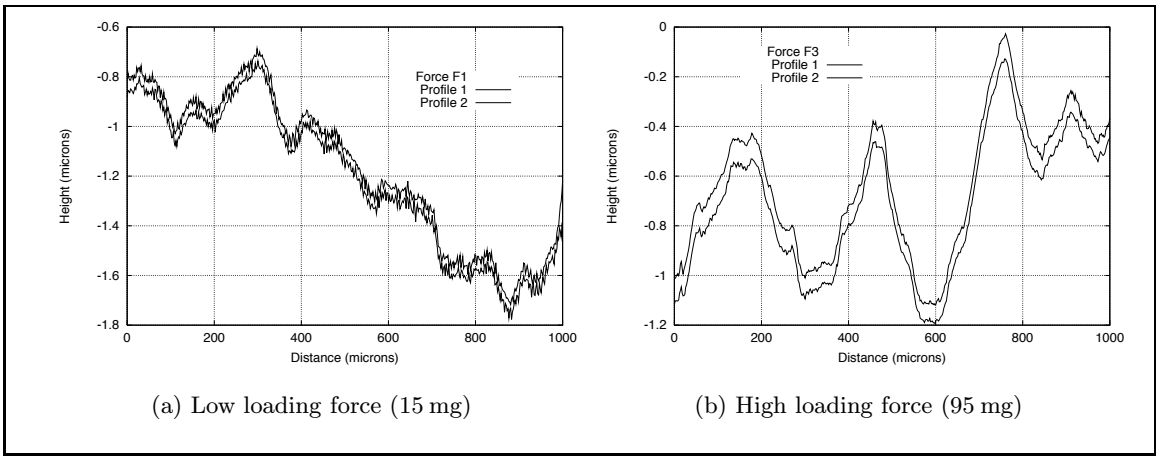

(a) Low loading force (15 mg) (b) High loading force (95 mg)

Fig. 5.8 Repetitive profiles on NRL 15/5

etration of the stylus on the profiles collected. Is there any permanent deformation taking place? Does the stylus have a significant impact on the traces collected?

Scans were collected at the same location on the surface at constant travel speed of 200 μm/s with varying stylus loads: F_1, F_2 and F_3 equal respectively to approximately 15 mg, 50 mg and 90 mg. Silgan® J-501 on steel, RTV11 on glass, NRL 15/5 on Silgan® J-501/steel and Exsil® 2200 on Silgan® J-501/fiber glass samples were incorporated in the study. Multiple scans at the same starting location and under exactly similar testing conditions were also collected to investigate whether or not permanent deformation is taking place.

Figure 5.8 illustrates that there is no difference in the features recorded by two scans started at the same initial location and run under the same scanning conditions, and that regardless of the level of loading force applied to the stylus. We can tentatively conclude that there is no permanent deformation taking place (other than what could be taking place during the first scan).

Figure 5.9 illustrates the effect of changing the loading force on the profile output. As the stylus force increases from low loading force (F_1) to high loading force (F_3), the shape of the features of the surfaces is greatly affected. Reducing the stylus force back to F_1 from high loading force (F_3), the surface features initially observed are restored and the scan is similar to the initial scan collected with a stylus force F_1. The increasing stylus force greatly affects the profile shape as well it increases the initial depth of penetration.

In conclusion, it is important to collect all scans under the same stylus force since

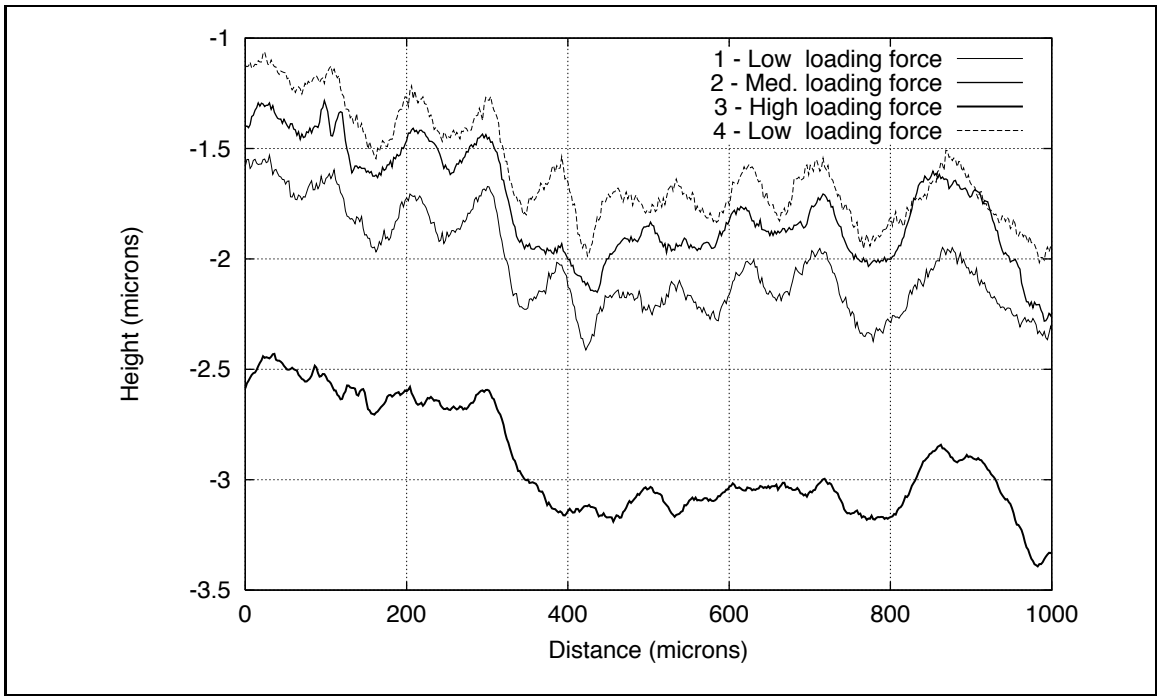

Fig. 5.9 Effect of the stylus loading force on profiles collected on NRL 15/5 samples

the readings are consistent for one given load. Since the traces collected under the low stylus force remain unaffected by multiples scans at increasing load confirms that there is negligible permanent deformation.

The measurement error on the wear data has been evaluated (Appendix **??**) based on experimental observations. It was shown to be within reason with reference to the absolute value of the wear data.

In conclusion, the profiler is a appropriate method to collect wear data of soft elastomeric coatings as long as the wear scar is no wider than 10 mm and the depth of the groove is less than 300 μm.

Statistical analysis The factorial design utilized for the present experiments was adapted because only two parameters were studied. Due to difficulties encountered as a result of defects in the coatings of different thickness resulting in different contact stresses, which ultimately resulted in altered wear rate, the full factorial design with repeated measures had to be modified to account for these problems. Nevertheless, the subdivided statistical models were efficient.

5.3 Parallel with other durability tests

The first step to establish the correlation between our tests and field conditions is to compare our results with results obtained with other testing apparatus. The durability of easy-release coatings has been evaluated with alternate tests as discussed in section 2.4.4. They can be classified into two groups: fundamental tests under well-controlled conditions and simulative brushing tests.

Tests carried out under well-defined conditions allow the fundamental understanding of basic processes of wear. As previously discusses, scratch tests are conducted at the NRL as well as at NSWCCD (Kohl et al., 1997; Haslbeck et al., 1997). Blade tests as well as indentation tests was carried out at the NRL as well. This discussion compares the results obtained by these institutions for the same candidate coatings, i.e. the NRL and the EXS samples. Additional data are available for the Silgan® J-501 coatings as well. The thicknesses of the various layers of the candidate coatings tested were comparable to those of the coatings tested in this project.

Simulative studies

Results Simulative tests, as their name indicates, are designed to simulate service life of the samples. SUNY-Buffalo adapted an abrasion tester for the specific evaluation of fouling release coatings (Meyer and Baier, 1997). A general description of the apparatus is included in the literature review (section 2.4.4).

Similar coatings were tested at SUNY-Buffalo with the abrasion tester. The wear resistance is quantified by measuring the depth of the wear scar with a depth gauge. For all samples of interest, the depths of the scars reported after 145,000 brush strokes are much less than that obtained in the present brush abrasion tester. Indeed, the depth of wear was less than 4 mils for the Silgan® J-501 and the EXS coatings while it was even less than 3 mils for the NRL samples. This can be explained by the difference in stiffness of the brushes used in both tests as well as by the chosen method to apply load. Indeed, as the brushes load onto the tests samples, the brushes tend to be accelerated as they contact the samples. Therefore, it should be expected that the wear be irregular across its length. The onset of increased wear in the leading edge of the sample might lead to increased wear overall. Assuming that the wear rate is similar, the ranking of the three groups of samples

Table 5.6 Comparison of wear testers

	SUNY-Buffalo	Virginia Tech
Principle	Discontinuous	Continuous
Applied load	Dead weight	Dead weight
Rotational speed	67 RPM	40 – 400 RPM
Brushes type	Toothbrushes	Toothbrushes
Number of brushes	Up to 4	Variable, 1 –3
Brush strokes rate	Up to 250	Function of number of brushes
Sample size	Variable	Variable
Environment	Variable	Variable
Test duration	145,000 brush strokes	180,000;190,000 brush strokes[a]

[a]Function of brushes rotational speed.

tested is surprisingly different than that obtained with our tests. Indeed, even though the stiffness of the brushes in the SUNY-Buffalo tests was much lower than that of the brushes used in our tests, the Silgan® J-501 coatings were reported to be less wear resistant than the NRL coatings. This different result remains unexplained. The wear resistance of the Exsil® 2200 samples was reported comparable to that of the Silgan® J-501 coatings. No indication is given on the wear mode of the coatings.

It was also evidenced that that samples with no oil or with low content of oil were more wear resistant than coatings with oil. Depths up to 9 mils were reported for methyl silicones containing mineral oil. However, we don't know if it is for the same polymer matrix or if this is true for all methyl silicone rubbers, regardless of the specific kind.

Testing methodology, choice of operating parameters The brushing rate of the brushes in the Buffalo tests is equivalent to the brushing rate under low speed setting of our tests. The operating parameters are summarized in table 5.6.

Chapter 6

Conclusions

A wear testing apparatus was custom designed for the study of durability of elastomeric fouling release coatings. The requirements were to simulate the action of cleaning brushes typically used in the maintenance of the U.S. Navy ship hulls.

The wear tester hereby designed provides accelerated and simulative testing of candidate fouling release coatings. The design of the apparatus was accentuated towards versatility and ease of use. It can be easily adapted at low cost to many coatings and brushes. The testing protocol developed is flexible as well. The wear tester presents the advantages of variable operating variables and systematic evaluation of cleaning needs. Cleaning tests can be conducted on specimens with pseudo-barnacles or fouled coatings by evaluating the load and speed necessary for the removal of the barnacles.

Two series of multi-layered coatings, the NRL series, developed by the Naval Research Laboratories, and the EXS series, developed by General Electric Company, with similar design characteristics were tested. The results show that:

- Depending on the speed and loading conditions, EXS samples are tow to six times more wear resistant than NRL samples.
- The wear rate of Silgan® J-501, material utilized to bond the outer layer to the substrate in both samples series, is one order of magnitude lower than that of the top coats of the EXS and NRL samples.
- The load and the wear rate are proportional for both the EXS and the NRL samples.
- Multiplying the sliding speed by three results in a decrease in the wear rate by two fold for the NRL samples. The effect of increased sliding speed could not be determined

for the EXS samples as it was not statistically significant.

- The wear rates are independent of the relative thicknesses of the layers of the duplex coatings.
- The wear rates are independent of the sliding distance.
- For NRL samples, the combination of circumferential scratches and radial ridges (abrasion pattern) are observed in the wear scar. For the EXS samples, only circumferential scratches can be seen in the wear scar.

Analysis of the results indicates that:

- Miscible oils contained in the top coat of the EXS samples may be responsible for enhanced wear resistance.
- Inclusion of fillers with good reinforcing characteristics results in improved wear resistance.
- Accumulation of soft debris between the bristles alters the contact and leads to the formation of abrasion patterns which are associated with reduced wear resistance.
- The wear rate is independent of the relative thicknesses of the layers constituting the duplex coatings under brushing conditions. The thickness of the top coat determines the total life of the coating system.
- Wear debris and misalignment of the brushes with the sample surface are responsible for high initial wear rates.

Chapter 7

Recommendations for future work

7.1 Improvements

The present methodology can be improved either by partially modifying the design of the wear tester or by refining some of the experimental procedures.

7.1.1 Apparatus design

Alignment

The difficulty to align correctly and precisely the sample surface and the plane formed by the brushes is the major handicap of the present testing apparatus. The ideal self-aligning system would require the complete re-design of the present apparatus. The basic principle for aligning the sample with the brushes is adequate but its sensitivity must be enhanced. Substituting the dial indicator used in this project with an equivalent device with accuracy higher than 0.5 mil would enhance the sensitivity of the alignment system, and therefore constitute a major improvement over the existing system.

Counter

The use of a counter could be implemented to closely monitor the total number of brush strokes, and to limit the associated error. This is particularly critical in short tests at high speed. The counter could also be programmed to automate the operation of the electric motor, and specifically stop the electric motor upon completion of the pre-set desired number of brush strokes.

Frequency measurements

The use of an acceleration transducer bonded to the surface of the specimen could be implemented to continuously monitor the vibrations generated during frictional sliding (Fukahori and Yamazaki, 1994a), to identify relevant frequencies and to correlate them with dynamic mechanical analysis.

Friction measurement

Information can be gained from knowledge of the level of the friction force. The existing system should be improved or a new device should be designed to precisely monitor the friction force.

XY table

A XY table could be incorporated to the present testing apparatus. It would allow the study of an additional operational parameter, the traveling speed, and allow a closer simulation of cleaning processes.

7.1.2 Methodology

Profilometry

With the present profiler available, as explained in section 3.1.3 (page 62), the maximum vertical range is 300 μm. In order to study coatings with thicker coats, it is proposed to install the high vertical range option on the profiler (Tencor Instruments, 1994). The maximum vertical range which could be read would be as high as 2000 μm (80 mil). Hence, the cross-sectional area of 80 mil deep wear scars would be measurable. When profilometry is not available or not suitable, coatings should be applied to thinner substrates which could be weighted.

Criteria for the end of experiment

To increase the method sensitivity, the criteria for the end of the tests could be altered. Indeed, presently, the end of the test is dictated by a pre-defined fixed duration based on the desirable total number of brush strokes. In order to compare results for samples with significantly different wear resistance, the removal of the coating could be chosen as the

criteria dictating the end of the test. Instead of the wear volume after the set duration, the amount of time required either to break through the top layer or for the thickness to decrease to a given value is recorded. This methodology presents two advantages over the currently employed methodology. The number of potential samples which could be correctly studied is increased and the duration of the tests is reduced (if a maximum allowable time is set). The problems associated with the new methodology is that it would require to continuously monitor the sample thickness. With the present apparatus, this can not be achieved. Two alternatives are proposed: either visually determine when the brushes wear through the top coat (hence the selected thickness is by the initial thickness of the coating) or implement a way to continuously monitor thickness if the self aligning system is implemented. The former alternative implies that an operator be alert at all times, and is not very accurate either.

Analysis of the test fluid and wear debris

Study of the lubricant is very important to understand the fundamental structure-properties relationship when information on the samples is limited.

The implementation of a systematic analysis of the test fluid would be beneficial at two levels: analysis of the wear debris collected as well as the analysis of the exudates present in the test fluid at the end of the test. It has been recognized that the identification of wear debris, with SEM, can provide fundamental information not only on the basic physical processes but also on the wear behavior as a whole for the materials of interest. Analysis of the exudates present in the test fluid at the end of the wear test (as is done at SUNY-Buffalo (Meyer et al., 1994, 1995) with MAIR-IR) would compensate the lack of information provided for the candidate coatings tested. In particular, it is important to know whether or not hydrocarbons are present, i.e. oils or other additives which can influence the wear mechanism, the wear resistance or the friction data.

SEM characterization

Scanning Electron Microscopy could be utilized to provide additional information on the morphology of the material inside and outside the wear track as well as on the morphology of debris or debris clusters.

7.2 Additional testing

7.2.1 Wear tests

Additional wear tests can be run in order to investigate the wear resistance characteristics of new candidate coatings as well as to investigate the effects of supplementary operational parameters. The additional test variables which could easily be varied are:

- the characteristics of the brushes: stiffness, composition, geometry...,
- the nature of the environment: air, water or slurry, or
- the nature of motion (unidirectional or 'oscillating').

The results can be incorporated in a factorial design as was done in the present study of the effects of load and speed. The use of fractional factorial design, also known as the Taguchi method (Mok and Gorman, 1995b,a), could be implemented in order to accelerate the experimental program.

In order to better understand the formation of the abrasion pattern on NRL samples, tests with continuous removal of debris generated should be designed. Also, as suggested by Grosch and Schallamach (1966), the influence of the motion of the brushes (oscillating or not) should be investigated to verify whether or not abrasion pattern plays a significant role in the decreased wear resistance of the NRL samples.

7.2.2 Parallel tests

Tests to verify speed effects assumptions

It is essential to document better the speed effect recorded on NRL samples.

- Additional replications of the tests would increase the significant difference between the two levels of speed.
- In order to verify if the hydrodynamic lubrication hypothesis is valid, Dr. Furey suggested running wear tests in test liquids with differing viscosity as well as for the two speed levels.
- It was suggested that abrasion is a visco-elastic phenomenon. This could be validated by systematic and precise recording of the vibrations in the specimen samples when subjected to the action of brushes (multiple contacts) and individual indenter (single contact). The procedure for DMA can be refined by using a frequency sweep mode at a given temperature in order to identify critical frequencies. Also, DMA tests should

be conducted on samples in presence of salt water in order to study the effect of swelling fluids on the behavior of the top coat materials.

- A temperature sensor could be added to monitor changes of the temperature of the test fluid. A temperature-controlled environment would allow tests to be conducted at constant sliding speeds and varying test temperatures. Subsequently, the WLF transform (Ferry, 1961) could be applied to obtain a master curve for the wear area as a function of temperature or sliding speed.
- Bristle bending should be monitored to investigate whether or not it is proportional to the accumulation of wear debris and to the wear rate.

Cleaning tests

All of the tests conducted in the project and the proposed subsidiary tests are so-called wear tests. Keeping in mind the application for which these coatings have been designed, it is necessary to conduct cleaning tests on naturally or, when possible, pseudo-fouled coupons. A controlled testing procedure can be designed such that the brushing force is incrementally increased allowing the results to be presented in terms of "necessary cleaning force to remove fouling". The brushing force can be altered through the combined effects of increasing the rotational speed and the applied load by increments for a set period of time.

Fouling release properties evaluation

As it was originally proposed in the original proposal, re-evaluation of fouling release properties after wear tests needs to be implemented. Various methods could be investigated. The most common methods are comprehensive contact angle measurements (Meyer et al., 1994), pseudo-barnacle adhesion measurements (Schultz and Swain, 1997) and micro-fouling tests conducted by Mittelman et al. (1993). Each of the previous methods shows short-comings. The measurement of comprehensive contact angles is dependent upon the surface roughness of the samples. Pseudo-barnacle adhesion measurements have been proven to be valid only for silicone coatings containing no fillers. Finally, the micro-fouling tests might not be sufficiently sensitive to detect differences between the wear scar and the undamaged surface surrounding the wear scar. Combining these methods is a better alternative for the laboratory evaluation of fouling release properties. The best evaluation would be short-term testing in one of the immersion sites.

Material properties evaluation

Mechanical properties of the materials can be monitored as they change with time due to exposure to salt water.

Bibliography

Alberte, R. S., Snyder, S., Zahuranec, B. J., and Whetstone, M., 1992, "Biofouling research needs for the United States Navy: program history and goals." *Biofouling*, Vol. 6, pp. 91–95.

Alzieu, C., Thibaud, Y., Heral, M., and Boutier, B., 1980, "Evaluation des risques dus a l'emploi des peintures anti-salissures dans les zones conchylicoles," *Rev. Trav. Inst. Peches Marit.*, Vol. 44, No. 4, pp. 301–348.

Arnell, R., Davies, P., Halling, J., and Whomes, T., 1991, *Tribology: principles and design applications*, 1st edn., Springer-Verlag, New-York.

ASTM D3623, 1993, "Standard test method for testing antifouling panels in shallow submergence," Tech. rep., American Standard for Testing of Materials.

ASTM D4938 - 89, 1989, "Standard test method for erosion testing of antifouling paints using high velocity water," Tech. rep., American Standard for Testing of Materials.

ASTM D4939 - 89, 1989, "Standard test method for subjecting marine antifouling coatings to biofouling and fluid shear force in natural sea water," Tech. rep., American Standard for Testing of Materials.

ASTM D5618, 1994, "Standard test method for measurement of barnacle adhesion strength in shear," Tech. rep., American Standard for Testing of Materials.

ASTM D968, 1991, "Test method for abrasion resistance of organic coatings by falling abrasive," .

Baier, R. E. and Meyer, A. E., 1986, "Biosurface chemistry for fun and profit," *Chemtec*, pp. 178–185.

Baier, R. E. and Meyer, A. E., 1992, "Surface analysis of fouling-resistant marine coatings," *Biofouling*, Vol. 6, pp. 165–180.

Baier, R. E., Meyer, A. E., and Forsberg, R. L., 1997, "Certification of properties of nontoxic coatings exposed to abrasion and long-term abrasion," *Naval Research Reviews*, Vol. XLIX, No. 4, pp. 60–65.

Barquins, M., 1992, "Adherence, friction and wear of rubber-like materials," in: *Wear and friction of elastomers, ASTM STP 1145*, eds. R. Denton and M. K. Keshavan, American Society for Testing and Materials, Philadelphia, pp. 1–28.

Beke, A. L., 1967, "Functional stiffness characteristics of toothbrush bristles," *J. Dent. Res.*, Vol. 46, pp. 666–671.

Bhowmick, A. K. and Stephens, H. L., eds., 1988, *Handbook of elastomers: new development and technology*, Marcel Dekker, N.Y.

Bolster, R. N. and Singer, I. L., 1996, "Indentation studies of RTV silicones," Tech. rep., Naval Research Laboratory.

Bowden, F. P. and Tabor, D., 1950, *Friction and lubrication of solids*, Clarendon Press, Oxford.

Briscoe, B. J., 1980, "The friction of polymers: a short review," in: *Friction and traction*, eds. D. Dowson, C. M. Taylor, M. Godet, and D. Berthe, pp. 81–92.

Briscoe, B. J., 1982, *Physicochemical aspects of polymer surfaces*, Chap. Tribology of polymers: State of the art, Plenum press.

Bueche, A. M. and Flom, D. G., 1958/59, "Surface friction and dynamic mechanical properties of polymers," *Wear*, Vol. 2, pp. 168–182.

Bunshah, R. F., 1982, "Selection and use of wear tests for coatings," in: *Selection and use of wear tests for coatings, ASTM STP 769*, ed. R. G. Bayer, American Society for Testing and Materials, pp. 3–15.

Butterworth Systems, 1981, "SCAMP® Underwater Hull Cleaning Machine," Specification sheet.

Carroll, K. M., Harblin, O. M., and Rubinsztajn, S., 1997, "Foul release system," U.S. Patent No. 5691019.

Cologer, C. P., Bohlander, G. S., and Preiser, H. S., 1977, "Review of underwater cleaning methods and their interaction on Navy antifouling paint systems," *Journal of Coatings Technology*, Vol. 49, No. 628, pp. 51–60.

Conn, A. F. and Johnson Jr., V. E., 1974, "Further applications of the cavijet™ (cavitating water jet) method," in: *Second international symposium on jet cutting technology*, Cambridge, England, pp. 7–20.

Delaney, R., 1982, "Clean Navy hulls cut costs," *Marine Engineering Log*, pp. 89–136.

Efraimsen, H. E., Johansen, J. R., Haugen, E., and Holland, R. I., 1990, "The abrasive effect of a rotating electrical toothbrush on dentin," *Clinical preventive dentistry*, Vol. 12, No. 4, pp. 13–18.

Eiss Jr., N. S., 1991, *Physical methods of chemistry*, Vol. VII: Determination of elastic and mechanical properties, Chap. The measurement of friction and wear, 2nd edn., John Wiley and Sons, pp. 101–138.

Eiss Jr., N. S., 1994, *Characterization of polymers*, Chap. 11: Friction and wear (tribology), Butterworth-Heinemann, pp. 262–294.

Ferry, J. D., 1961, *Viscoelastic properties of polymers*, John Wiley and Sons, Inc., New York.

Fukahori, Y. and Yamazaki, H., 1994a, "Mechanism of rubber abrasion. Part 1: Abrasion pattern formation in natural rubber vulcanizate," *Wear*, Vol. 171, pp. 195–202.

Fukahori, Y. and Yamazaki, H., 1994b, "Mechanism of rubber abrasion. Part 2. General rule in abrasion pattern formation in rubber-like materials," *Wear*, Vol. 178, No. 1-2, pp. 109–116.

Fukahori, Y. and Yamazaki, H., 1995, "Mechanism of rubber abrasion. Part 3: How is friction linked to fracture in rubber abrasion?" *Wear*, Vol. 188, pp. 19–26.

Furukawa, J., 1996, "Chemical aspects concerning The friction and abrasion of rubber," *Bull. Chem. Soc. Jpn*, Vol. 69, pp. 2999–3006.

Gent, A. N. and Pulford, C. T. R., 1983, "Mechanisms of rubber abrasion," *Journal of applied polymer science*, Vol. 28, No. 3, pp. 943–960.

Gilliam, D. R., 1985, "A study of contact between a profile meter stylus and polymer films on roughened substrates," M.S. Thesis, Virginia Polytechnic Institute and State University.

Golding, P. S., 1981, "The development of the toothbrush. II." *Dental hygiene*, Vol. 55, pp. 10–15.

Griffith, J. R., 1995, "Non toxic antifouling systems," U.S. Patent No. 5449553.

Griffith, J. R., 1997, "Non toxic antifouling systems," U.S. Patent No. 5593732.

Grosch, K. A., 1963, *Proc. Roy. Soc.*, Vol. A274, pp. 21.

Grosch, K. A. and Schallamach, A., 1966, "Relation between abrasion and strength of rubber," *Rubber Chemistry and Technology*, Vol. 39, No. 1-3, pp. 287–305.

Haluska, L. A., 1982, "Wear testing of abrasion-resistant coated plastics," in: *Selection and use of wear tests for coatings, ASTM STP 769*, ed. R. G. Bayer, American Society for Testing and Materials, pp. 16–27.

Harper, C. A., 1992, *Handbook of plastics, elastomers, and composites*, second edition edn., McGraw Hill, Inc.

Haslbeck, E., Montemarano, J. A., and Ross, A., 1997, "Scratch resistance evaluation of foul-release coatings (Naval Surface Warfare Center, Carderock Division, code 641)," in: *Duplex Foul-Release Coatings*, NSWCCD, pp. 27–29.

Heilmann, P. and Rigney, D. A., 1981, "An energy-based model of friction and its application to coated systems," *Wear*, Vol. 72, pp. 195–217.

Hertz, H., 1896, *Miscellaneous papers by H. Hertz*, Macmillan, London.

Hilaris, J. A. and Labus, T. J., 1979, "Marine applications of high-pressure waterjets," in: *Erosion: prevention and useful applications, ASTM STP 664*, ed. W. F. Adler, American Society for Testing and Materials, pp. 582–596.

Hinkelmann, K. and Kempthorne, O., 1994, *Design and analysis of experiments*, Vol. 1, John Wiley and Sons.

Jahanmir, S., 1978, "On the wear mechanisms and the wear equations," in: *Fundamentals of tribology*, Massachusetts Institute of Technology, Massachusetts.

James, D. I., 1967, *Abrasion of rubber*, Mac Laren.

Johnson, K. L., 1980, "Aspects of friction," in: *Friction and traction*, eds. D. Dowson, C. M. Taylor, M. Godet, and D. Berthe, pp. 3–12.

Kohl, J. G., Singer, I. L., and Griffith, J. R., 1997, "Scratch test rankings of duplex foul-release coatings (Naval Research Laboratory, code 6176)," in: *Duplex Foul-Release Coatings*, NSWCCD, pp. 21–26.

Lancaster, J. K., 1982, "Assessment of the wear of composite coatings in reciprocating line contact conditions," in: *Selection and use of wear tests for coatings, ASTM STP 769*, ed. R. G. Bayer, American Society for Testing and Materials, pp. 92–117.

Lancaster, J. K., 1990, "Material-specific wear mechanisms: relevance to wear modeling," *Wear*, Vol. 141, pp. 159–183.

Leidheiser Jr., H. and Kendig, M. W., 1978, "Conjectures on delamination of organic coatings by corrosion," *Ind. Eng. Chem. Prod. Res. Dev.*, Vol. 17, No. 1, pp. 54–55.

Ludema, K. C. and Tabor, D., 1966, "The friction and viscoelastic properties of polymeric solids," *Wear*, Vol. 9, pp. 329–348.

Lyman Ott, R., 1992, *An introduction to statistical methods and data analysis*, Duxbury.

Lynch, W., 1978, *Handbook of silicone rubber fabrication*, Van Nostrand Reinhold, N.Y.

Mark, J. E., 1990, *Silicon-based polymer science, a comprehensive resource*, Chap. 2: Silicon-Containing Polymers, American Chemical Society, pp. 47–63.

Meyer, A. E. and Baier, R. E., 1997, "Abrasion test for determining fouling resistance breakthrough(State University of New York at Buffalo)," in: *Duplex Foul-Release Coatings*, NSWCCD, pp. 4–20.

Meyer, A. E., Baier, R. E., and Forsberg, R. L., 1994, "Field trials of non toxic fouling-release coatings," in: *Proceedings of the 4th international zebra mussel and other aquatic nuisance organisms conference.*, pp. 273–290.

Meyer, A. E., Baier, R. E., and Forsberg, R. L., 1995, "Degradation of non toxic fouling release coatings as a result of abrasion and long-term exposure," in: *Proceedings of the 5th international zebra mussel and other aquatic nuisance organisms conference*, pp. 337–342.

Mittelman, M. W., Packard, J., Arrage, A. A., Bean, S. L., Angel, P., and White, D. C., 1993, "Test systems for determining antifouing coating efficacy using on-line detection of bioluminescence and fluorescence in a laminar-flow environment," *Journal of Microbiology Methods*, Vol. 18, pp. 51–60.

Mok, S. H. and Gorman, D. G., 1995a, "Investigation of factors affecting wear characteristics in rubber-metal sliding contact," *Journal of Engineering Tribology*, Vol. 1, No. 209, pp. 137–143.

Mok, S. H. and Gorman, D. G., 1995b, "Using Taguchi experimental design to investigate operating variables that significantly affect wear in mud pumps," *Journal of Engineering Tribology*, Vol. 209, No. 1, pp. 29–40.

Moore, D. F., 1972, *The friction and lubrication of elastomers*, Vol. 9, Pergamon Press Ltd., Oxford.

Moore, D. F., 1983, "Tribological properties of rubber-like materials," in: *Physicochemical aspects of polymer surfaces*, Vol. 1, Plenum Publishing Corporation, pp. 413–424.

NAVSEA, 1989, *Chapter 081: Waterborne underwater hull cleaning of Navy ships*, Naval Ships' technical manual, ref. S9086–CQ–STM–010.

Nygaard-Ostby, P., Edvardsen, S., and Spydevold, B., 1979, "Access to interproximal tooth surfaces by different bristle designs and stiffnesses of toothbrushes," *Scand. J. Dent. Res.*, Vol. 87, pp. 424–430.

Owen, M. J., 1990, *Silicon-based polymer science, a comprehensive resource*, Chap. 40: Siloxan Surface Activity, American Chemical Society, pp. 705–739.

Payne, N. G. and Bayer, R. G., 1991, "Friction and wear tests for elastomers," *Wear*, Vol. 150, pp. 67–77.

Preiser, H. S. and Halpern, E. H., 1983, "Organic coatings evaluation and performance prediction: an overview," in: *Mechanical properties, performance and failure modes of*

coatings. Proc. 37th meeting of mechanical failures prevention group, National Bureau of Standards, Gaithersburg, MD, pp. 63–71.

Qiu, X. and Plesha, M. E., 1991, "A theory for dry wear based on energy," *J. Tribology*, Vol. 113, pp. 442.

Rabinowicz, E., 1995, *Friction and wear of materials*, 2nd edn., John Wiley and Sons, Inc.

Rawls, H. R., Casella, R., and Mkwayi-Tulloch, N. J., 1993, "An *in vitro* and *in vivo* study of toothbrush bristle splaying," *J. Dent. Res.*, Vol. 72, No. 5, pp. 947–952.

Rawls, H. R., Mkwayi-Tulloch, N. J., and Krull, M. E., 1990, "A mathematical model for predicting toothbrush stiffness," *Dental materials*, Vol. 6, pp. 111–117.

Roark, R. and Young, W., 1989, *Formulas for stress and strain*, McGraw-Hill, New York.

Saltzman, G. A., 1982, "Wet-sand rubber wheel abrasion test for thin coatings," in: *Selection and use of wear tests for coatings, ASTM STP 769*, ed. R. G. Bayer, American Society for Testing and Materials, pp. 71–91.

Schallamach, A., 1952a, "Abrasion of rubber by a needle," *Journal of polymer science*, Vol. 9, No. 5, pp. 385–404.

Schallamach, A., 1952b, "Abrasion pattern on rubber," *I. R. I. Transactions*, Vol. 28, pp. 256–266.

Schallamach, A., 1953, "The velocity and temperature dependence of rubber friction," *Proc. Phys. Soc.*, Vol. B66, pp. 386–392.

Schallamach, A., 1954, *Proc. Phys. Soc.*, Vol. B67, pp. 883.

Schallamach, A., 1958, "Friction and abrasion of rubber," *Wear*, Vol. 1, pp. 384–395.

Schallamach, A., 1968, *Rubber Chem. and Tech.*, Vol. 41, pp. 209.

Schallamach, A., 1971, "How does rubber slide?" *Wear*, Vol. 17, pp. 301–312.

Schultz, M. P. and Swain, G. W., 1997, "Barnacle adhesion data for coatings (Florida Institute of Technology)," in: *Duplex Foul-Release Coatings*, NSWCCD, pp. 30–40.

Schumacher, K. W., 1996, "An instrumented rotating brush device to evaluate the removal of biofouling from non-toxic antifouling coatings," M.S. Thesis, Florida Institute of Technology.

Schwartz, S. S. and Goodman, S. H., 1982, "Silicones," in: *Plastics Materials and Processes*, Van Nostrand Reinhold Company, N.Y., pp. 403–415.

Seaward Marine Services Inc., 1993, "Underwater Hull Cleaning," Technical Data sheet.

Swain, G. W., J. R. Griffith, J. D. B., and Vincent, H. L., 1992, "The use of barnacle adhesion measurements for the field evaluation of non toxic fouling release surfaces," *Biofouling*, Vol. 6, No. 2, pp. 105–114.

Swain, G. W. and Schultz, M. P., 1996, "The testing and evaluation of non toxic antifouling coatings," *Biofouling*, Vol. 10, pp. 187–197.

Swain, G. W., Schultz, M. P., Griffith, J. G., and Snyder, S., 1997, "Paper 10: The relationship between barnacle and pseudo-barnacle adhesion measurements: a method to predict the foul release properties of silicones?" in: *U.S. Pacific Rim Workshop "Emerging nonmetallic materials for the marine environment"*, Hawaii.

Taylor, S. A. and Chapman, G., 1991, "Cleaning pipelines using high-pressure water jets," *MP*, pp. 25–28.

Tencor Instruments, 1994, *User manual for the Alpha-Step 500 Surface Profiler.*

Uetz, H. and Fohl, J., 1978, "Wear as an energy transformation process," *Wear*, Vol. 49, pp. 253–264.

Wathen, T. L., 1994, "The design of a brush technology for the evaluation of non-toxic foul release coatings," M.S. Thesis, Florida Institute of Technology.

Zahavi, J. and Schmitt Jr., G. F., 1982, "Solid particle erosion of coatings on transparent polycarbonate and reinforced composites, ASTM STP 769," in: *Selection and use of wear tests for coatings*, ed. R. G. Bayer, American Society for Testing and Materials, pp. 28–71.

Zhang, S. W., 1992, "Wet abrasion of polymers," *Wear*, Vol. 158, pp. 1–13.

Appendix A

Duplex coating application

This appendix describes the procedure for the application of the duplex coatings.

1. Approximately 6 inches apart, apply two strips of masking tape on the epoxy-covered steel substrate for the Doctor's blade to glide on.
2. Prepare the mist (tack) coat:
   (a) Mix Epon 828 epoxy (55 wt. %) with Versamid 140 (45 wt. %)
   (b) Stir thoroughly until it becomes milky
   (c) Let it stand at room temperature ($\simeq 25°C$) for one half-hour.
   (d) Add 80 wt. % of n-butanol to the mixture (20 wt. %)
   (e) Stir until the mixture is homogeneous and transparent
3. Brush a thin mist coat uniformly on the epoxy-covered steel substrate. Wait $\simeq 1$ hour at room temperature for the mist coat to become tacky to the touch.
4. Using a doctor's blade, apply Wacker's Silgan® J-501. [1] Let the Wacker's J501 coat cure at room temperature. It takes $\simeq 3$ hours for a 20-mil-thick coat to cure completely.
5. Remove the masking tape strips
6. Prepare GE's RTV11:
   (a) Stir RTV11 until it is homogeneous.
   (b) Add 0.5 wt. % of dibutyl tin dilaureate (catalyst), which should be included in the GE's RTV11 package.
   (c) Stir again. Once the catalyst has been added to the homogeneous RTV11 prepolymer mixture, the mixture should be applied to the Wacker Silgan® J-501 coat within one half-hour.
7. Draw down GE's RTV11[2] onto the substrate. Wait $\simeq 3$ to 4 hours before moving the samples

[1] The thickness of Wacker's Silgan® J-501 decreases by approximately 20% upon curing.
[2] The thickness of GE's RTV11 decreases by approximately 50% upon curing.

Appendix B

Calibration of the electric motor

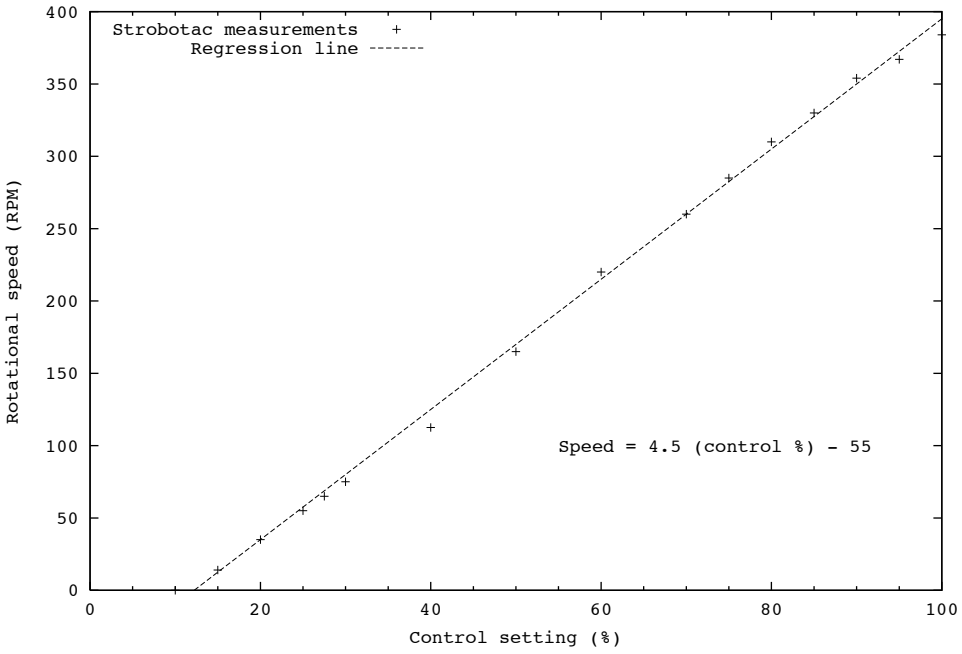

Fig. B.1 Calibration plot for the Baldor electric motor including regression data

The control settings are read from the control box. Rotational speeds are measured with a Strobotac instrument. The data presented was obtained under no load. The motor rotational speed is independent of load within the range applied on toothbrushes.

Appendix C

Data acquisition program

C.1 Introduction

The following code was written by Frank Caldwell at Virginia Tech, and further edited by Anne-Claire Christiaen. It is written in basic and compiled with PCLAB. This code allows the collection of voltage readings from the current sensor circuit, in order to monitor the torque of the electric motor.

C.2 Code `voltage.bas`

```
        DECLARE FUNCTION MEASURE.VOLTS% CDECL
                (BYVAL CHANNEL%, SEG VOLTS!)
10      CLS
15      GOSUB 100
16      LOCATE 15,5
17      INPUT "Before you start, have you copied avg.dat"; OUI$
        CLOSE: END

" Input test parameters
        OPEN "AVG.DAT" FOR OUTPUT AS #2
22      LOCATE 2,40: PRINT "HIGH SPEED -> 1"
        LOCATE 3,40: PRINT "LOW SPEED -> 2"
24      LOCATE 4,40: PRINT "                    "
        LOCATE 4,40: INPUT "SELECT SPEED: "; SPD%
        LOCATE 5,40: PRINT "                    "
        IF SPD%=1 OR SPD%=2 THEN 28 ELSE 24
28      LOCATE 5,40: INPUT "PHASE: 1, 2, 3 OR 4 "; TEST%
        IF TEST%=1 OR TEST%=2 OR TEST%=3 OR TEST%=4
                THEN GOSUB 200 ELSE 28

" Prints on the screen the start and finish times, which can be
" manually changed if necessary (using subroutine 3)
30      LOCATE 6,35: PRINT "START TIME IS: "; SRT$
```

```
        LOCATE 7,35: PRINT "END TIME IS: "; END$
        LOCATE 8,35: PRINT "                                                    "
        LOCATE 8,35: INPUT "IS IT CORRECT: y or n"; ANS$
        LOCATE 9,35
        IF ANS$ = "n" OR ANS$ = "N" THEN GOSUB 300 else goto 50


"Prints on the screen the test parameters selected right
"before starting data acquisition
50      CLS
        LOCATE 3,60: PRINT "TEST.DAT, AVG.DAT"
        LOCATE 4,60: IF SPD%=1 THEN PRINT "LOW SPEED"
                ELSE PRINT "HIGH SPEED"
        LOCATE 5,60: PRINT "PHASE #: "; TEST%
        LOCATE 6,60: PRINT "START: "; : PRINT USING "      "; SRT$
        LOCATE 7,60: PRINT "FINISH: "; : PRINT USING "      "; END$
        LOCATE 2,1: INPUT "READY TO START"; REP%
        LOCATE 2,1: PRINT "                                                    "
        LOCATE 13,1: PRINT "————————-"
        LOCATE 15,1: PRINT " Wait 2 MIN. "
        LOCATE 17,1: PRINT "————————-"
        LOCATE 1,55: PRINT "Hit a key to terminate..."
        TIME$=SRT$

" Starts reading data from channel 1, prints it on the screen.
        CHANNEL%=1: STATUS%=0: VOLTS!=0: L%=1: COL%=1
59      T$=TIME$: C$=RIGHT$(T$,1)
60      STATUS%=MEASURE.VOLTS%(CHANNEL%,VOLTS!)
        LOCATE 20+CHANNEL%,60
        PRINT CHANNEL%; " "; : PRINT USING "+##.####"; VOLTS!
61      T$=TIME$
        SUM! = SUM! + VOLTS!
64      IF RIGHT$(T$,1)=C$ THEN 65 ELSE 66
65      COUNT% = COUNT% + 1
        IF INKEY$="" THEN 60
        CLOSE: END
66      IF RIGHT$(T$,1)="0" GOTO 68 ELSE 59
68      AVG! = SUM! / COUNT%
        LOCATE L%,COL%
        PRINT USING " "; T$;: PRINT " ";: PRINT USING "+##.####"; AVG!
        LOCATE ,COL%: PRINT "                                                  "
        L%=L%+1: IF L%>22 THEN 70 ELSE 75
70      L%=1: IF COL%=1 THEN COL%=26 ELSE COL%=1
75      PRINT #2, T$,: PRINT #2, USING "+##.######"; AVG!,
        PRINT #2,"    ",: PRINT #2, USING "+##.######"; VOLTS!,
        PRINT #2,"    ",: PRINT #2, COUNT%
        COUNT% = 0: SUM! = 0: AVG! = 0: C$=RIGHT$(T$,1)
82      IF T$=END$ THEN GOSUB 400
```

```
83      IF T$=TEND$ THEN GOSUB 500
        IF INKEY$="" GOTO 60
        CLOSE: END

" ======== Subroutine 1: Declare constants for test durations
100     MIN$="00:01:00": REP%=1: SPD%=2: ANS$="n"
        SRT11$="00:00:00": END11$="00:35:00": TEND11$="00:37:00"
        SRT12$="00:37:00": END12$="01:29:00": TEND12$="01:31:00"
        SRT13$="01:31:00": END13$="02:40:00": TEND13$="02:42:00"
        SRT14$="02:42:00": END14$="04:16:00": TEND14$="04:18:00"
        SRT21$="00:00:00": END21$="01:42:00": TEND21$="01:44:00"
        SRT22$="01:44:00": END22$="04:16:00": TEND22$="04:18:00"
        SRT23$="04:18:00": END23$="07:40:00": TEND23$="07:42:00"
        SRT24$="07:42:00": END24$="12:19:00": TEND24$="12:21:00"
        COUNT%=0: SUM!=0: AVG!=0
        RETURN

" ======== Subroutine 2: sets time constants
        " — low speed —
200     IF SPD%=1 THEN 235 ELSE 254
235     IF TEST%=1 THEN 237 ELSE 240
237     SRT$=SRT11$: END$=END11$: TEND$=TEND11$: GOTO 30
240     IF TEST%=2 THEN 242 ELSE 245
242     SRT$=SRT12$: END$=END12$: TEND$=TEND12$: GOTO 30
245     IF TEST%=3 THEN 247 ELSE 250
247     SRT$=SRT13$: END$=END13$: TEND$=TEND13$: GOTO 30
250     IF TEST%=4 THEN 252 ELSE 30
252     SRT$=SRT14$: END$=END14$: TEND$=TEND14$
        " — high speed —
254     IF SPD%=2 THEN 255 ELSE 30
255     IF TEST%=1 THEN 257 ELSE 260
257     SRT$=SRT21$: END$=END21$: TEND$=TEND21$: GOTO 30
260     IF TEST%=2 THEN 262 ELSE 265
262     SRT$=SRT22$: END$=END22$: TEND$=TEND22$: GOTO 30
265     IF TEST%=3 THEN 267 ELSE 270
267     SRT$=SRT23$: END$=END23$: TEND$=TEND23$: GOTO 30
270     IF TEST%=4 THEN 272 ELSE 30
272     SRT$=SRT24$: END$=END24$: TEND$=TEND24$
299     RETURN

" ====== Subroutine 3: change start and finish times
300     LOCATE 14,30: PRINT "START TIME -> 1"
        LOCATE 15,30: PRINT "END TIME -> 2"
        LOCATE 16,30: PRINT "BOTH -> 3"
        LOCATE 17,30: PRINT "NONE -> 4"
        LOCATE 18,30: PRINT ""
305     LOCATE 19,30: PRINT "                                                    "
        LOCATE 19,30: INPUT "WHICH DO YOU WISH TO CHANGE"; REP%
```

```
        LOCATE 20,30: PRINT "                                                    "
        IF REP%=1 OR REP%=2 OR REP%=3 OR REP%=4 THEN 307 ELSE 305
307     IF REP%=1 THEN 310 ELSE 320
310     LOCATE 20,30: PRINT "                                                    "
        LOCATE 20,30: INPUT "NEW START TIME: ",SRT$: GOTO 399
320     IF REP%=2 THEN 325 ELSE 330
325     LOCATE 20,30: PRINT "                                                    "
        LOCATE 20,30: INPUT "NEW END TIME: ",END$: GOTO 399
330     IF REP%=3 THEN 335 ELSE 340
335     LOCATE 20,30: PRINT "                                                    "
        LOCATE 20,30: INPUT "NEW START & END TIMES: "; SRT$,END$
340     IF REP%=4 THEN GOTO 399
399     RETURN 30

" ====== Subroutine 4: take load off signal
400     CLS: LOCATE 10,40: PRINT "————————————————"
        LOCATE 12,40: PRINT "PHASE "; TEST%; : PRINT" IS OVER"
        LOCATE 14,40: PRINT "————————————————"
        LOCATE 16,40: PRINT "Take load OFF immediately and"
        LOCATE 17,40: PRINT "collect data for 2 more minutes..."
        LOCATE 18,40: PRINT ""
        LOCATE 19,40: PRINT "The time for no-load is: "; TIME$
        LOCATE 20,40: PRINT ""
        L%=1: COL%=1
440     BEEP: T$=TIME$: IF T$=END$ THEN 440
499     RETURN 82

" ====== Subroutine 5: the test is OVER
500     CLS: BEEP
        LOCATE 10,40: PRINT "The final time is: "; TIME$
        LOCATE 11,40: PRINT ""
        LOCATE 19,40: PRINT "Go ahead and turn it off..."
570     FT$=RIGHT$(TIME$,1)
        LOCATE 13,40: PRINT "==== ———— ===="
        LOCATE 17,40: PRINT "==== ———— ===="
        LOCATE 15,40: PRINT " TEST "; TEST%; : PRINT" IS DONE"
        IF INKEY$="" THEN 580 ELSE CLOSE: END
580     STOP
```

Appendix D

Statistical design and analysis of experiments

Figure D.1 illustrates the logical steps of scientific experimentation involved in statistical design.

D.1 Factorial experiments

A factorial experiment is an experiment in which the response y (i.e., wear area, maximum depth or wear rate) is observed at all factor-level combinations of the independent variables. Factorial experiments can incorporate two or more factors, each with two or more levels (Lyman Ott, 1992). Treatments are assigned to experimental units at random. The factor-level combinations correspond to the "treatments" of a completely randomized design. When two factors, each with two levels, are studied, then the statistical experiment is called a "2 $\times$ 2 factorial experiment".

The model for a two-factor experiment with no interaction between the levels of factors A and B is:

$$y_{ij} = \mu + \alpha_i + \beta_j + \epsilon_{ij} \tag{D.1}$$

where α_i and β_j are constants and represent the average effect of, respectively, the ith level of factor A and the jth level of factor B. ϵ_{ij} is the random error. They are independent, normally distributed with mean 0 and variance σ_ϵ^2. y_{ij} represents an observation taken at the ith level of factor A and the jth level of factor B. μ is the population mean. This model

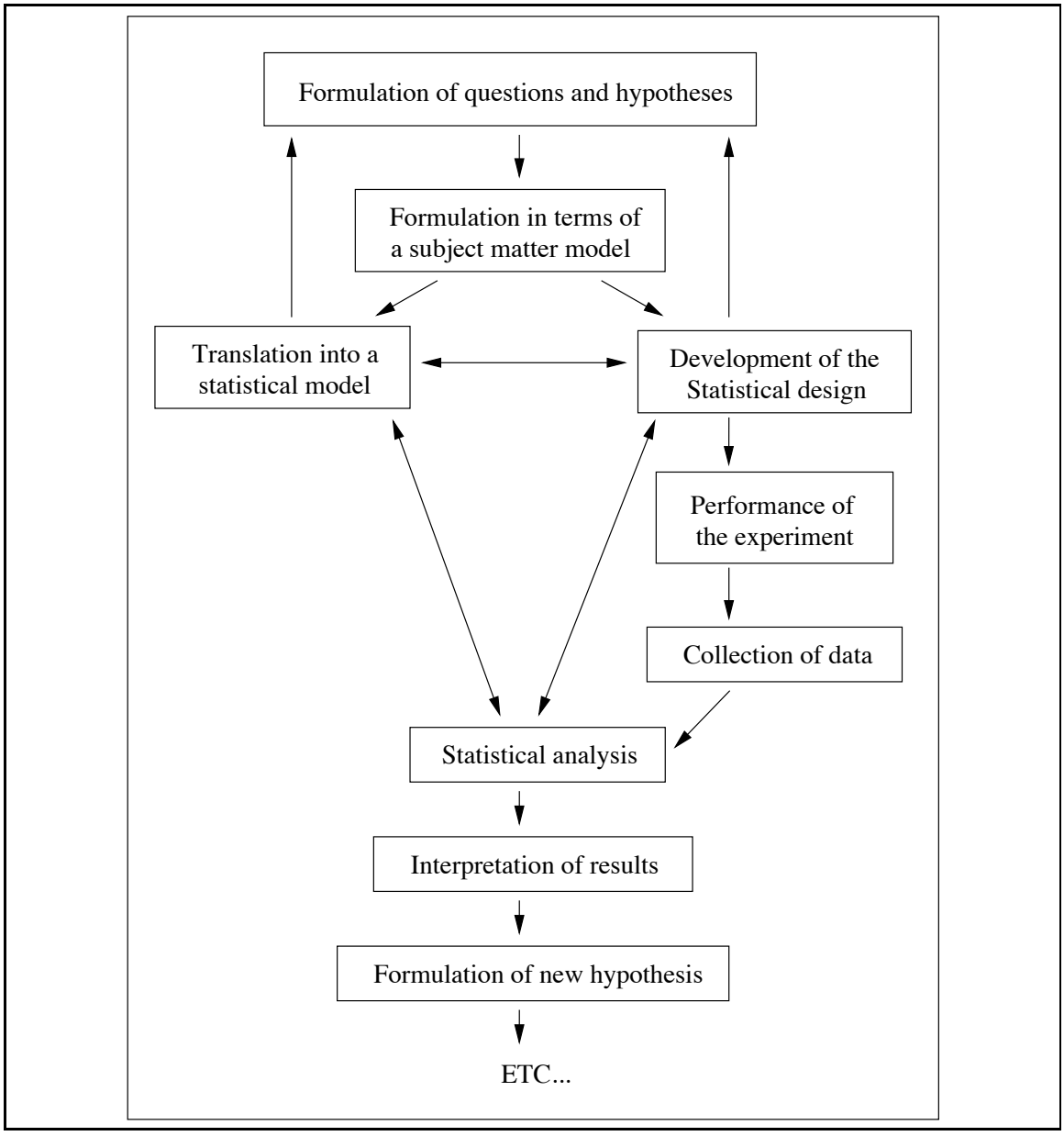

Fig. D.1 Logical steps of scientific experimentation by Hinkelmann and Kempthorne (1994)

is often called the additive model. The expected values for a 2 × 2 factorial experiment are shown in table D.1. The model assumes that there is no interaction, i.e. the difference in means for any two levels of factor A is the same no matter what level of factor B is considered.

Table D.1 Expected values for a 2 × 2 factorial experiment

	Factor B	
Factor A	Level 1	Level 2
Level 1	$\mu + \alpha_1 + \beta_1$	$\mu + \alpha_1 + \beta_2$
Level 2	$\mu + \alpha_2 + \beta_1$	$\mu + \alpha_2 + \beta_2$

Interaction can be accounted for in another model. If a two-factor factorial experiment with n replicates per factor-level combination (treatment) is considered, the model is:

$$y_{ijk} = \mu + \alpha_i + \beta_j + \alpha\beta_{ij} + \epsilon_{ijk} \tag{D.2}$$

where y_{ijk} is the response obtained for the kth replicate at the ith level of factor A and jth level of factor B and $\alpha\beta_{ij}$ is an effect due to the ith level of A and the jth level of B. The expected values for a 2 × 2 factorial experiment with n replicates per cell are represented in table D.2. This notion of interaction is often illustrated with profile plots as seen in figure D.2. Saying that two factors do not interact is equivalent to saying that the effect of one factor is the same for both levels of the other factor.

When significant interaction exist between treatments, the analysis of the effect of the main factors can not always be conducted.

When several observations are made per replicate, an additional term appears on

Table D.2 Expected values for a 2 × 2 factorial experiment with replications

	Factor B	
Factor A	Level 1	Level 2
Level 1	$\mu + \alpha_1 + \beta_1 + \alpha\beta_{11}$	$\mu + \alpha_1 + \beta_2 + \alpha\beta_{12}$
Level 2	$\mu + \alpha_2 + \beta_1 + \alpha\beta_{21}$	$\mu + \alpha_2 + \beta_2 + \alpha\beta_{22}$

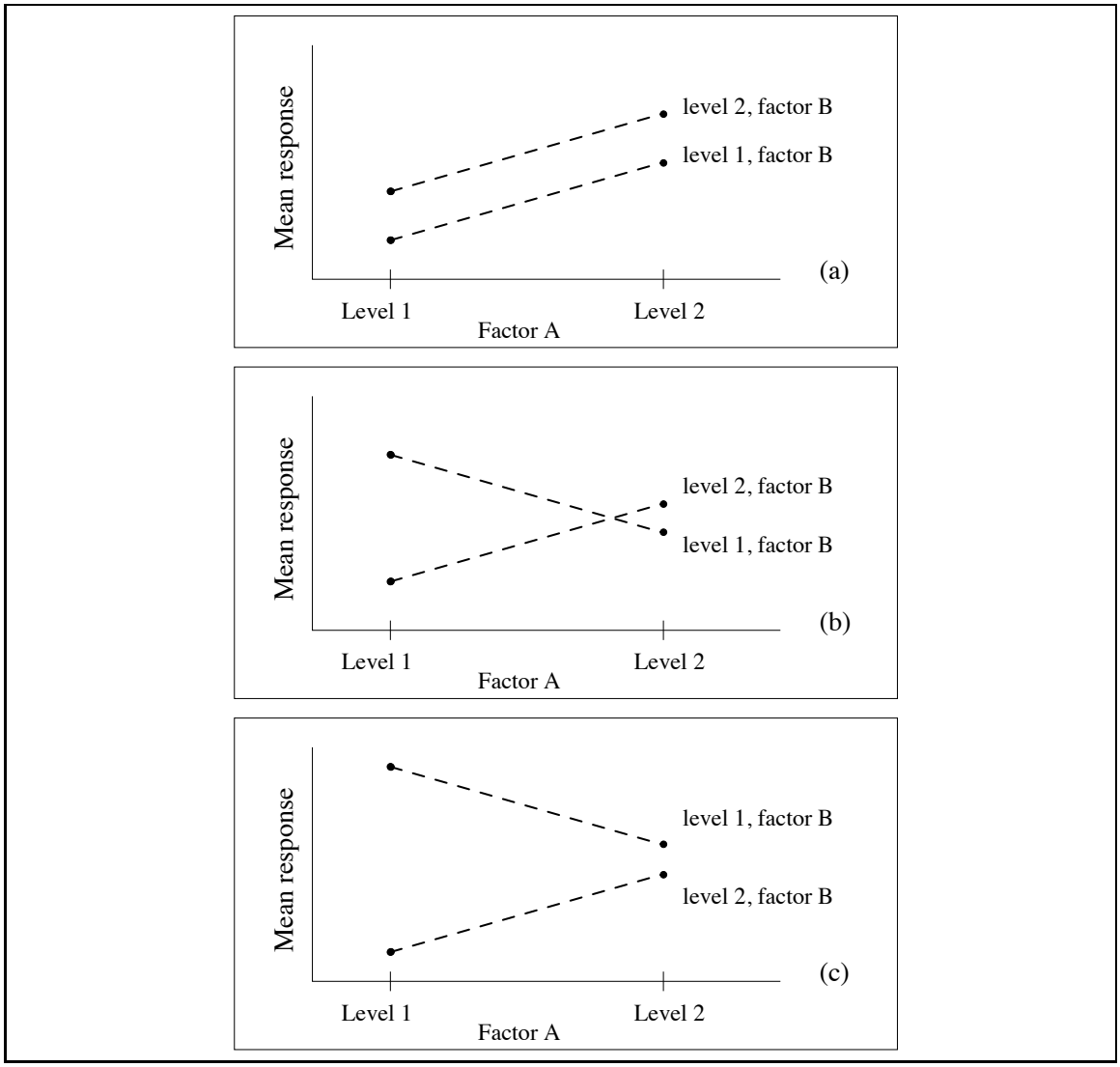

Fig. D.2 Interaction plots for a 2 × 2 factorial experiment: (a) No interaction between factors A and B; (b) and (c) Interaction between factors A and B

the model equation as shown below for the non-additive model:

$$y_{ijkl} = \mu + \alpha_i + \beta_j + \alpha\beta_{ij} + \epsilon_{ijk} + \eta_{ijkl} \tag{D.3}$$

where y_{ijkl} is the response obtained for the lth observation for the kth replicate at the ith level of factor A and jth level of factor B and η_{ijkl} is called the observational error associated with the ith level of factor A, the jth level of factor B and the kth replicate. It is independent and normally distributed with mean 0 and variance σ_η^2.

D.2 SAS

The software SAS was used to perform the statistical analysis. This section includes an example of the code written for a factorial design with repeated measures as well as the output generated by the sofware.

D.2.1 Code e-matrix.sas

In the following code, w is the load, v is the speed, t is the phase number (or time), rep is the replicate.

```
options nonumber ls=80 date;
data matrix;
input   w $     v $     t       rep     rate    wear    depth;
datalines;
        low     low     1       1       0.28    78.00   -2.70
        ⋮                       ⋮                       ⋮

;
run;
proc print data=matrix;
run;

proc mixed data=matrix;
class w v t rep;
model rate=w v w*v t w*t v*t w*v*t/p clm;
random rep(w*v) t*rep(w*v);
lsmeans w v w*v t w*t v*t w*v*t
run;
```

D.2.2 Results `e-matrix.lst`

The MIXED Procedure
Class Level Information

Class	Levels	Values
W	2	high low
V	2	high low
T	4	1 2 3 4
REP	2	1 2

The MIXED Procedure
REML Estimation Iteration History

Iteration	Evaluations	Objective	Criterion
0	1	-258.8140052	
1	2	-271.7168988	0.00000000

Convergence criteria met.

The MIXED Procedure
Covariance Parameter Estimates (REML)

Cov Parm	Ratio	Estimate	Std Error	Z	Pr $>\|Z\|$
REP(W*V)	0.35071392	0.00792012	0.00660120	1.20	0.2302
T*REP(W*V)	0.00000000	0.00000000	.	.	.
Residual	1.00000000	0.02258286	0.00307314	7.35	0.0000

The MIXED Procedure
Model Fitting Information for RATE

Description	Value
Observations	128.0000
Variance Estimate	0.0226
Standard Deviation Estimate	0.1503
REML Log Likelihood	32.9373
Akaike's Information Criterion	29.9373
Schwarz's Bayesian Criterion	25.8596
-2 REML Log Likelihood	-65.8747

The MIXED Procedure

Solution for Fixed Effects

Parameter	Estimate	Std Error	DDF	T	Pr $>\|T\|$
INTERCEPT	0.08438750	0.08235849	96	1.02	0.3081

The MIXED Procedure
Solution for Fixed Effects

Parameter	Estimate	Std Error	DDF	T	Pr $> \|T\|$
W high	0.06932500	0.11647249	96	0.60	0.5531
W low	0.00000000	.	.	.	.
V high	0.00055000	0.11647249	96	0.00	0.9962
V low	0.00000000	.	.	.	.
W*V high high	0.09481250	0.16471697	96	0.58	0.5662
W*V high low	0.00000000	.	.	.	.
W*V low high	0.00000000	.	.	.	.
W*V low low	0.00000000	.	.	.	.
T 1	0.08247500	0.07513798	96	1.10	0.2751
T 2	-0.00376250	0.07513798	96	-0.05	0.9602
T 3	-0.02887500	0.07513798	96	-0.38	0.7016
T 4	0.00000000	.	.	.	.
W*T high 1	0.11861250	0.10626115	96	1.12	0.2671
W*T high 2	0.14331250	0.10626115	96	1.35	0.1806
W*T high 3	0.09877500	0.10626115	96	0.93	0.3549
W*T high 4	0.00000000	.	.	.	.
W*T low 1	0.00000000	.	.	.	.
W*T low 2	0.00000000	.	.	.	.
W*T low 3	0.00000000	.	.	.	.
W*T low 4	0.00000000	.	.	.	.
V*T high 1	0.03573750	0.10626115	96	0.34	0.7374
V*T high 2	0.01068750	0.10626115	96	0.10	0.9201
V*T high 3	0.02077500	0.10626115	96	0.20	0.8454
V*T high 4	0.00000000	.	.	.	.
V*T low 1	0.00000000	.	.	.	.
V*T low 2	0.00000000	.	.	.	.
V*T low 3	0.00000000	.	.	.	.
V*T low 4	0.00000000	.	.	.	.
W*V*T high high 1	-0.11515000	0.15027596	96	-0.77	0.4454
W*V*T high high 2	-0.14141250	0.15027596	96	-0.94	0.3491
W*V*T high high 3	-0.06797500	0.15027596	96	-0.45	0.6520
W*V*T high high 4	0.00000000	.	.	.	.
W*V*T high low 1	0.00000000	.	.	.	.
W*V*T high low 2	0.00000000	.	.	.	.
W*V*T high low 3	0.00000000	.	.	.	.
W*V*T high low 4	0.00000000	.	.	.	.
W*V*T low high 1	0.00000000	.	.	.	.
W*V*T low high 2	0.00000000	.	.	.	.
W*V*T low high 3	0.00000000	.	.	.	.
W*V*T low high 4	0.00000000	.	.	.	.
W*V*T low low 1	0.00000000	.	.	.	.
W*V*T low low 2	0.00000000	.	.	.	.
W*V*T low low 3	0.00000000	.	.	.	.
W*V*T low low 4	0.00000000	.	.	.	.

The MIXED Procedure
Tests of Fixed Effects

Source	NDF	DDF	Type III F	Pr > F
W	1	4	5.93	0.0716
V	1	4	0.13	0.7411
W*V	1	4	0.01	0.9251
T	3	12	4.92	0.0187
W*T	3	12	0.40	0.7585
V*T	3	12	0.24	0.8699
W*V*T	3	12	0.34	0.7963

Appendix E

DSC and DMA results

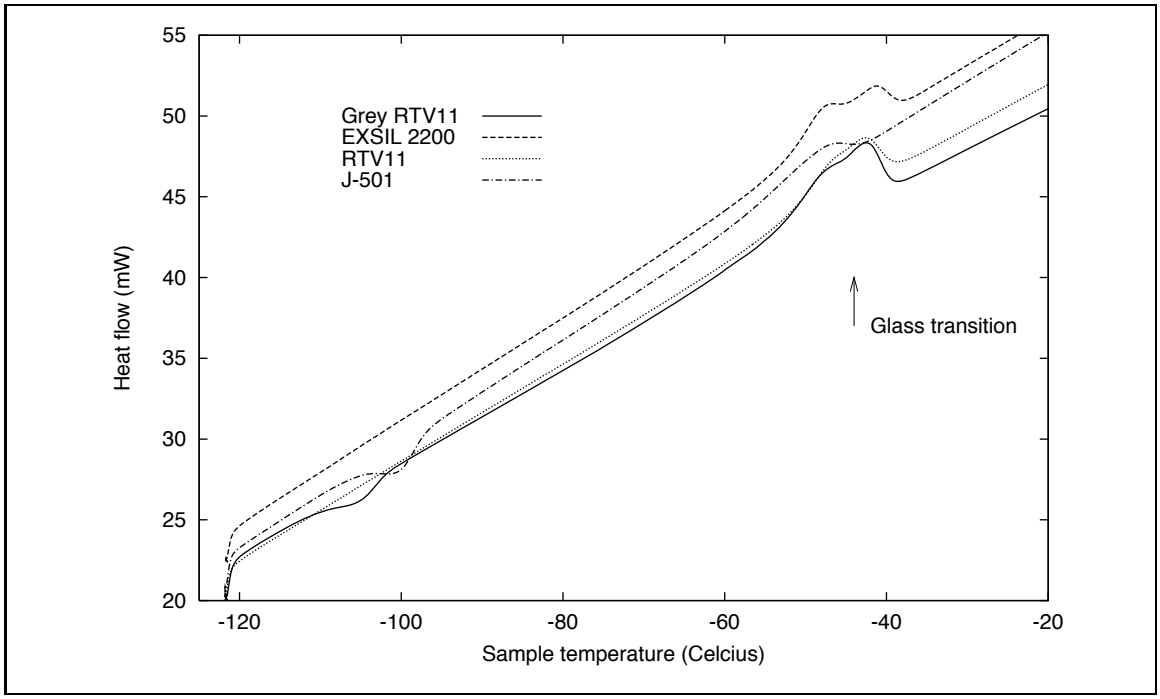

Fig. E.1 Second DSC traces for four silicone rubber materials. Heating rate is 10°C/min.

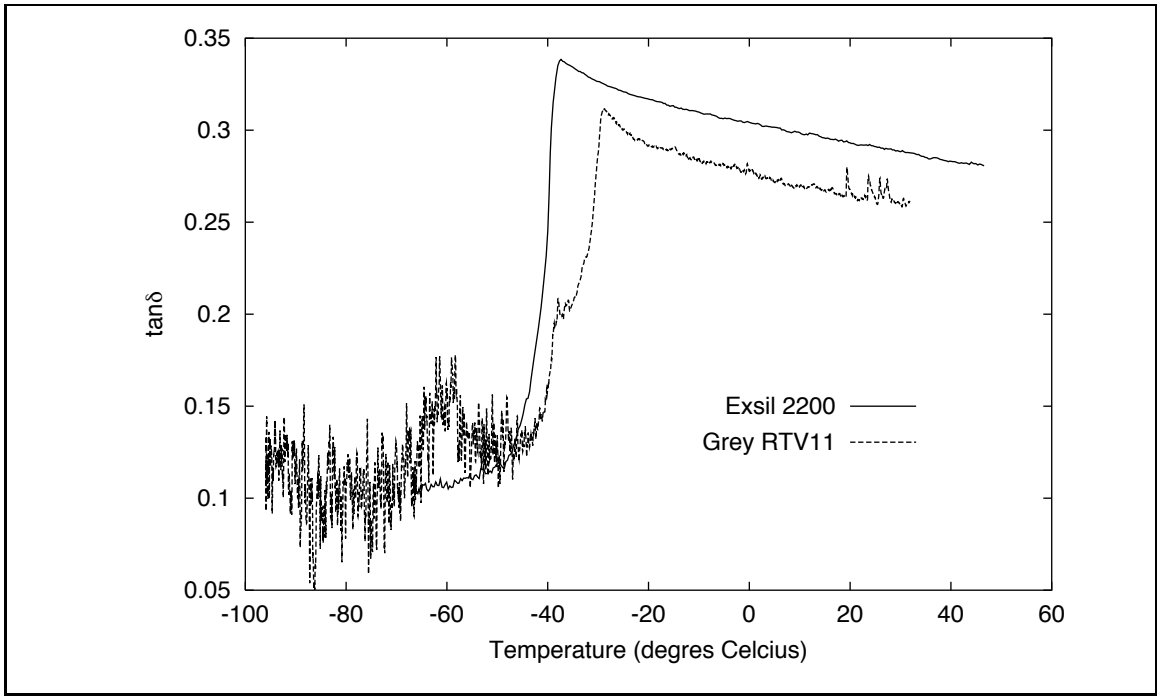

Fig. E.2 Plot of the loss tangent, tanδ, as a function of temperature for grey RTV11 and Exsil® 2200

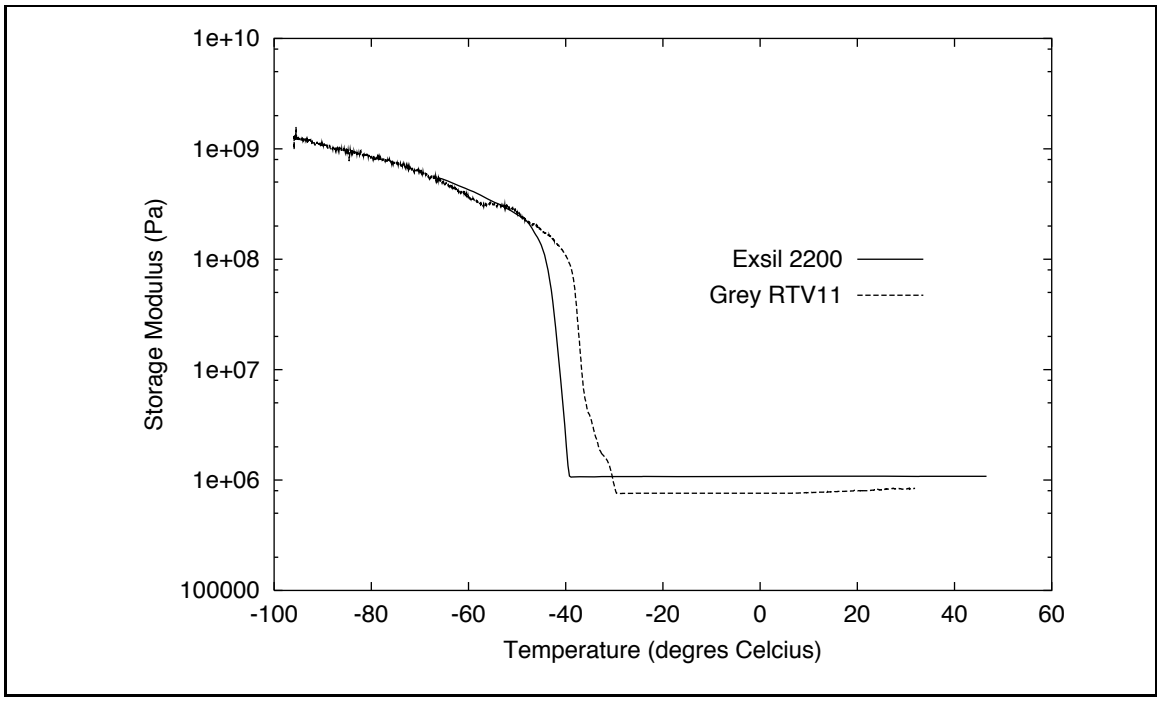

Fig. E.3 Plot of the storage modulus, E, as a function of temperature for grey RTV11 and Exsil® 2200

Appendix F

Penetration of the profiler stylus into the specimen

The depth of penetration of the profiler stylus into the samples can be estimated by theoretical considerations as well as experimental investigations. Indeed, the Hertzian theory of contact stresses (Hertz, 1896) can be applied to evaluate the radius of the contact area between an indenter and a surface of known geometries. Knowing the radius of the contact area and the shape of the stylus is sufficient to estimate the depth of penetration. Experimental investigation can be conducted by measuring the width of the track left by a profiler stylus on a sample. This chapter deals with the theoretical approach in a first time and with the experimental approach in a second time.

F.1 Hertzian theory

The penetration of the profiler stylus in the top layer of a specimen sample is estimated using the Hertzian theory of contact. The calculations are conducted for GE RTV11 as well as for Wacker Silgan® J-501.

F.1.1 Assumptions

The profiler stylus is a diamond stylus which is approximated, as seen on figure F.1, as a cone with a spherical tip. Table F.1 summarizes the characteristics and the mechanical properties for the materials used as well as the contact conditions.

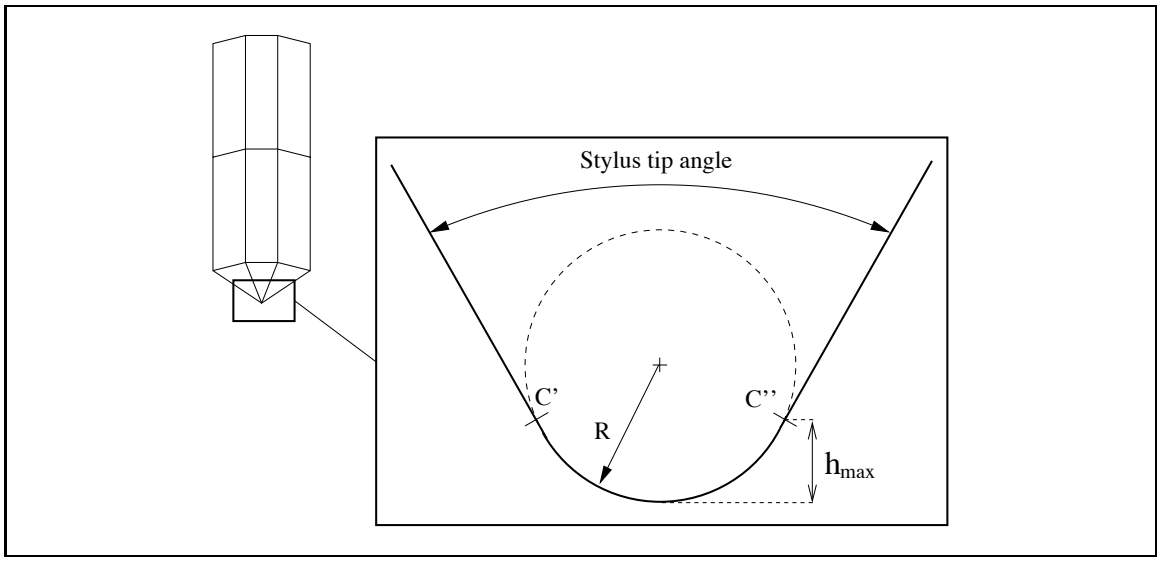

Fig. F.1 Schematic representation of the profiler stylus

Table F.1 Characteristics of the indenter and the indented surface

		Indenter (1)	**Surface (2)**	
Geometry		Sphere	Flat	
Radius	(μm)	R_1=12.5	$R_2 = \infty$	
Material		Diamond	RTV11	Silgan® J-501
Modulus of Elasticity, E	(GPa)	724	n/a	n/a
Poisson's ratio, ν		0.3	n/a	n/a
Effective mod. of elasticity[1], E^*	(GPa)	795.6	0.003[2]	0.023[2]
Tensile yield	(MPa)	19600	n/a	n/a
Applied load	(N)		15×10^{-5}	

[1]Defined as: $E^* = (E/(1-\nu^2))$

[2]Data obtained with a Fischerscope continuous indentation tester at the N.R.L. by Dr. Singer.

In order to apply the Hertzian theory of contact to the profiler stylus contacting the coatings, the following assumptions are made:

- the coatings surface is ideally flat and the stylus surface is ideally smooth;
- there is no flow of material around the stylus,
- there is no friction effect,
- the coatings are sufficiently thick to behave as bulk material: the substrate does not affect the contact conditions, i.e. we assume that the depth of penetration of the stylus does not exceed 1/10th of the thickness of the top layer of the multi-layered coating, and
- the coating behaves as a linear ideal elastic material, i.e. $\sigma = \mathrm{E}\epsilon$ (Hooke's law).

Since no permanent deformation can be observed with the microscope, we assume that, for the test conditions and the given materials, the regime of the deformation is purely elastic.

F.1.2 Results

Figure F.2 (a) represents the projected contact area, A_{ps}, between the stylus and the flat under static conditions. The contact radius, a, under Hertzian elastic contact of a spherical indenter on a flat surface is:

$$a = \left(\frac{3}{4}\frac{WR}{E'}\right)^{\frac{1}{3}} \tag{F.1}$$

where a is the contact radius, W is the applied normal load, R is the effective radius of curvature and E' is the effective contact modulus.

The relationship between the penetration depth h_s, the stylus radius R and the contact radius a, under static conditions, is given by:

$$h_s = R - (R^2 - a^2)^{\frac{1}{2}} \tag{F.2}$$

Figure F.2 (b) represents the projected contact area, A_{pv}, between the stylus and the flat under sliding conditions. Since the load is assumed constant, the projected area A_{pv} is equal to A_{ps}:

$$A_{pv} = \frac{1}{2}\pi r^2 = A_{ps} \tag{F.3}$$

where r is the contact radius under sliding conditions as shown on figure F.2 (b) and r is equal to $a\sqrt{2}$. The relationship between the penetration depth h_v, the stylus radius R and

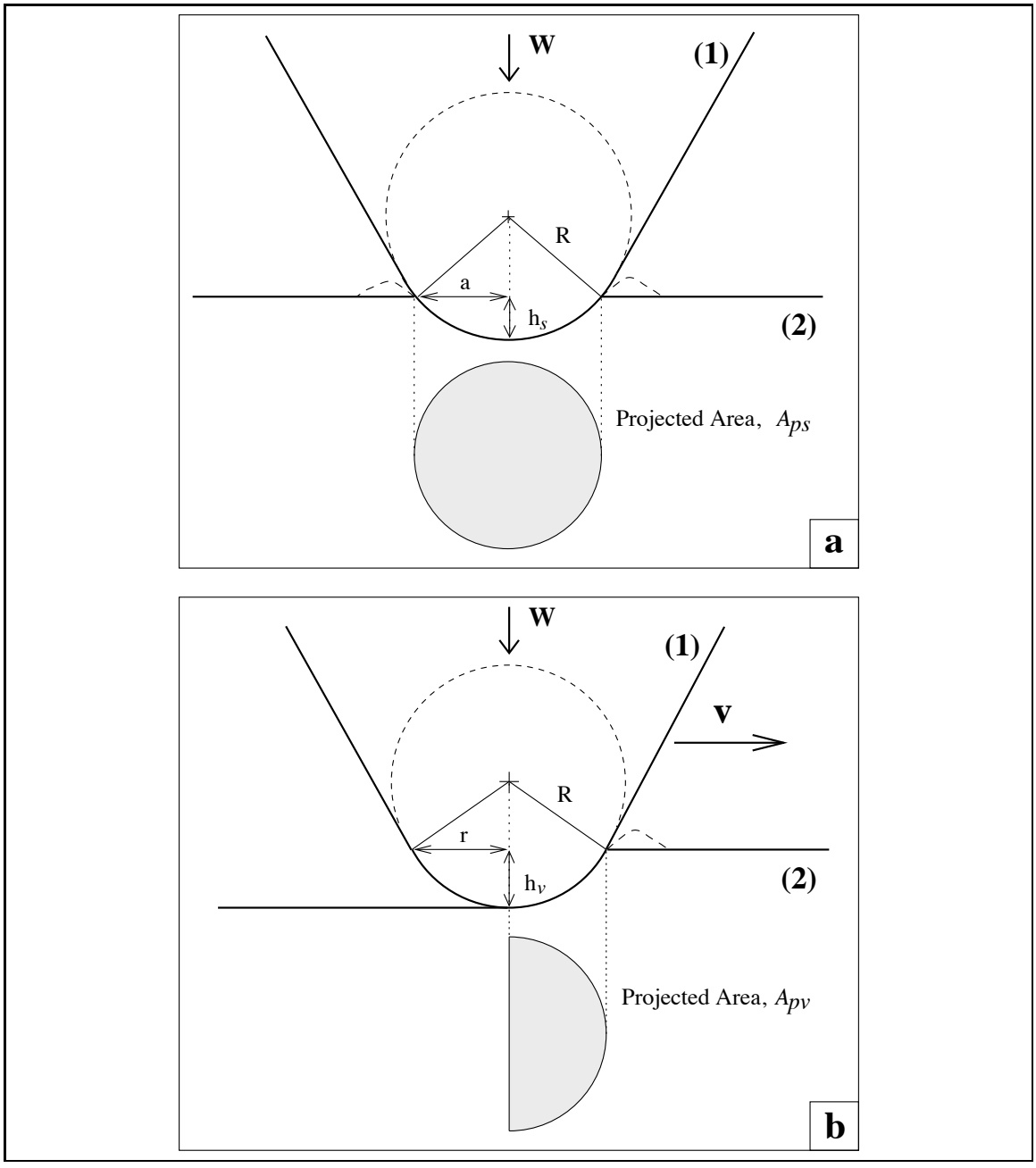

Fig. F.2 Schematic representation of the area of contact between a spherical indenter and a flat surface in (a) the static case and (b) the sliding case

Table F.2 Values of the contact radius and depth of penetration (Hertzian theory) under static and sliding conditions using values from table F.1

		RTV11		Silgan® J-501	
Test conditions		Static	Sliding	Static	Sliding
Contact radius	μm (mil)	7.77 (0.31)	10.99 (0.43)	3.94 (0.16)	5.6 (0.22)
Penetration depth	μm (mil)	2.71 (0.11)	6.54 (0.26)	0.64 (0.025)	1.31 (0.05)

the contact radius r, under sliding conditions, is given by:

$$h_v = R - (R^2 - r^2)^{\frac{1}{2}} \tag{F.4}$$

Equations F.2 and F.4 lead to the evaluation of the depths of penetration in the static and sliding cases. Results are presented in table F.2.

This shows that the diamond stylus traveling on G.E. RTV11 coatings indents the surface more readily than it indents Silgan® J-501 coatings. However, even in the most severe case of the sliding contact, the depth of penetration of the diamond stylus in RTV11 calculated is 6.54 μm. This represents about 5% of the dry film thickness for the thinnest coatings considered in this study (5 mil or 127 μm thick top coats). For the evaluation of the wear area, this amount of indentation is assumed constant throughout the overall scan and therefore it is neglected.

Figure F.3 illustrates the effect of varying the loading force on the depth of penetration of the diamond stylus in the coatings, in both the static and the sliding cases. The Hertzian theory predicts that, in the case of a soft surface such as RTV11 under sliding conditions, a small increase in the load from 15 mg would result in a rapid increase in the depth of penetration. Under the assumptions stated here, a load of 15 mg is an acceptable choice.

F.1.3 Discussion

The previous results were obtained using the Hertzian theory based on specific assumptions.

Bulk Behavior The depth of penetration does not exceed 5% of the thickness of the coatings. This is well under the limit of 10% where it was previously observed that the substrate starts to influence the contact conditions (Bolster and Singer, 1996).

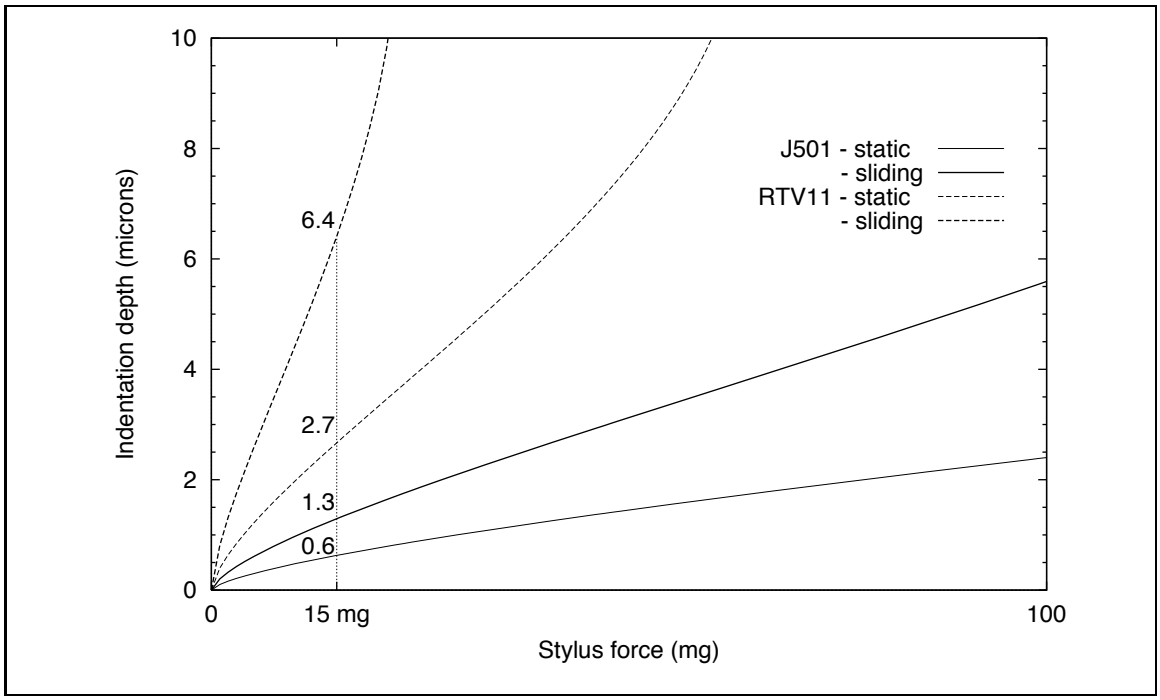

Fig. F.3 Depth of indentation as a function of stylus force

Spherical stylus We have assumed that the profiler stylus can be schematically represented as a cone with a spherical tip (figure F.1). If the stylus penetrates the sample exceedingly, the assumption of spherical indenter will no longer be valid. C' and C" on figure F.1 represent the geometrical points where the cone shape of the stylus can no longer be neglected. The contact radius, r_{max}, and the indentation depth, h_{max}, corresponding to these points are equal to, respectively, $r_{max} = 10.82\,\mu$m and $h_{max} = 6.25\,\mu$m. As can be seen in figure F.3, for 15 mg, the values calculated for the indentation depths are below these limiting values. However, for higher loads, the estimated value of the penetration depth for RTV11 under sliding conditions is much larger than h_{max}. In conclusion, the assumption of spherical tip is valid for low loads for soft substrates such as RTV11 and for all loads (up to 100 mg) for harder substrates such as Silgan® J-501.

Contact radius $\ll$ stylus radius R? This is not always verified by the calculation and is a major limitation to using the Hertzian theory of contact stresses.

Visco-elastic properties In this theory, the visco-elastic properties of the material are not taken into account as Hooke's law is assumed valid. For a highly visco-elastic

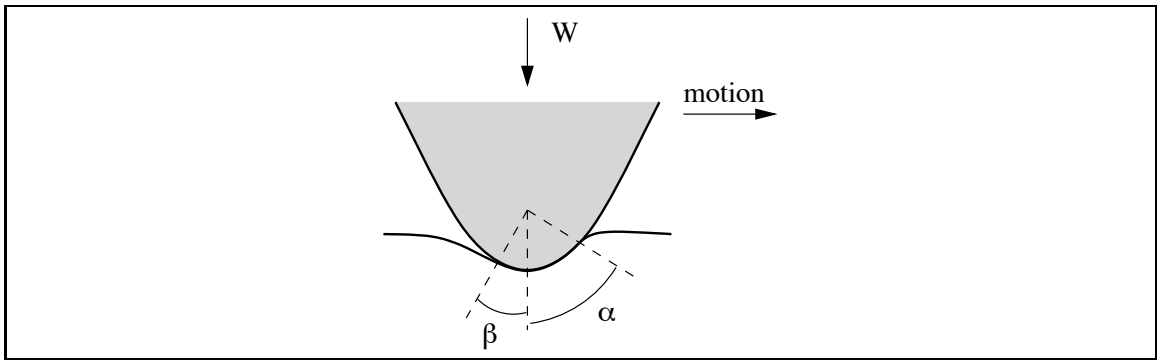

Fig. F.4 Elastically deformed material under sliding conditions

material under sliding conditions, the geometry of the contact is characterized by Fig. F.4 where the angles α and β are dependent upon test conditions. β is determined by the rate of elastic recovery of the material. As the velocity increases, the resistance to penetration increases (Gilliam, 1985). Therefore, the depth of penetration decreases as well.

F.2 Measurement of the stylus track width

When the shape of the indenter is known and when the surface is assumed ideally flat, the depth of penetration can be related to the width of the contact area, i.e. the width of the track left by a stylus in a surface. In order to complement the previous analysis, an experimental study of the stylus track was conducted.

Visco-elastic properties of the material studied are assumed negligible in the Hertzian theory. However, Gilliam (1985) reported that for visco-elastic materials, as the travel speed of the stylus increases, the viscous damping property increases and the resistance to deformation is greater. As a result, the stylus does not indent the material as much.

In this section is discussed an experimental investigation of the width of the stylus track and its dependence upon parameters such as stylus force, stylus traveling speed, and sample materials.

F.2.1 Experiments

In order to visualize the track under the microscope, the samples were lightly coated with glycerin before a profile was taken. Following the profiler run, the sample was examined with the microscope under polarized light and the width of the stylus track was measured.

Table F.3 Test parameters for the characterization of stylus track width

Factor	*Stylus force (mg)*	*Travel speed ($\mu m/s$)*
Level 1 (low)	15	10
Level 2 (high)	95	200

Samples tested	*Thickness (top/bond) (μm)*
RTV11 on Silgan® J-501/ glass	**450**/150
NRL15/5 on Silgan® J-501/ steel	**450**/350
Silgan® J-501 on steel	0/**500**
Exsil® 2200 on Silgan® J-501/ fiber glass	**250**/250

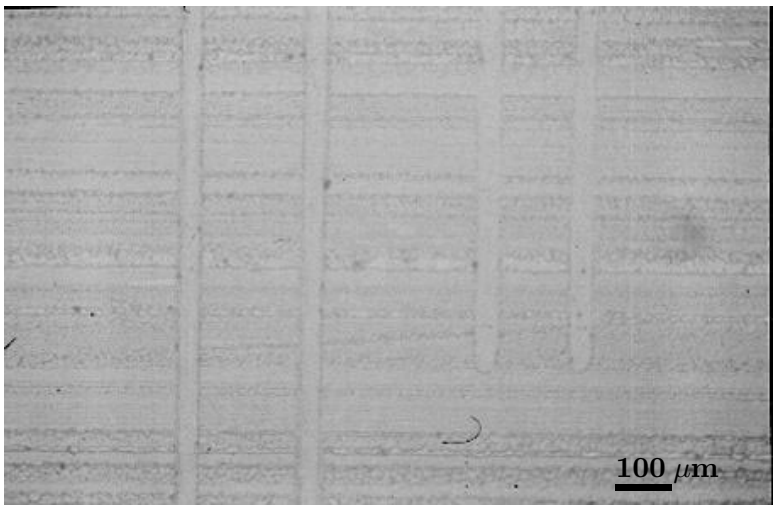

Fig. F.5 Microscopic picture of the RTV11 coated sample showing the 4 tracks left by the stylus at high load level (95 mg). Short traces correspond to low speed scanning and long traces to high speed scanning.

Spreading glycerin on the coatings helps locate the tracks left by the stylus.

Profiles of four different samples were collected, for two levels of stylus force (low and high), and for two levels of traveling speed (low and high) as seen in table F.3.

Figure F.5 is a microscopic picture of tracks left by the stylus on a RTV11 coating with a loading force of 95 mg. The shorter tracks correspond to the low level of speed and the longest ones to the high level speed. For one set of test conditions, the profiles were collected twice at different locations on the sample. The width is measured using the video camera and the TV monitor, and the average of 4 values is recorded.

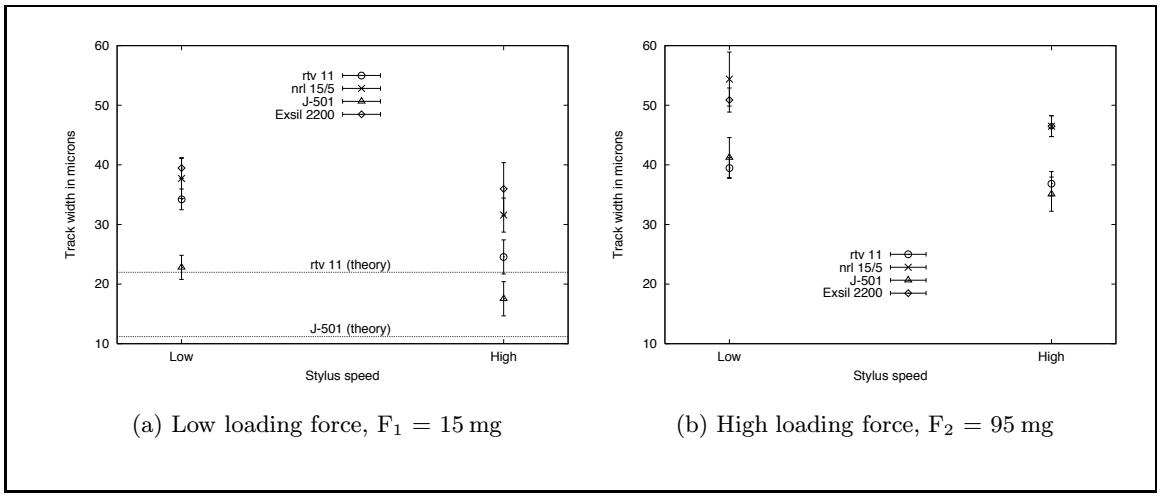

(a) Low loading force, $F_1 = 15$ mg

(b) High loading force, $F_2 = 95$ mg

Fig. F.6 Effect of the stylus speed on the depth of indentation of a 12.5 μm diamond stylus under (a) low loading force and (b) high loading force

F.2.2 Results

The results are plotted on figures F.6 (a) and F.6 (b). The theoretical values of the depth of penetration found in the previous section with the Hertzian theory for RTV11 and Silgan® J-501 are plotted as well as horizontal lines.

For all samples, the track width increases with an increasing stylus force, regardless of the speed level. This trends is very pronounced for sample Silgan® J-501, for which the width of the track nearly doubled upon load increase. The track width decreases as the traveling speed increases for all samples studied as observed and discussed previously by Gilliam (1985). Therefore, the combination of a low loading force and a high traversing speed lead to the lowest depth of penetration for all samples. Under these former conditions, the samples studied can be ranked in terms of track width, from a low value to a high value, as follows: Silgan® J-501 < RTV11 < NRL15/5 < Exsil® 2200. Assuming that the relationship between the track width, $2r$, and the depth of penetration is established by the geometry and not by other factors (such as tackiness of a sample versus another), the above ranking of the samples can be tentatively generalized to depth of penetration as well. A statistical analysis (Tukey's test) conducted on the width data reveals that there is no significant difference between the Exsil® 2200 sample and the NRL samples. However, there is significant differences between Silgan® J-501, RTV11 and (Exsil® 2200 or NRL). The statistical analysis also confirms that there are significant differences between load levels and speed levels with p-values of 0.0001.

The thicknesses are indicated in table F.3 for the various layers of the candidate samples. No relationship between the width of the track with the sample thickness can be observed.

F.2.3 Discussion

This is a rough experimental verification of the phenomenon. It would be interesting to use scanning electron microscopy to see if any microscopic permanent damage occurs after one pass of the stylus on the surface.

As can be seen on figure F.6 (a), the values of the stylus track widths under low load are all larger than the theoretical values derived in the previous section. This may be explained by penetration of the stylus past h_{max}, as well as by conformation of the surface to the stylus due to its high elasticity. Also, the use of glycerin introduces some error in the measured width of the wear track as it spreads differently on the samples depending on their surface energy. This was particularly observed for Silgan® J-501 where the glycerin appeared to "retract" and therefore the low value of track width could be due to the error induced by the spreading of glycerin, not by the actual surface properties. We can also note that the measured values for the track width all exceed the stylus diameter. The tests conditions chosen in the overall study (low load, high speed) to limit the penetration and deformation of the surface by the stylus are low stylus force (15 mg) and high speed (200 μm). This study confirms that the selection of a high scanning speed coupled with a low loading stylus force is appropriate for the samples studied.

Appendix G

Stiffness of brushes

Studies of toothbrushes are divided into three categories.

The first and most frequent category deals with the evaluation of toothbrush performance as a function of design characteristics, mechanical properties or test conditions (Rawls et al., 1990; Nygaard-Ostby et al., 1979). A toothbrush is designed to create efficient cleaning forces and to easily access difficult areas where plaque can be detrimental. As a results, the criteria used is the interproximal access. It has been shown to be greatly dependent upon changes in the brush design. Stiffness of a toothbrush is directly related to its design characteristics, therefore it has been recognized as a primary player for brush efficiency (Golding, 1981; Nygaard-Ostby et al., 1979).

The second category of tests involving brushes are tests which evaluate brush wear, either for toothbrushes or for electrical brushes.

The third and last category is the least frequent and is one that evaluates damage caused to the sample by the brushes (Efraimsen et al., 1990). Permanent splaying is the most visually apparent manifestation of brush wear, and therefore is the accepted criteria. For commercial toothbrushes, Rawls et al. (1993) showed that design features are not significant to brush wear. However, the cleaning efficacy of a brush decreases as the brush wears out. The typical bend recovery of commercial toothbrushes exceeds 94%. Permanent splaying was shown to increase linearly at first (3,000 revolutions) and then it slows down and forms a plateau (Rawls et al., 1993).

Since stiffness is such an important characteristic of the brushes, the first section of this chapter presents a mathematical model by Rawls et al. (1990), model which relates

stiffness to brush characteristics. In the second section, it is utilized to evaluate the stiffness of the brushes used in the experiments conducted.

G.1 Mathematical model for toothbrush stiffness

Rawls et al. (1990) studied how the stiffness of individual bristles can influence the overall brush stiffness and developed a first-order model which can serve as a guide for studying the effects of toothbrush parameters, or for improving toothbrush design. The base of his model is that the stiffness of a brush is the sum of all the stiffnesses of the component bristles in addition to any contribution from bristle interactions. As a consequence, factors such as bristle modulus, diameter, length, cross-sectional shape, and composition as well as bristle interaction are important (Golding, 1981).

According to its engineering definition, stiffness (N/m) is the force developed to bend a bristle divided by the bristle deflection. The stiffness G_b of a single bristle is:

$$G_b = F_b/d \tag{G.1}$$

where F_b is the force applied to the bristle and d is the deflection of the bristle at the point of loading. For the overall brush, the stiffness is equal to the sum of all the stiffness of the component bristles, i.e.

$$G_{\text{brush}} = N_b G_b = N_b F_b / d_{\text{avg}} \tag{G.2}$$

where G_b is the stiffness of a single bristle, N_b is the number of bristles per brush and d_{avg} is the average deflection of a single bristle within the brush.

Rawls et al. (1990) computed stiffness values for various brands of toothbrushes with two methods: the "calculated" and the "measured" methods. Both methods are based on beam theory to calculate the force versus deflection relationship.

Beam theory applied to a bristle If a bristle is assumed to bend as a beam when loaded in the transverse direction, the maximum deflection, $d_{\max}$, is equal to:

$$d_{\max} = F_b A^2 (3L - A)/(6EI) \tag{G.3}$$

where the moment of inertia I is function of the beam cross-sectional geometry (Roark and

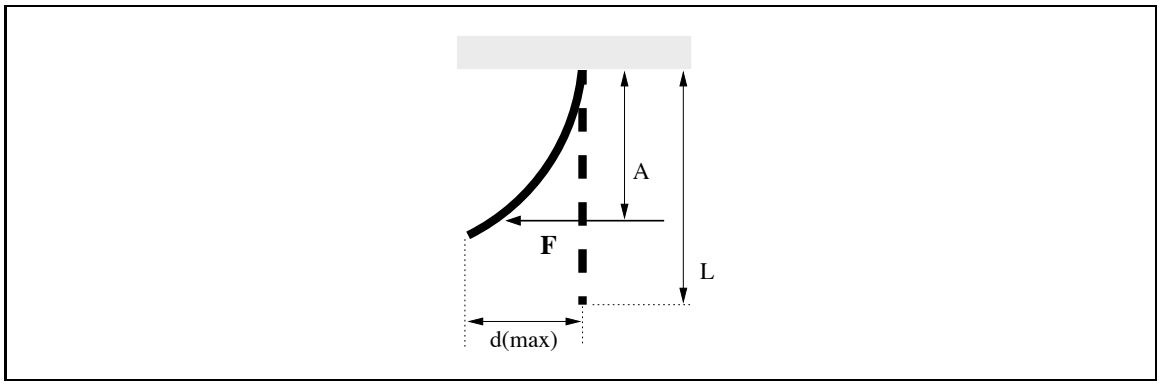

Fig. G.1 Brush bristle modelled as a flexible cantilever beam per Rawls et al. (1990). F is the applied force, A is the point where the force is applied (loading point), $d_{\max}$ is the maximum deflection and L is the length of the bristles.

Young, 1989). A, L and $d_{\max}$ are defined on figure G.1. A multiplicative factor corrects for the axial loading and Eqn. G.3 becomes:

$$d_{\max} = 1.65 F_b A^2 (3L - A)/(6EI). \tag{G.4}$$

"Calculated" bristle stiffness In this method, bristle geometry and material properties, in particular the tensile modulus, are of consideration. It has been shown that the tensile modulus is proportional to bending modulus (Beke, 1967) for small deflections. The tensile modulus of bristles can be determined easily with standard tensile testing techniques.

If the bristle force, F_b, is assumed proportional to the deflection, d, then:

$$G_b = F_b/d = K \tag{G.5}$$

where K is a function of bristle geometry and the modulus of elasticity E of the bristle material.

Rawls et al. (1990) assumed that the point of loading remained fixed as the bristle deflects ($A = 2/3L$). For cylindrical bristles, the maximum deflection and the "calculated" bristle stiffness, G_c are then equal to:

$$d_{\max} = 0.285 F_b L^3/EI \tag{G.6}$$

$$G_c = F_b/d = 3.5 E \pi D_B^4/64L^3 \tag{G.7}$$

"Measured" bristle stiffness Values of the brushing forces determined experimentally are used to calculate the deflection of the bristles and subsequently bristle stiffness. Details of the experimental apparatus and procedure can be found elsewhere (Rawls et al., 1990). The buckling load, P_{cr}, which is defined as the axial load under which the bristle will buckle, can also be estimated since

$$P_{cr} = \pi^2 EI/(4L^2). \tag{G.8}$$

Brush stiffness The brush stiffness is estimated using both the experimental and the theoretical approaches. The correlation between the "measured" and the "calculated" stiffness is $G_m = 0.725\ G_c$. The variation between the measured stiffness and the calculated stiffness is due to the presence of friction effects, rate-dependent effects and other assumptions in the description of the bristle stiffness.

Assuming that bristles have circular cross-sections and are packed into circular tuft holes in a hexagonal close-packing organization, Eqn. G.2 becomes

$$G_{\text{brush}} = N_b G_b = N_T P_f (D_T/D_B)^2 G_b \tag{G.9}$$

where N_T is the number of tufts in the brush, P_f is the area of the tuft hole occupied by the bristles divided by the total tuft hole area, D_T is the diameter of the tuft hole, D_B is the diameter of the bristle and G_b is the stiffness of a single bristle.

Substituting equation G.7 into equation G.9 and using the correlation between G_m and G_c, the brush stiffness is then reduced to:

$$G_{\text{brush}} = 0.125 E (D_T D_B)^2 N_T P_f / L^3. \tag{G.10}$$

Equation G.10 is semi-empirical and combines the various assumptions, approximations, empirical adjustment factors, and constants into a single constant, 0.125. The other parameters are representative of the bristle material properties (E), the bristle geometry (D_B and L), and the brush design characteristics (D_T, P_f and N_T).

Rawls et al. (1990) found that the assumption of constant load point in the "calculated" stiffness is a major source of error. Indeed, if the loading point is maintained constant, the maximum deflection resulting from it would be smaller than that obtained under a load point varying from $2L/3$ to L. Therefore, the calculated stiffness is slightly overestimated.

It is important to note that static properties were used in the derivation of equation G.10. Flexible bristles are visco-elastic materials and therefore will tend to respond differently depending on the rate of force delivery. Indeed, Rawls et al. (1990) observed that stiffness of controlled toothbrushes increases as the brushing rate increases above 100 RPM. Other factors such as environmental effects and fatigue will reduce stiffness during use (Rawls et al., 1990) and alter cleaning efficacy.

Other factors which also influence the actual stiffness, such as water adsorption or frictional heating can not be neglected. Indeed, upon water adsorption, the glass temperature of nylon decreases. The temperature of a fiber subjected to frictional heating may rise above the glass temperature, resulting in softening of the fiber, decrease of the modulus of elasticity, and reduction of the initial stiffness.

G.2 Computation of the brush stiffness

Three designs of brushes were considered in the study: the so-called original, first and second designs. Figure 3.10 on page 55 illustrates the geometrical differences of the three designs and table 3.6 summarizes the properties and characteristics of each brush, including information pertinent to bristles and tufts.

The brush stiffness is calculated based on equation G.11, which is a semi-empirical equation derived in the previous section,

$$G_{\text{brush}} = 0.125 \times N_b \times E\frac{D_b^4}{L^3} \tag{G.11}$$

where G_{brush} is the stiffness of the brush, N_b is the number of bristles per brush, E is the modulus of elasticity of the bristles, D_b is the diameter of the bristles and L is the length of each bristle.

G.2.1 Modulus of elasticity of brush bristles

With the Minimat texture analyzer (section 3.3.1), the modulus of elasticity of nylon bristles was measured. Bristles were randomly cut off toothbrushes and half were soaked in salt water for a minimum of 24 hours. The fibers were tested in tension at 1, 2 and 5 mm/min. Figure G.2 shows a typical curve obtained for a wet bristle at 5 mm/min.

Figure G.3 plots the modulus of elasticity for dry and wet bristles. Lines for the average value of the measurements are plotted as well. We observe that the mean value

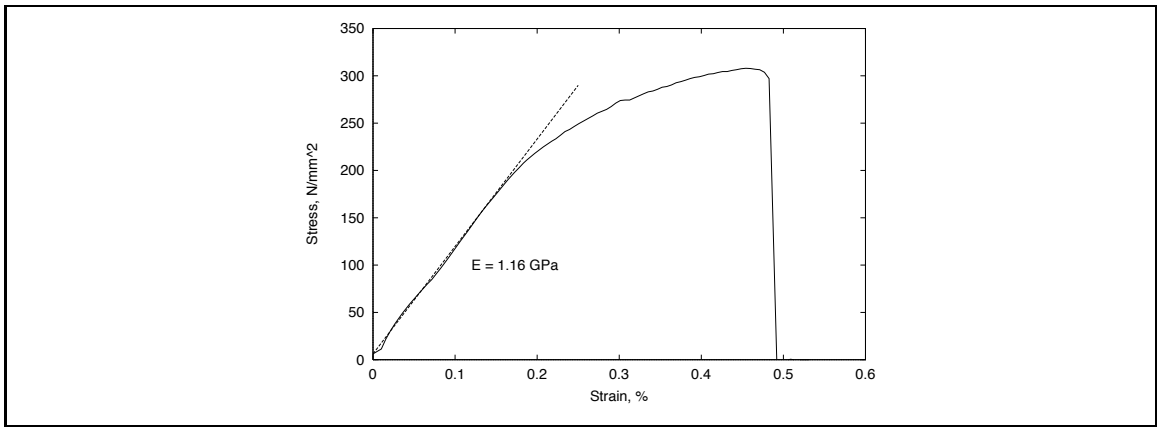

Fig. G.2 Strain-stress curve in tension for a wet nylon bristle. Speed is 5 mm/min

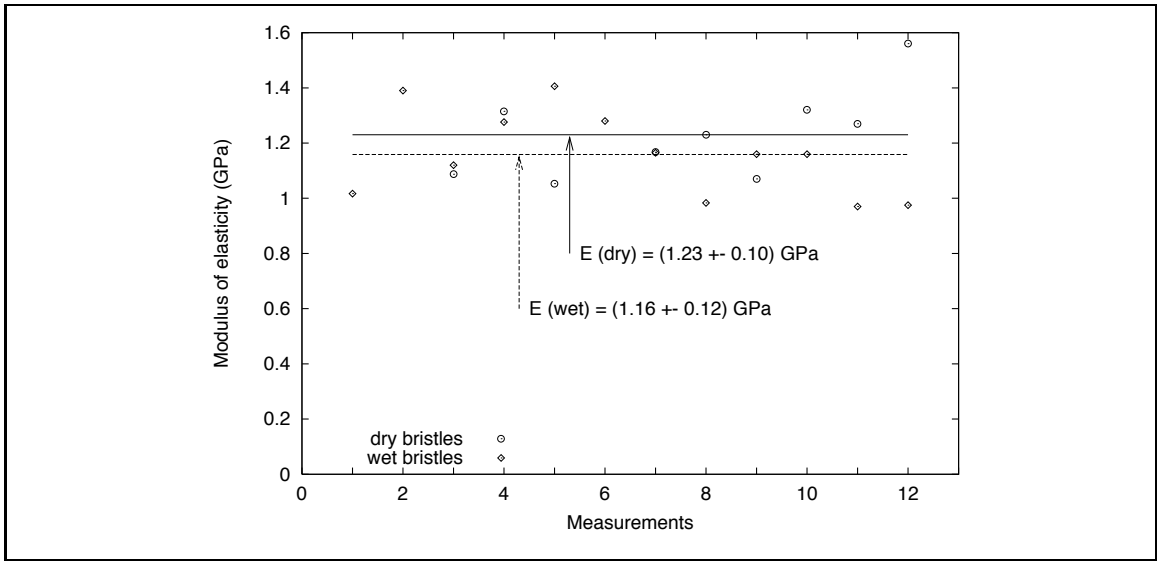

Fig. G.3 Modulus of elasticity of dry and wet nylon bristles, with mean lines.

for the wet bristles is lower than the mean value for the dry bristles. However, the 95% confidence interval for the difference between the means is [-0.0718 ; 0.2158]. Since the interval includes zero, we can conclude that there is no significant differences between the two calculated means. For further computation, the average modulus of elasticity for wet fibers is retained, i.e. $E = 1.16\,\text{GPa}$.

G.2.2 Brush stiffness for three designs

The calculation of the stiffness of a toothbrush head depends on the test configuration, more precisely on the axis of rotation selected. With the 3-brush holder, the axis of rotation is

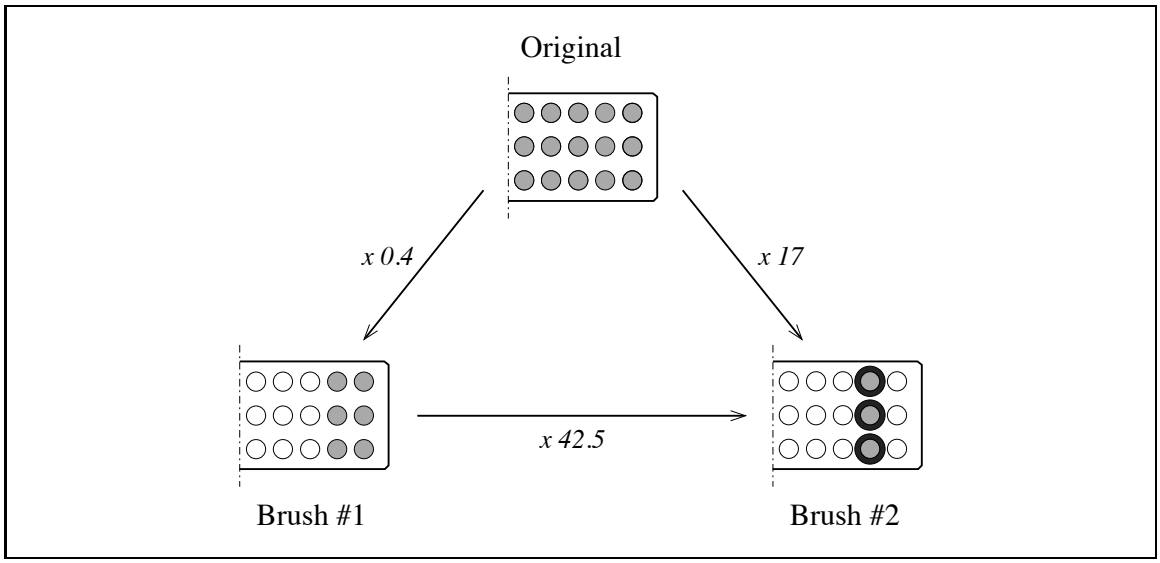

Fig. G.4 Relationship between the brush design and its stiffness. Open circles represent empty tuft holes, grey circles represent original tufts of bristles and black rings indicate stiffened tufts.

located at a point equidistant from the center of the three brushes. In this case, the overall brush stiffness is relevant. In the single-brush holder, the axis of rotation matches with the center of the toothbrush head. Therefore, a given toothbrush is equivalent to two brushes and the stiffness is calculated for half of the overall toothbrush head.

As seen in equation G.11, the important parameters are the modulus of elasticity E and design characteristics such as the number of bristles, the diameter and the length of the individual bristle. The values of these parameters as well as the corresponding stiffness, G_{brush}, are presented in table G.1 for the three brush designs illustrated on figure G.4. All calculations were conducted for the single-brush holder case.

Nylon brush Changes in the design characteristics of the original toothbrush head resulted in multiplying the initial value of stiffness by 17 for brush design #2. Also, as seen by the variation in stiffness data, the reinforcing procedure of the brush tufts was necessary as the stiffness of the brush with design #1 is only equal to 176 N/m, i.e. less than half the stiffness of the original brush head.

Steel brush As shown in table G.1, a similar calculation was conducted for a steel brush with dimensions and characteristics corresponding to a hybrid design, between design #1 and design #2. This particular design was selected to allow a direct comparison between a

Table G.1 Stiffness of three nylon brushes: the Colgate Classic toothbrush head and altered brush heads (Fig. G.4) and an equivalent steel brush

Design	E (GPa)	N_b	D_b (mm)	L (mm)	G_{brush} (N/m)
Original	1.16	570	0.29	11	438
Design #1	1.16	228	0.29	11	176
Design #2	1.16	114	0.29	2.5	7,470
Steel	200	114	0.29	11	15,145

nylon brush of design #2 and a steel brush without the reinforcing construction.

Despite the increase in stiffness due to the reinforcing procedure, the stiffness of a nylon brush with design #2 is lower than an equivalent steel brush. Its stiffness is equal to half that of the steel brush.

G.2.3 Conclusions

It is a very useful equation to quantify the stiffness of a brush. However, its derivation was based on a specific brush configuration and specific experimental analysis. Indeed, the factor 0.125 groups many assumptions and characteristics, in particular the interaction between tufts, interaction which is important in the case of the original design or design #1. However, for the case design #2, the bristles are shortened to such an extent that the interaction in between each tuft is extremely limited, if at all present.

Also, in the equation shown here, we can see that increasing the number of bristles per tuft is equivalent to increasing the number of tufts. However, on a physical point of view, these two procedures are different since the interactions bristle-bristle or tuft-tuft result in different magnitude of stiffness. Therefore, this semi-empirical model is only valid for toothbrushes and should only be applied to other brushes with extreme caution.

The values of stiffness reported here refer strictly to initial conditions and do not take into account environmental effects or fatigue. However, it provides a simple way to define the stiffness of a brush and perhaps a possible correlation with cleaning efficacy.

Appendix H

Experimental error analysis

Reporting experimental results can not be done without estimating the experimental error and its sources. Not only it prevents one from drawing incorrect conclusions, but it also allows one to try to reduce the error level while experimenting.

In the present methodology, sources of error in the wear data are very diverse. Characteristics of the samples, the wear tester as well as the profiler will contribute to the overall error.

Sources of error

Specimen samples The error may arise from the specimen itself. Indeed, the history of the sample affects its behavior. Stress or thermal history (cutting of samples) may alter their structure or morphology of specimen under study. The roughness, waviness and irregularities in the sample may have an impact on the amount of wear. Bubbles trapped in the coatings during curing will decrease the resistance to wear undoubtedly.

Wear tester The alteration of the brushes groups the bristles together, and reduces their ability to conform to the surface. In the case of a soft brushes, any irregularity of the tuft or bristles is not as important.

The alignment of the specimen with the brushes some error as well, particularly when stiff brushes are used. The misalignment of the brushes with respect to the surface of the sample affects the wear area measured. Similarly, as shown in figure H.1, the alignment of the brushes in the holder as well as the alignment of the holder on the motor shaft affect

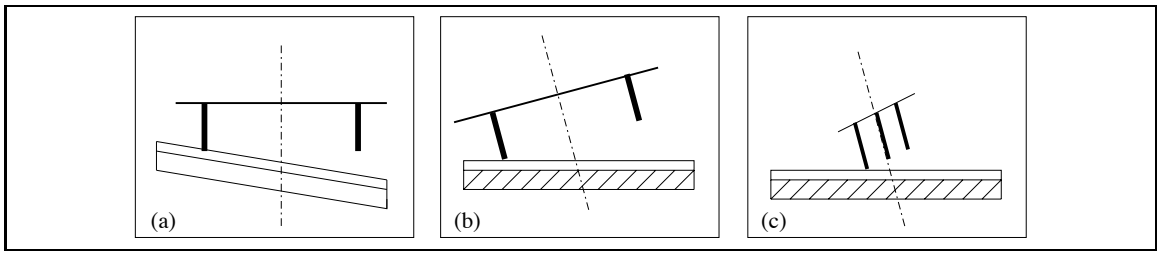

Fig. H.1 Sources of misalignment of the brushes with the sample: (a) misalignment of the specimen sample, (b) misalignment of the holder or brushes, (c) misalignment of the brushes. Phenomena are greatly exaggerated as figures are not at scale for better representation.

the contact conditions and subsequently the wear data.

The estimated number of brush strokes introduces some error as well. Indeed, the number of brush strokes is estimated based on the motor speed (calibration chart included in Appendix B) and on the timer set by the operator. Both elements are sources of errors which will induce some error in the true number of brush strokes.

Profiler Finally, some error in reported values of wear many come from the profilometer itself. This is referred to as the measurement error. The wear area is computed based on the height measurement of the surface features, and therefore it is dependent on the accuracy of the profiler. The depth of penetration of the stylus is likely to be larger for a soft coating. If the depth of penetration of the stylus is constant throughout the scan, then the profile will be representative of the true surface and the error will be minimized. However, if the depth of penetration varies with the coating's thickness, then the measured heights will be affected. For the samples studied, it was estimated that the depth of penetration is less than 5% of the film thickness Hence, this effect can be neglected. Plastic deformation has also been previously ruled out. Another factor which may affect the height measurements is the selection of recipe parameters such as filters. In order to minimize this error, the same recipe was used throughout the experimental tests.

On surfaces where the wear scar is not well defined compared to surface defects or surface roughness, the measurement of the wear area and the maximum depth are affected. Indeed, leveling a surface profile is based on the arbitrary selection of 2 points. When the wear area is well defined with reference to its baseline as shown in figure H.2 (a), the error is minimized. However, when the profile is such as in figure H.2 (b), the selection of leveling cursors will affect the computed wear area and the reported maximum depth.

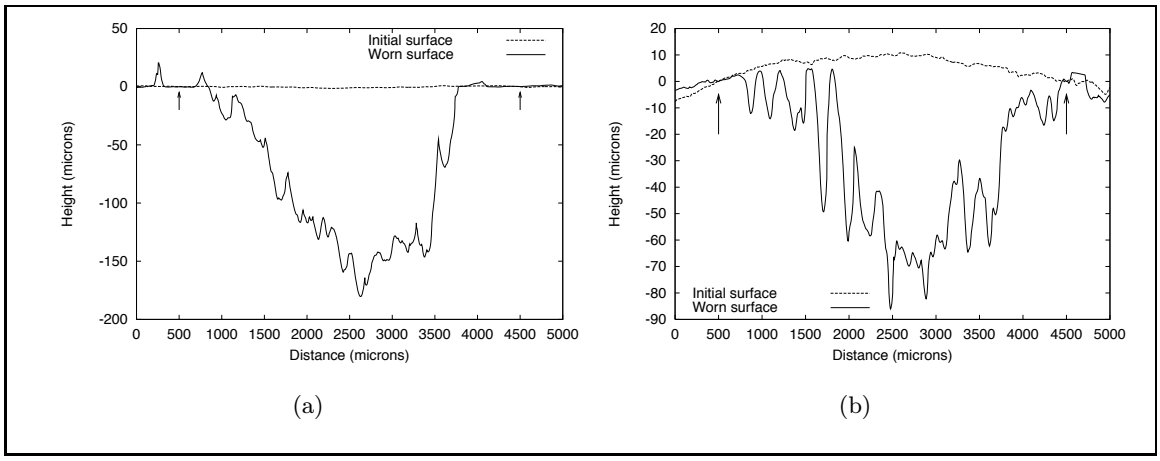

Fig. H.2 Errors in the wear area induced by arbitrary selection of leveling cursors (indicated by arrows)

Procedure to limit errors Monitoring the specimen surface prior to running a wear test is a way to estimate the error caused by the roughness or waviness of the surface.

In order to limit the error introduced as a result of misalignments, the procedure described in Chapter 3 was implemented. Also, the wear area was monitored at four equidistant locations (Fig. 3.23), and averaged out. This is considered to be a bias error.

Careful manipulation of the speed of the motor and of the timer provided a reduced error on the number of brush strokes.

Experimental and theoretical investigations of the effect of the stylus penetration concluded that the value of the penetration is constant throughout a profile as well as repeatable. Therefore, error associated with the profiler is negligible and leveling is performed on a case by case basis.

Error is also introduced by the inability to collect traces at the exact same location in between test phases.

In conclusion, to limit error in data, careful and consistent manipulation is critical.

Measurement error The measurement error on the wear area and the maximum depth are estimated. The measurement error on the wear rate is deducted from the measurement error of the wear area.

The first step is assuming that the variation of the wear area along the wear scar is linear. Therefore, the wear area, $A_{\text{meas.}}$, is assumed equal to the average of four measurement points, made at four equidistant locations on the wear scar (as shown on figure 3.23 on

page69).

$$A_{\text{meas.}} = \frac{(a_1 + a_2 + a_3 + a_4)}{4} \tag{H.1}$$

where a_i are the values for the wear areas at location i.

The measurement error is then:

$$\Delta A_{\text{meas.}} = \frac{(\Delta a_1 + \Delta a_2 + \Delta a_3 + \Delta a_4)}{4} \tag{H.2}$$

Δa_i is the measurement error on the wear area a_i. It represents the error due to the stylus and to the process of leveling the profile.

$$\Delta a_i = \Delta a_{\text{lev}} + \Delta a_{\text{stylus}} \tag{H.3}$$

The first source of error on a_i is proportional to the amount of wear. Experimental verification led to the approximated value of 5%. The second source of error is very dependent on the sample initial surface roughness. Indeed, as determined by the experimental calculations, it is equal to 20, 10 or 5 mil^2 for, respectively, EXS 5/15, NRL and EXS samples (except EXS 5/15), and for Silgan® J-501 coated samples.

Equation H.3 becomes

$$\Delta a_{\text{i}} = \Delta a_{\text{lev}} + 0.05 \times a_i \tag{H.4}$$

where Δa_{lev} is constant for a given coating formula.

Another contribution to the error magnitude, ΔA_{M}, is the deviation to the assumption of a linear model as described previously such that

$$\Delta A_{\text{tot.}} = \Delta A_{\text{m}} + \Delta A_{\text{M}}. \tag{H.5}$$

This term can be evaluated experimentally by measuring the wear area at various equidistant locations around the wear scar. The wear area is then plotted in terms of the distance between measurement and the deviation from linearity is evaluated. The deviation from linearity for NRL and EXS samples is approximately equal to ± 20, ± 10 and ± 5 mil^2 for, respectively, EXS 5/15, NRL and EXS samples (except EXS 5/15), and for Silgan® J-501 coated samples.

Therefore:

$$\Delta A_{\text{tot.}} = Constant + \Delta A_{\text{stylus}} \tag{H.6}$$

$$\Delta A_{\text{stylus}} = 0.0125 \times \frac{(a_1 + a_2 + a_3 + a_4)}{4} \tag{H.7}$$

with Constant equal to ± 30, ± 20 and ± 10 mil^2 for, respectively, EXS 5/15, NRL and EXS samples (except EXS 5/15), and for Silgan® J-501 coated samples.

The procedure to evaluate the measurement error on the wear depth is similar to that of the wear area.

The measurement error for the wear rate is estimated as follows. The wear rate is defined by

$$\text{rate} = \frac{A}{\text{brush strokes}} \tag{H.8}$$

where A is the wear area.

Therefore, the error is

$$\Delta\text{rate} = \frac{\text{brush strokes} \times \Delta A_{\text{tot}} + A_{\text{tot}} \times \Delta\text{brush strokes}}{(\text{brush strokes})^2} \tag{H.9}$$

where Δbrush strokes is approximately equal to 130 brush strokes and ΔA_{tot} is defined by equation H.6.

Vita

Anne-Claire Christiaen, daughter of Anne-Marie and Jean Christiaen, was born on December 15, 1970, in Versailles, France. In 1988, she enrolled as a chemical engineer student at the University of Technology of Compiègne, France. In 1992, for the fifth and final year of her undergraduate studies, she took part of the exchange program with Virginia polytechnic Institute and State University as a Master of Science student. In 1993, she received her B.S. in Chemical Engineering from the University of Technology of Compiègne, France and pursued her M.S. in Surface Science at Virginia Tech under the supervision of Dr. D. F. Cox. In August 1994, she received her Master of Science degree in Chemical Engineering specializing in surface science. Upon completion of her Ph.D., she will work at Battelle Memorial Institute, in Columbus OH, as a research scientist.

Permanent Address: 8, rue Verlaine
78960 Voisins-le-Bx, France

This dissertation was typeset with LaTeX 2_ε[1] by the author.

[1] LaTeX 2_ε is an extension of LaTeX. LaTeX is a collection of macros for TeX. TeX is a trademark of the American Mathematical Society. The macros used in formatting this dissertation were written by Greg Walker, Department of Mechanical Engineering, Virginia Tech.